TECHNICAL REPORT

FOR

NASA Grant NAG-2-541

NASA Technical Monitor: Alex Woo

Grant Title: A NEW TECHNIQUE FOR SIMULATING COMPOSITE MATERIAL

Institution: The Radiation Laboratory
Department of Electrical Engineering
and Computer Science
The University of Michigan
Ann Arbor, MI 48109-2122

Period Covered: February 1990 - September 1990

Report Title: Electromagnetic Scattering from Two-Dimensional Thick Material Junctions

Report Authors: M.A Ricoy and J.L. Volakis

Principal Investigator: John L. Volakis
Telephone: (313) 764-0500

engn
UMR 0378

Electromagnetic Scattering From Two-Dimensional Thick Material Junctions

August, 1990

M. A. Ricoy and J. L. Volakis

Radiation Laboratory
Department of Electrical Engineering and Computer Science
The University of Michigan
Ann Arbor, Michigan 48109-2122

Abstract-Because material junctions are commonplace on structures whose radar cross section is of interest, it is essential that their scattering properties be adequately characterized. The standard impedance boundary condition (SIBC) has been employed in the past along with function theoretic techniques to develop simple scattering models of material junctions with thin and/or high loss slabs. To extend these models to more general slabs, generalized impedance boundary conditions (GIBCs) and generalized sheet transition conditions (GSTCs) have been proposed. Unfortunately, the solutions obtained with these are usually non-unique in the form of unknown constants, and although the constants have been resolved for a few special cases, previous efforts were unable to determine them in the general case.

This report examines the problem of the plane wave diffraction by an arbitrary symmetric two-dimensional junction, where Generalized Impedance Boundary Conditions (GIBCs) and Generalized Sheet Transition Conditions (GSTCs) are employed to simulate the slabs. In chapter 2, GIBCs and GSTCs are constructed for multilayer planar slabs of arbitrary thickness and the resulting GIBC/GSTC reflection coefficients are compared with exact counterparts to evaluate the GIBCs/GSTCs. In chapter 3 the plane wave diffraction by a multilayer material slab recessed in a perfectly conducting ground plane is formulated and solved via the Generalized Scattering Matrix Formulation (GSMF) in conjunction with the dual integral equation approach. Various scattering patterns are computed and validated with exact results where possible.

In chapter 4, the diffraction by a material discontinuity in a thick dielectric/ferrite slab is considered by modelling the constituent slabs with GSTCs. A non-unique solution in terms of unknown constants is obtained, and these constants are evaluated for the recessed slab geometry of chapter 3 by comparison with the solution obtained therein. Several other simplified cases are also presented and discussed. In chapter 5 an eigenfunction expansion method is introduced to determine the unknown solution constants in the general case. This procedure is applied to the solution of chapter 4, and scattering patterns are presented for various slab junctions and compared with alternative results where possible. Chapter six presents a short summary of this report and some recommendations for future work.

TABLE OF CONTENTS

LIST OF FIGURES iii

LIST OF TABLES viii

CHAPTER

I. INTRODUCTION . . . . .

II. DERIVATION OF GENERALIZED TRANSITION/ BOUNDARY CONDITIONS FOR PLANAR MULTIPLE LAYER STRUCTURES 10

2.1 Derivation of Infinite Order Conditions 14
2.2 Low and High Contrast Approximations for Matrix Element Operators 22
2.3 Evaluation of the Boundary/Transition Conditions 27
2.4 Concluding Remarks 43

III. DIFFRACTION BY A MULTILAYER SLAB RECESSED IN A GROUND PLANE VIA GENERALIZED IMPEDANCE BOUNDARY CONDITIONS 44

3.1 Description of GSMF Procedure 48
3.2 Plane Wave Diffraction and Mode Coupling 51
3.3 Reflection and Launching of a Waveguide Mode 56
3.4 Computation of Spectra for Material Insert in a Perfectly Conducting Ground Plane 58
3.5 Specialization to the GIBC Representation 59
3.6 Numerical Results 62
3.7 Summary 69

IV GENERAL SOLUTION OF THE DIFFRACTION BY A MATERIAL DISCONTINUITY IN A THICK DIELECTRIC FERRITE SLAB 73

4.1 Dual Integral Equation Formulation 76
4.2 Solution of the Dual Integral Equations 82
4.3 Discussion of the Solution and Some Applications 86
4.3.1 Diffraction by thin single layer discontinuous slabs . 86
4.3.2 Diffraction by a resistive-resistive junction 92
4.3.3 Diffraction by grounded metal-dielectric junctions . 93
4.3.4 Diffraction by a thin dielectic/ferrite half plane . . . 99
4.4 Conclusion 99

V. RESOLUTION OF NON-UNIQUENESS ASSOCIATED WITH THE GIBC/GSTC SOLUTION 101

5.1 Modal Decomposition for the Symmetric Slab Problem 103
5.1.1 Exterior Cross Section Functions 105
5.1.2 Interior Cross Section Functions 107
5.2 Recasting of the Dual Integral Equation Solution for a Material Discontinuity 111
5.3 Determination of the Constants 122
5.4 Validation of the Solution 128
5.5 Summary 132

VI. SUMMARY 153

APPENDICES 157

BIBLIOGRAPHY 161

LIST OF FIGURES

Figure

1.1 Structures modelled by SIBCs. 2

1.2 Resistive/conductive sheet simulation of thin slab. 4

2.1 Infinite multilayer slab. 11

2.2 (a) Multilayer coating on ground plane. (b) Equivalent opaque sheet. 12

2.3 (a) Zero thickness resistive and conductive sheet similation of multilayer slab. (b) Distributed resistive and conductive sheet simulation of multilayer slab. 13

2.4 Coordinate system for reflection and transmission coefficient derivation. 27

2.5 E_y polarization low contrast simulation of a single layer having relative constitutive parameters $\epsilon = 2$, $\mu = 1.2$ 30

2.6 E_y polarization low contrast simulation of a single layer having relative constitutive parameters $\epsilon = 3.5$, $\mu = 2$. 31

2.7 E_y polarization high contrast simulation of a single layer having $\epsilon = 3.5$, $\mu = 2$ 32

2.8 E_y polarization high contrast simulation of a single layer having $\epsilon = 5$, $\mu = 3$ 33

2.9 H_y polarization low contrast simulation of a single layer having relative constitutive parameters $\epsilon = 2$, $\mu = 1.2$ 36

2.10 H_y polarization low contrast simulation of a single layer having relative constitutive parameters $\epsilon = 3.5$, $\mu = 2$. 37

2.11 H_y polarization high contrast simulation of a single layer having $\epsilon = 3.5$, $\mu = 2$ 38

2.12 H_z polarization high contrast simulation of a single layer having $\epsilon = 5$, $\mu = 3$ 39

2.13 Simulation of a three layer slab using a 14^{th} order condition. 40

2.14 Simulation of a three layer coating on a PEC ground plane using a 14^{th} order condition. 41

2.15 Simulation of a three layer coating on a PMC ground plane using a 14^{th} order condition. 42

3.1 (a) Multilayer slab recessed in a PEC ground plane. (b) Representation of slab as surface with reflection coefficient R. 45

3.2 Illustration of recessed stub geometry (a) and associated subproblems: (b) direct diffraction, (c) mode coupling, (d) stub reflection, (e) mode reflection at the waveguide mouth, (f) mode launching. 46

3.3 H_z polarization backscatter echo width for a material insert with $\tau = .2\lambda$, $\epsilon = 2 - j.0001$, $\mu = 1.2$ modeled by low contrast GIBCs (see Table 3.1 for an explanation of the legend entries). (a) direct diffraction component (b) modal component (c) composite. 63

3.4 H_z polarization backscatter echo width for a material insert with $\tau = .4\lambda$, $\epsilon = 3.5 - j.0001$, $\mu = 2$ modeled by low contrast GIBCs (see Table 3.1 for an explanation of the legend entries). (a) direct diffraction component (b) modal component (c) composite. 64

3.5 H_z polarization backscatter echo width for a material insert with $\tau = .4\lambda$, $\epsilon = 3.5 - j.0001$, $\mu = 2$ modeled by high contrast GIBCs (see Table 3.2 for an explanation of the legend entries). (a) direct diffraction component (b) modal component (c) composite. 66

3.6 H_z polarization backscatter echo width for a material insert with $\tau = .4\lambda$, $\epsilon = 11. - j.0001$, $\mu = 7$ modeled by high contrast GIBCs (see Table 3.2 for an explanation of the legend entries). 70

3.7 H_z polarization backscatter echo width for a three-layer material insert with ($\tau_1 = .4\lambda$, $\epsilon_1 = 11. - j.0001$, $\mu_1 = 7$), ($\tau_2 = .4\lambda$, $\epsilon_2 = 3.5 - j.0001$, $\mu_2 = 2$), ($\tau_3 = .2\lambda$, $\epsilon_3 = 2. - j.0001$, $\mu_3 = 1.2$). In the legend entry a,b,c(d,e), a and b denote the approximation in κ^{-1} of the high constrast layers 1 and 2, c denotes the approximation in τ of the low constast layer 3, while d is the order of the composite GIBC and e is the total number of modes. 71

4.1 (a) Distributed sheet. (b) Distributed sheet discontinuity. 74

4.2 Geometries modeled by a discontinuous distributed sheet. (a) Material half-plane. (b) Material-material join. (c) Grounded join. . . . 75

4.3 (a) Illustration of C contour in the complex α plane and (b) complex λ plane. 79

4.4 Thin slab structures and their distributed sheet representation (a) Material-material junction. (b) Material-metallic join. (c) Material half-plane. (d) Equivalent distributed sheet. 87

4.5 (a) Recessed slab (PEC stub) (b) Grounded slab with truncated upper plate (c) Recessed slab (PMC stub) (d) GIBC sheet 94

4.6 H_z polarization backscatter echo width for a material insert having $w = .04\lambda$, $\epsilon = 2 - j.0001$, $\mu = 1.2$ modeled with $O(w)$ low contrast GIBCs 97

4.7 H_z polarization backscatter echo width for a material insert having $w = .10\lambda$, $\epsilon = 2 - j.0001$, $\mu = 1.2$ modeled with $O(w^3)$ low contrast GIBCs; $b_{10} = -.4578 + j.2593$, $b_{11} = -.0408 - j.0111$, $b_{20} = -.0401 - j.0388$. 98

5.1 Symmetric multilayer slab discontinuity illuminated by a plane wave 102

5.2 Symmetric multilayer slab with irregular termination illuminated by a polarized field excitation 103

5.3 (a) C contour in the complex λ plane. (b) Deformation for region 1 integrals. (c) Deformation for region 2 integrals. 115

5.4 Indexing scheme for constants. 124

5.5 H_z polarization backscatter echo width for a recessed slab with $\tau = .4$, $\epsilon = 2$, $\mu = 1.2$ modeled by $O(\tau)$ second order low contrast GIBC (see Table 5.2 for constants). 133

5.6 H_z polarization backscatter echo width for a recessed slab with $\tau = .1$, $\epsilon = 2$, $\mu = 1.2$ modeled by $O(\tau^3)$ fourth order low contrast GIBC (see Table 5.2 for constants). 134

5.7 H_z polarization backscatter echo width for a recessed slab with τ = .4, $\epsilon = 5$, $\mu = 3$ modeled by $O(\kappa^{-1})$ second order high contrast GIBC (see Table 5.2 for constants). 135

5.8 H_z polarization backscatter echo width for a material half-plane with τ = .005, $\epsilon = 2$, $\mu = 1.2$ modeled by $O(\tau)$ low contrast GSTC (see Table 5.2 for constants). 136

5.9 H_z polarization backscatter echo width for a material half-plane with τ = .05, $\epsilon = 2$, $\mu = 1.2$ modeled by $O(\tau)$ low contrast GSTC (see Table 5.2 for constants). 137

5.10 H_z polarization backscatter echo width for a material half-plane with τ = .10, $\epsilon = 2$, $\mu = 1.2$ modeled by $O(\tau)$ low contrast GSTC (see Table 5.2 for constants). 138

5.11 H_z polarization backscatter echo width for a material half-plane with τ = .20, $\epsilon = 2$, $\mu = 1.2$ modeled by $O(\tau)$ and $O(\tau^3)$ low contrast GSTC (see Table 5.2 for constants). 139

5.12 H_z polarization backscatter echo width for a material half-plane with τ = .01, $\epsilon = 5$, $\mu = 3$ modeled by $O(\kappa^0)$ (even symmetry) and $O(\kappa^{-1})$ (odd symmetry) high contrast GSTC. The free space side is modeled by $O(\tau)$ (even symmetry) $O(\tau^2)$ (odd symmetry) low contrast GSTC. (see Table 5.3 for constants). 140

5.13 H_z polarization backscatter echo width for a material half-plane with τ = .05, $\epsilon = 5$, $\mu = 3$ modeled by $O(\kappa^0)$ (even symmetry) and $O(\kappa^{-1})$ (odd symmetry) high contrast GSTC. The free space side is modeled by $O(\tau)$ (even symmetry) $O(\tau^2)$ (odd symmetry) low contrast GSTC. (see Table 5.3 for constants). 141

5.14 H_z polarization backscatter echo width for a two layer .07λ symmetric material half-plane with $\tau_1 = .005$, $\epsilon_1 = 5$, $\mu_1 = 3$ and $\tau_2 = .03$, $\epsilon = 2$, $\mu = 1.2$. Layer 1 is modeled by $O(\kappa^0)$ GSTC, layer 2 and the free space layer are modeled by $O(\tau)$ (even symmetry) $O(\tau^2)$ (odd symmetry) low contrast GSTC (see Table 5.3 for constants). 142

5.15 H_z polarization backscatter echo width curves for different thickness material half-planes with $\epsilon = 2$, $\mu = 1.2$. All cases are modeled by $O(\tau)$ low contrast GSTC (see Table 5.3 for constants). 143

5.16 H_z polarization backscatter echo width curves for different thickness grounded slabs with $\epsilon = 5$, $\mu = 3$. The number to the left of the colon denotes the $O(\tau)$ of the l.c. GIBC for the free space side, and the number to the right of the colon denotes the $O(\kappa^{-1})$ of the h.c. slab GIBC. 144

5.17 H_z polarization backscatter echo width curves for different thickness grounded slabs with $\epsilon = 11$, $\mu = 7$. The number to the left of the colon denotes the $O(\tau)$ of the l.c. GIBC for the free space side, and the number to the right of the colon denotes the $O(\kappa^{-1})$ of the h.c. GIBC for the right hand slab. 145

5.18 H_z polarization backscatter echo width curves for different thickness grounded junctions, with $\epsilon_1 = 2$, $\mu_1 = 1.2$ and $\epsilon_2 = 5$, $\mu_2 = 3$. The number to the left of the colon denotes the $O(\tau)$ of the l.c. GIBC for the left hand slab and the number to the right of the colon denotes the $O(\kappa^{-1})$ of the h.c. GIBC for the right hand slab. 146

5.19 H_z polarization backscatter echo width curves for different thickness grounded junctions, with $\epsilon_1 = 5$, $\mu_1 = 3$ and $\epsilon_2 = 11$, $\mu_2 = 7$. The number to the left of the colon denotes the $O(\kappa^{-1})$ of the h.c. GIBC for the left hand slab and the number to the right of the colon denotes the $O(\kappa^{-1})$ of the h.c. GIBC for the right hand slab. 147

5.20 H_z polarization backscatter echo width curves a grounded junctions, with $\epsilon_1 = 2$, $\mu_1 = 1.2$, $\tau_1 = .025$ and $\epsilon_2 = 5$, $\mu_2 = 3$. The first number to the left of the colon denotes the $O(\tau)$ of the l.c. GIBC for the left hand slab and the first number to the right of the colon denotes the $O(\kappa^{-1})$ of the h.c. GIBC for the right hand slab. The second number on either side of the colon denotes the $O(\tau)$ of the l.c. GIBC for the free space slab needed to give the two sides the same thickness. 148

5.21 H_z polarization backscatter echo width curves a grounded junctions, with $\epsilon_1 = 5$, $\mu_1 = 3$, $\tau_1 = .05$ and $\epsilon_2 = 11$, $\mu_2 = 7$. The first number to the left of the colon denotes the $O(\kappa^{-1})$ of the h.c. GIBC for the left hand slab and the first number to the right of the colon denotes the $O(\kappa^{-1})$ of the h.c. GIBC for the right hand slab. The second number on either side of the colon denotes the $O(\tau)$ of the l.c. GIBC for the free space slab needed to give the two sides the same thickness. 149

LIST OF TABLES

Table

2.1 Low constrast approximations to q_{ij} operators. 2

2.2 High constrast approximations to q_{ij} operators. 2

3.1 Low contrast approximation to waveguide modes for a layer with $\epsilon = 3.5 - j.0001, \mu = 2.0$, and $\tau = .4\lambda$. For each low contrast boundary condition, the three numbers of the column headings indicate the order of the approximation in thickness τ, the order of the resulting boundary condition, and the total number of modes (see chapter two). 67

3.2 High contrast approximation to waveguide modes for a layer with $\epsilon = 3.5 - j.0001, \mu = 2.0$, and $\tau = .4\lambda$. For each high contrast boundary condition, the three numbers of the column headings indicate the approximation in the index of refraction κ^{-1}, the order of the resulting boundary condition, and the total number of modes. 68

4.1 Odd symmetry parameters for distributed sheet similation of right hand side material $x > 0$. See Appendix 1 for definition of M_+ split functions. 90

4.2 Even symmetry parameters for distributed sheet similation of right hand side material $x > 0$. See Appendix 1 for definition of M_+ split functions. 91

5.1 Asymptotic behavior of integrand for the functions $F_{diff}(x = 0^{\pm}, y)$. 127

5.2 Values of solution constants for curves presented in Figures 5 to 12 . 150

5.3 Values of solution constants for curves presented in Figures 12 to 15 151

CHAPTER I

INTRODUCTION

The use of non-metallic materials is now commonplace on airborne vehicles, and frequently two material slabs of different composition will abut each other to form a junction. For example, thin radar-absorber material (RAM) strips of different composition are often joined end-to-end on a metal surface for radar cross section reduction. Also, in microstrip antenna configurations a discontinuity in substrate composition is used to suppress unwanted surface waves and in many cases a planar array is terminated at a metal-dielectric junction. The electromagnetic effectiveness of structures and devices such as RAM coatings or microstrip antennas is influenced by the scattering behavior of any material junctions present. It is therefore important to obtain a characterization of their behavior.

The scattering behavior of a material slab junction is revealed by an examination of its plane wave diffraction, and this is the overall topic of the dissertation. For discussion purposes, it is useful to divide these into non-penetrable and penetrable slab junctions. The scattering problem associated with non-penetrable junctions was aided greatly by the introduction of standard impedance boundary conditions (SIBCs) [35], introduced to model thin metal backed coatings and layers of high loss (see Figure 1.1). Conceptually, SIBCs are first order boundary conditions

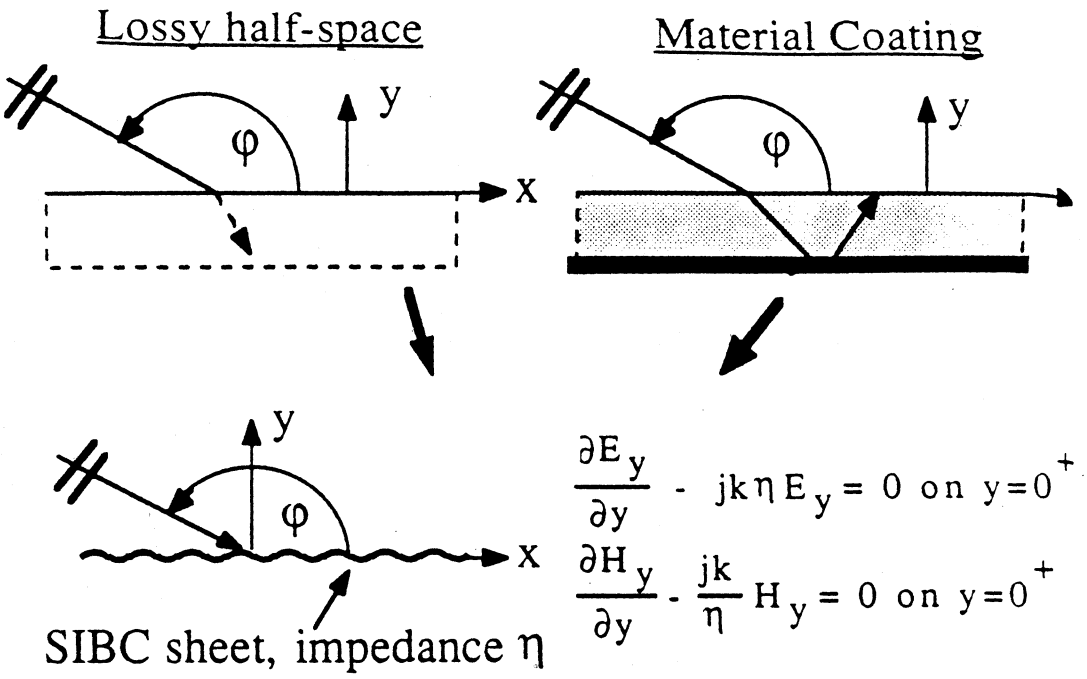

Figure 1.1: Structures modelled by SIBCs.

which replace the original material slab with an equivalent "sheet," on which the tangential electric and magnetic fields are related through a simple proportionality factor known as the "impedance" of the sheet. Alternatively, the SIBC relates the normal field components and their normal derivatives by the same proportionality factor. The SIBC model thus eliminates the need to consider the field interior to the slab, reducing a two-medium problem to a one-medium one.

Following this modeling scheme, grounded slab junctions and coated half-planes are represented as discontinuous SIBC sheets, which readily permit the application of function theoretic techniques such as the Weiner-Hopf method to obtain diffraction solutions. These techniques yield a unique solution upon application of the standard edge condition [49], which dictates that the stored energy in the vicinity of the

[1]the order of a boundary or transition condition refers to the order of the highest derivative present when the condition is cast in its normal derivative format

discontinuity must remain finite. This two step approach in computing the diffraction from slab junctions has been successfully exploited by many researchers [34] [18] [47] [27] [30]. However, the approach is predicated on the validity of the SIBC, which is restricted to modeling very thin and/or lossy coatings. More general slab junctions must therefore be characterized by other methods.

With regard to junctions formed by penetrable slabs, a close analog to the SIBC sheet model is the "resistive" and "conductive" sheet simulation [12] [37]. These sheets are characterized by simple first order transition conditions which relate the tangential fields across the sheets. In particular, a resistive sheet (see Figure 1.2), supports an equivalent electric current which produces a discontinuity in the tangential magnetic field across the sheet. The proportionality factor relating the tangential magnetic field discontinuity to the equivalent electric current is denoted as the "resistivity" Similarly, the conductive sheet model is the dual of the resistive sheet and supports an equivalent magnetic current, with the resulting proportionality factor denoted as the "conductivity" of the sheet. Like the SIBC models above, resistive and conductive sheets models of slab half-planes and junctions are amenable to Weiner-Hopf methods for the computation of diffraction solutions [1] [44], with the same comments given above applying here also. We remark, however, that the resistive and conductive sheet models are very restrictive (much more so than SIBC models) and cannot be used unless the modeled slabs are very thin and of high permittivity and/or permeability. Hence, as in the case of impenetrable slab junctions, alternative methods are needed to model more general junctions.

One such exact approach was employed by Aoki and Uchida [3] to tackle the problem of plane wave diffraction from a penetrable single-layer slab junction. Their method involved rewriting the junction field components in terms of a Fourier se-

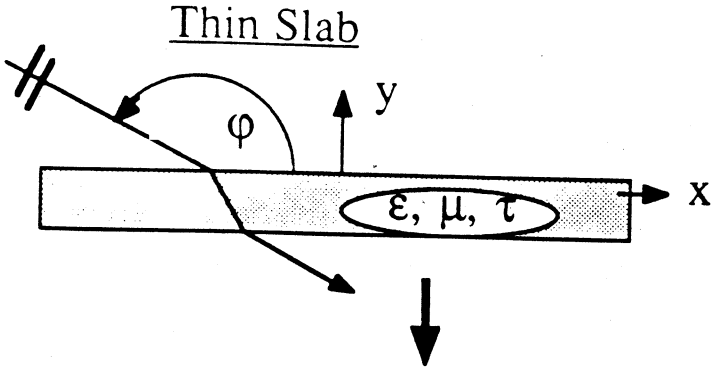

$$\tau \to 0$$
$$\varepsilon \to \infty$$
$$\mu \to \infty$$
$$jk\tau(\varepsilon-1) \to 1/\mathcal{R}_e$$
$$jk\tau(\mu-1) \to 1/\mathcal{R}_m$$

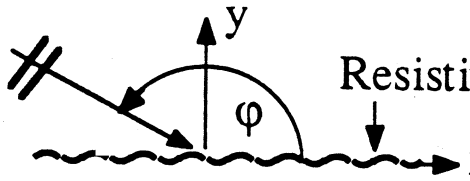

$$E_x^+ + E_x^- = 2\mathcal{R}_e Z_o (H_z^+ - H_z^-) \;,\; E_z^+ + E_z^- = -2\mathcal{R}_e Z_o (H_x^+ - H_x^-)$$

+

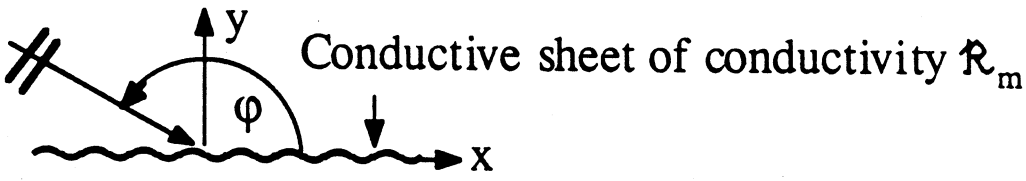

$$Z_o (H_x^+ + H_x^-) = -2\mathcal{R}_m (E_z^+ - E_z^-) \;,\; Z_o (H_z^+ + H_z^-) = 2\mathcal{R}_m (E_x^+ - E_x^-)$$

Figure 1.2: Resistive/conductive sheet simulation of thin slab.

ries representation. This approach subsequently led to the generation of Weiner-Hopf equations expressed in terms of unknown spectral functions. However, explicit expressions for these functions could not be obtained, and the resulting solution involved a cumbersome iterative procedure requiring knowledge of rather complex integrals and functions.

Another possible approach to modeling thicker and more penetrable layered discontinuities is to replace the SIBC and resistive sheet transition conditions (STC) by generalized impedance boundary conditions (GIBC) [15] [17] [23] and generalized sheet transition conditions (GSTC) [59] [39], respectively. The GIBC and GSTC are equivalent one- and two-sided sheet representations which, unlike their SIBC and STC counterparts, display second and possibly higher order derivatives of the field components on the equivalent sheet. These higher order derivatives are responsible for the increased accuracy of the GIBC/GSTC relative to the SIBC/STC, and the effectiveness of the GIBC/GSTC is roughly proportional to their order. This, of course, implies that an adequate GIBC/GSTC modeling of any layered material is possible, provided that GIBC or GSTC of sufficient order are employed. Many GIBCs and GSTCs have been derived to model all types of single and multiple layers [59] [39] [4] [31] [43]. However, most of these GIBC/GSTC are either limited in order (usually second) or else are only valid for specific geometries. This, of course, points to the need for developing more general GIBC and GSTC capable of simulating a wide variety of layered slabs and coatings.

Once a slab junction is represented as a discontinuous GIBC/GSTC sheet, then function-theoretic techniques may again be applied to compute the plane wave diffraction, as in the SIBC/STC case. However, function theoretic solutions based on the application of GIBC/GSTC simulations yield solutions which are non-unique

even after the application of the standard edge condition [32] [41] [43] [56]. Also, reciprocity is not necessarily satisfied [14] [4] [7], unless this condition is explicitly enforced. Uniqueness is required of any physical solution, whereas reciprocity with respect to the transmitter and receiver is necessary when the scattering body is electrically passive. As noted in [41], one may take advantage of this inherent non-uniqueness to force a solution which is at least reciprocal, if not unique. The non-uniqueness of the solution is usually manifested in terms of unknown constants [41] for finite-order GIBC/GSTC and unknown entire functions [32] for infinite-order GIBC/GSTC. Most GIBC/GSTC diffraction solutions to date have been obtained using second order GIBC/GSTC, and some of these have put forth arguments dealing with the cancellation of non-physical poles to propose a unique solution [53] [54] [43] [5]. However, these previous efforts offer no method of determining the unknown constants for more general GIBC/GSTC simulations.

If left unresolved, this issue would seriously impede the practical utilization of GIBC/GSTC for a characterization of material junctions. In an attempt to resolve it, the unknown constant appearing in a second order GIBC solution was recently related to the field at the sheet discontinuity [42]. Unfortunately, the edge field is seldom known apriori and this relation is not therefore of practical use. Nevertheless, it demonstrated that a unique solution may be possible with a GIBC/GSTC simulation. An example where it was possible to obtain a unique solution is given by Leppington [21], who considered the surface wave reflection by an abrupt change in slab thickness. The slab was modelled using second order transition conditions equivalent to those given in [59] and [39]. Leppington was able to determine the reflection coefficient uniquely in the limiting case of vanishing thickness by matching the interior field far from the junction with a static representation of the interior field in the vicinity of

the junction. This suggests the possibiltiy of working with internal fields to resolve the uniqueness issue, an approach which to date has received little attention and is exploited herein.

The goal of this dissertation is to develop a plane wave diffraction model for general symmetric thick multilayer slab junctions. Four main chapters follow dealing with the derivation of the GIBC/GSTC, the formulation and formal solution of the plane wave diffraction by certain GIBC/GSTC approximated slab junctions, and the subsequent resolution and explanation of the non-uniqueness phenomenon described above.

In chapter two, arbitrary order GIBC and GSTC are constructed for multilayered planar slabs of arbitrary thickness. Initially, recurrence relations are derived for the fields in adjacent layers and are then employed to develop infinite order boundary/transition conditions that are conveniently expressed as a matrix product. Approximations to the matrix element operators for low and high contrast materials are subsequently employed to obtain finite order boundary/transition conditions. Finally, numerical results are presented in which the exact reflection coefficients are compared with those implied by the GIBC/GSTC to provide a measure of the conditions accuracy and utility.

In chapter three, the plane wave diffraction by a multilayer material slab recessed in a perfectly conducting ground plane is formulated and solved via the Generalized Scattering Matrix Formulation (GSMF) in conjunction with the dual integral equation approach. This problem is significant in that a unique GIBC solution is obtained which can be used as a benchmark to test other GIBC/GSTC solutions. In the first part of the chapter we summarize the GSMF procedure. The dual integral equation method is then employed to formulate each of the subproblems and the necessary

solutions are obtained for both E_z and H_z polarizations. These are given in terms of symbolic split functions which are then evaluated for the specific case of a multilayer grounded slab by casting the reflection coefficient in a form compatible with a GIBC simulation of chapter two. A number of scattering patterns are presented and the accuracy of the GIBC simulation is examined by comparison with known results for homogeneous slabs.

In chapter four, the diffraction by a material discontinuity in a thick dielectric/ferrite slab is considered by modelling the slab as a distributed current sheet obeying generalized sheet transition conditions (GSTC). In the first section of the chapter, the GSTC representation of the distributed sheet discontinuity is used to develop dual integral equations in terms of the unknown spectral functions proportional to the sheet currents. These equations are then solved in the standard manner to yield expressions for the spectral functions in terms of unknown constants. The constants are dependent on the geometry and properties of the discontinuity, and are identified in this chapter for a few specific discontinuous layers whose diffraction solution is available.

Chapter five deals specifically with the determination of the unknown constants for the solution presented in chapter four. This is accomplished by introducing a general eigenfunction expansion which is valid everywhere and subsequently recasting the solution obtained in chapter four into this format. This field is then analytically continued to the slab interior and continuity is applied at the material junction to provide the remaining constraints for determining the unknown constants. Specifically a point matching scheme is proposed in which an overdetermined system of equations is generated and solved for the constants using a least-squares technique. Various diffraction patterns are given validating the obtained solution for certain

electric half-planes and metal-dielectric junctions on a ground plane. Finally curves are given for various thick half-planes and junctions to illustrate their diffraction behavior as a function of thickness.

CHAPTER II

DERIVATION OF GENERALIZED TRANSITION/BOUNDARY CONDITIONS FOR PLANAR MULTIPLE LAYER STRUCTURES

A GIBC/GSTC diffraction coefficient can only be as good or as versatile as its constituent GIBC/GSTC. Therefore, before diffraction coefficients of any generality can be developed it is necessary to construct GIBC/GSTC which are valid across all ranges of slab composition and thickness, and this is the task of this chapter. The two configurations considered herein are the multilayered slab having symmetric or non-symmetric material composition (about its center) and the multilayered coating on a ground plane, as illustrated in Figures 2.1 and 2.2(a), respectively. The derivation of the GIBC/GSTC is accomplished via the Taylor series expansion method, whose versatility enables the treatment of non-planar as well as planar layers. In effect, the resulting conditions allow the simulation of the multilayered configuration as an opaque or transparent sheet (see Figures 2.2(b) and 2.3(b), respectively).

In proceeding with the development of the GIBC/GSTC, we initially derive recurrence relations for the fields in adjacent layers. These are subsequently employed to develop infinite order boundary/transition conditions that are conveniently expressed as a matrix product. Approximations to the matrix element operators

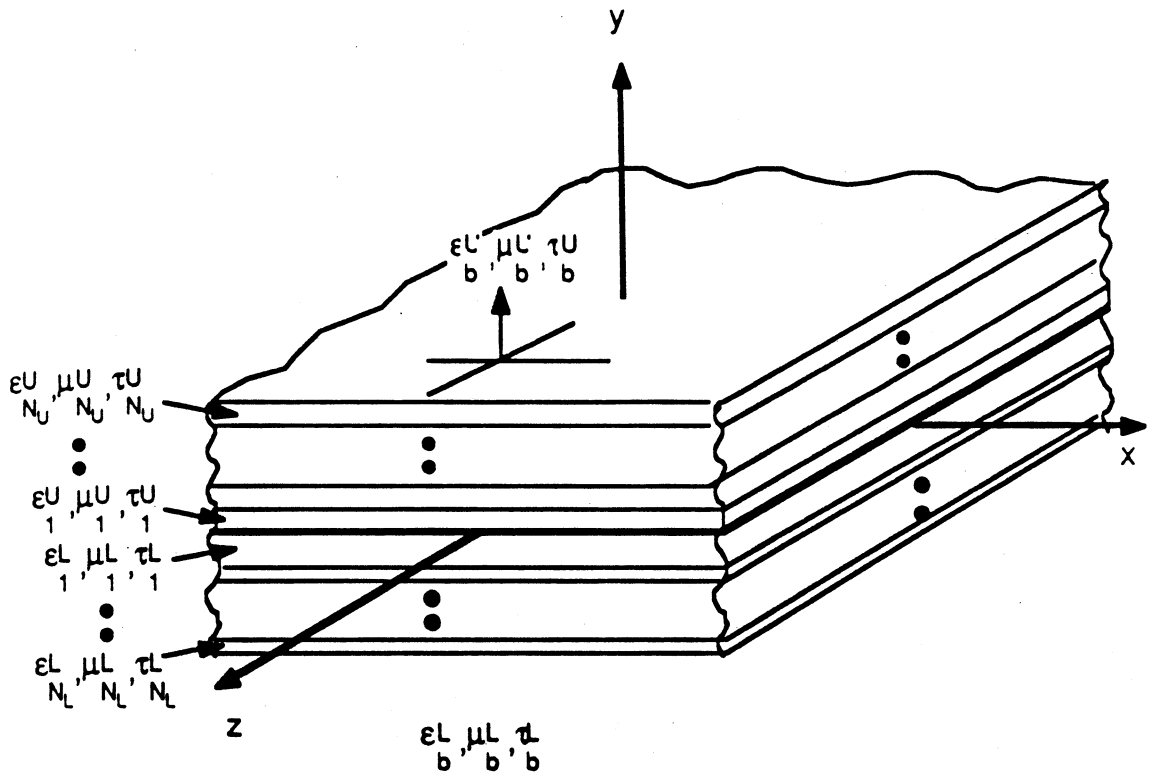

Figure 2.1: Infinite multilayer slab.

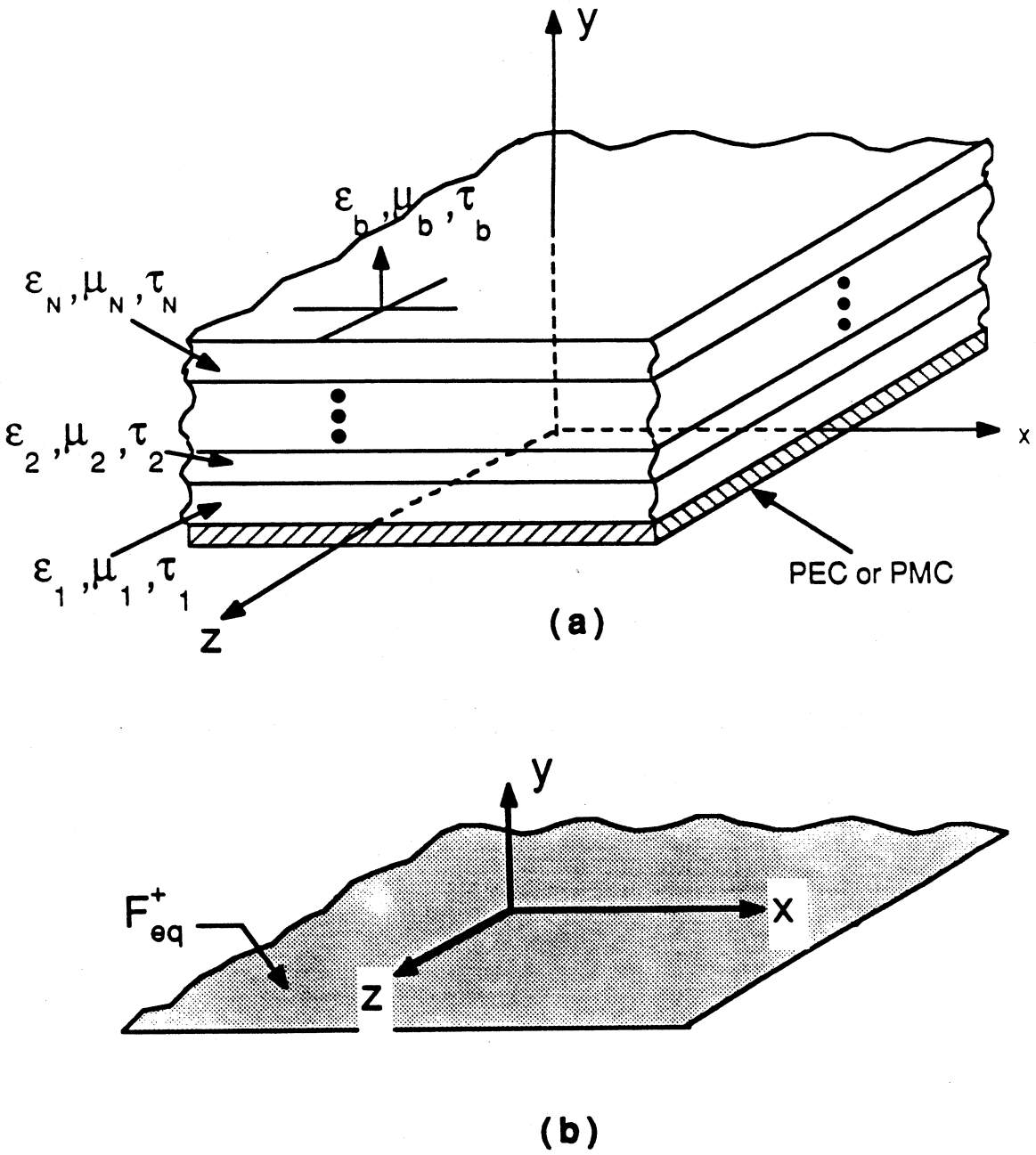

Figure 2.2: (a) Multilayer coating on ground plane. (b) Equivalent opaque sheet.

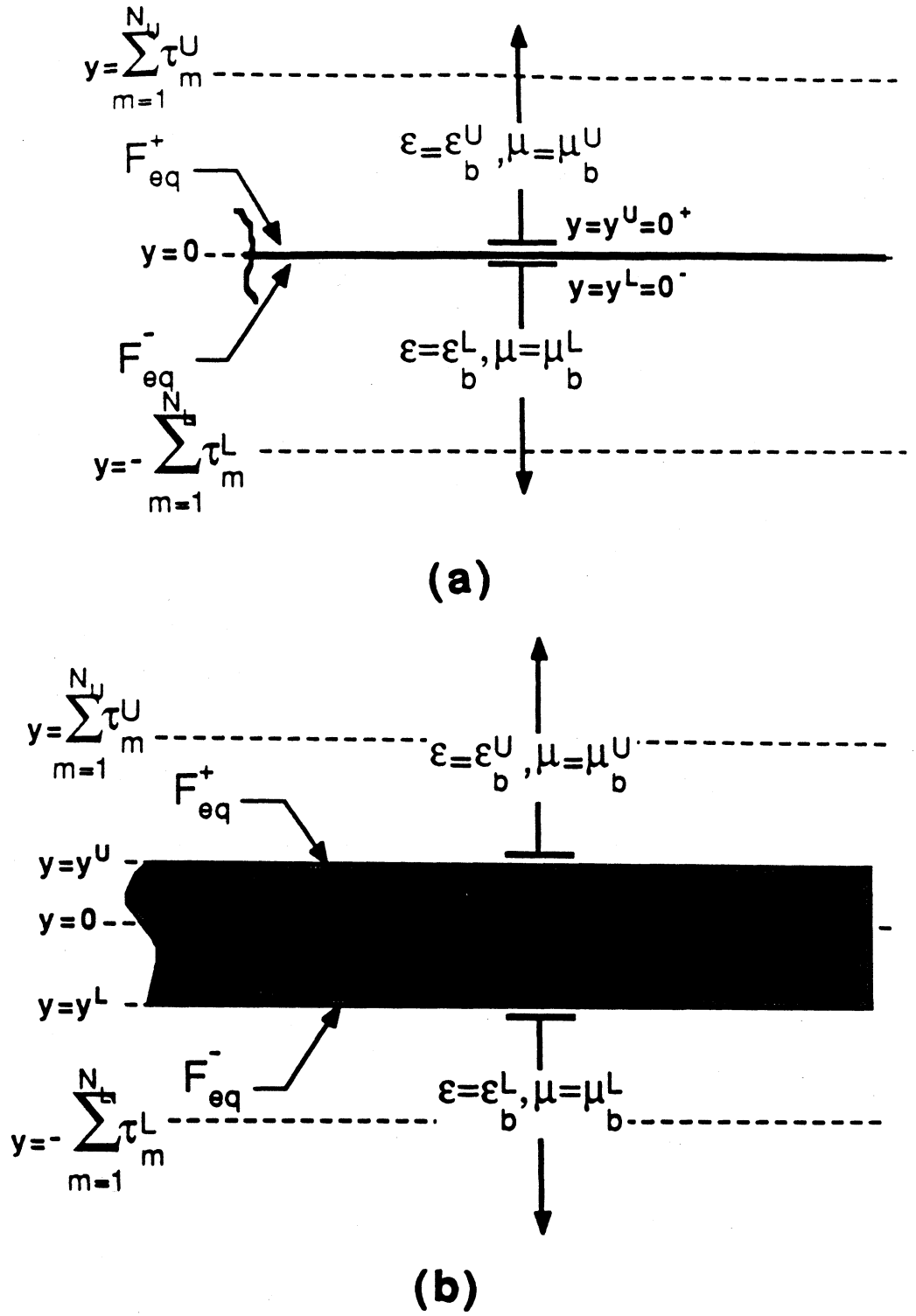

Figure 2.3: (a) Zero thickness resistive and conductive sheet similation of multilayer slab. (b) Distributed resistive and conductive sheet simulation of multilayer slab.

low and high contrast materials then lead to finite order boundary conditions. Finally, numerical results are presented in which the exact reflection coefficients are compared with those implied by the GIBC/GSTC to provide a measure of the conditions' accuracy and utility.

2.1 Derivation of Infinite Order Conditions

Consider the multiple layer slab with N_U upper layers ($y > 0$) and N_L lower layers ($y < 0$) as illustrated in Figure 2.1. The physical parameters corresponding to the m^{th} upper layer are denoted by $\epsilon_m^U, \mu_m^U, \kappa_m^U, \tau_m^U$ which refer to the relative permittivity and permeability, the index of refraction and the layer thickness, respectively. In a similar manner, the physical parameters corresponding to the m^{th} lower layer are given by $\epsilon_m^L, \mu_m^L, \kappa_m^L, \tau_m^L$. In the following we derive transition conditions to effectively replace their presence with a distributed current sheet. We begin this derivation by first introducing a relation between the fields on the two sides of a single layer. This is generalized to relate the fields of distant layers and those at the upper and lower boundaries of the fictitious current sheet. For convenience, we may consider both polarizations simultaneously by introducing the definitions

$$\begin{aligned} F_y &= \begin{cases} E_y, & E_y \text{ polarization } (H_y = 0) \\ H_y, & H_y \text{ polarization } (E_y = 0) \end{cases} \\ u &= \begin{cases} \epsilon, & E_y \text{ polarization} \\ \mu, & H_y \text{ polarization} \end{cases} \end{aligned} \tag{2.1}$$

Using a Taylor series expansion, the normal field components at the top and bottom of the m^{th} upper layer may be related as

$$u_m F_y\big|_{y=\tau_1^U+\tau_2^U+\cdots+(\tau_{m-1}^U)^+} = u_m \sum_{l=0}^{\infty} \frac{(jk\tau_m)^l}{(l)!} \delta_y^l F_y\big|_{y=\tau_1^U+\cdots+\tau_{m-1}^U+(\tau_m^U)^-} \tag{2.2}$$

$$\delta_y F_y\big|_{y=\tau_1^U+\cdots+(\tau_{m-1}^U)^+} = \sum_{l=0}^{\infty} \frac{(jk\tau_m)^l}{(l)!} \delta_y^{l+1} F_y\big|_{y=\tau_1^U+\tau_2^U+\cdots+\tau_{m-1}^U+(\tau_m^U)^-} \tag{2.3}$$

where

$$\tau^{\pm} = \tau \pm 0^{+} \tag{2.4}$$

and δ_y is an operator defined as

$$\delta_y = \frac{j}{k}\frac{\partial}{\partial y} \tag{2.5}$$

Clearly, (2.2) - (2.3) provide relations of the fields within a single layer and if we are to derive a condition relating the fields at the top and/or lower surface of the slab, it is necessary to establish similar relations among the fields in different layers. As a first step towards this goal we may proceed to express the right hand sides of (2.2) and (2.3) in terms of the fields above the boundary $y = \tau_1^U + \ldots + \tau_m^U$. To do so, it is instructive to resolve the right hand sides of (2.2) and (2.3) into a summation of odd and even derivatives of F_y. Subsequently, the wave equation may be invoked to rewrite the normal derivatives in tangential form, thus allowing the application of the field continuity conditions. We have

$$\delta_y^2 = \epsilon_m^U \mu_m^U - \delta_t^2, \tag{2.6}$$

with

$$\delta_t^2 = \delta_x^2 + \delta_z^2 \tag{2.7}$$

where

$$\begin{aligned} \delta_x &= \frac{j}{k}\frac{\partial}{\partial x} \\ \delta_z &= \frac{j}{k}\frac{\partial}{\partial z}. \end{aligned} \tag{2.8}$$

Invoking now the continuity of $u_m F_y$ and $\delta_y^l F_y$ (including their tangential derivatives) across the layer boundaries, (2.2) and (2.3) may be rewritten as

$$\bar{F}\big]_{y=\tau_1^U+\tau_2^U+\ldots+(\tau_{m-1}^U)^+} = \bar{\bar{Q}}_U(u_m^U, \kappa_m^U, \tau_m^U, \delta_t^2) \cdot \bar{F}\big]_{y=\tau_1^U+\tau_2^U+\ldots+(\tau_m^U)^+}. \tag{2.9}$$

In this,

$$\bar{F} = \begin{pmatrix} uF_y \\ \delta_y F \end{pmatrix} \tag{2.10}$$

$$\bar{\bar{Q}}_L(u,\kappa,\tau,\delta_t^2) = \begin{pmatrix} q_{11}(u,\kappa,\tau,\delta_t^2) & q_{12}(u,\kappa,\tau,\delta_t^2) \\ q_{21}(u,\kappa,\tau,\delta_t^2) & q_{22}(u,\kappa,\tau,\delta_t^2) \end{pmatrix} \tag{2.11}$$

$$\begin{aligned} q_{11}(u,\kappa,\tau,\delta_t^2) &= \cos\left(k_o\tau\sqrt{\kappa^2-\delta_t^2}\right) \\ q_{12}(u,\kappa,\tau,\delta_t^2) &= ju\frac{\sin\left(k_o\tau\sqrt{\kappa^2-\delta_t^2}\right)}{\sqrt{\kappa^2-\delta_t^2}} \\ q_{21}(u,\kappa,\tau,\delta_t^2) &= \frac{j}{u}\sqrt{\kappa^2-\delta_t^2}\sin\left(k_o\tau\sqrt{\kappa^2-\delta_t^2}\right) \\ q_{22}(u,\kappa,\tau,\delta_t^2) &= \cos\left(k_o\tau\sqrt{\kappa^2-\delta_t^2}\right). \end{aligned} \tag{2.12}$$

Expressions relating the normal fields in adjacent lower layers may be obtained in a similar manner. We have,

$$\bar{F}\big]_{y=-\tau_1^L-\tau_2^L-\ldots-(\tau_{m-1}^L)^+} = \bar{\bar{Q}}_L(u_m^L,\kappa_m^L,\tau_m^L,\delta_t^2)\cdot\bar{F}\big]_{y=-\tau_1^L-\tau_2^L-\ldots-(\tau_m^L)^+} \tag{2.13}$$

where now

$$\bar{\bar{Q}}_L(u,\kappa,\tau,\delta_t^2) = \begin{pmatrix} q_{11}(u,\kappa,\tau,\delta_t^2) & -q_{12}(u,\kappa,\tau,\delta_t^2) \\ -q_{21}(u,\kappa,\tau,\delta_t^2) & q_{22}(u,\kappa,\tau,\delta_t^2) \end{pmatrix} \tag{2.14}$$

Equations (2.9) - (2.14) constitute fundamental recurrence relations for developing multilayer GIBC/GSTC. Each of the q_{11}, q_{12}, etc. is an infinite-order linear differential operator in even powers of δ_t^2. This is evident when the *sin* and *cos* terms are cast in their Taylor series representation (note that the square root functions appearing in (2.12) do not have branch cuts). The finite-order boundary conditions are then derived by truncating the Taylor series representation of q_{11}, q_{12}, q_{21}, and q_{22}.

Applying (2.9) and (2.13) recursively, we may establish a relation between the fields at the top and bottom of the layer. We have

$$\left[\prod_{m=1}^{N_L}\bar{\bar{Q}}_L(u_m^L,\kappa_m^L,\tau_m^L,\delta_t^2)\right]\cdot\bar{F}\big]_{y=-\tau_1^L-\tau_2^L-\ldots-(\tau_{N_L}^L)^+} = \bar{F}\big]_{y=0^-} \tag{2.15}$$

$$\left[\prod_{m=1}^{N_U}\bar{\bar{Q}}_U(u_m^U,\kappa_m^U,\tau_m^U,\delta_t^2)\right]\cdot\bar{F}\big|_{y=\tau_1^U+\tau_2^U+\ldots+(\tau_{N_U}^U)^+} = \bar{F}\big|_{y=0^+} \tag{2.16}$$

and since $\bar{F}$ is continuous across $y=0$, (2.15) - (2.16) imply the GSTC condition

$$\left[\prod_{m=1}^{N_L}\bar{\bar{Q}}_L(u_m^L,\kappa_m^L,\tau_m^L,\delta_t^2)\right]\cdot\bar{F}\big|_{y=-\tau_1^L-\tau_2^L-\ldots-(\tau_{N_L}^L)^+} \tag{2.17}$$
$$=\left[\prod_{m=1}^{N_U}\bar{\bar{Q}}_U(u_m^U,\kappa_m^U,\tau_m^U,\delta_t^2)\right]\cdot\bar{F}\big|_{y=\tau_1^U+\tau_2^U+\ldots+(\tau_{N_U}^U)^+}$$

The part of the slab occupying $y^U < y < \tau_1^U+\tau_2^U+\ldots+\tau_{N_U}^U$ may now be replaced by the upper background medium (with its geometrical and material parameters denoted by the subscript b and the superscript U) while the part of the slab occupying $y^L > y > -\tau_1^L-\tau_2^L-\ldots-\tau_{N_L}^L$ is replaced by the lower background material (with geometrical and material parameters denoted by the subscript b and the superscript L). Using a Taylor series expansion the boundary fields may be related to the equivalent fields at $y=y^U$ and $y=y^L$. In so doing, we obtain

$$\left[\prod_{m=1}^{N_L}\bar{\bar{Q}}_L(u_m^L,\kappa_m^L,\tau_m^L,\delta_t^2)\right]\bar{\bar{Q}}_U(u_b^L,\kappa_b^L,\tau_b^L,\delta_t^2)\cdot\bar{F}_{eq}\big|_{y=y^L}$$
$$=\left[\prod_{m=1}^{N_U}\bar{\bar{Q}}_U(u_m^U,\kappa_m^U,\tau_m^U,\delta_t^2)\right]\bar{\bar{Q}}_L(u_b^U,\kappa_b^U,\tau_b^U,\delta_t^2)\cdot\bar{F}_{eq}\big|_{y=y^U}. \tag{2.18}$$

where

$$\begin{aligned}\tau_b^L &= \sum_{l=1}^{N_L}\tau_l^L-(-y^L)\\ \tau_b^U &= \sum_{l=1}^{N_U}\tau_l^U-(y^U)\end{aligned} \tag{2.19}$$

Although compact, the transition conditions (2.18) provide little insight into the physics they represent. It is therefore instructive to reorganize them in a form that leads to its physical interpretation. To this end we introduce the definitions

$$\left[\prod_{m=1}^{N_L}\bar{\bar{Q}}_L(\epsilon_m^L,\kappa_m^L,\tau_m^L,\delta_t^2)\right]\bar{\bar{Q}}_U(\epsilon_b^L,\kappa_b^L,\tau_b^L,\delta_t^2) \stackrel{\text{def}}{=} \begin{pmatrix}\mathcal{L}_{11}^e(\delta_t^2) & \mathcal{L}_{12}^e(\delta_t^2)\\ \mathcal{L}_{21}^e(\delta_t^2) & \mathcal{L}_{22}^e(\delta_t^2)\end{pmatrix}$$

$$\left[\prod_{m=1}^{N_L}\bar{\bar{Q}}_L(\mu_m^L,\kappa_m^L,\tau_m^L,\delta_t^2)\right]\bar{\bar{Q}}_L(\mu_b^L,\kappa_b^L,\tau_b^L,\delta_t^2) \stackrel{\text{def}}{=} \begin{pmatrix}\mathcal{L}_{11}^h(\delta_t^2) & \mathcal{L}_{12}^h(\delta_t^2)\\ \mathcal{L}_{21}^h(\delta_t^2) & \mathcal{L}_{22}^h(\delta_t^2)\end{pmatrix}$$

$$\left[\prod_{m=1}^{N_U}\bar{\bar{Q}}_U(\epsilon_m^U,\kappa_m^U,\tau_m^U,\delta_t^2)\right]\bar{\bar{Q}}_L(\epsilon_b^U,\kappa_b^U,\tau_b^U,\delta_t^2) \stackrel{\text{def}}{=} \begin{pmatrix}\mathcal{U}_{11}^e(\delta_t^2) & \mathcal{U}_{12}^e(\delta_t^2)\\ \mathcal{U}_{21}^e(\delta_t^2) & \mathcal{U}_{22}^e(\delta_t^2)\end{pmatrix}$$

$$\left[\prod_{m=1}^{N_U}\bar{\bar{Q}}_U(\mu_m^U,\kappa_m^U,\tau_m^U,\delta_t^2)\right]\bar{\bar{Q}}_L(\mu_b^U,\kappa_b^U,\tau_b^U,\delta_t^2) \stackrel{\text{def}}{=} \begin{pmatrix}\mathcal{U}_{11}^h(\delta_t^2) & \mathcal{U}_{12}^h(\delta_t^2)\\ \mathcal{U}_{21}^h(\delta_t^2) & \mathcal{U}_{22}^h(\delta_t^2)\end{pmatrix} \quad (2.20)$$

Substituting these into (2.18) yields

$$\begin{pmatrix}[\mathcal{L}_{11}^e+\mathcal{U}_{11}^e](\delta_t^2) & [\mathcal{L}_{12}^e+\mathcal{U}_{12}^e](\delta_t^2)\\ [\mathcal{L}_{21}^e+\mathcal{U}_{21}^e](\delta_t^2) & [\mathcal{L}_{22}^e+\mathcal{U}_{22}^e](\delta_t^2)\end{pmatrix}\begin{pmatrix}\Delta F_J^e\\ \Delta F_M^e\end{pmatrix} = \begin{pmatrix}[\mathcal{L}_{11}^e-\mathcal{U}_{11}^e](\delta_t^2) & [\mathcal{L}_{12}^e-\mathcal{U}_{12}^e](\delta_t^2)\\ [\mathcal{L}_{21}^e-\mathcal{U}_{21}^e](\delta_t^2) & [\mathcal{L}_{22}^e-\mathcal{U}_{22}^e](\delta_t^2)\end{pmatrix}\begin{pmatrix}M^e\\ J^e\end{pmatrix} \quad (2.21)$$

$$\begin{pmatrix}[\mathcal{L}_{11}^h+\mathcal{U}_{11}^h](\delta_t^2) & [\mathcal{L}_{12}^h+\mathcal{U}_{12}^h](\delta_t^2)\\ [\mathcal{L}_{21}^h+\mathcal{U}_{21}^h](\delta_t^2) & [\mathcal{L}_{22}^h+\mathcal{U}_{22}^h](\delta_t^2)\end{pmatrix}\begin{pmatrix}\Delta F_M^h\\ \Delta F_J^h\end{pmatrix} = \begin{pmatrix}[\mathcal{L}_{11}^h-\mathcal{U}_{11}^h](\delta_t^2) & [\mathcal{L}_{12}^h-\mathcal{U}_{12}^h](\delta_t^2)\\ [\mathcal{L}_{21}^h-\mathcal{U}_{21}^h](\delta_t^2) & [\mathcal{L}_{22}^h-\mathcal{U}_{22}^h](\delta_t^2)\end{pmatrix}\begin{pmatrix}J^h\\ M^h\end{pmatrix} \quad (2.22)$$

In (2.21) -(2.22) $\Delta F_J^{e,h}$ and $\Delta F_M^{e,h}$ are given as

$$\begin{aligned}\Delta F_J^e &= \epsilon_b^U E_y^+ - \epsilon_b^L E_y^- = \frac{1}{j\omega}\hat{y}\cdot\bar{\delta}_t\times\left[\bar{H}_t^+ - \bar{H}_t^-\right]\\ \Delta F_M^e &= \delta_y\left[E_y^+ - E_y^-\right] = -\bar{\delta}_t\cdot\left[\bar{E}_t^+ - \bar{E}_t^-\right]\\ \Delta F_M^h &= \mu_b^U H_y^+ - \mu_b^L H_y^- = \frac{-1}{j\omega}\hat{y}\cdot\bar{\delta}_t\times\left[\bar{E}_t^+ - \bar{E}_t^-\right]\\ \Delta F_J^h &= \delta_y\left[H_y^+ - H_y^-\right] = -\bar{\delta}_t\cdot\left[\bar{H}_t^+ - \bar{H}_t^-\right],\end{aligned} \quad (2.23)$$

whereas $M^{e,h}$ and $J^{e,h}$ are defined as

$$\begin{aligned}M^e &= \epsilon_b^U E_y^+ + \epsilon_b^L E_y^- = \frac{1}{j\omega}\hat{y}\cdot\bar{\delta}_t\times\left[\bar{H}_t^+ + \bar{H}_t^-\right]\\ J^e &= \delta_y\left[E_y^+ + E_y^-\right] = -\bar{\delta}_t\cdot\left[\bar{E}_t^+ + \bar{E}_t^-\right]\\ J^h &= \mu_b^U H_y^+ + \mu_b^L H_y^- = \frac{-1}{j\omega}\hat{y}\cdot\bar{\delta}_t\times\left[\bar{E}_t^+ + \bar{E}_t^-\right]\\ M^h &= \delta_y\left[H_y^+ + H_y^-\right] = -\bar{\delta}_t\cdot\left[\bar{H}_t^+ + \bar{H}_t^-\right],\end{aligned}$$

$$
\begin{aligned}
\bar{\delta}_t &\stackrel{\text{def}}{=} \delta_x\hat{x} + \delta_z\hat{z} \\
\bar{E}_t &\stackrel{\text{def}}{=} E_x\hat{x} + E_y\hat{y} \\
\bar{H}_t &\stackrel{\text{def}}{=} H_x\hat{x} + H_y\hat{y} \\
E_y^+ &\stackrel{\text{def}}{=} E_y^{eq}\big]_{y=y^U} \\
E_y^- &\stackrel{\text{def}}{=} E_y^{eq}\big]_{y=y^L} \\
H_y^+ &\stackrel{\text{def}}{=} H_y^{eq}\big]_{y=y^U} \\
H_y^- &\stackrel{\text{def}}{=} H_y^{eq}\big]_{y=y^L}.
\end{aligned}
\tag{2.25}
$$

We also note that the superscript notation e and h refer to E_y and H_y polarized excitations, respectively.

In view of (2.24), the transition conditions given by (2.21) and (2.22) are now readily interpreted as a representation of "distributed" resistive and conductive sheets occupying the volume $y^U < y < y^L$ and supporting equivalent electric and magnetic currents (see Figure 2.3a). These, of course, give rise to discontinuities in the fields (and their tangential derivatives) at the upper and lower boundary of the sheets. The equivalent electric and magnetic currents are denoted by $J^{e,h}$ and $M^{e,h}$, respectively, and are defined in (2.24) above. Additionally, the subscripts J and M appearing in (2.23) denote field discontinuities traditionally associated with the presence of electric or magnetic currents, respectively. For convenience, the currents and resulting discontinuities ΔF are presented in terms of both normal and tangential fields. When $y^U = 0^+$ and $y^L = 0^-$ (see Figure 2.3b), the distributed resistive and conductive sheets are "compressed" onto an infinitely thin sheet occupying the plane $y = 0$. Such thin sheet representations are attractive for the application of transform techniques in diffraction problems and are generalizations of the resistive-conductive

sheet simulations given in [59], [39] and [31]. In contrast to the referenced simulations, the ones given here exhibit coupled electric and magnetic currents, whose presence complicates the application of analytical techniques. This coupling is attributable to the distributed nature of the polarization currents across the original slab configuration. If, however, the multilayered slab is symmetric about $y = 0$ and $y^U = -y^L$, then it can be shown that M and J decouple. In particular, for this special case

$$\begin{aligned} \mathcal{L}_{11} &= \mathcal{U}_{11} \\ \mathcal{L}_{12} &= -\mathcal{U}_{12} \\ \mathcal{L}_{21} &= -\mathcal{U}_{21} \\ \mathcal{L}_{22} &= \mathcal{U}_{22}, \end{aligned} \tag{2.26}$$

leading to

$$\begin{aligned} \mathcal{U}^e_{11}(\delta_t^2)\{\Delta F^e_J\} &= -\mathcal{U}^e_{12}(\delta_t^2)\{J^e\} \\ \mathcal{U}^e_{22}(\delta_t^2)\{\Delta F^e_M\} &= -\mathcal{U}^e_{21}(\delta_t^2)\{M^e\} \\ \mathcal{U}^h_{11}(\delta_t^2)\{\Delta F^h_M\} &= -\mathcal{U}^h_{12}(\delta_t^2)\{M^h\} \\ \mathcal{U}^h_{22}(\delta_t^2)\{\Delta F^h_J\} &= -\mathcal{U}^h_{21}(\delta_t^2)\{J^h\} \end{aligned} \tag{2.27}$$

when substituted into (2.21) and (2.22). Evidently, the coupling of the current components depends on the degree of asymmetry in the slab and an assessment on the level of coupling can be obtained by comparing the magnitude of the operator coefficients in $\mathcal{L}_{11} - \mathcal{U}_{11}$, $\mathcal{L}_{12} + \mathcal{U}_{12}$, $\mathcal{L}_{21} + \mathcal{U}_{21}$ and $\mathcal{L}_{22} - \mathcal{U}_{22}$ relative to those in $\mathcal{L}_{11} + \mathcal{U}_{11}$, $\mathcal{L}_{12} - \mathcal{U}_{12}$, $\mathcal{L}_{21} - \mathcal{U}_{21}$ and $\mathcal{L}_{22} + \mathcal{U}_{22}$.

If a ground plane is inserted in the symmetric slab at $y = 0$, the resulting structure becomes opaque and its sheet simulation is further simplified. For the case where the

ground plane is a perfect electric conductor (PEC), the electric currents are shorted out and the second and third equations of (2.27) become the boundary conditions corresponding to a coated PEC. Conversely, a perfect magnetic conductor (PMC) shorts out the magnetic currents, leaving the first and fourth equations of (2.27) as the corresponding sheet simulation. An alternative approach to deriving the GIBC corresponding to coatings is to employ image theory in conjunction with (2.27). The field components in the equivalent image configuration of a PEC grounded slab are related as

$$\begin{aligned} E_y(y>0) &= E_y(y<0) \\ \delta_y E_y(y>0) &= -\delta_y E_y(y<0) \\ H_y(y>0) &= -H_y(y<0) \\ \delta_y H_y(y>0) &= \delta_y H_y(y<0) \end{aligned} \tag{2.28}$$

and when these are subsequently introduced in (2.27) we obtain the boundary conditions

$$\begin{aligned} \epsilon_b^U \mathcal{U}_{21}^e(\delta_t^2)\{E_y^+\} + \mathcal{U}_{22}^e(\delta_t^2)\{\delta_y E_y^+\} &= 0 \\ \mu_b^U \mathcal{U}_{11}^h(\delta_t^2)\{H_y^+\} + \mathcal{U}_{12}^h(\delta_t^2)\{\delta_y H_y^+\} &= 0. \end{aligned} \tag{2.29}$$

corresponding to a slab on a PEC. Similarly, the image fields for a slab on a PMC satisfy the relations

$$\begin{aligned} E_y(y>0) &= -E_y(y<0) \\ \delta_y E_y(y>0) &= \delta_y E_y(y<0) \\ H_y(y>0) &= H_y(y<0) \\ \delta_y H_y(y>0) &= -\delta_y H_y(y<0) \end{aligned} \tag{2.30}$$

$$\epsilon_b^U \mathcal{U}_{11}^e(\delta_t^2)\{E_y^+\} + \mathcal{U}_{12}^e(\delta_t^2)\{\delta_y E_y^+\} = 0$$
$$\mu_b^U \mathcal{U}_{21}^h(\delta_t^2)\{H_y^+\} + \mathcal{U}_{22}^h(\delta_t^2)\{\delta_y H_y^+\} = 0. \quad (2.3)$$

when substituted in (2.27). Expressions (2.29) and (2.31) represent opaque conductive and resistive sheets, respectively, and are the dual of each other. We note that if $N_U = 1$, (2.29) reduce to those given in [31].

To summarize the above development, sheet simulations were derived that model (or replace the presence of) the multilayer slab and coating. Equations (2.21) through (2.27) are referred to as generalized sheet transition conditions (GSTC) for the transparent resistive/conductive sheet representation of the multilayered slab. On the other hand, equations (2.29) and (2.31) are described as generalized impedance boundary conditions (GIBC) for the opaque sheet representation of the coated ground plane. They are given in a compact matrix form and are valid for any arbitrary finite number of layers. Their versatility, however, is offset by the presence of infinite order derivatives as implied by the definition of the operators, thus, limiting their applicability to analytical and numerical treatments. It is therefore appropriate to consider finite order approximations of the operators leading to conditions of practical use. In the following we consider such approximations of the operators on the assumption of low contrast (small κ) and high contrast (large κ) layers or coatings.

2.2 Low and High Contrast Approximations for Matrix Element Operators

Low contrast approximations to the matrix element operators may be derived by replacing the trigonometric functions in (2.12) by their Taylor series expansions

which are then truncated. To $O(\tau^M)$ these become

$$\begin{aligned}
q_{11}(u,\kappa,\tau,\delta_t^2) &= q_{22}(u,\kappa,\tau,\delta_t^2) \approx \sum_{l=0}^{int(\frac{M}{2})} \left[\sum_{m=l}^{int(\frac{M}{2})} a_1(\kappa,\tau,l,m) \right] \left(\delta_t^2\right)^l \\
q_{12}(u,\kappa,\tau,\delta_t^2) &\approx ju \sum_{l=0}^{int(\frac{M-1}{2})} \left[\sum_{m=l}^{int(\frac{M-1}{2})} a_2(\kappa,\tau,l,m) \right] \left(\delta_t^2\right)^l \\
q_{21}(u,\kappa,\tau,\delta_t^2) &\approx \frac{j}{u} \sum_{l=0}^{int(\frac{M+1}{2})} \left[\sum_{m=l}^{int(\frac{M+1}{2})} a_3(\kappa,\tau,l,m) \right] \left(\delta_t^2\right)^l \quad m \neq 0
\end{aligned} \tag{2.32}$$

where

$$\begin{aligned}
a_1(\kappa,\tau,l,m) &= \frac{(-1)^{l+m}(m)!(k_o\tau)^{2m}\kappa^{2(m-l)}}{(m-l)!(l)!(2m)!} \\
a_2(\kappa,\tau,l,m) &= \frac{(-1)^{l+m}(m)!(k_o\tau)^{2m+1}\kappa^{2(m-l)}}{(m-l)!(l)!(2m+1)!} \\
a_3(\kappa,\tau,l,m) &= -\frac{(-1)^{l+m}(m)!(k_o\tau)^{2m-1}\kappa^{2(m-l)}}{(m-l)!(l)!(2m-1)!}
\end{aligned} \tag{2.33}$$

It is a simple matter to demonstrate that the substitutions

$$\begin{aligned}
\kappa &\rightarrow \sqrt{\kappa^2 - \kappa_b^2} \stackrel{\text{def}}{=} \tilde{\kappa} \\
\delta_t^2 &\rightarrow -\delta_y^2
\end{aligned} \tag{2.34}$$

applied to (2.32) lead to a normal derivative representation of $q_{11} - q_{22}$.

To obtain high contrast (large κ) approximations for q_{ij}, it is necessary to utilize the binomial expansion

$$\sqrt{\kappa^2 - \delta_t^2} = \kappa \left[1 - \frac{1}{2}\left(\frac{\delta_t}{\kappa}\right)^2 - \frac{1}{2\cdot 4}\left(\frac{\delta_t}{\kappa}\right)^4 - \frac{1\cdot 3}{2\cdot 4\cdot 6}\left(\frac{\delta_t}{\kappa}\right)^6 - \cdots \right] \quad ; \quad |\frac{\delta_t\{\}}{\kappa}| < 1. \tag{2.35}$$

Substituting this into (2.12) and again employing a Taylor series representation for the trigonometric functions, we obtain to $O(\kappa^{-M})$ the approximations

$$q_{11}(u,\kappa,\tau,\delta_t^2) \approx \cos(k_o\tau\kappa)$$

$$
\begin{aligned}
&- \sum_{p=1}^{M} \left[\sum_{l=max\{1,2p-M\}}^{M} \frac{T_1(l,\kappa,\tau)\Upsilon(l,0,p)}{\kappa^{2p-l}} \right] \left(\delta_t^2\right)^p \\
q_{12}(u,\kappa,\tau,\delta_t^2) &\approx \frac{ju}{\kappa}\sin(k_o\tau\kappa) \\
&- ju \sum_{p=1}^{M-1} \left[\sum_{l=max\{1,2p-M+1\}}^{M-1} \frac{T_2(l,\kappa,\tau)\Upsilon(l,0,p)}{\kappa^{2p+1-l}} \right] \left(\delta_t^2\right)^p \\
&+ ju \sum_{p=1}^{M-2} \left[\sum_{l=max\{1,2p-M+2\}}^{M-2} \frac{T_2(l-1,\kappa,\tau)\Upsilon(l-1,1,p)}{\kappa^{2p+2-l}} \right] \left(\delta_t^2\right)^p \\
q_{21}(u,\kappa,\tau,\delta_t^2) &\approx \frac{j\kappa}{u}\sin(k_o\tau\kappa) \\
&+ \frac{j}{u} \sum_{p=1}^{M+1} \left[\sum_{l=max\{1,2p-M-1\}}^{M+1} \frac{T_2(l,\kappa,\tau)\Upsilon(l,0,p)}{\kappa^{2p-1-l}} \right] \left(\delta_t^2\right)^p \\
&- \frac{j}{u} \sum_{p=1}^{M} \left[\sum_{l=max\{1,2p-M\}}^{M} \frac{T_2(l-1,\kappa,\tau)\Upsilon(l,0,p)}{\kappa^{2p-l}} \right] \left(\delta_t^2\right)^p \qquad (2.36)
\end{aligned}
$$

$$
\begin{aligned}
T_1(l,\kappa,\tau) &= \frac{(-1)^{int(l/2)}(k_o\tau)^l}{(l)!} \begin{cases} \cos(k_o\tau\kappa) & ; l \text{ is even} \\ \sin(k_o\tau\kappa) & ; l \text{ is odd} \end{cases} \\
T_2(l,\kappa,\tau) &= \frac{(-1)^{int(l/2)}(k_o\tau)^l}{(l)!} \begin{cases} \sin(k_o\tau\kappa) & ; l \text{ is even} \\ -\cos(k_o\tau\kappa) & ; l \text{ is odd} \end{cases} \\
\Upsilon(l_1,l_2,p) &= \sum b_1(i_1)b_1(i_2)\cdots b_1(i_{l_1})b_2(i_{l_1+1})\cdots b_2(i_{l_1+l_2}) \\
b_1(p) &= \frac{(2p-3)!!}{2^p p!} \\
b_2(p) &= \frac{(2p-1)!!}{2^p p!} \\
X!! &\stackrel{def}{=} X(X-2)(X-4)\ldots(3)(1) \;;\; (-1)!! \stackrel{def}{=} 1 \qquad (2.37)
\end{aligned}
$$

The sum defining the function $\Upsilon(l_1, l_2, p)$ includes all product terms satisfying the relation $\sum_m i_m = p$. It should also be noted that l_1 and l_2 denote the number of b_1 and b_2, respectively, comprising the product terms. For example, if $l_1 = 2$, $l_2 = 1$ and $p = 3$ then $\Upsilon(2,1,3) = b_1(1)b_1(1)b_2(1)$; if $l_1 = 2$, $l_2 = 1$ and $p = 4$ then $\Upsilon(2,1,4) = b_1(2)b_1(1)b_2(1) + b_1(1)b_1(2)b_2(1) + b_1(1)b_1(1)b_2(2)$ and if $l_1 = 2$, $l_2 = 0$ and $p = 4$ then $\Upsilon(2,0,4) = b_1(1)b_1(3) + b_1(2)b_1(2) + b_1(3)b_1(1)$. Corresponding

Order	Low contrast q_{ij} coefficients
τ_1^0	$q_{11} = q_{22} = 1,\ q_{12} = q_{21} = 0$
τ_1^1	$q_{11} = q_{22} = 1,\ q_{12} = ju_1 k\tau_1,\ q_{21} = \frac{j}{u_1} k\tau_1 (\kappa^2 - \delta_t^2)$
τ_1^2	$q_{11} = q_{22} = 1 - \frac{(k\tau_1)^2}{2}(\kappa^2 - \delta_t^2),\ q_{12} = ju_1 k\tau_1,\ q_{21} = \frac{j}{u_1} k\tau_1 (\kappa^2 - \delta_t^2)$
τ_1^3	$q_{11} = q_{22} = 1 - \frac{(k\tau_1)^2}{2}(\kappa^2 - \delta_t^2),\ q_{12} = ju_1 k\tau_1 \left[1 - \frac{(k\tau_1)^2}{6}(\kappa^2 - \delta_t^2)\right],$ $q_{21} = jk\tau_1 (\kappa^2 - \delta_t^2)/u_1 \left[1 - \frac{(k\tau_1)^2}{6}(\kappa^2 - \delta_t^2)\right]$
τ_1^4	$q_{11} = q_{22} = 1 - \frac{(k\tau_1)^2}{2}(\kappa^2 - \delta_t^2) + \frac{(k\tau_1)^4}{24}(\kappa^2 - \delta_t^2)^2$ $q_{21} = jk\tau_1 (\kappa^2 - \delta_t^2)/u_1 \left[1 - \frac{(k\tau_1)^2}{6}(\kappa^2 - \delta_t^2)\right]$

Table 2.1: Low constrast approximations to q_{ij} operators.

expressions in terms of normal derivatives can also be obtained by employing (2.34) in (2.36).

Expressions (2.32) - (2.37) represent finite order approximations to the operators q_{11}, q_{12}, q_{21}, and q_{22}, and can be used to generate finite order GIBC or GSTC. To do so for a specific multilayered slab or coating, one first examines each constituent layer and approximates the corresponding matrix elements by their low contrast expressions (2.32) - (2.33) or high contrast expressions (2.36) - (2.37), as appropriate. As an example, basic low contrast and high constrast approximations to the q_{ij} operators are give in Tables 2.1 and 2.2. These finite order expressions are then substituted into the matrices $\bar{\bar{Q}}_U$ and $\bar{\bar{Q}}_L$ given by (2.11) - (2.14). The resulting expressions for the $\mathcal{U}$ and $\mathcal{L}$ matrix operators are finite polynomials in even powers of δ_t^2. In passing, we note that the simulations presented here-in may also be extended to model a longitudinally inhomogeneous slab once this is approximated as a layered slab such as that shown in Figure 2.1.

Order	High constrast q_{ij} coefficients
κ^0	$q_{11} = q_{22} = \cos(\kappa k\tau_1),\ q_{12} = 0, q_{21} = \frac{j\kappa}{u_1}\sin(\kappa k\tau_1) - \frac{jk\tau_1\delta_r^2}{2u_1}\cos(\kappa k\tau_1)$
κ^{-1}	$q_{11} = q_{22} = \cos(\kappa k\tau_1) + \sin(\kappa k\tau_1)\frac{k\tau_1\delta_r^2}{2\kappa},\ q_{12} = \frac{ju_1}{\kappa}\sin(\kappa k\tau_1)$ $q_{21} = \frac{j\kappa}{u_1}\sin(\kappa k\tau_1)\left\{1 - \frac{\delta_r^2}{2\kappa^2} - \frac{(k\tau_1)^2\delta_r^4}{8\kappa^2}\right\} - \frac{jk\tau_1\delta_r^2}{2u_1}\cos(\kappa k\tau_1)$
κ^{-2}	$q_{11} = q_{22} = \cos(\kappa k\tau_1)\left\{1 - \frac{(k\tau_1)^2\delta_r^4}{8\kappa^2}\right\} + \sin(\kappa k\tau_1)\frac{k\tau_1\delta_r^2}{2\kappa},$ $q_{12} = \frac{ju_1}{\kappa}\sin(\kappa k\tau_1) - \frac{ju_1k\tau_1\delta_r^2}{2\kappa^2}\cos(\kappa k\tau_1),$ $q_{21} = \frac{j\kappa}{u_1}\sin(\kappa k\tau_1)\left\{1 - \frac{\delta_r^2}{2\kappa^2} - \frac{(k\tau_1)^2\delta_r^4}{8\kappa^2}\right\}$ $-\frac{j\kappa}{u_1}\cos(\kappa k\tau_1)\left\{\frac{k\tau_1\delta_r^2}{2\kappa} - \frac{k\tau_1\delta_r^4}{8\kappa^3} - \frac{(k\tau_1)^3\delta_r^6}{48\kappa^3}\right\}$
κ^{-3}	$q_{11} = q_{22} = \cos(\kappa k\tau_1)\left\{1 - \frac{(k\tau_1)^2\delta_r^4}{8\kappa^2}\right\}$ $+\sin(\kappa k\tau_1)\left\{\frac{k\tau_1\delta_r^2}{2\kappa} + \frac{k\tau_1\delta_r^4}{8\kappa^3} - \frac{(k\tau_1)^3\delta_r^6}{48\kappa^3}\right\},$ $q_{12} = \frac{ju_1}{\kappa}\sin(\kappa k\tau_1)\left\{1 + \frac{\delta_r^2}{2\kappa^2} - \frac{(k\tau_1)^2\delta_r^4}{8\kappa^2}\right\} - \frac{ju_1k\tau_1\delta_r^2}{2\kappa^2}\cos(\kappa k\tau_1),$ $q_{21} = \frac{j\kappa}{u_1}\sin(\kappa k\tau_1)\left\{1 - \frac{\delta_r^2}{2\kappa^2} - \frac{(k\tau_1)^2\delta_r^4}{8\kappa^2} - \frac{\delta_r^4}{8\kappa^4} + \frac{(k\tau_1)^4\delta_r^8}{388\kappa^4}\right\},$ $-\frac{j\kappa}{u_1}\cos(\kappa k\tau_1)\left\{\frac{k\tau_1\delta_r^2}{2\kappa} - \frac{k\tau_1\delta_r^4}{8\kappa^3} - \frac{(k\tau_1)^3\delta_r^6}{48\kappa^3}\right\},$

Table 2.2: High constrast approximations to q_{ij} operators.

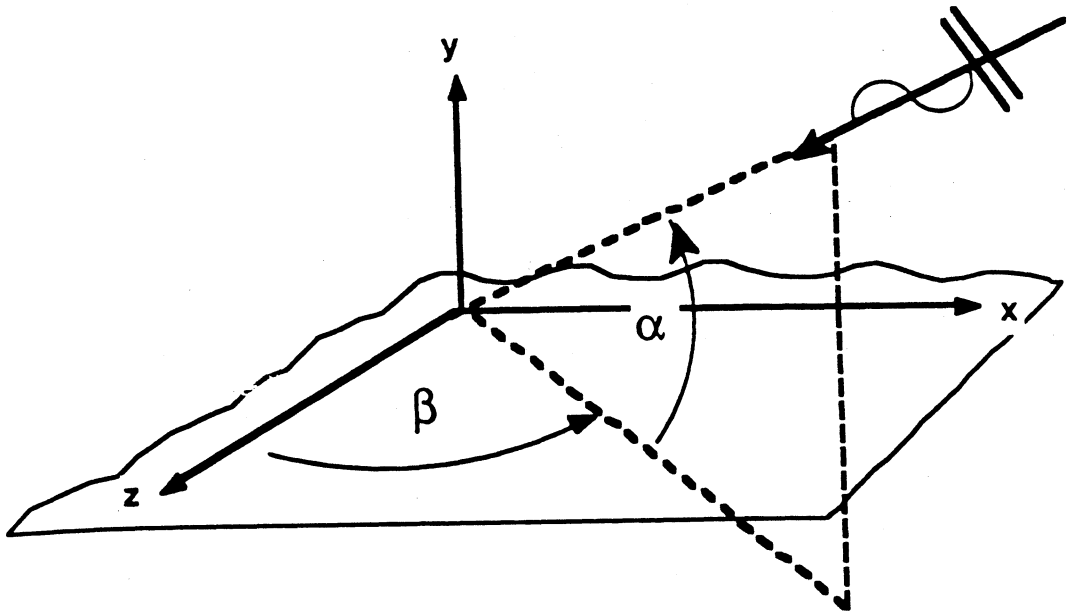

Figure 2.4: Coordinate system for reflection and transmission coefficient derivation.

2.3 Evaluation of the Boundary/Transition Conditions

To evaluate the accuracy of the derived boundary/transition conditions one approach is to compare the plane wave reflection and transmission coefficients implied by the finite order sheet simulation with the corresponding exact coefficients.

Consider the plane wave

$$\begin{Bmatrix} E_y^i \\ H_y^i \end{Bmatrix} = \begin{Bmatrix} E_{y0} \\ H_{y0} \end{Bmatrix} e^{jk\kappa_b^U (x\cos\alpha\sin\beta + y\sin\alpha + z\cos\alpha\cos\beta)} \tag{2.38}$$

incident upon the sheet satisfying a given GIBC or GSTC (see Figure 2.4). The generated reflected field can then be written as

$$\begin{Bmatrix} E_y^r \\ H_y^r \end{Bmatrix} = \begin{Bmatrix} R_E E_{y0} \\ R_H H_{y0} \end{Bmatrix} e^{jk\kappa_b^U (x\cos\alpha\sin\beta - y\sin\alpha + z\cos\alpha\cos\beta)} \tag{2.39}$$

and in the case of a GSTC, the transmitted field takes the form

$$\left\{ \begin{array}{c} E_y^t \\ H_y^t \end{array} \right\} = \left\{ \begin{array}{c} T_E E_{y0} \\ T_H H_{y0} \end{array} \right\} e^{jk\kappa_b^e (x\cos\alpha' \sin\beta' + y\sin\alpha' + z\cos\alpha'\cos\beta')} \tag{2.40}$$

To find the reflection coefficients $R_{E,H}$ and corresponding transmission coefficients $T_{E,H}$ we substitute (2.38) - (2.40) into one of the boundary or transition conditions given by (2.21), (2.22), (2.27), (2.29) or (2.31). By carrying out the differentiations in a straightforward manner we find

$$R_E = \begin{cases} \dfrac{R^e_{\text{pec}}\tilde{R}^e_{\text{pmc}} - \tilde{R}^e_{\text{pec}}R^e_{\text{pmc}}}{\tilde{R}^e_{\text{pmc}} - \tilde{R}^e_{\text{pec}}} & \text{multilayer slab} \\ \frac{1}{2}R^e_{\text{pec}} + \frac{1}{2}R^e_{\text{pmc}} & \text{multilayer symmetric slab} \\ R^e_{\text{pec}} & \text{multilayer coating on PEC} \\ R^e_{\text{pmc}} & \text{multilayer coating on PMC} \end{cases} \tag{2.41}$$

$$T_E = \begin{cases} \dfrac{R^e_{\text{pec}} - R^e_{\text{pmc}}}{\tilde{R}^e_{\text{pec}} - \tilde{R}^e_{\text{pmc}}} & \text{multilayer slab} \\ \frac{1}{2}R^e_{\text{pec}} - \frac{1}{2}R^e_{\text{pmc}} & \text{multilayer symmetric slab} \end{cases} \tag{2.42}$$

$$R_H = \begin{cases} \dfrac{R^h_{\text{pmc}}\tilde{R}^h_{\text{pec}} - \tilde{R}^h_{\text{pmc}}R^h_{\text{pec}}}{\tilde{R}^h_{\text{pec}} - \tilde{R}^h_{\text{pmc}}} & \text{multilayer slab} \\ \frac{1}{2}R^h_{\text{pmc}} + \frac{1}{2}R^h_{\text{pec}} & \text{multilayer symmetric slab} \\ R^h_{\text{pec}} & \text{multilayer coating on PEC} \\ R^h_{\text{pmc}} & \text{multilayer coating on PMC} \end{cases} \tag{2.43}$$

$$T_H = \begin{cases} \dfrac{R^h_{\text{pmc}} - R^h_{\text{pec}}}{\tilde{R}^h_{\text{pmc}} - \tilde{R}^h_{\text{pec}}} & \text{multilayer slab} \\ \frac{1}{2}R^h_{\text{pmc}} - \frac{1}{2}R^h_{\text{pec}} & \text{multilayer symmetric slab.} \end{cases} \tag{2.44}$$

In (2.41) - (2.44),

$$R^e_{\text{pec}} = \frac{\kappa_b^U \sin\alpha\, \mathcal{U}^e_{22}\left[(\kappa_b^U)^2\cos^2\alpha\right] - \epsilon_b^U \mathcal{U}^e_{21}\left[(\kappa_b^U)^2\cos^2\alpha\right]}{\kappa_b^U \sin\alpha\, \mathcal{U}^e_{22}\left[(\kappa_b^U)^2\cos^2\alpha\right] + \epsilon_b^U \mathcal{U}^e_{21}\left[(\kappa_b^U)^2\cos^2\alpha\right]} e^{j2k\kappa_b^U y^U \sin\alpha}$$

$$R^e_{\text{pmc}} = \frac{\kappa_b^U \sin\alpha\, \mathcal{U}^e_{12}\left[(\kappa_b^U)^2\cos^2\alpha\right] - \epsilon_b^U \mathcal{U}^e_{11}\left[(\kappa_b^U)^2\cos^2\alpha\right]}{\kappa_b^U \sin\alpha\, \mathcal{U}^e_{12}\left[(\kappa_b^U)^2\cos^2\alpha\right] + \epsilon_b^U \mathcal{U}^e_{11}\left[(\kappa_b^U)^2\cos^2\alpha\right]} e^{j2k\kappa_b^U y^U \sin\alpha}$$

$$\tilde{R}^e_{\text{pec}} = \frac{\kappa_b^L \sin\alpha'\, \mathcal{L}^e_{22}\left[(\kappa_b^U)^2\cos^2\alpha\right] - \epsilon_b^L \mathcal{L}^e_{21}\left[(\kappa_b^U)^2\cos^2\alpha\right]}{\kappa_b^U \sin\alpha\, \mathcal{U}^e_{22}\left[(\kappa_b^U)^2\cos^2\alpha\right] + \epsilon_b^U \mathcal{U}^e_{21}\left[(\kappa_b^U)^2\cos^2\alpha\right]} e^{jk\left[\kappa_b^L y^L \sin\alpha' + \kappa_b^U y^U \sin\right.}$$

$$\tilde{R}^{e}_{\text{pmc}} = \frac{\kappa_b^L \sin\alpha' \, \mathcal{L}^e_{12} \left[(\kappa_b^U)^2 \cos^2\alpha\right] - \epsilon_b^L \mathcal{L}^e_{11} \left[(\kappa_b^U)^2 \cos^2\alpha\right]}{\kappa_b^U \sin\alpha \, \mathcal{U}^e_{12} \left[(\kappa_b^U)^2 \cos^2\alpha\right] + \epsilon_b^U \mathcal{U}^e_{11} \left[(\kappa_b^U)^2 \cos^2\alpha\right]} e^{jk\left[\kappa_b^L y^L \sin\alpha' + \kappa_b^U y^U \sin\alpha\right]}$$

$$\tilde{R}^{e}_{\text{pec}} = \frac{\kappa_b^U \sin\alpha \, \mathcal{L}^h_{12} \left[(\kappa_b^U)^2 \cos^2\alpha\right] - \mu_b^U \mathcal{L}^h_{11} \left[(\kappa_b^U)^2 \cos^2\alpha\right]}{\kappa_b^U \sin\alpha \, \mathcal{U}^h_{12} \left[(\kappa_b^U)^2 \cos^2\alpha\right] + \mu_b^U \mathcal{U}^h_{11} \left[(\kappa_b^U)^2 \cos^2\alpha\right]} e^{j2k\kappa_b^U y^U \sin\alpha}$$

$$\tilde{R}^{h}_{\text{pmc}} = \frac{\kappa_b^U \sin\alpha \, \mathcal{U}^h_{22} \left[(\kappa_b^U)^2 \cos^2\alpha\right] - \mu_b^U \mathcal{U}^h_{21} \left[(\kappa_b^U)^2 \cos^2\alpha\right]}{\kappa_b^U \sin\alpha \, \mathcal{U}^h_{22} \left[(\kappa_b^U)^2 \cos^2\alpha\right] + \mu_b^U \mathcal{U}^h_{21} \left[(\kappa_b^U)^2 \cos^2\alpha\right]} e^{j2k\kappa_b^U y^U \sin\alpha}$$

$$\tilde{R}^{h}_{\text{pec}} = \frac{\kappa_b^L \sin\alpha' \, \mathcal{L}^h_{12} \left[(\kappa_b^U)^2 \cos^2\alpha\right] - \mu_b^L \mathcal{L}^h_{11} \left[(\kappa_b^U)^2 \cos^2\alpha\right]}{\kappa_b^U \sin\alpha \, \mathcal{U}^h_{12} \left[(\kappa_b^U)^2 \cos^2\alpha\right] + \mu_b^U \mathcal{U}^h_{11} \left[(\kappa_b^U)^2 \cos^2\alpha\right]} e^{jk\left[\kappa_b^L y^L \sin\alpha' + \kappa_b^U y^U \sin\alpha\right]}$$

$$\tilde{R}^{h}_{\text{pmc}} = \frac{\kappa_b^L \sin\alpha' \, \mathcal{L}^h_{22} \left[(\kappa_b^U)^2 \cos^2\alpha\right] - \mu_b^L \mathcal{L}^h_{21} \left[(\kappa_b^U)^2 \cos^2\alpha\right]}{\kappa_b^U \sin\alpha \, \mathcal{U}^h_{22} \left[(\kappa_b^U)^2 \cos^2\alpha\right] + \mu_b^U \mathcal{U}^h_{21} \left[(\kappa_b^U)^2 \cos^2\alpha\right]} e^{jk\left[\kappa_b^L y^L \sin\alpha' + \kappa_b^U y^U \sin\alpha\right]}$$

(2.45)

and from Snell's law

$$\kappa_b^L \sin\alpha' = \sqrt{(\kappa_b^L)^2 - (\kappa_b^U)^2 \cos^2\alpha}. \tag{2.46}$$

To obtain a composite sheet simulation of a multilayer slab or coating, it is necessary to first model each layer individually through its $\bar{\bar{Q}}_U$ matrix. The matrices are subsequently combined to yield the $\mathcal{L}$ and $\mathcal{U}$ operators of the composite boundary condition. Thus, the accuracy of the overall simulation can be assessed by examining that of the individual layers comprising the slab or coating. In the case of a single layer simulation (with non-shifted surface) the $\mathcal{L}$ and $\mathcal{U}$ operators reduce to $\mathcal{L}_{11} = \mathcal{L}_{22} = 1$, $\mathcal{L}_{12} = \mathcal{L}_{21} = 0$ and $\mathcal{U}_{ij} = q_{ij}$. This simplifies the analysis and in the following we examine the accuracy of the proposed GSTC simulation as a function of the condition's order. Only the E_y-polarization incidence is discussed but similar results apply to the H_y-polarization case as well.

Figures 2.5, 2.6, 2.7 and 2.8 present the maximum error in $|R_{ex} - R_{gstc}|$ over real angles as the layer thickness is varied. The data in Figure 2.5 corresponds to a low contrast simulation with $\epsilon_r = 2$ and $\mu_r = 1.2$ as the order of the transition condition increases from 2 to 9. In the region where $|R_{ex} - R_{gstc}|$ is less than .15

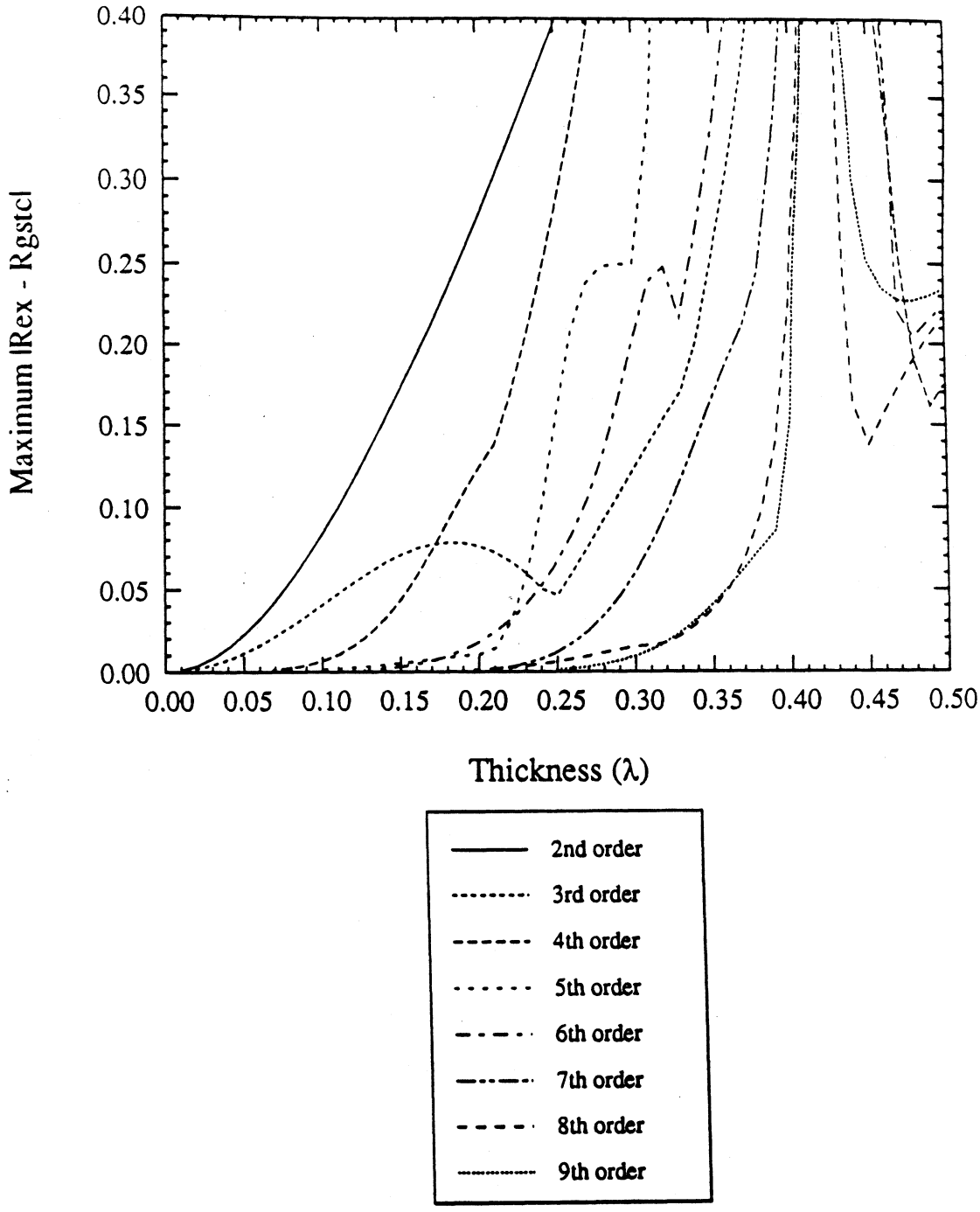

Figure 2.5: E_y polarization low contrast simulation of a single layer having relative constitutive parameters $\epsilon = 2$, $\mu = 1.2$

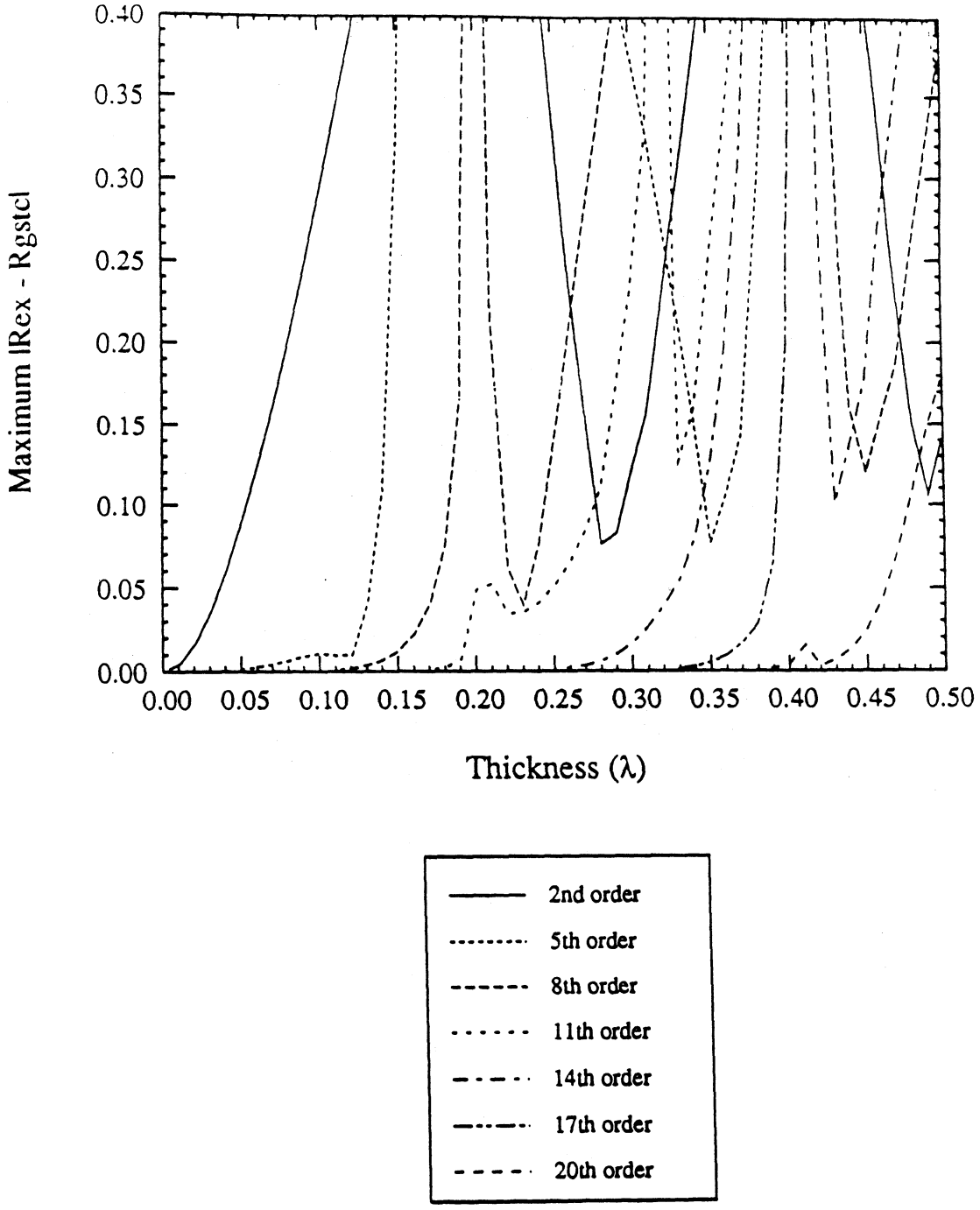

Figure 2.5: E_y polarization low contrast simulation of a single layer having relative constitutive parameters $\epsilon = 3.5$, $\mu = 2$.

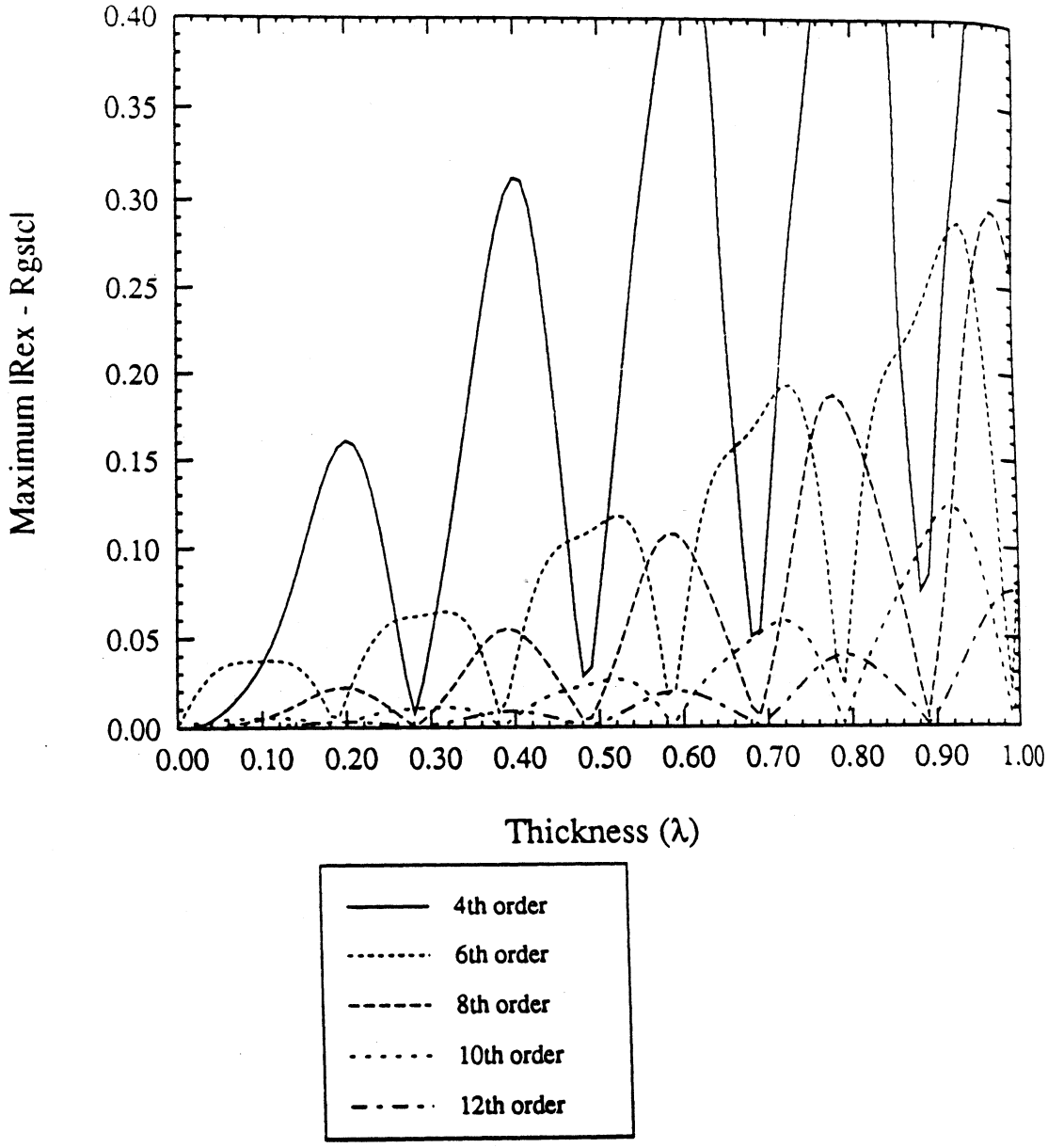

Figure 2.7: E_y polarization high contrast simulation of a single layer having $\epsilon = 3.5$, $\mu = 2$

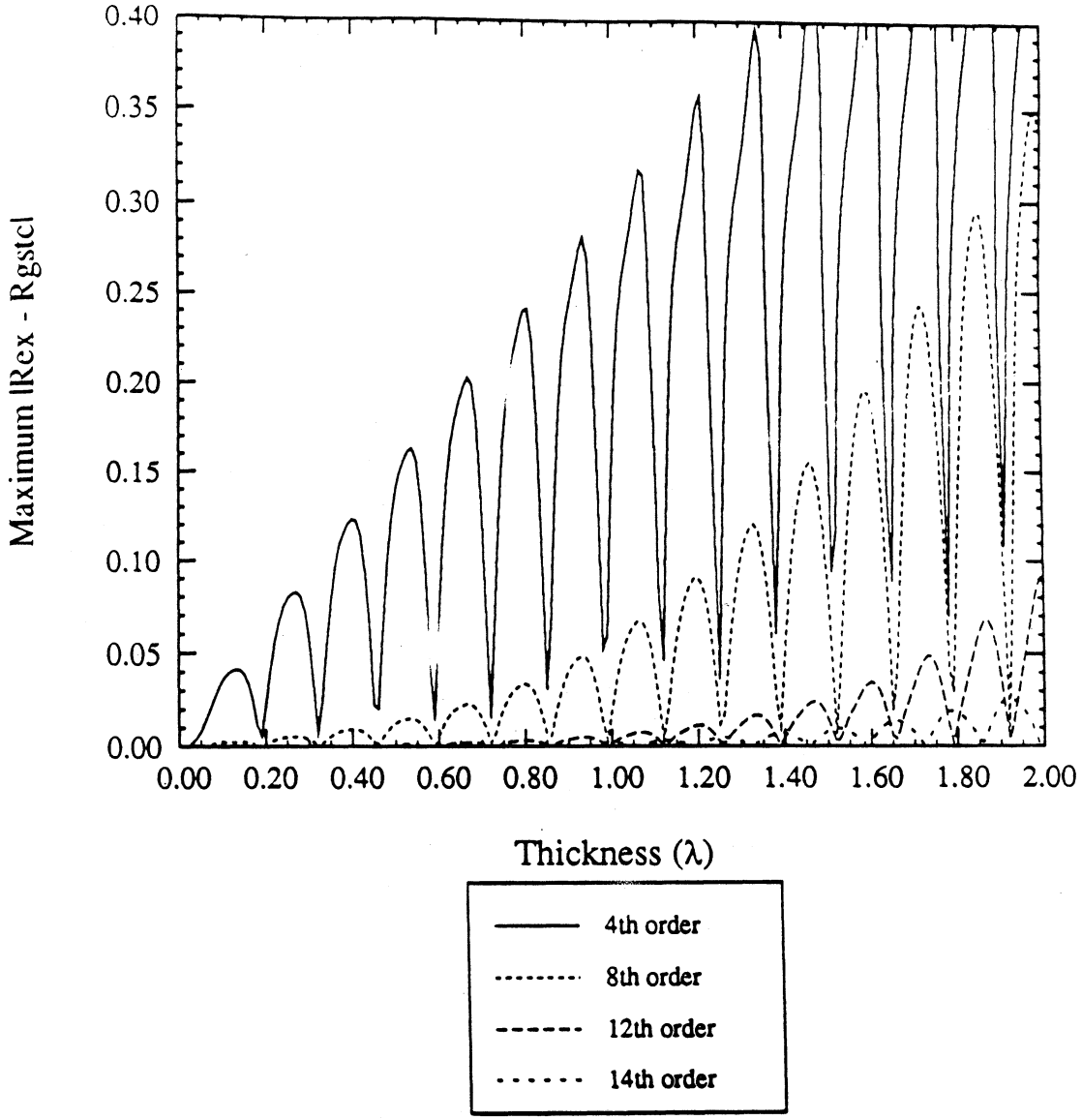

Figure 2.8. E_y polarization high contrast simulation of a single layer having $\epsilon = 5$, $\mu = 3$

(to be considered as an acceptable error) each curve displays a quadratic shape possibly with small "kinks" or perturbations superimposed[1]. In general, the range of simulation improves as the order increases, although in certain instances it may actually deteriorate slightly.

In Figure 2.6 the material parameters are increased to $\epsilon_r = 3.5$ and $\mu_r = 2$. We now observe that the maximum allowable thickness to maintain the same error as in Figure 2.5 is smaller when employing the same order transition condition. In particular, the degradation is such that a 17^{th} order condition is required to equal the performance of the 10^{th} order condition in Figure 2.5. As before the maximum allowable thickness or performance of the condition increases with the order.

To compare the performance of the low and high contrast approximations, the curves in Figures 2.5 and 2.6 were recomputed using high contrast transition conditions. The results are given in Figures 2.7 and 2.8 where the curves now follow an oscillatory behavior unique to the high contrast conditions. In general, the high contrast conditions provide an improved simulation for this choice of constitutive parameters. For example, when the order of the condition is increased from 4 to 12, the allowable thickness that can be accurately simulated increases 7-fold, significantly better than the performance of the low contrast conditions. Most importantly, the high contrast conditions allow the simulation of much thicker layers with the same error criteria. A typical example are the 11^{th} and 10^{th} order simulations in Figure 2.6 and 2.7, respectively; whereas the low contrast simulation allows a maximum thickness of only 0.28λ, this increases to beyond 1λ when employing a high contrast condition of comparable order. Inherent with their derivation, the high contrast conditions are expected to provide improved simulations as the refractive index in-

[1] As a reference, when $|R_{ex} - R_{gstc}| = .1743$, the corresponding phase error is 10° when $|R_{gstc}| = |R_{ex}| = 1$.

creases. This is indeed observed in Figure 2.8 where the layer's relative constitutive parameters are $\epsilon_r = 5$ and $\mu_r = 3$. As shown, a layer of up to 2λ thick can be accurately simulated with a 12^{th} order condition. Figures 2.5, 2.6, 2.7 and 2.8 are recomputed for H_y polarization in Figures 2.9, 2.10, 2.11 and 2.12, respectively. The results are very similar to the E_y polarization case, and the same remarks made above are applicable here.

Using the single layer data, such as those presented in Figure 2.5-2.12, it is possible to synthesize a multilayer simulation. As an example, consider an E_y polarized plane wave incident on a three layer slab having $\epsilon_1^U = 5 - j0$, $\mu_1^U = 3 - j0$, $\tau_1^U = .4$ for the first layer, $\epsilon_2^U = 3.5 - j0$, $\mu_2^U = 2 - j0$, $\tau_2^U = .4$ for the second layer and $\epsilon_3^U = 2 - j0$, $\mu_3^U = 1.2 - j0$, $\tau_3^U = .2$ for the last top layer (see Figure 2.13). To select the individual layer models for E_y polarization we conjecture that the maximum error of $|R_{ex} - R_{gstc}|$ for the composite sheet will be bounded by the sum of the maximum errors of $|R_{ex} - R_{gstc}|$ of the constituent layers in isolation. Examining Figures 2.5-2.8, we observe that the sum of the errors of the 6^{th} order high contrast representations of the bottom and middle layers and the 5^{th} order low contrast representation of the top layer amounts to .062 as required by the design criteria. This suggests that the composite sheet employing these representations will have an acceptable performance when the total thickness is 1λ. The actual maximum error of the designed simulation is compared with the sum of the isolated layer errors in Figures 2.13. The corresponding errors with a PEC and a PMC inserted at $y = 0$ are also plotted in Figures 2.14 and 2.15. We note that the sum of the isolated layer errors serves as a reasonable upper bound for the new simulation design.

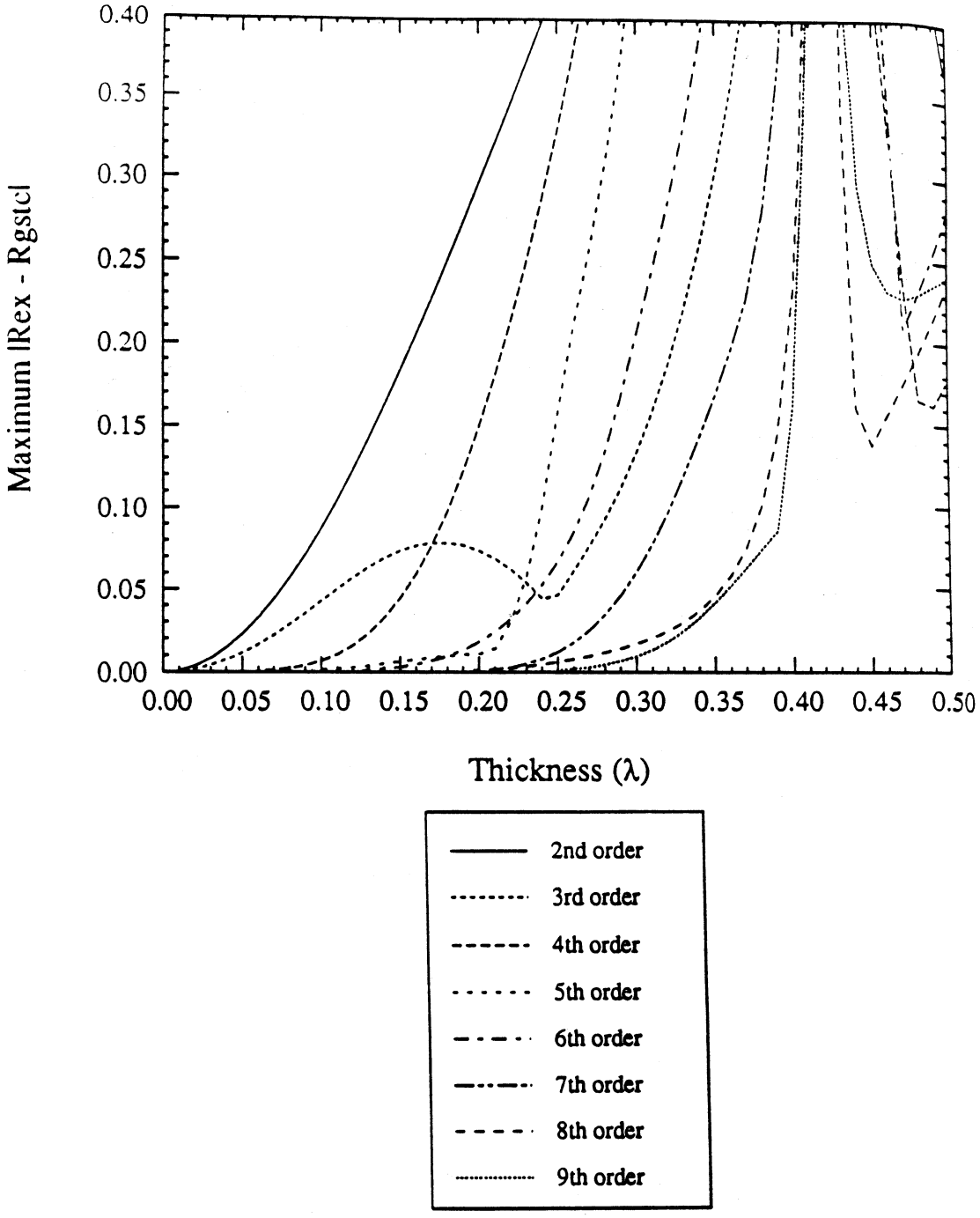

Figure 2.9: H_y polarization low contrast simulation of a single layer having relative constitutive parameters $\epsilon = 2$, $\mu = 1.2$

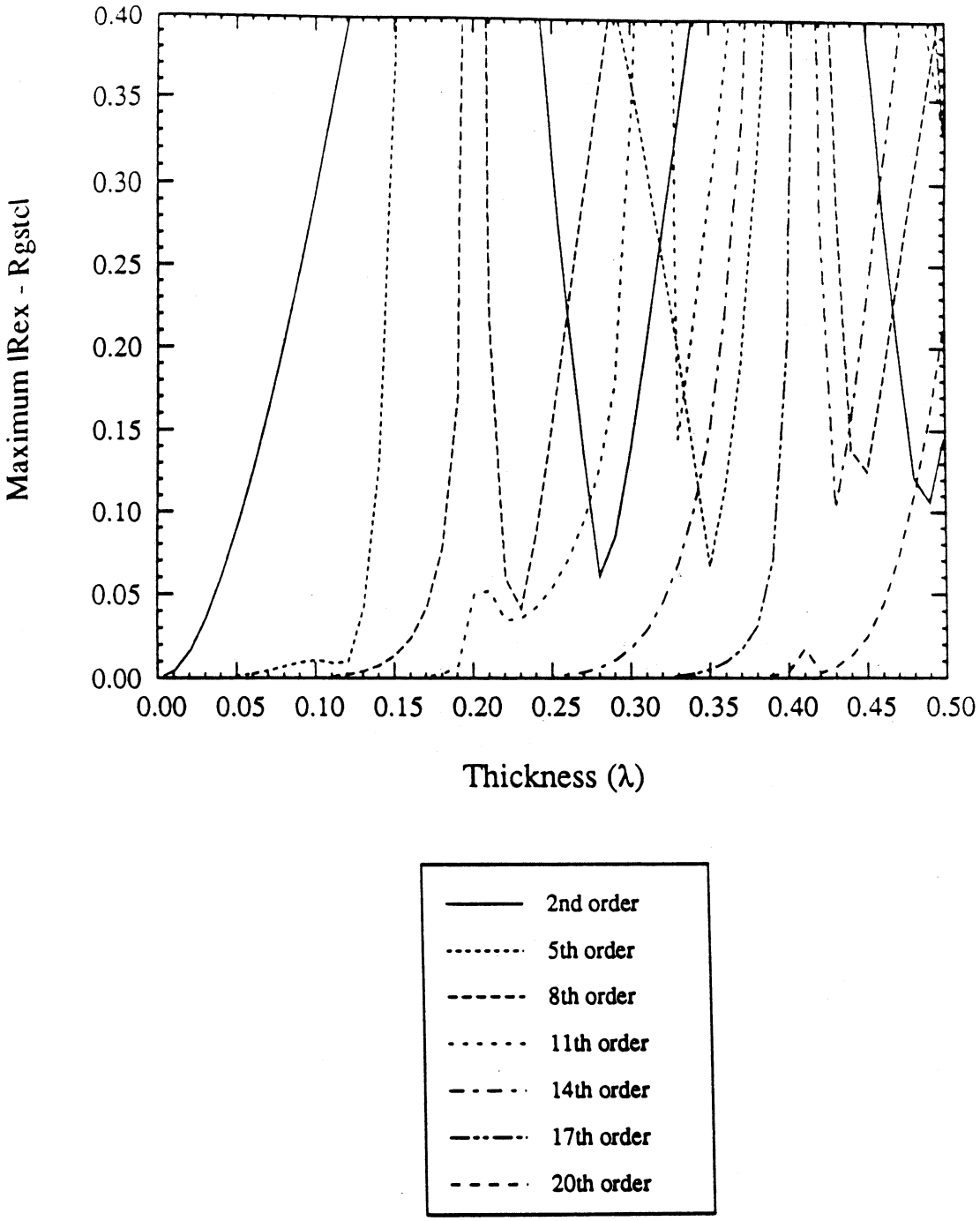

Figure 2.10: H_y polarization low contrast simulation of a single layer having relative constitutive parameters $\epsilon = 3.5$, $\mu = 2$.

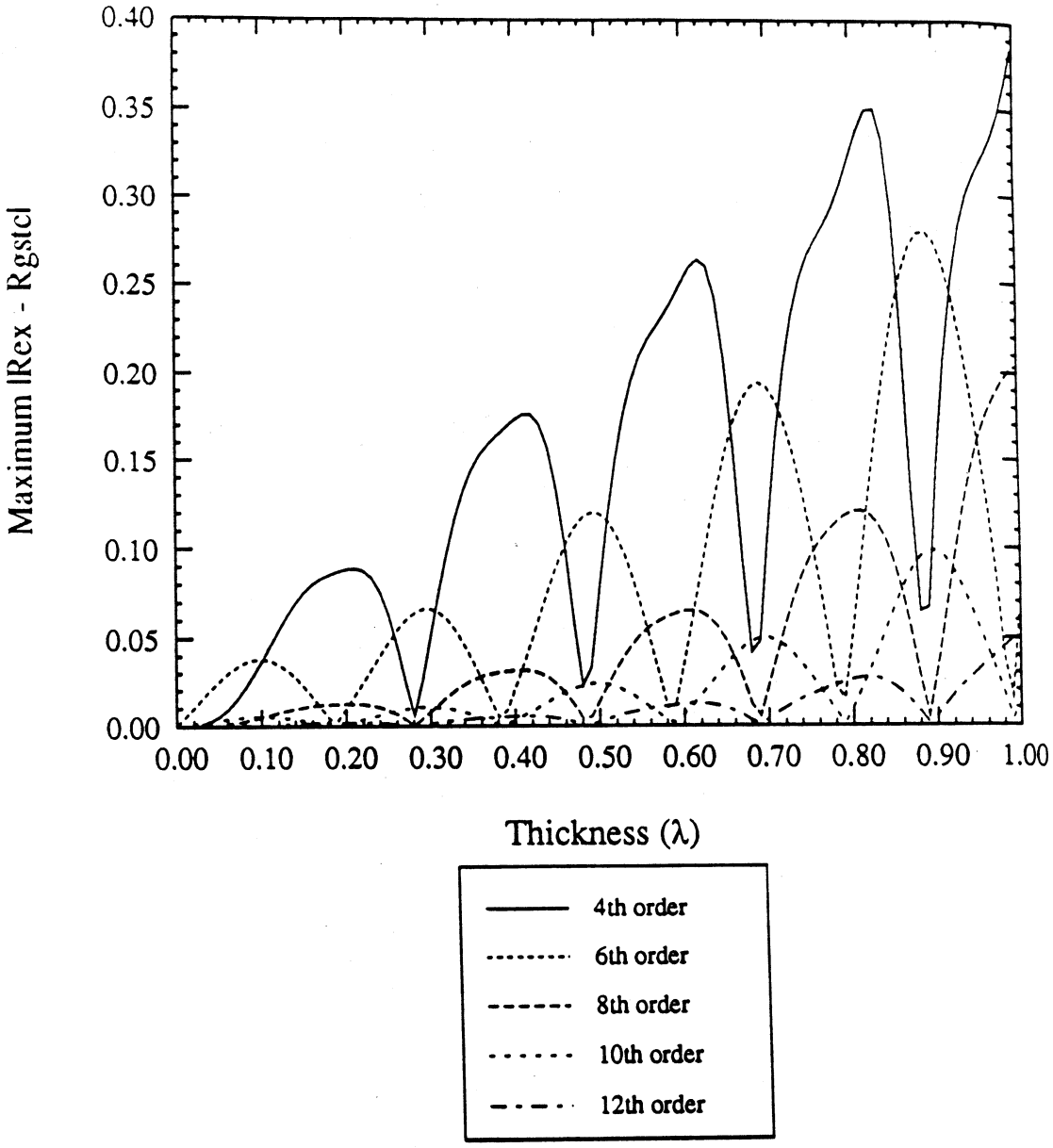

Figure 2.11: H_y polarization high contrast simulation of a single layer having $\epsilon = 3.5$, $\mu = 2$

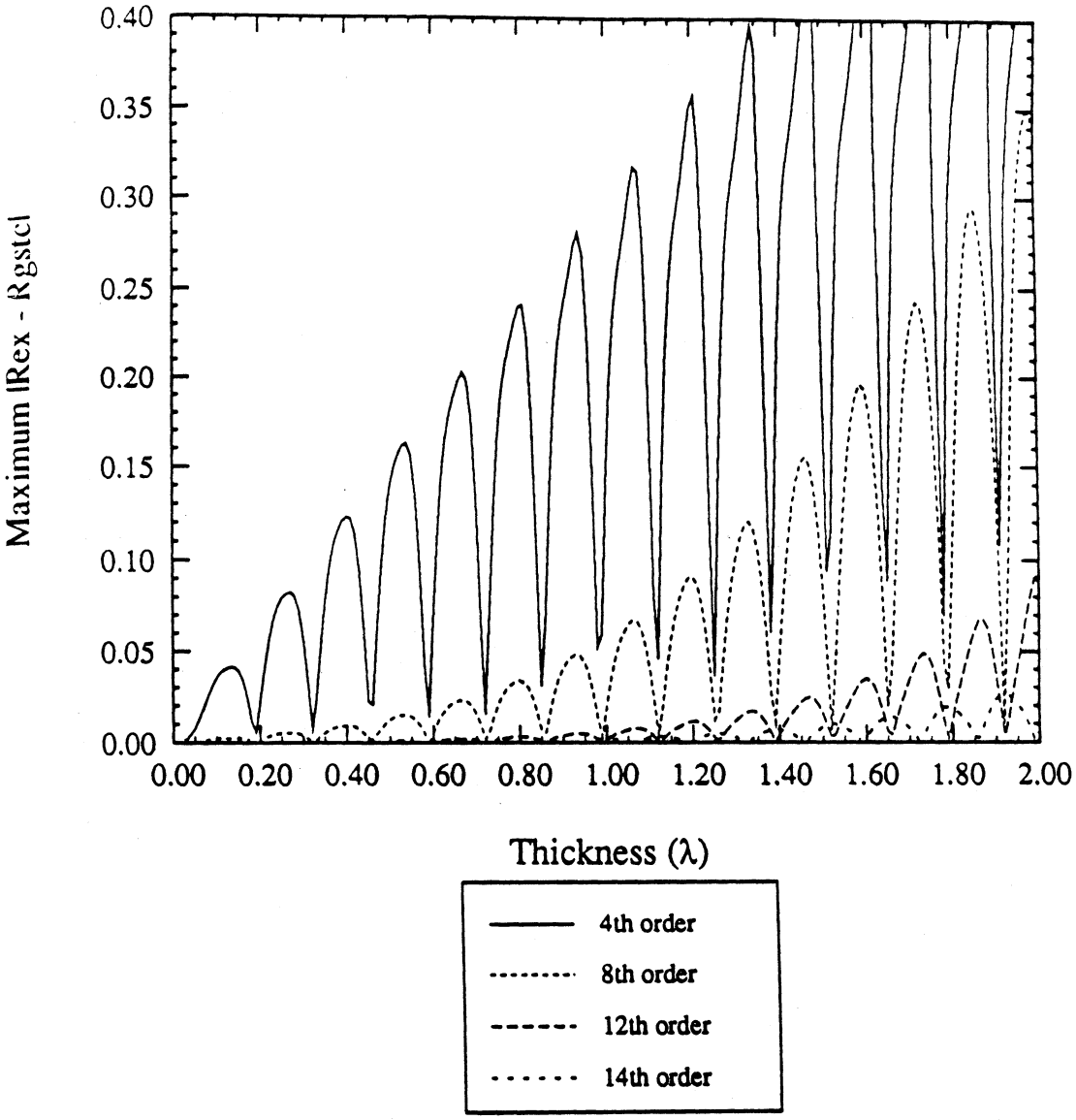

Figure 2.12: H_y polarization high contrast simulation of a single layer having $\epsilon = 5$, $\mu = 3$

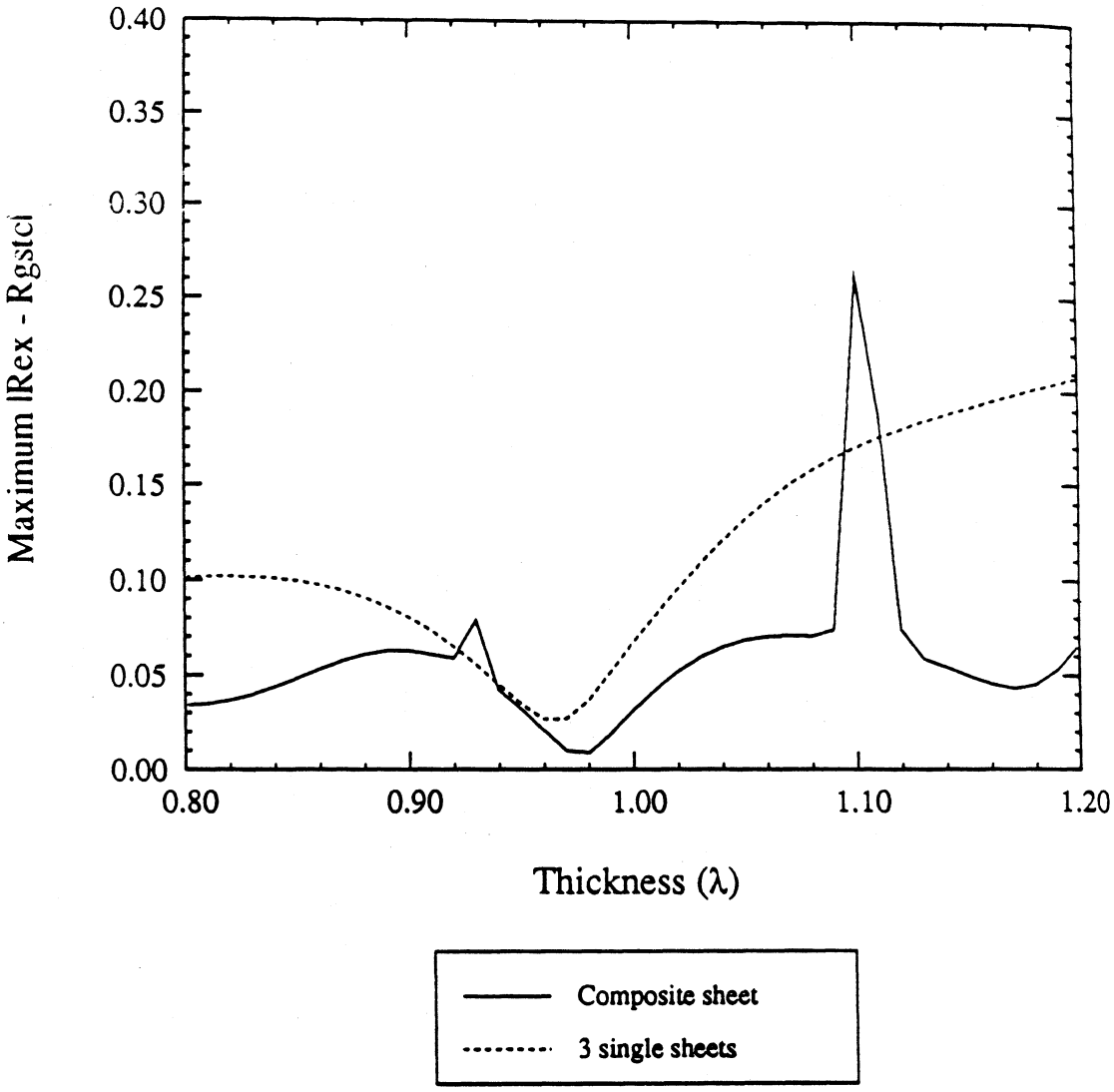

Figure 2.13: Simulation of a three layer slab using a 14^{th} order condition.

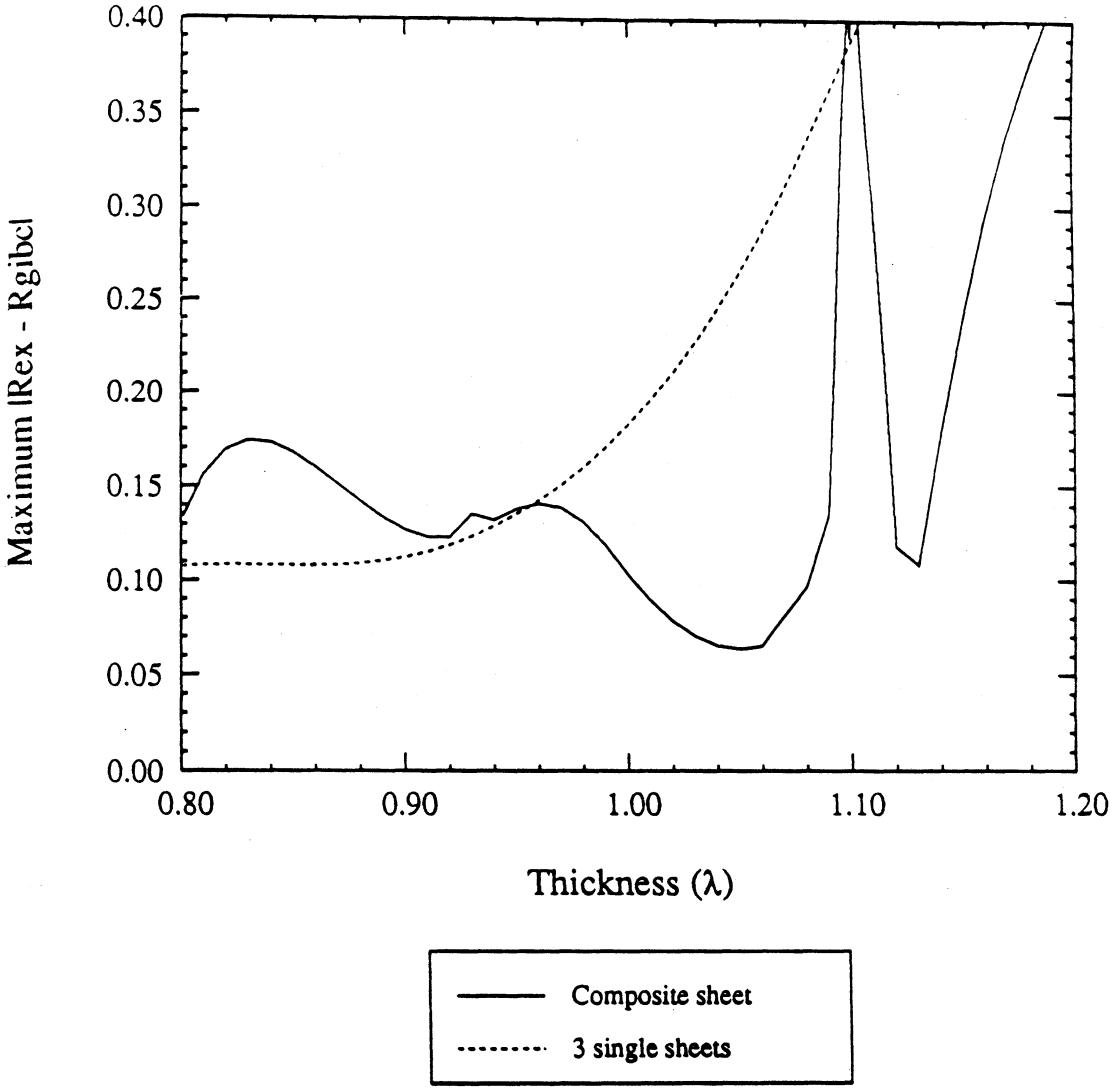

Figure 2.14: Simulation of a three layer coating on a PEC ground plane using a 14^{th} order condition.

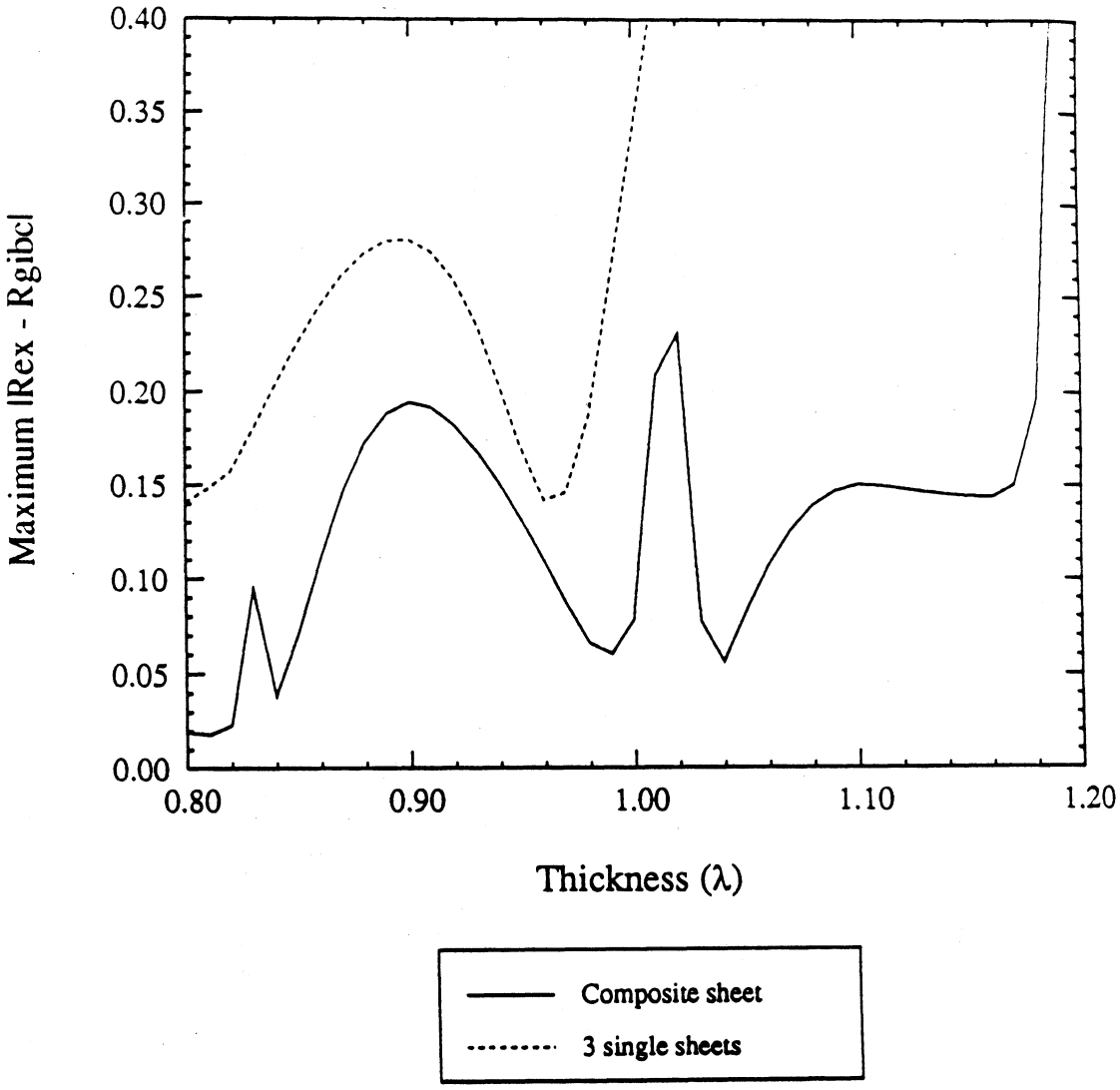

Figure 2.15: Simulation of a three layer coating on a PMC ground plane using a 14^{th} order condition.

2.4 Concluding Remarks

This chapter has dealt with the development of generalized impedance boundary and transition conditions for multilayer coatings and layers. A major effort was also devoted to present them in a form which is compact and convenient for further usage. Because of the generality of the derived conditions they are ideally suited for use in the following chapters where general diffraction coefficients are developed.

CHAPTER III

DIFFRACTION BY A MULTILAYER SLAB RECESSED IN A GROUND PLANE VIA GENERALIZED IMPEDANCE BOUNDARY CONDITIONS

The canonical geometry formed by two semi-infinite planar slabs joined end-to-end is a difficult one to model properly, particularly if the slabs are thick. For this reason very few computed results exist to verify GIBC/GSTC diffraction solutions obtained for thick slab junctions. This need is addressed herein by computing a unique alternative GIBC/GSTC solution for a specialized thick slab geometry. This solution provides a benchmark which can be used to partially verify more general GIBC/GSTC diffraction solutions. The special problem considered in this chapter is the plane wave diffraction by a multilayer slab recessed in a ground plane in Figure 3.1, and the alternative method used is the generalized scattering matrix formulation (GSMF) [25].

Related but simpler geometries have been studied in the past [2] [6] [20] [11] [26] [8] [48] [9] [52] [58] [28], and most of these solutions involved the interior and exterior fields. This is alleviated herein by modeling the slab as a surface characterized by a plane wave reflection coefficient $R(\cos\phi_o)$ (see Figure 3.1), where ϕ_o can be extended through analytic continuation in the complex plane. This enables us to carry out

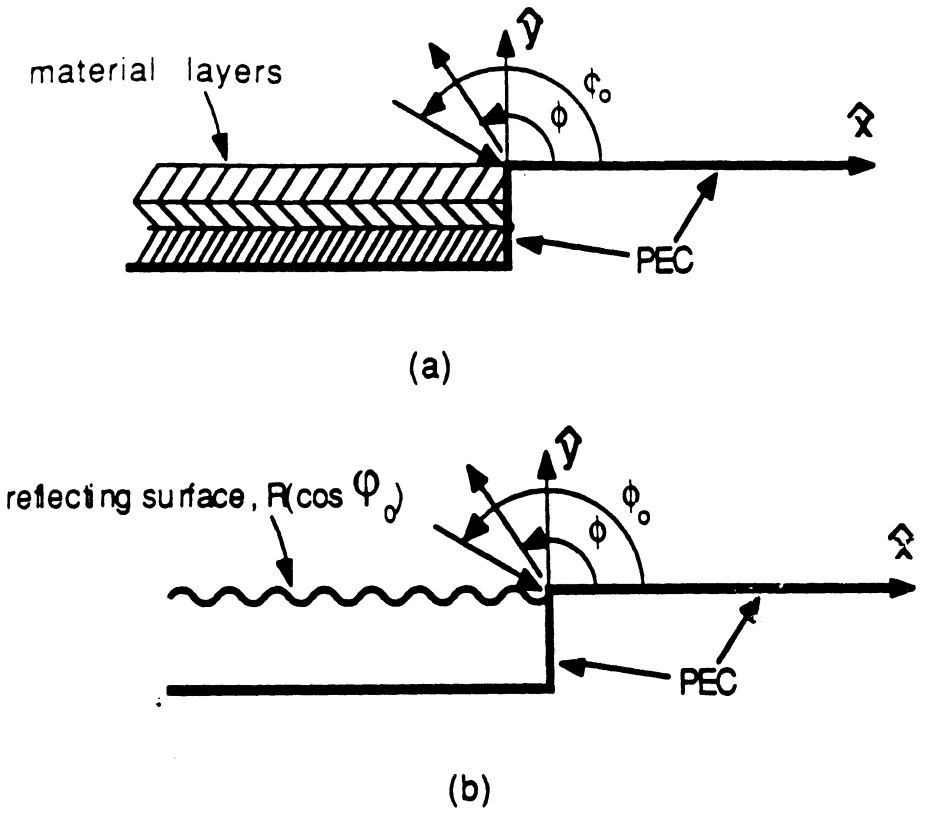

Figure 3.1: (a) Multilayer slab recessed in a PEC ground plane. (b) Representation of slab as surface with reflection coefficient R.

the analysis in a symbolic manner regardless of the inhomogeneity profile of the layer. Hence, although our focus in this chapter is the multilayer recessed slab, the derivations will be applicable to any vertically inhomogeneous slab.

The problem herein is formulated via the dual integral equation approach [10] in conjunction with the GSMF. The GSMF is applied to the recessed stub structure of Figure 3.2(a), depicting a perfectly conducting half plane elevated a distance δ above a reflecting surface with a perfectly conducting stub recessed a distance d away from the half plane edge. This formulation requires the solution to a number of individual subproblems. As illustrated in Figure 3.2(b)-(f), they correspond to the problems of direct diffraction, mode coupling, mode reflection, and mode radiation.

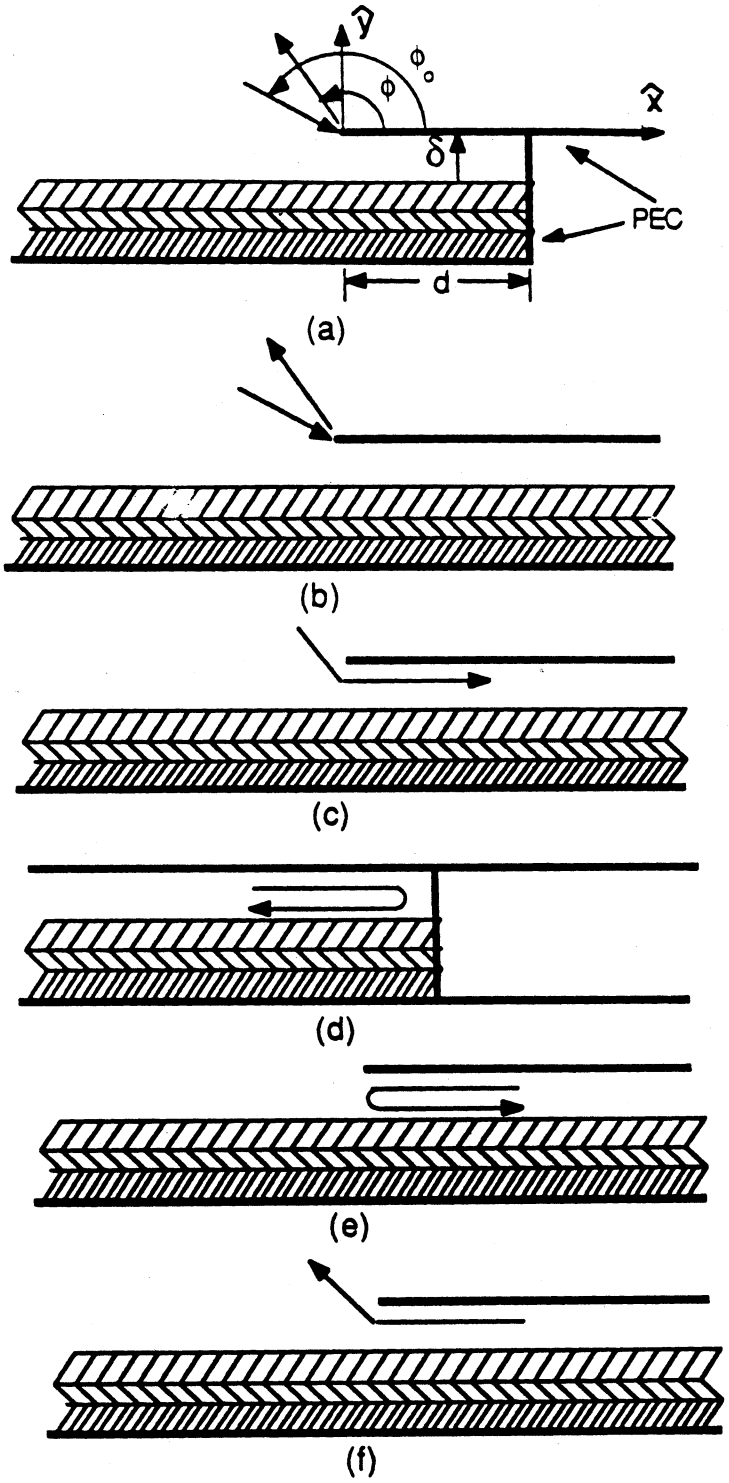

Figure 3.2: Illustration of recessed stub geometry (a) and associated subproblems: (b) direct diffraction, (c) mode coupling, (d) stub reflection, (e) mode reflection at the waveguide mouth, (f) mode launching.

Once solutions to each of these subproblems have been obtained via the dual integral equation method, they can be combined in accordance with the GSMF prescription to yield the diffraction for the original structure in Figure 3.1(a).

Unfortunately, the conversion of the symbolic solution into one of practical use proves to be a formidable task when the reflection coefficient of the grounded slab is obtained in its exact form. The fundamental difficulties are related to:

- the factorization or splitting of the associated Weiner-Hopf functions into components regular in the upper and lower half complex plane, and
- the extraction of the complex zeros (i.e., the waveguide modes) associated with the split functions.

The pertinent Weiner-Hopf functions cannot be factored analytically and one must therefore resort to a numerical scheme (e.g., see [28]). Also, in solving for the complex roots of the pertinent split functions, it is necessary to employ a search algorithm in the complex plane, a process which is numerically intensive. We circumvent these difficulties by replacing the grounded slab by an opaque sheet satisfying a GIBC of the form given in chapter two. Under a GIBC approximation, the approximate reflection coefficient is cast as a ratio of polynomials in $\cos\phi$ or $\sin\phi$, making the determination of the complex poles and zeros of the reflection coefficient a simple task. As a result, the required Weiner-Hopf factorizations can be obtained analytically leading to computationally efficient solutions.

In the first part of the chapter the GSMF procedure is summarized. The dual integral equation method is subsequently employed to formulate each of the subproblems and the necessary solutions are obtained for both E_z and H_z polarizations. These are given in terms of symbolic split functions which are then evaluated for the

specific case of a multilayer grounded slab by casting the reflection coefficient in a form compatible with a GIBC simulation of the slab given in chapter two. Results are given and the accuracy of the GIBC simulation is examined by comparison with known results for homogeneous slabs.

3.1 Description of GSMF Procedure

In this section, the generalized scattering matrix formulation (GSMF) is applied to the geometry given in Figure 3.2(a). This consists of a perfectly conducting half-plane located a distance δ above the grounded slab, with a perfectly conducting stub recessed a distance d away from the half-plane edge. To concurrently treat both the E_z and H_z polarizations of incidence, the quantities F_z and F_x are introduced. They are defined as

$$F_z = \begin{cases} E_z, & E_z \text{ polarization,} \\ Z_o H_z, & H_z \text{ polarization.} \end{cases} \tag{3.1}$$

$$F_x = \begin{cases} Z_o H_x, & E_z \text{ polarization,} \\ E_x, & H_z \text{ polarization.} \end{cases} \tag{3.2}$$

and from Maxwell's equations

$$F_x = -\frac{jv_1}{k}\frac{\partial F_z}{\partial y} \tag{3.3}$$

where

$$v_1 = \begin{cases} -1, & E_z \text{ polarization,} \\ 1, & H_z \text{ polarization.} \end{cases} \tag{3.4}$$

The individual problems to be considered in the GSMF prescription [25] are as follows:

1. Evaluation of the direct diffracted field by the substructure in Figure 3.2(b) due to a plane wave incidence. This field can be expressed as

$$F_z^{dd}(\phi, \phi_o) = \int_C P_{dd}(\cos\alpha, \cos\phi_o; \delta)\, e^{-jk_o\rho\cos(\alpha-\phi)} d\alpha$$

where P_{zz} is the spectrum associated with the currents induced on the half plane and (ρ, ϕ) are the usual cylindrical coordinates of the observation point. Additionally, C is the complex contour composed of the directed line segments $[0 - j\infty, 0 - j0], [0 - j0, \pi - j0], [\pi - j0, \pi + j\infty]$ in the complex α plane.

2. Evaluation of the field coupled into the waveguide due to a plane wave incidence (Figure 3.2(c)) as illustrated. We denote the field corresponding to the n^{th} coupled mode as

$$F^c_{zn}(\phi_o) = C_n(\cos\phi_o; \delta)\, e^{-jk_n x} \tag{3.6}$$

where $C_n(\cos\phi_o; \delta)$ is usually referred to as the coupling coefficient and k_n is the propagation constant associated with the n^{th} mode.

3. Evaluation of the modal field reflected at the stub (Figure 3.2(d)). This can be expressed as $\Gamma_{mn} e^{jk_m x}$ where Γ_{mn} is the stub reflection coefficient of the n^{th} mode to the m^{th} mode.

4. Evaluation of the reflected field at the waveguide mouth due to the n^{th} mode (Figure 3.2(e). This can be expressed by $R_{mn}(\delta)\, e^{-jk_m x}$ where $R_{mn}(\delta)$ is the reflection coefficient of the n^{th} mode to the m^{th} mode.

5. Evaluation of the radiated field attributed to the m^{th} mode incident at the waveguide mouth (Figure 3.2(f). This field can be expressed as

$$F^l_{zm}(\phi) = \int_C P_m(\cos\alpha; \delta)\, e^{-jk_o \rho \cos(\alpha - \phi)} d\alpha \tag{3.7}$$

where $P_m(\cos\alpha, \delta)$ is proportional to the spectrum of the currents induced on the half plane due to the incident m^{th} mode.

Accordingly, the scattered field by the recessed stub geometry in Figure 3.2(a) is given by (for $y > \delta$)

$$F_z^s(\rho, \phi_o, \delta, d) = \int_C [P_{dd}(\cos\alpha, \cos\phi_o; \delta) + P_{mod}(\cos\alpha, \cos\phi_o; \delta, d)]\, e^{-jk_o\rho\cos(\alpha-\phi)} d\alpha \tag{3.8}$$

where $P_{mod}(\cos\alpha, \cos\phi_o; \delta, d)$ is associated with the presence of the stub and includes the contribution of the waveguide modal fields. It can be written in a matrix form as [25]

$$\begin{aligned} P_{mod}(\cos\alpha, \cos\phi_o; \delta, d) \;=\; & \\ & [P_m(\cos\alpha; \delta)]^T \{[I] - [W_{mn}(d)][\Gamma_{mn}][W_{mn}(d)][R_{mn}(\delta)]\}^{-1} \\ & \cdot [W_{mn}(d)][\Gamma_{mn}][W_{mn}(d)][C_n(\cos\phi_o; \delta)] \end{aligned} \tag{3.9}$$

in which the brackets signify column or square matrices depending on whether one or two subscripts appear, respectively. In addition, $[I]$ denotes the identity matrix and $[W_{mn}(d)]$ is the modal propagation matrix whose elements are given by

$$W_{mn}(d) = \begin{cases} e^{-jk_n d}, & m = n \\ 0, & m \neq n. \end{cases} \tag{3.10}$$

To obtain the field scattered by the recessed material slab it is only required to set d and δ to 0 in (3.8) and (3.9). In this case, $[W_{mn}(d = 0)]$ becomes the identity matrix and $[\Gamma_{mn}]$ reduces to $[I]$ or $-[I]$ for H_z and E_z polarizations, respectively. Thus, P_{mod} becomes

$$\begin{aligned} P_{mod}(\cos\alpha, \cos\phi_o) \;&\stackrel{def}{=}\; P_{mod}(\cos\alpha, \cos\phi_o; \delta = 0, d = 0) \\ &=\; [P_m(\cos\alpha)]\{[I] - v_1[R_{mn}]\}^{-1}[v_1 C_n(\cos\phi_o)] \end{aligned} \tag{3.11}$$

where

$$P_m(\cos\alpha) \;\stackrel{def}{=}\; P_m(\cos\alpha; \delta = 0)$$

$$C_n(\cos\phi_o) \stackrel{def}{=} C_n(\cos\phi_o;\delta=0)$$
$$R_{mn} \stackrel{def}{=} R_{mn}(\delta=0). \tag{3.12}$$

Hence, the field scattered by the vertically inhomogeneous recessed slab can be expressed as

$$F_z^s(\rho,\phi_o) = \int_C P_{rs}(\cos\alpha,\cos\phi_o)\, e^{-jk_o\rho\cos(\alpha-\phi)}d\alpha\ :\ y>0 \tag{3.13}$$

where

$$P_{rs}(\cos\alpha,\cos\phi_o) = P_{id}(\cos\alpha,\cos\phi_o) + P_{mod}(\cos\alpha,\cos\phi_o). \tag{3.14}$$

The steepest descent method can then be employed to evaluate (3.13) and obtain the diffracted field.

3.2 Plane Wave Diffraction and Mode Coupling

Consider the plane wave

$$F_z^i = e^{jk_o(x\cos\phi_o+y\sin\phi_o)} \tag{3.15}$$
$$F_x^i = v_1\sin\phi_o e^{jk_o(x\cos\phi_o+y\sin\phi_o)} \tag{3.16}$$

incident at an angle ϕ_o upon the structure depicted in Figure 3.2(b). In the absence of the perfectly conducting half-plane, the total fields may be written as (for $y>0$)

$$F_z^{pw} = F_z^i + F_z^r \tag{3.17}$$
$$F_x^{pw} = F_x^i + F_x^r \tag{3.18}$$

with

$$F_z^r = R(\cos\phi_o)\, e^{jk_o(x\cos\phi_o-y\sin\phi_o)} \tag{3.19}$$
$$F_x^r = -v_1 R(\cos\phi_o)\sin\phi_o e^{jk_o(x\cos\phi_o-y\sin\phi_o)} \tag{3.20}$$

where $R(\cos\alpha_o)$ denotes the plane wave reflection coefficient of the grounded slab referred to $y = 0$. For the general case of a plane wave incident at an angle α on a vertically inhomogeneous ground plane coating, $R(\lambda = \cos\alpha)$ may be represented as

$$R(\lambda) = -\left[\frac{A(\lambda) - \sqrt{1-\lambda^2}B(\lambda)}{A(\lambda) + \sqrt{1-\lambda^2}B(\lambda)}\right]. \tag{3.21}$$

where $A(\lambda)$ and $B(\lambda)$ are even functions of λ, with any branch cuts in $A(\lambda)$ also appearing in $B(\lambda)$ and vice versa.

The introduction of the perfectly conducting half plane at $y = \delta$ generates an additional scattered field component F_z^s so that the total fields become

$$F_z = F_z^{pw} + F_z^s \tag{3.22}$$

$$F_x = F_x^{pw} + F_x^s \tag{3.23}$$

This scattered field is due to induced currents on the perfectly conducting half-plane, and can thus be represented by an angular spectrum of plane waves. A suitable representation is [10]

$$F_z^s = \begin{cases} \int_C P(\cos\alpha)\, e^{jk_o\delta\sin\alpha} e^{-jk_o\rho\cos(\phi-\alpha)} d\alpha & y > \delta, \\ \int_C Q(\cos\alpha)\, e^{-jk_o\delta\sin\alpha}\left[e^{-jk_o\rho\cos(\phi+\alpha)}\right. & \\ \qquad \left. + R(\cos(\pi-\alpha))\, e^{-jk_o\rho\cos(\phi-\alpha)}\right] d\alpha & 0 < y < \delta, \end{cases} \tag{3.24}$$

implying

$$F_x^s = \begin{cases} -\int_C v_1 \sin\alpha\, P(\cos\alpha)\, e^{jk_o\delta\sin\alpha} e^{-jk_o\rho\cos(\phi-\alpha)} d\alpha & y > \delta, \\ \int_C v_1 \sin\alpha\, Q(\cos\alpha)\, e^{-jk_o\delta\sin\alpha}\left[e^{-jk_o\rho\cos(\phi+\alpha)}\right. & \\ \qquad \left. - R(\cos(\pi-\alpha))\, e^{-jk_o\rho\cos(\phi-\alpha)}\right] d\alpha & 0 < y < \delta, \end{cases} \tag{3.25}$$

in which $P(\cos\alpha)$ and $Q(\cos\alpha)$ are the unknown spectral functions to be determined from the boundary conditions at $y = 0$. These are

B1: Continuity of the tangential electric fields at $y = \delta$, $-\infty < x < \infty$

B2: Continuity of the tangential magnetic fields at $y = \delta$, $x < 0$

B3: Vanishing tangential electric field on the perfectly conducting half-plane at $y = \delta$, $x > 0$

and we note that the boundary condition at the slab surface is implicitly taken into account by the representation (3.24) and (3.25).

The application of (B1)-(B3) in conjunction with (3.24) and (3.25) is straightforward. It results in the set of equations

$$P(\lambda) = -v_1 Q(\lambda)\left[1 - v_1 R(\lambda)\, e^{-j2k_o\delta\sqrt{1-\lambda^2}}\right]. \tag{3.26}$$

$$\int_{-\infty}^{\infty} Q(\lambda)\, v_2(\lambda)\, e^{-jk_o x\lambda} d\lambda = 0 \quad ; \quad x < 0. \tag{3.27}$$

$$\int_{-\infty}^{\infty} Q(\lambda)\, v_3(\lambda)\left[1 - v_1 R(\lambda)\, e^{-2jk_o\delta\sqrt{1-\lambda^2}}\right] e^{-jk_o x\lambda} d\lambda =$$
$$-v_3(\lambda_o)\sqrt{1-\lambda_o^2}\, e^{jk_o\delta\sqrt{1-\lambda_o^2}}\left[1 - v_1 R(\lambda_o)\, e^{-2jk_o\delta\sqrt{1-\lambda_o^2}}\right] e^{jk_o x\lambda_o} \; ; x > 0 \tag{3.28}$$

where we have set $\lambda = \cos\alpha$, $\lambda_o = \cos\phi_o$ and

$$v_2(\lambda) = \begin{cases} 1, & E_z \text{ polarization,} \\ 1/\sqrt{1-\lambda^2}, & H_z \text{ polarization.} \end{cases} \tag{3.29}$$

$$v_3(\lambda) = \begin{cases} 1/\sqrt{1-\lambda^2}, & E_z \text{ polarization,} \\ 1, & H_z \text{ polarization.} \end{cases} \tag{3.30}$$

These are sufficient to obtain a solution for $Q(\lambda)$ and $P(\lambda)$. However, before proceeding, it is necessary to rewrite certain terms in the integrands of (3.27) and (3.28) as products of "upper" and "lower" functions, that is, functions free of poles, zeros, and branch cuts in the upper and lower half λ planes, respectively. In the process of doing so, we introduce the definitions

$$v_2(\lambda) \stackrel{def}{=} v_2^+(\lambda)\, v_2^-(\lambda) \tag{3.31}$$

$$v_3(\lambda) \stackrel{def}{=} v_3^+(\lambda)\, v_3^-(\lambda) \tag{3.32}$$

$$1 - v_1 R(\lambda)\, e^{-2jk_o\delta\sqrt{1-\lambda^2}} \stackrel{def}{=} \frac{L_w(\lambda;\delta)\, U_w(\lambda;\delta)}{L_s(\lambda)\, U_s(\lambda)}. \tag{3.33}$$

in which

$$L_w(\lambda;\delta)\, U_w(\lambda;\delta) = A(\lambda)\left(1 + v_1\, e^{-2jk_o\delta\sqrt{1-\lambda^2}}\right) + \sqrt{1-\lambda^2}B(\lambda)\left(1 - v_1\, e^{-2jk_o\delta\sqrt{1-\lambda^2}}\right) \tag{3.34}$$

$$L_s(\lambda)\, U_s(\lambda) = A(\lambda) + \sqrt{1-\lambda^2}B(\lambda). \tag{3.35}$$

In these, $L_s(\lambda)$, $L_w(\lambda;\delta)$, $v_2^-(\lambda)$, $v_3^-(\lambda)$ are lower functions while $U_s(\lambda)$,$U_w(\lambda;\delta)$, $v_2^+(\lambda)$, $v_3^+(\lambda)$ denote upper functions. We also note that L_wU_w is a function characteristic to the loaded parallel plate waveguide and its zeros correspond to modes in the waveguide. On the other hand, L_sU_s is a function characteristic to the grounded slab with its zeros corresponding to the surface wave modes supported by the slab.

Substituting (3.31)-(3.35) into (3.27) and (3.28), we have

$$\int_{-\infty}^{\infty} Q(\lambda)\, v_2^+(\lambda)\, v_2^-(\lambda)\, e^{-jk_ox\lambda} d\lambda = 0 \quad ; \quad x < 0, \tag{3.36}$$

$$\int_{-\infty}^{\infty} Q(\lambda)\, v_3^+(\lambda)\, v_3^-(\lambda)\, \frac{L_w(\lambda;\delta)\, U_w(\lambda;\delta)}{L_s(\lambda)\, U_s(\lambda)} e^{-jk_ox\lambda} d\lambda = -v_3^+(\lambda_o)\, v_3^-(\lambda_o)\sqrt{1-\lambda_o^2}\, e^{jk_o\delta\sqrt{1-\lambda_o^2}} \frac{L_w(\lambda_o;\delta)\, U_w(\lambda_o;\delta)}{L_s(\lambda_o)\, U_s(\lambda_o)} e^{jk_ox\lambda_o} \; ; \; x > 0 \tag{3.37}$$

These coupled dual integral equations can be solved for the unknown spectra by examining the analytic properties of the integrands, and the reader is referred to [10] and [58] for a more explicit description of this process. From (3.36) and (3.37) the unknown spectra are determined to be

$$Q(\lambda) = \frac{L_w(\lambda_o;\delta)\, U_s(\lambda)}{2\pi j U_w(\lambda;\delta)\, L_s(\lambda_o)} \left[\frac{v_2^+(\lambda_o)\, v_3^-(\lambda_o)\sqrt{1-\lambda_o^2}}{v_2^-(\lambda)\, v_3^+(\lambda)(\lambda+\lambda_o)}\right] e^{jk_o\delta\sqrt{1-\lambda_o^2}} \tag{3.38}$$

$$P(\lambda) = \frac{-v_1 L_w(\lambda;\delta)\, L_w(\lambda_o;\delta)}{2\pi j L_s(\lambda)\, L_s(\lambda_o)} \left[\frac{v_2^+(\lambda_o)\, v_3^-(\lambda_o)\sqrt{1-\lambda_o^2}}{v_2^-(\lambda)\, v_3^+(\lambda)(\lambda+\lambda_o)}\right] e^{jk_o\delta\sqrt{1-\lambda_o^2}}. \tag{3.39}$$

Recognizing that $P_{11}(\lambda) = P(\lambda)$, we may then set $\delta = 0$ and substitute for the polarization dependent functions to obtain

$$P^e_{11}(\lambda) = \frac{L_w(\lambda)\,L_w(\lambda_o)}{2\pi j L_s(\lambda)\,L_s(\lambda_o)} \frac{\sqrt{1-\lambda}\sqrt{1-\lambda_o}}{(\lambda+\lambda_o)} \tag{3.40}$$

$$P^h_{11}(\lambda) = -\frac{L_w(\lambda)\,L_w(\lambda_o)}{2\pi j L_s(\lambda)\,L_s(\lambda_o)} \frac{\sqrt{1+\lambda}\sqrt{1+\lambda_o}}{(\lambda+\lambda_o)} \tag{3.41}$$

where the superscripts e and h refer to the spectra associated with E_z and H_z polarizations, respectively.

To solve for the field coupled into the region $0 < y < \delta$, $x > 0$, (3.21), (3.33) and (3.38) are substituted into (3.24) to obtain the integral expression

$$F^s_z = \int_{-\infty}^{\infty} \frac{v_2^+(\lambda_o)\,v_3^-(\lambda_o)\sqrt{1-\lambda_o^2}}{2\pi j v_2^-(\lambda)\,v_3^-(\lambda)(\lambda+\lambda_o)} \frac{L_w(\lambda_o;\delta)\,e^{jk_o\delta\left[\sqrt{1-\lambda_o^2}-\sqrt{1-\lambda^2}\right]}}{L_s(\lambda_o)\,L_s(\lambda)\,U_w(\lambda;\delta)} \cdot \left[2jA(\lambda)\frac{\sin\left(ky\sqrt{1-\lambda^2}\right)}{\sqrt{1-\lambda^2}} + 2B(\lambda)\cos\left(k_o y\sqrt{1-\lambda^2}\right)\right] e^{-jkx\lambda} d\lambda \tag{3.42}$$

for $0 < y < \delta$. This can be evaluated by closing the path of integration via a semi-infinite contour in the lower half λ plane. The sum of the residues of the captured poles then yields

$$F^s_z = \sum_{n=1}^{N} C_n(\lambda_o)\left\{jA(\lambda_n)\frac{\sin\left(k_o y\sqrt{1-\lambda_n^2}\right)}{\sqrt{1-\lambda_n^2}} + B(\lambda_n)\cos\left(k_o y\sqrt{1-\lambda_n^2}\right)\right\} e^{-jk_o x\lambda_n} \tag{3.43}$$

where $\{\lambda_n\}$ are the zeros of $U_w(\lambda;\delta)$,

$$C_n(\lambda_o) = -2\,e^{jk_o\delta\sqrt{1-\lambda_o^2}-\sqrt{1-\lambda_n^2}} \frac{L_w(\lambda_o;\delta)}{L_s(\lambda_n)\,L_s(\lambda_o)\,U'_w(\lambda_n;\delta)} \frac{v_2^+(\lambda_o)\,v_3^-(\lambda_o)\sqrt{1-\lambda_o^2}}{v_2^-(\lambda_n)\,v_3^+(\lambda_n)(\lambda_n+\lambda_o)}, \tag{3.44}$$

and

$$U'_w(\lambda_n;\delta) = \left.\frac{dU_w}{d\lambda}\right|_{\lambda=\lambda_n}. \tag{3.45}$$

Substituting (3.29) and (3.30) into (3.44) with $\delta = 0$, we obtain the more explicit

forms for $C_n(\lambda_o)$ as

$$C_n^e(\lambda_o) = -\frac{2L_w(\lambda_o)}{L_s(\lambda_n)\,L_s(\lambda_o)\,U_w'(\lambda_n)}\,\frac{\sqrt{1-\lambda_o}\sqrt{1-\lambda_n}}{\lambda_o+\lambda_n} \tag{3.47}$$

$$C_n^h(\lambda_o) = -\frac{2L_w(\lambda_o)}{L_s(\lambda_n)\,L_s(\lambda_o)\,U_w'(\lambda_n)}\,\frac{\sqrt{1+\lambda_o}\sqrt{1+\lambda_n}}{\lambda_o+\lambda_n} \tag{3.48}$$

for E_z and H_z polarizations, respectively.

3.3 Reflection and Launching of a Waveguide Mode

Consider now then n^{th} waveguide mode field (for $0 < y < \delta$)

$$\begin{cases} F_{zn} = \left[jA(\lambda_n)\,\dfrac{\sin\left(k_o y\sqrt{1-\lambda_n^2}\right)}{\sqrt{1-\lambda_n^2}} + B(\lambda_n)\cos\left(k_o y\sqrt{1-\lambda_n^2}\right)\right] e^{jk_o x\lambda_n} \\ F_{xn} = \left[v_1 A(\lambda_n)\cos\left(k_o y\sqrt{1-\lambda_n^2}\right) + jv_1 B(\lambda_n)\sqrt{1-\lambda_n^2}\sin\left(k_o y\sqrt{1-\lambda_n^2}\right)\right] e^{jk_o x\lambda_n} \end{cases} \tag{3.48}$$

incident at the waveguide opening (Figure 3.2(e)). The radiated fields due to this excitation may be again represented by (3.24) - (3.25). Subsequent application of the boundary conditions (B1)-(B3) then yields the dual integral equations (with the usual transformation to the λ plane)

$$\int_{-\infty}^{\infty} Q(\lambda)\,v_3^+(\lambda)\,v_3^-(\lambda)\,\frac{L_w(\lambda;\delta)\,U_w(\lambda;\delta)}{L_s(\lambda)\,U_s(\lambda)}\,e^{-jk_o x\lambda}d\lambda = 0 \quad ; \quad x > 0 \tag{3.49}$$

$$\int_{-\infty}^{\infty} Q(\lambda)\,v_2^+(\lambda)\,v_2^-(\lambda)\,e^{-jk_o x\lambda}d\lambda = \frac{-v_4 e^{jk_o x\lambda_n}}{2\cos\left(k_o\delta\sqrt{1-\lambda_n^2}\right)} \quad ; \quad x < 0, \tag{3.50}$$

where

$$v_4 = \begin{cases} A(\lambda_n) & , E_z \text{ polarization} \\ B(\lambda_n) & , H_z \text{ polarization.} \end{cases} \tag{3.51}$$

The solution of those proceeds in a manner parallel to the previous case. The resulting spectra are determined to be

$$Q(\lambda) = \frac{-v_4 L_w(\lambda_n;\delta)U_s(\lambda)\,v_3^-(\lambda_n)}{4\pi j\cos\left(k_o\delta\sqrt{1-\lambda_n^2}\right)L_s(\lambda_n)U_w(\lambda;\delta)\,v_2^-(\lambda)\,v_2^-(\lambda_n)\,v_3^+(\lambda)\,(\lambda+\lambda_n)} \tag{3.52}$$

$$P(\lambda) = \frac{v_1 v_4 L_w(\lambda_n;\delta)L_w(\lambda;\delta)\,v_3^-(\lambda_n)}{4\pi j\cos\left(k_o\delta\sqrt{1-\lambda_n^2}\right)L_s(\lambda_n)L_s(\lambda)\,v_2^-(\lambda)\,v_2^-(\lambda_n)\,v_3^+(\lambda)\,(\lambda+\lambda_n)} \tag{3.53}$$

with L_w, L_s, $v^{\pm}$, etc. as defined in (3.34), (3.35) and (3.31), (3.32).

Substituting (3.47), (3.29), (3.30), (3.51) and (3.33) into (3.53) and setting $\delta = 0$ we have

$$P_n^e(\lambda) = \left[\frac{-A(\lambda_n)}{\sqrt{1-\lambda_n^2}}\right] \frac{L_w(\lambda)\,L_w(\lambda_n)}{4\pi j L_s(\lambda)\,L_s(\lambda_n)} \frac{\sqrt{1-\lambda}\sqrt{1-\lambda_n}}{\lambda+\lambda_n} \tag{3.54}$$

$$P_n^h(\lambda) = B(\lambda_n) \frac{L_w(\lambda)\,L_w(\lambda_n)}{4\pi j L_s(\lambda)\,L_s(\lambda_n)} \frac{\sqrt{1+\lambda}\sqrt{1+\lambda_n}}{\lambda+\lambda_n} \tag{3.55}$$

corresponding to the spectra for the E_z and H_z polarizations, respectively. The modal field reflected back into the guide may be computed by substituting (3.52), (3.21) and (3.33) into (3.24) and employing the usual transformation to the λ plane to obtain (for $0 < y < \delta$)

$$\begin{aligned} F_z^s = \int_{-\infty}^{\infty} & \left[\frac{-v_4 v_3^-(\lambda_n)}{4\pi j \cos\left(k_o\delta\sqrt{1-\lambda_n^2}\right) v_2^-(\lambda)\,v_2^-(\lambda_n)\,v_3^+(\lambda)\,(\lambda+\lambda_n)}\right] \\ & \cdot \frac{L_w(\lambda_n;\delta)\; e^{-jk_o\delta\sqrt{1-\lambda^2}}}{L_s(\lambda)\,L_s(\lambda_n)\,U_w(\lambda;\delta)} \\ & \cdot \left[2jA(\lambda)\frac{\sin\left(k_o y\sqrt{1-\lambda^2}\right)}{\sqrt{1-\lambda^2}} + 2B(\lambda)\cos\left(k_o y\sqrt{1-\lambda^2}\right)\right] e^{-jk_o x\lambda} d\lambda \end{aligned} \tag{3.56}$$

As in the case of coupling, this integral can again be evaluated by closing the path of integration in (3.56) via a semi-infinite contour in the lower half λ plane to obtain

$$F_{zm}^s = \sum_{m=1}^{N} R_{mn}\left\{jA(\lambda_m)\frac{\sin\left(k_o y\sqrt{1-\lambda_m^2}\right)}{\sqrt{1-\lambda_m^2}} + B(\lambda_m)\cos\left(k_o y\sqrt{1-\lambda_m^2}\right)\right\} e^{-jk_o x\lambda_m} \tag{3.57}$$

where R_{mn} are the mode reflection coefficients given by

$$\begin{aligned} R_{mn} = & \frac{v_4 v_3^-(\lambda_n)\; e^{-jk_o\delta\sqrt{1-\lambda_m^2}}}{\cos\left(k_o\delta\sqrt{1-\lambda_n^2}\right) v_2^-(\lambda_m)\,v_2^-(\lambda_n)\,v_3^+(\lambda_m)\,(\lambda_m+\lambda_n)} \\ & \frac{L_w(\lambda_n;\delta)}{L_s(\lambda_m)\,L_s(\lambda_n)\,U_w'(\lambda_m;\delta)}. \end{aligned} \tag{3.58}$$

When δ is set to zero, this reduces to

$$R_{mn}^e = \frac{A(\lambda_n)}{\sqrt{1-\lambda_n^2}} \frac{L_w(\lambda_n)}{L_s(\lambda_m)\,L_s(\lambda_n)\,U_w'(\lambda_m)} \frac{\sqrt{1-\lambda_m}\sqrt{1-\lambda_n}}{\lambda_m+\lambda_n} \tag{3.59}$$

$$R^h_{mn} = B(\lambda_n)\frac{L_w(\lambda_n)}{L_s(\lambda_m)L_s(\lambda_n)U'_w(\lambda_m)}\frac{\sqrt{1+\lambda_m}\sqrt{1+\lambda_n}}{\lambda_m+\lambda_n} \tag{3.60}$$

for the E_z and H_z polarizations, respectively.

3.4 Computation of Spectra for Material Insert in a Perfectly Conducting Ground Plane

We now have all the necessary components required for constructing the spectra P^e_{rs} associated with the multilayer slab recessed in a ground plane as defined in (3.14). Substituting (3.40), (3.46), (3.54), (3.59) and (3.11) into (3.14) we obtain the E_z polarization result

$$P^e_{rs}(\lambda,\lambda_o) = \frac{L_w(\lambda)L_w(\lambda_o)}{2\pi j L_s(\lambda)L_s(\lambda_o)}\frac{\sqrt{1-\lambda}\sqrt{1-\lambda_o}}{\lambda+\lambda_o}\left[1+\sum_{m=1}^{N}\sum_{n=1}^{N}\frac{\tilde{V}^e_{mn}}{\lambda_o+\lambda_n}\left(\frac{\lambda+\lambda_o}{\lambda+\lambda_m}\right)\right] \tag{3.61}$$

where

$$\tilde{V}^e_{mn} = \frac{-A(\lambda_m)}{\sqrt{1-\lambda_m^2}}\frac{L_w(\lambda_m)}{L_s(\lambda_m)L_s(\lambda_n)U'_w(\lambda_n)}\sqrt{1-\lambda_m}\sqrt{1-\lambda_n}V^e_{mn} \tag{3.62}$$

$$V^e_{mn} = \{[I]+[R_{mn}]\}^{-1}_{mn}. \tag{3.63}$$

For H_z polarization, the spectra may be obtained by substituting (3.41), (3.47), (3.55), (3.60) and (3.11) into (3.14) to find

$$P^h_{rs}(\lambda,\lambda_o) = \frac{-L_w(\lambda)L_w(\lambda_o)}{2\pi j L_s(\lambda)L_s(\lambda_o)}\frac{\sqrt{1+\lambda}\sqrt{1+\lambda_o}}{\lambda+\lambda_o}\left[1+\sum_{m=1}^{N}\sum_{n=1}^{N}\frac{\tilde{V}^h_{mn}}{\lambda_o+\lambda_n}\left(\frac{\lambda+\lambda_o}{\lambda+\lambda_m}\right)\right] \tag{3.64}$$

where

$$\tilde{V}^h_{mn} = B(\lambda_m)\frac{L_w(\lambda_m)}{L_s(\lambda_m)L_s(\lambda_n)U'_w(\lambda_n)}\sqrt{1+\lambda_m}\sqrt{1+\lambda_n}V^h_{mn} \tag{3.65}$$

$$V^h_{mn} = \{[I]-[R_{mn}]\}^{-1}_{mn}. \tag{3.66}$$

Expressions (3.61) and (3.64) can now be substituted into (3.13) and the resulting integral can be evaluated by the method of steepest descents to yield the far

non-uniform diffracted field

$$F^s(\cos\phi,\cos\phi_0) \sim \sqrt{\frac{2\pi}{k_0}}e^{j\pi/4}P_{rs}(\cos\phi,\cos\phi_0)\frac{e^{-jk_0\rho}}{\sqrt{\rho}}, \tag{3.67}$$

where (ρ,ϕ) denote the usual cylindrical coordinates. In (3.67), F^s and P_{rs} refer to E_z^s and P_{rs}^e in the case of E_z incidence and to $Z_0H_z^s$, P_{rs}^h for H_z polarization. Although not apparent, (3.67) is reciprocal with respect to $\cos\phi$ and $\cos\phi_0$, as it should. We also note that $P_{rs}(\lambda,\lambda_0)$ is a combination of an inhomogeneous solution (direct diffracted term) and a sum of homogeneous solutions (modal contribution). It may also be easily shown from the asymptotic behavior of (3.61) and (3.64) that the homogeneous terms do not affect the edge condition.

3.5 Specialization to the GIBC Representation

To obtain numerical results, we must first provide expressions for the multilayered grounded slab reflection coefficient (i.e. $A(\lambda)$ and $B(\lambda)$), as well as the associated split functions and corresponding complex roots (waveguide modes). To accomplish these tasks in a simple manner, we consider the general GIBC approximation to $R(\lambda)$. This amounts to setting

$$\begin{aligned} A(\lambda) &= \sum_{n=0}^{N_A} A_n\left(1-\lambda^2\right)^n \\ B(\lambda) &= \sum_{n=0}^{N_B} B_n\left(1-\lambda^2\right)^n, \end{aligned} \tag{3.68}$$

where A_n and B_n are constants specific to the multilayered slab and are given in chapter two. Introducing (3.68) into (3.21) yields

$$R(\lambda) = -\left[\frac{\sum_{n=0}^{N_A}A_n(1-\lambda^2)^n - \sqrt{1-\lambda^2}\sum_{n=0}^{N_B}B_n(1-\lambda^2)^n}{\sum_{n=0}^{N_A}A_n(1-\lambda^2)^n + \sqrt{1-\lambda^2}\sum_{n=0}^{N_B}B_n(1-\lambda^2)^n}\right] \tag{3.69}$$

and note that for a given order of approximation, N_A and N_B are finite and in general $N_A = N_B$ or $N_A = N_B + 1$, with the order of the condition equal to

$$N_S = max\,(2N_A, 2N_B + 1)\,. \tag{3.70}$$

To evaluate the split functions $L_w(\lambda;\delta)$ and $U_w(\lambda;\delta)$, (3.68) is substituted into (3.34) and by setting $\delta = 0$ we obtain

$$L_w(\lambda)\,U_w(\lambda) = \begin{cases} 2\sqrt{1-\lambda^2}\sum_{n=0}^{N_B} B_n\,(1-\lambda^2)^n & E_z \text{ polarization} \\ 2\sum_{n=0}^{N_A} A_n\,(1-\lambda^2)^n & H_z \text{ polarization.} \end{cases} \tag{3.71}$$

The split functions are then trivially obtained as

$$U_w(\lambda) = L_w(-\lambda) = \begin{cases} \sqrt{2B_{N_B}}\sqrt{1-\lambda}\,\prod_{n=1}^{N_B}\left[\sqrt{1-\xi_n}-\lambda\right] & E_z \text{ polarization} \\ \sqrt{2A_{N_A}}\,\prod_{n=1}^{N_A}\left[\sqrt{1-\xi_n}-\lambda\right] & H_z \text{ polarization.} \end{cases} \tag{3.72}$$

where $Im\sqrt{1-\xi_n} < 0$ and $\{\xi_n\}$ are the N_A zeros of $\sum_{n=0}^{N_B} B_n\chi^n$ for E_z polarization or $\sum_{n=0}^{N_A} A_n\chi^n$ for H_z polarization. It is apparent from (3.44) and (3.72) that the pertinent waveguide mode propagation constants are given by $k_0\sqrt{1-\xi_n}$.

In a similar fashion, we may substitute (3.68) into (3.35) to obtain

$$\begin{aligned} L_s(\lambda)\,U_s(\lambda) &= \sum_{n=0}^{N_A} A_n\sqrt{1-\lambda^2}^{\,2n} + \sum_{n=0}^{N_B} B_n\sqrt{1-\lambda^2}^{\,2n+1} \\ &= \sum_{n=0}^{N_S} S_n\sqrt{1-\lambda^2}^{\,n} \qquad (3.73) \\ &= S_0\prod_{n=1}^{N_S}\left(1+\frac{\sqrt{1-\lambda^2}}{\gamma_n}\right) \qquad (3.74) \end{aligned}$$

where

$$\begin{aligned} S_n &= \begin{cases} A_{n/2} & n \text{ is even} \\ B_{(n-1)/2} & n \text{ is odd,} \end{cases} \\ \{\gamma_n\} &= \{\text{zeros of the polynomial } \sum_{l=0}^{N_S}\frac{S_l}{S_0}(-1)^l\gamma^l\}. \end{aligned} \tag{3.75}$$

The factorization of (3.74) is again trivial upon making use of the well known splitting germaine to the impedance half plane problem [34]. Noting that

$$1+\eta\sqrt{1-\lambda^2} \stackrel{def}{=} \frac{\sqrt{1-\lambda^2}}{K_+(\lambda;\eta)\,K_-(\lambda;\eta)} \tag{3.76}$$

we have,

$$U_s(\lambda) = L_s(-\lambda) = \frac{\left(\sqrt{1-\lambda}\right)^{N_S}\sqrt{S_0}}{\prod_{n=1}^{N_S} K_+(\lambda;1/\gamma_n)} \tag{3.77}$$

where

$$K_+(\lambda;\eta) = K_-(-\lambda;\eta) \;=\; \begin{cases} \widetilde{K}_+(\lambda;\eta) & Re(\eta)\geq 0 \\ \left\{j\eta\left(\lambda-\sqrt{1-1/\eta^2}\right)\widetilde{K}_+(\lambda;\eta)\right\}^{-1} & Re(\eta)<0. \end{cases} \tag{3.78}$$

and

$$\widetilde{K}_-(\cos\alpha;\eta) = \frac{\sqrt{2}\sin\alpha/2\sqrt{\frac{2}{\pi}}\left[\Psi_\pi(3\pi/2-\alpha-\theta)\,\Psi_\pi(\pi/2-\alpha+\theta)\right]^2}{\Psi_\pi^4(\pi/2)\left[1+\sqrt{2}\cos\left(\frac{\pi/2-\alpha+\theta}{2}\right)\right]\left[1+\sqrt{2}\cos\left(\frac{3\pi/2-\alpha-\theta}{2}\right)\right]} \tag{3.79}$$

In the above $Re\,(\eta\geq 0)$, $Im\left(\sqrt{1-1/\eta^2}\right)\leq 0$, $\theta=\sin^{-1}(\eta), 0\leq Re(\theta)$, and Ψ_π is the Maliuzhinets function [22], whose evaluation in algebraic form has been given in [50]. Whereas the zeros of $U_w(\lambda)$ represent the waveguide modes, the zeros of $L_s(\lambda)$ (which are the poles of K_-) correspond to the surface waves supported by the material layer. Although not required in this analysis, these are easily extracted from (3.78) and (3.79).

The expressions (3.68) through (3.79) provide a complete description of a GIBC implementation and permit the simulation of any multilayered coating. We remark that a unique GIBC modeling of a given coating does not exist; in fact one may employ GIBCs of substantially different character to simulate the same configuration. This point is discussed in the following section and some numerical results are provided for illustration purposes.

3.6 Numerical Results

In this section GIBC simulations of various material inserts are presented and compared with exact results available for the case of a single layer. Due to its greater interest, data is presented only for the H_z polarization case. The GIBC employed here-in are given in chapter two. These are valid for arbitrary multilayer coatings and are therefore suited for this application. In particular, these multilayer GIBC are synthesized by combining the component-layer GIBC in an appropriate manner, pointing to the necessity of understanding single layer simulations in order to construct multilayer ones.

Figure 3.3 shows the far zone pattern of a single layer insert ($\epsilon = 2 - j.0001, \mu = 1.2, \tau = .2\lambda$) modeled by various "low contrast" GIBC (i.e. those GIBC which improve as the layer thickness or index of refraction decreases). To illustrate their relative contributions to the far zone pattern, the direct diffraction and modal contributions have been isolated in Figures 3.3(a) and 3.3(b), respectively, with the overall result presented in Figure 3.3(c). We note that for this low contrast GIBC, an 8^{th} order simulation provides a reasonable approximation to the diffraction pattern.

In Figure 3.4, both the thickness and the index of refraction have been increased in a low contrast simulation of a (single layer) material insert with $\epsilon = 3.5 - j.0001$, $\mu = 2.0$, and $\tau = .4\lambda$. In contrast to the previous figure we now observe that a 20^{th} order simulation is required to obtain a converged result. This degradation with increasing index of refraction proves typical of low contrast simulations and illustrates the need for other types of GIBC whose performance improves in this range of material parameters.

In Figure 3.5 the same material insert corresponding to the data of Figure 3.4

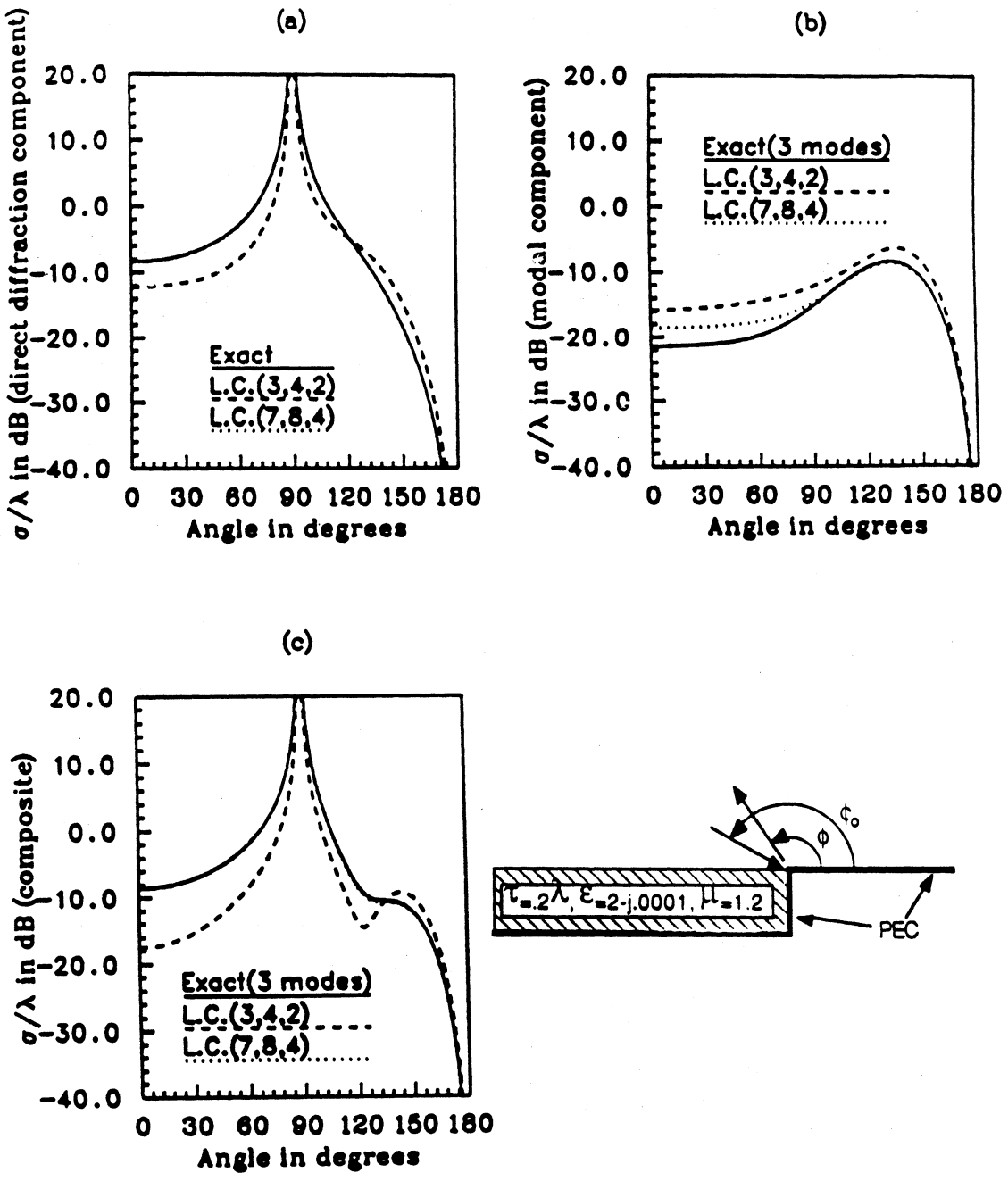

Figure 3.3: H_z polarization backscatter echo width for a material insert with $\tau = .2\lambda$, $\epsilon = 2 - j.0001$, $\mu = 1.2$ modeled by low contrast GIBCs (see Table 3.1 for an explanation of the legend entries). (a) direct diffraction component (b) modal component (c) composite.

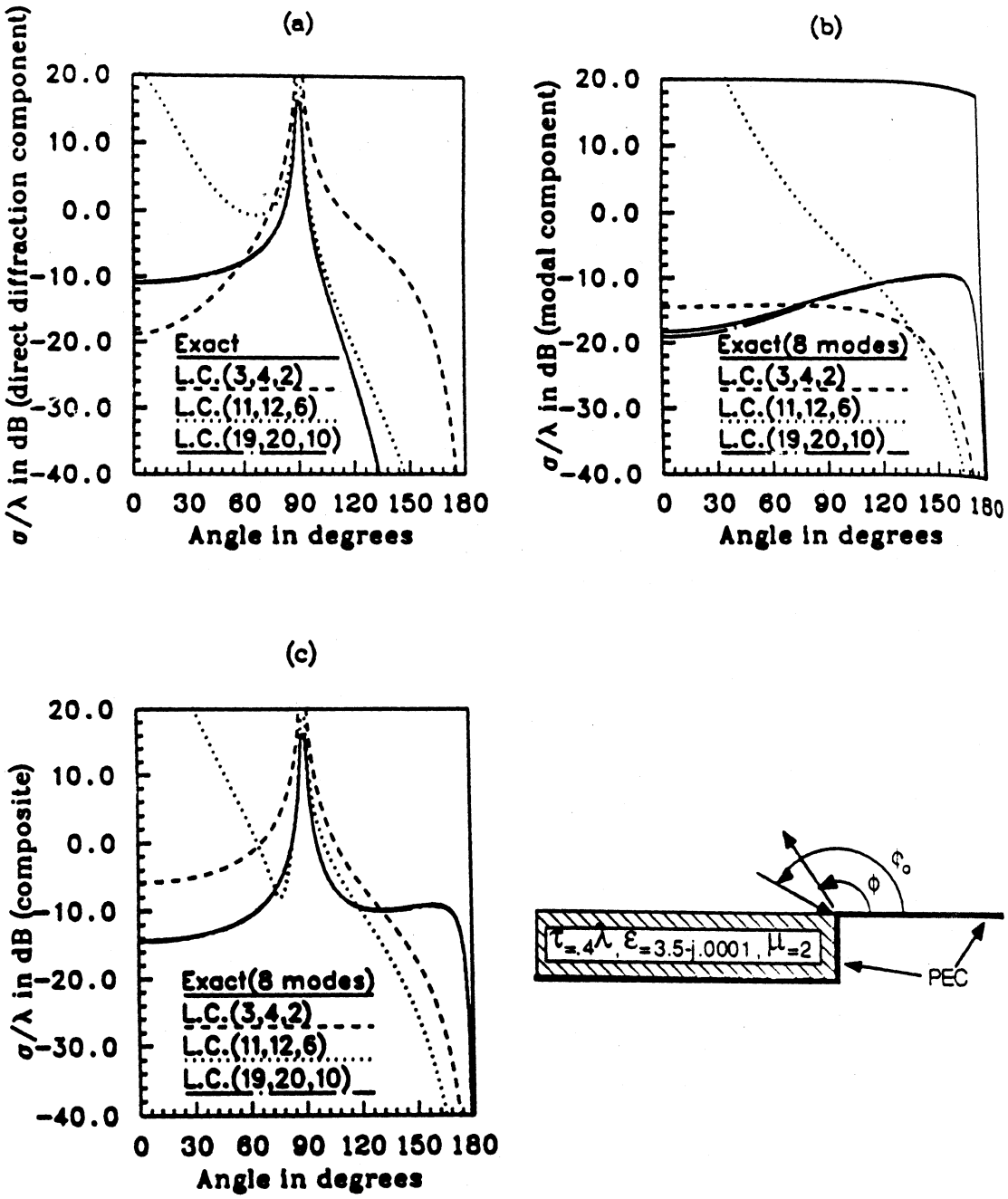

Figure 3.4: H_z polarization backscatter echo width for a material insert with $\tau = .4\lambda$, $\epsilon = 3.5 - j.0001$, $\mu = 2$ modeled by low contrast GIBCs (see Table 3.1 for an explanation of the legend entries). (a) direct diffraction component (b) modal component (c) composite.

is simulated with high contrast GIBC (i.e., a GIBC which improves as the index of refraction increases or as the layer thickness decreases). In contrast to the data in Figure 3.4, we now observe that only a second order high contrast GIBC simulation is required to accurately evaluate the far zone scattering. This difference in performance between the low and high contrast GIBC stems from the type of approximation employed in their derivation and the reader is referred to chapter two for a more in depth discussion. Some insight on the type of simulation provided by the low and high contrast GIBC may be gained through an examination of the waveguide modes predicted by the different simulations. These are presented in Tables 3.1 and 3.2 for the single layer simulations corresponding to the data in Figure 3.4 and 3.5.

The exact modes given in the table are generated by the equation

$$\lambda_n = \sqrt{\epsilon_r \mu_r - \left(\frac{n\pi}{k_0 \tau}\right)^2}, \quad n = 0, 1, 2, \ldots. \tag{3.80}$$

We observe that as the order of the low contrast simulation is increased, the data in Table 3.1 reveal that the waveguide modes are "picked up" in a sequential manner corresponding to increasing n in (3.80). On the other hand (see Table 3.2), the high contrast GIBCs pick up the $n = 2$ exact mode immediately and then "branch off" to pick up the other modes. The discrepency in pattern convergence between Figures 3.4 and 3.5 clearly suggests that the $n = 2$ mode is the most significant in terms of diffraction (for this particular configuration). We explain this physically by noting that the $n = 2$ mode may be resolved into its constituent rays which strike the interface at a characteristic angle (say θ_2^{mod}) which is greater than the critical angle θ^c of the material insert. On the other hand, the $n = 0$ and $n = 1$ modes are associated with characteristic angles less than the critical angle. This implies that upon coupling into the slab, the $n = 2$ waveguide mode is partially transmitted into free space while the lower order waveguides modes remain bound.

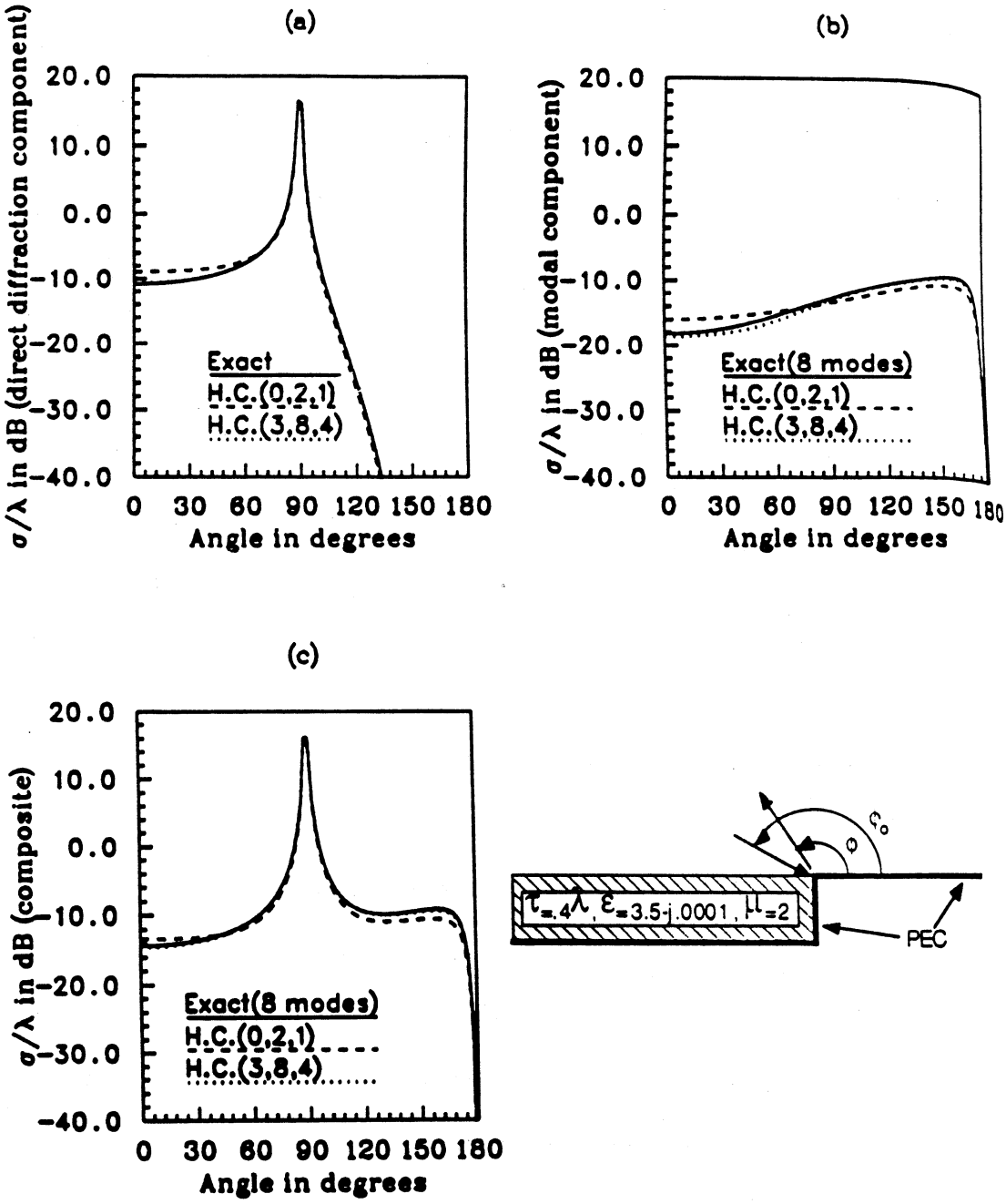

Figure 3.5: H_z polarization backscatter echo width for a material insert with $\tau = .4\lambda$, $\epsilon = 3.5 - j.0001$, $\mu = 2$ modeled by high contrast GIBCs (see Table 3.2 for an explanation of the legend entries). (a) direct diffraction component (b) modal component (c) composite.

Exact Modes	L. C.(1,2,1)	L.C.(5,6,3)	L.C.(9,10,5)	L.C.(13,14,7)	L.C.(17,18,9)	L.C.(21,22,11)
$2.6458 - j0$	$2.6458 - j0$	$2.6458 - j0$	$2.6458 - j0$	$2.6458 - j0$	$2.6458 - j0$	$2.6458 - j0$
$2.3318 - j0$		$2.3324 - j.1518$	$2.3303 - j0$	$2.3318 - j0$	$2.3318 - j0$	$2.3318 - j0$
$0.8660 - j0.0001$		$-2.3324 - j.1517$	$1.7608 - j.0001$	$1.1583 - j.0001$	$0.8782 - j.0001$	$0.86612 - j.0001$
$0 - j2.6575$			$2.3156 - j.1518$	$1.5228 - j1.4058$	$0.8198 - j1.9935$	$0.3937 - j2.6289$
$0 - j4.2464$			$-2.3156 - j.1517$	$-1.5227 - j1.4058$	$-0.8197 - j1.9934$	$-0.3936 - j2.6289$
$0 - j5.6624$				$3.0782 - j2.1345$	$2.2444 - j2.6318$	$1.6576 - j3.1906$
$0 - j7.0178$				$-3.0782 - j2.1344$	$-2.2444 - j2.6318$	$-1.6576 - j3.1906$
$0 - j8.3404$					$4.1090 - j2.8858$	$3.1642 - j3.5300$
$0 - j9.6437$					$-4.1090 - j2.8858$	$-3.1642 - j3.5300$
$0 - j10.9348$						$5.2491 - j3.5008$
$0 - j12.2168$						$-5.2491 - j3.5008$

Table 3.1: Low contrast approximation to waveguide modes for a layer with $\epsilon = 3.5 - j.0001, \mu = 2.0$, and $\tau = .4\lambda$. For each low contrast boundary condition, the three numbers of the column headings indicate the order of the approximation in thickness τ, the order of the resulting boundary condition, and the total number of modes (see chapter two).

Exact Modes	H. C.(0,2,1)	H.C.(1,4,2)	H.C.(2,6,3)	H.C.(3,8,4)	H.C.(4,10,5)
$2.6458 - j0$				$7.9636 - j.0032$	$3.2862 - j.0001$
$2.3318 - j0$		$5.5825 - j.0023$	$2.2571 - j.0001$	$2.2813 - j0$	$2.2714 - j0$
$0.8660 - j0.0001$	$0.8667 - j.0001$	$0.8649 - j.0001$	$0.8660 - j.0001$	$0.8660 - j.0001$	$0.8660 - j.0001$
$0 - j2.6575$			$0 - j2.1309$	$0 - j2.0694$	$0.6002 - j2.2920$
$0 - j4.2464$					$-0.6002 - j2.2920$

Table 3.2: High contrast approximation to waveguide modes for a layer with $\epsilon = 3.5 - j.0001, \mu = 2.0$, and $\tau = .4\lambda$. For each high contrast boundary condition, the three numbers of the column headings indicate the approximation in the index of refraction κ^{-1}, the order of the resulting boundary condition, and the total number of modes.

The above hypothesis may be tested by computing exact solutions in which the selection of the included waveguide modes parallels the order in which they are picked up depending on whether a low or high contrast GIBC simulation is employed. Figure 3.6 depicts a high contrast simulation of a single layer having $\epsilon = 11 - j.0001, \mu = 7$, and $\tau = .4\lambda$. The 10-mode result is a pattern obtained by adding in modes sequentially as determined from (3.80), thus paralleling a low contrast mode selection scheme. On the other hand, the single mode result contains the contribution of only the $n = 7$ mode (the mode with $\theta^m > \theta^c$), thus, paralleling the high contrast mode selection criteria. This clearly verifies that the most significant waveguide modes are those that are "visible", i.e. those with $\theta^m > \theta^c$.

Finally, Figure 3.7 provides a simulation of a three layer insert composed of two high contrast layers ($\epsilon = 11 - j.0001, \mu = 7$, and $\tau = .4\lambda$ and $\epsilon = 3.5 - j.0001, \mu = 2.0$, and $\tau = .4\lambda$) placed beneath a low contrast layer with $\epsilon = 2 - j.0001, \mu = 1.2$ and $\tau = .2\lambda$. These are precisely the layers considered earlier in isolation. One might, therefore, expect that the order of a GIBC which provided a converged result for the single layer simulation will also provide an equally acceptable simulation when the slab is part of a multilayer stack. For the case at hand this is indeed true, as evidenced by the converged 9^{th} order result. We also remark that the presence of the two high contrast layers enhances the modal contribution to the total diffraction when compared with the single layer data given in Figures 3.3(b) and 3.3(c).

3.7 Summary

In summary, the scattering from a vertically inhomogeneous slab recessed in a ground plane was obtained through application of the generalized scattering matrix technique in conjunction with the dual integral equation approach. The solution was

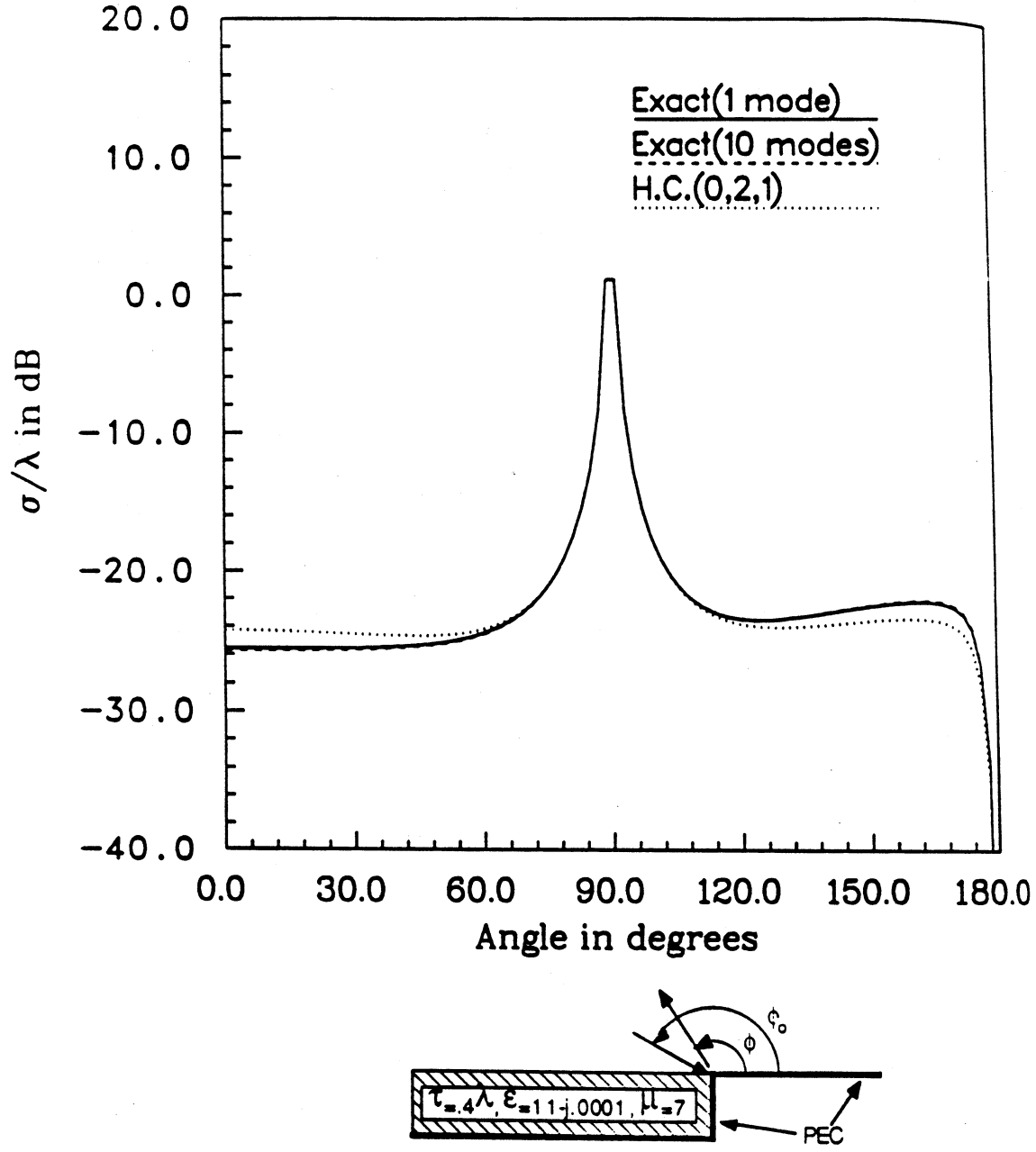

Figure 3.6: H_z polarization backscatter echo width for a material insert with $\tau = .4\lambda$, $\epsilon = 11. - j.0001$, $\mu = 7$ modeled by high contrast GIBCs (see Table 3.2 for an explanation of the legend entries).

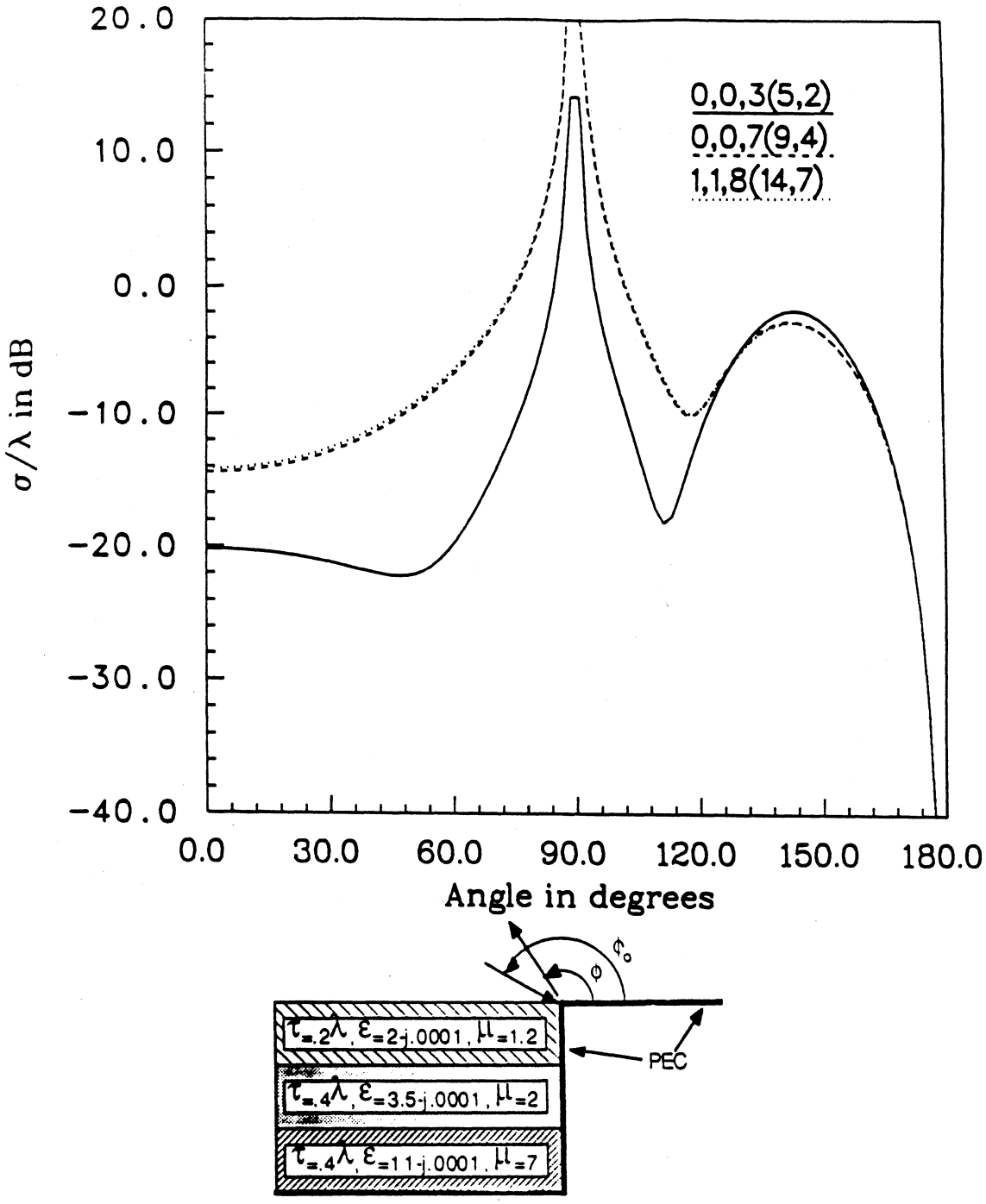

Figure 3.7: H_z polarization backscatter echo width for a three-layer material insert with ($\tau_1 = .4\lambda$, $\epsilon_1 = 11. - j.0001$, $\mu_1 = 7$), ($\tau_2 = .4\lambda$, $\epsilon_2 = 3.5 - j.0001$, $\mu_2 = 2$), ($\tau_3 = .2\lambda$, $\epsilon_3 = 2. - j.0001$, $\mu_3 = 1.2$). In the legend entry a.b,c(d,e), a and b denote the approximation in κ^{-1} of the high constrast layers 1 and 2, c denotes the approximation in τ of the low constast layer 3, while d is the order of the composite GIBC and e is the total number of modes.

specialized to the case of a multilayered slab simulated with a generalized impedance boundary condition (GIBC). Results were given for various single layer inserts and it was seen that in the case of materials having sufficiently high index of refraction high contrast GIBC simulations converged more rapidly (with respect to the order of the GIBC) and performed better than low contrast simulations. Finally, results were presented for a 1λ thick lossless three-layer insert containing both high and low contrast layers. It was shown that the simulation converged at the point predicted by the individual layer simulations, suggesting a method for constructing multilayer simulations.

CHAPTER IV

GENERAL SOLUTION OF THE DIFFRACTION BY A MATERIAL DISCONTINUITY IN A THICK DIELECTRIC/FERRITE SLAB

In this chapter and the following one it is demonstrated that a GIBC/GSTC sheet characterization can yield a unique solution when supplemented with certain conditions at the sheet discontinuity which do not require an apriori knowledge of the edge fields. As a vehicle for presenting this solution procedure we employ the dual integral equation method to consider the plane wave diffraction by a discontinuous distributed sheet (see Figure 4.1(b)). This very general model is capable of representing material half-planes, material junctions, and material discontinuities on grounded structures, such as those shown in Figure 4.2. In addition, a distributed sheet model typically renders the same degree of accuracy as the usual infinitely-thin sheet, but with a lower order condition. It is, therefore, of much practical interest.

In the first section of the chapter, the GSTC representation of the distributed sheet discontinuity is used to develop dual integral equations in terms of the unknown spectral functions proportional to the sheet currents. These equations are then solved in the standard manner to yield expressions for the spectral functions in terms of unknown constants. The constants are dependent on the material and geo-

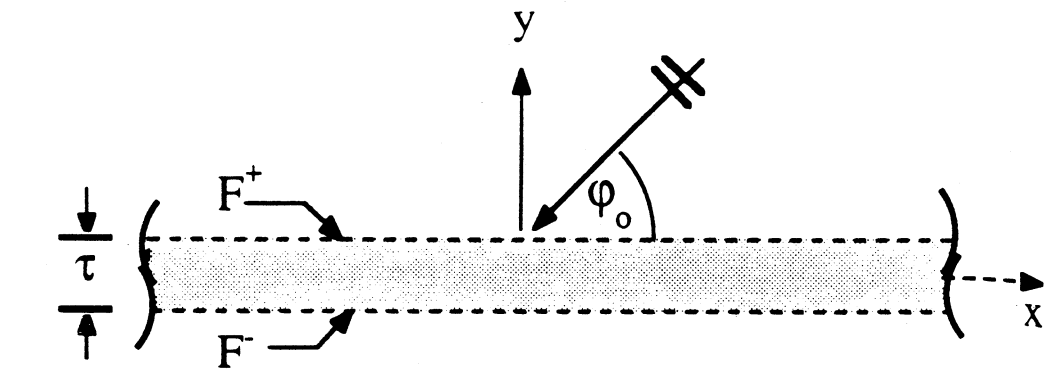

Odd GSTC: $u_{11}\left(-\frac{\partial x^2}{k^2}\right)\{F^+ - F^-\} + \frac{j}{k}u_{12}\left(-\frac{\partial x^2}{k^2}\right)\partial y[F^+ + F^-] = 0$

Even GSTC: $u_{21}\left(-\frac{\partial x^2}{k^2}\right)\{F^+ + F^-\} + \frac{j}{k}u_{22}\left(-\frac{\partial x^2}{k^2}\right)\partial y[F^+ - F^-] = 0$

(a)

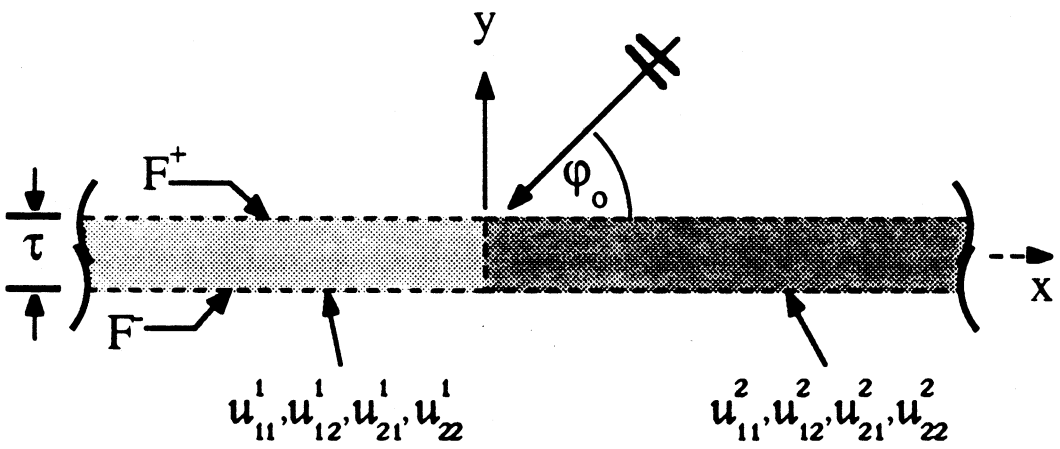

(b)

Figure 4.1: (a) Distributed sheet. (b) Distributed sheet discontinuity.

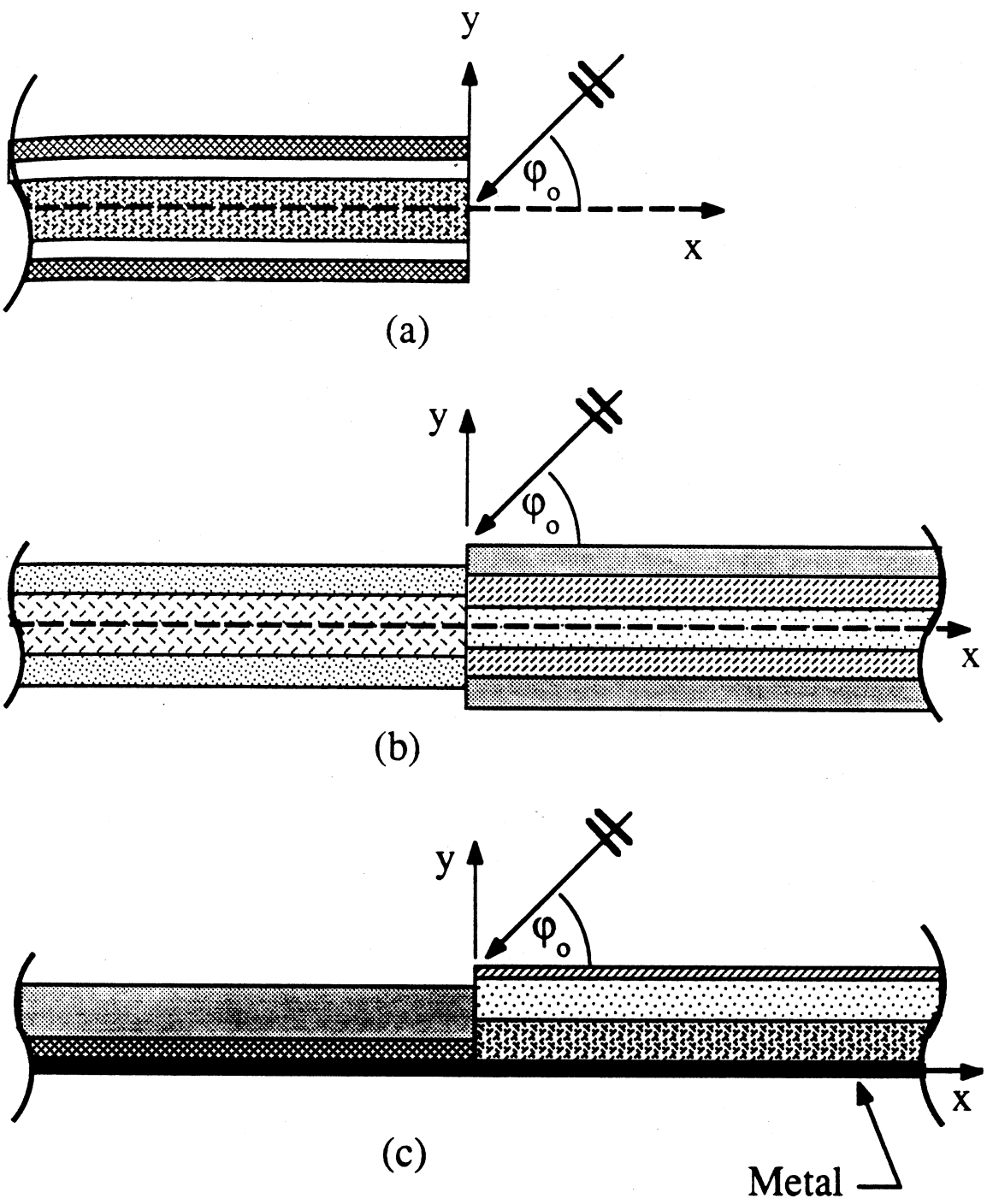

Figure 4.2: Geometries modeled by a discontinuous distributed sheet. (a) Material half-plane. (b) Material-material join. (c) Grounded join.

metrical properties of the discontinuity and their specific value is identified here for several discontinuities by comparison with a few known diffraction solutions. This demonstrates the validity of the presented solution, but in general, the determination of the constants requires the enforcement of additional constraints demanding field continuity accross the layer discontinuity. The development of these conditions and their use in solving for the constants are presented in chapter five.

4.1 Dual Integral Equation Formulation

Consider a distributed sheet of thickness τ illuminated by the plane wave

$$F_{inc} = e^{jk(x\cos\phi_o + y\sin\phi_o)} = \begin{cases} E_{z,inc}, & E_z \text{ polarization,} \\ Z_o H_{z,inc}, & H_z \text{ polarization,} \end{cases} \tag{4.1}$$

as shown in Figure 4.1(a). The excitation (4.1) induces reflected and transmitted fields which are explicitly given by the properties of the distributed sheet. If this sheet models a symmetric slab, then an appropriate GSTC representation is formally given by (see chapter 2)

$$\mathcal{U}^1_{11}\left(-\frac{\partial x^2}{k^2}\right)\left\{F^+ - F^-\right\} + \frac{j}{k}\mathcal{U}^1_{12}\left(-\frac{\partial x^2}{k^2}\right)\left\{\partial y\left[F^+ + F^-\right]\right\} = 0, \quad -\infty < x < \infty \tag{4.2}$$

$$\mathcal{U}^1_{21}\left(-\frac{\partial x^2}{k^2}\right)\left\{F^+ + F^-\right\} + \frac{j}{k}\mathcal{U}^1_{22}\left(-\frac{\partial x^2}{k^2}\right)\left\{\partial y\left[F^+ - F^-\right]\right\} = 0, \quad -\infty < x < \infty. \tag{4.3}$$

in which F is the total field, $F^{\pm} = F(x, y = \pm\tau/2)$, $\partial x F^{\pm} = \frac{\partial}{\partial x}F(x, y = \pm\tau/2)$, and $\partial y F^{\pm} = \frac{\partial}{\partial y}F(x,y)\,|_{y=\pm\tau/2}$. Also, $\mathcal{U}^1_{ij}\left(-\frac{\partial x^2}{k^2}\right)$ are differential operators which operate on the field quantity in the curly brackets, and are finite polynomials in $-\frac{\partial x^2}{k^2}$ whose coefficients depend on the slab modeled by the distributed sheet. To maintain the generality of the solution, the $\mathcal{U}^1_{ij}$ operators are left in symbolic form and the reader is referred to chapter two for their explicit representation in terms of the material

constants and thickness of the layers comprising the modeled slab. In general, the order of $\mathcal{U}_{11}$ (i.e. the highest derivative present) is usually the same or one more than that of $\mathcal{U}_{12}$ and similarly the order of $\mathcal{U}_{21}$ is the same or one more than the order of $\mathcal{U}_{22}$. Thus, we may define the orders of the GSTCs in (4.3) to be

$$\begin{aligned} N_1^{odd} &= \text{maximum}\left\{ \text{order of } \mathcal{U}_{11}^1\left(\lambda^2\right), 1 + \text{ order of } \mathcal{U}_{12}^1\left(\lambda^2\right)\right\} \\ N_1^{even} &= \text{maximum}\left\{ \text{order of } \mathcal{U}_{21}^1\left(\lambda^2\right), 1 + \text{ order of } \mathcal{U}_{22}^1\left(\lambda^2\right)\right\} \end{aligned} \tag{4.4}$$

The reflected and transmitted fields may now be easily determined by employing (4.3) to find

$$F_{refl} = R_1 e^{jk(x\cos\phi_o - y\sin\phi_o)} \tag{4.5}$$

$$F_{tran} = T_1 e^{jk(x\cos\phi_o + y\sin\phi_o)} \tag{4.6}$$

in which R_1 and T_1 are the reflection and transmission coefficients, respectively, and are given as

$$R_1 = \frac{e^{jk\tau\sin\phi_o}}{2}\left[R_1^{even} + R_1^{odd}\right] \tag{4.7}$$

$$T_1 = \frac{e^{jk\tau\sin\phi_o}}{2}\left[R_1^{even} - R_1^{odd}\right]. \tag{4.8}$$

with

$$R_1^{even} = \frac{\sin\phi_o\mathcal{U}_{22}^1(\cos^2\phi_o) - \mathcal{U}_{21}^1(\cos^2\phi_o)}{\sin\phi_o\mathcal{U}_{22}^1(\cos^2\phi_o) + \mathcal{U}_{21}^1(\cos^2\phi_o)} \tag{4.9}$$

$$R_1^{odd} = \frac{\sin\phi_o\mathcal{U}_{12}^1(\cos^2\phi_o) - \mathcal{U}_{11}^1(\cos^2\phi_o)}{\sin\phi_o\mathcal{U}_{12}^1(\cos^2\phi_o) + \mathcal{U}_{11}^1(\cos^2\phi_o)}. \tag{4.10}$$

We remark that in (4.9) and (4.10), $\mathcal{U}_{ij}^1(\cos^2\phi_o)$ now represent simple polynomial functions in $\cos^2\phi_o$, since $-\partial x^2/k^2 = \cos^2\phi_o$ in view of the field expressions (4.5) and (4.6).

Consider now the case where the right half of the distributed sheet in Figure 4.1(a) is replaced by another sheet of the same thickness, but of different properties, as illustrated in Figure 4.1(b). The GSTC representation of this modified sheet is

$$\begin{aligned} \mathcal{U}_{11}^1\left(-\frac{\partial x^2}{k^2}\right)\left\{F^+ - F^-\right\} + \frac{j}{k}\mathcal{U}_{12}^1\left(-\frac{\partial x^2}{k^2}\right)\left\{\partial y\left[F^+ + F^-\right]\right\} &= 0 \\ \mathcal{U}_{21}^1\left(-\frac{\partial x^2}{k^2}\right)\left\{F^+ + F^-\right\} + \frac{j}{k}\mathcal{U}_{22}^1\left(-\frac{\partial x^2}{k^2}\right)\left\{\partial y\left[F^+ - F^-\right]\right\} &= 0, \end{aligned} \quad (4.11)$$

for $-\infty < x < 0$ and

$$\begin{aligned} \mathcal{U}_{11}^2\left(-\frac{\partial x^2}{k^2}\right)\left\{F^+ - F^-\right\} + \frac{j}{k}\mathcal{U}_{12}^2\left(-\frac{\partial x^2}{k^2}\right)\left\{\partial y\left[F^+ + F^-\right]\right\} &= 0 \\ \mathcal{U}_{21}^2\left(-\frac{\partial x^2}{k^2}\right)\left\{F^+ + F^-\right\} + \frac{j}{k}\mathcal{U}_{22}^2\left(-\frac{\partial x^2}{k^2}\right)\left\{\partial y\left[F^+ - F^-\right]\right\} &= 0, \end{aligned} \quad (4.12)$$

for $0 < x < \infty$, where the superscripts 1 and 2 distinguish the left- and right-hand sheets, respectively. Referring to our previous discussion, the orders of the right hand side GSTCs are given as

$$\begin{aligned} N_2^{odd} &= \max\left\{\text{ order of } \mathcal{U}_{11}^2\left(\lambda^2\right) \text{ in } \lambda, 1 + \text{ order of } \mathcal{U}_{12}^2\left(\lambda^2\right) \text{ in } \lambda\right\} \\ N_2^{even} &= \max\left\{\text{ order of } \mathcal{U}_{21}^2\left(\lambda^2\right) \text{ in } \lambda, 1 + \text{ order of } \mathcal{U}_{22}^2\left(\lambda^2\right) \text{ in } \lambda\right\}. \end{aligned} \quad (4.13)$$

The modified right hand side sheet induces a scattered field F_s in the presence of the excitation (4.1), and the total field can now be represented as

$$F = \begin{cases} F_{inc} + F_{refl} + F_s & y > \tau/2 \\ F_{tran} + F_s & y < \tau/2 \end{cases} \quad (4.14)$$

where F_s is the unknown scattered field in the region $|y| > \tau/2$ and can be expressed as either [10] [52]

$$F^s(x,y) = \int_C \left[\frac{|y|}{y} P_{odd}(\cos\alpha) + P_{even}(\cos\alpha)\right] e^{-jk\sin\alpha(|y|-\tau/2)} e^{-jkx\cos\alpha} d\alpha.$$

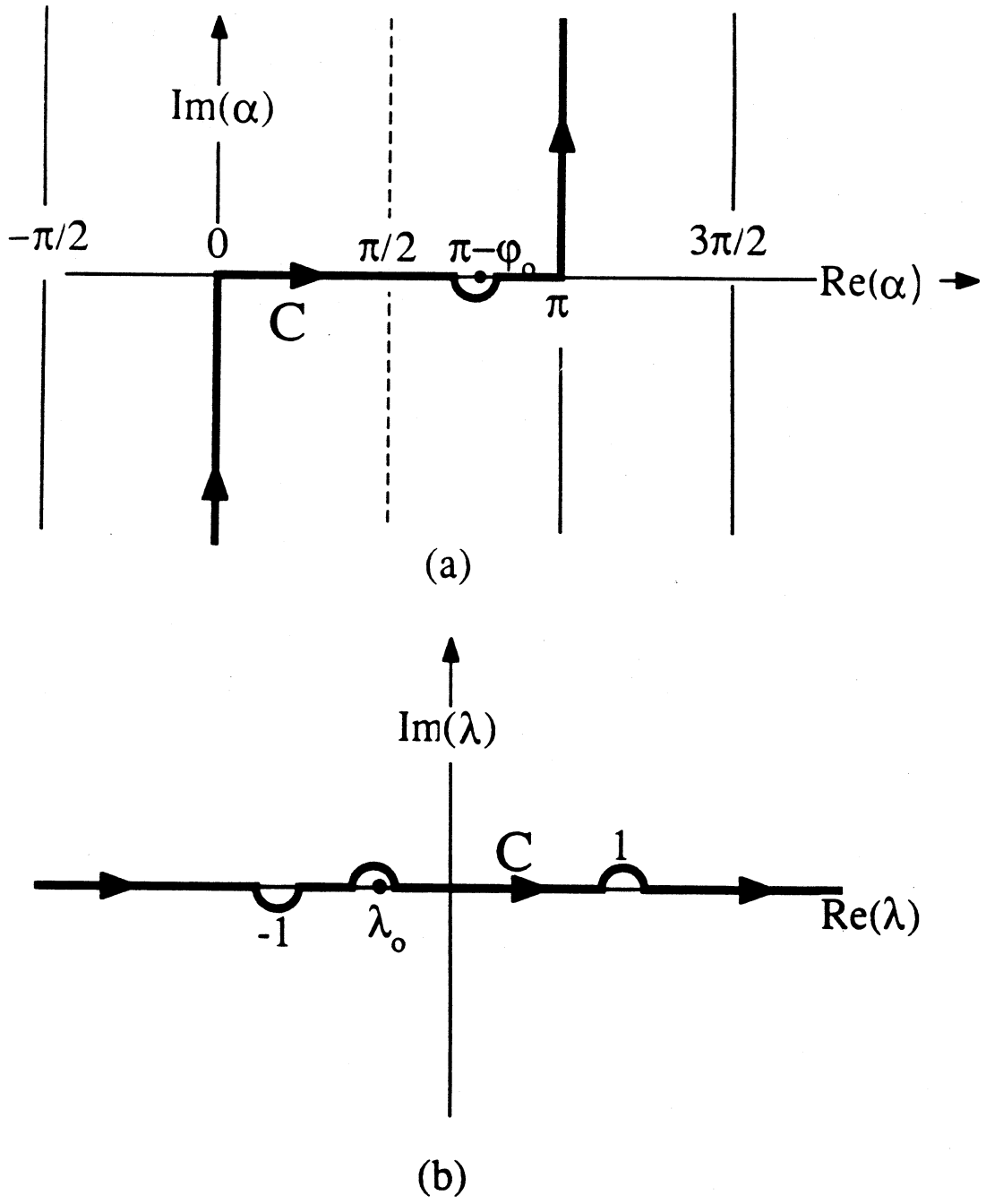

Figure 4.3: (a) Illustration of C contour in the complex α plane and (b) complex λ plane.

or

$$F^s(x,y) = \int_{-\infty}^{\infty} \left[\frac{|y|}{y} P_{odd}(\lambda) + P_{even}(\lambda) \right] e^{-jk\sqrt{1-\lambda^2}(|y|-\tau/2)} e^{-jkx\lambda} \frac{d\lambda}{\sqrt{1-\lambda^2}}. \quad (4.16)$$

upon invoking the transformation $\lambda = \cos\alpha$. The contour C in (4.15) is the integration path in the complex α plane shown in Figure 4.3(a), and its counterpart for the λ plane is illustrated in Figure 4.3(b). Also, the spectral functions $P_{odd}(\lambda)$ and $P_{even}(\lambda)$ are directly related to the Fourier transforms of the unknown equivalent currents

$$J_{odd} = F_s^+ - F_s^- \quad (4.17)$$

$$J_{even} = F_s^+ + F_s^-, \quad (4.18)$$

via the relations

$$J_{odd}(x) = 2\int_{-\infty}^{\infty} P_{odd}(\lambda)\, e^{-jkx\lambda} \frac{d\lambda}{\sqrt{1-\lambda^2}} \quad (4.19)$$

$$J_{even}(x) = 2\int_{-\infty}^{\infty} P_{even}(\lambda)\, e^{-jkx\lambda} \frac{d\lambda}{\sqrt{1-\lambda^2}}. \quad (4.20)$$

Assuming that

$$\begin{aligned} J_{odd}(x) &\sim x^{s_{odd}} \text{ as } x \to 0 \\ J_{even}(x) &\sim x^{s_{even}} \text{ as } x \to 0 \end{aligned} \quad (4.21)$$

with $0 < s_{odd} \leq 1$ and $0 < s_{even} \leq 1$, from (4.19) - (4.20) and the Abelian theorem we have

$$\begin{aligned} P_{odd}(\lambda) &\sim \lambda^{-s_{odd}} \text{ as } |\lambda| \to \infty \\ P_{even}(\lambda) &\sim \lambda^{-s_{even}} \text{ as } |\lambda| \to \infty \end{aligned} \quad (4.22)$$

From the asymptotic behavior of $P_{odd}(\lambda)$ and $P_{even}(\lambda)$, it may be easily seen that the integral representation (4.16) is well-behaved and convergent for all x and y.

Substituting (4.1), (4.5), (4.6), (4.14) and (4.16) into the transition conditions (4.11) and (4.12) we obtain

$$\int_{-\infty}^{\infty} \mathcal{G}_1^{odd}\left(\lambda^2\right) P_{odd}(\lambda)\, e^{-jkx\lambda} \frac{d\lambda}{\sqrt{1-\lambda^2}} = 0 \tag{4.23}$$

$$\int_{-\infty}^{\infty} \mathcal{G}_1^{even}\left(\lambda^2\right) P_{even}(\lambda)\, e^{-jkx\lambda} \frac{d\lambda}{\sqrt{1-\lambda^2}} = 0. \tag{4.24}$$

for $x < 0$ and

$$\int_{-\infty}^{\infty} 2\mathcal{G}_2^{odd}(\lambda^2)\, P_{odd}(\lambda)\, e^{-jkx\lambda} \frac{d\lambda}{\sqrt{1-\lambda^2}} = \frac{2\sin\phi_o e^{jkx\lambda_o} e^{jkr/2\sin\phi_o} Z_{odd}(\lambda_o^2)}{\mathcal{G}_1^{odd}(\lambda_o^2)} \tag{4.25}$$

$$\int_{-\infty}^{\infty} 2\mathcal{G}_2^{even}(\lambda^2)\, P_{even}(\lambda)\, e^{-jkx\lambda} \frac{d\lambda}{\sqrt{1-\lambda^2}} = \frac{2\sin\phi_o e^{jkx\lambda_o} e^{jkr/2\sin\phi_o} Z_{even}(\lambda_o^2)}{\mathcal{G}_1^{even}(\lambda_o^2)} \tag{4.26}$$

for $x > 0$, where $\lambda_o = \cos\phi_o$ and

$$\mathcal{G}_1^{odd}\left(\lambda^2\right) = \mathcal{U}_{11}^1\left(\lambda^2\right) + \sqrt{1-\lambda^2}\mathcal{U}_{12}^1\left(\lambda^2\right) \tag{4.27}$$

$$\mathcal{G}_1^{even}\left(\lambda^2\right) = \mathcal{U}_{21}^1\left(\lambda^2\right) + \sqrt{1-\lambda^2}\mathcal{U}_{22}^1\left(\lambda^2\right) \tag{4.28}$$

$$\mathcal{G}_2^{odd}\left(\lambda^2\right) = \mathcal{U}_{11}^2\left(\lambda^2\right) + \sqrt{1-\lambda^2}\mathcal{U}_{12}^2\left(\lambda^2\right) \tag{4.29}$$

$$\mathcal{G}_2^{even}\left(\lambda^2\right) = \mathcal{U}_{21}^2\left(\lambda^2\right) + \sqrt{1-\lambda^2}\mathcal{U}_{22}^2\left(\lambda^2\right) \tag{4.30}$$

$$Z_{odd}\left(\lambda_o^2\right) = \left[\mathcal{U}_{11}^1\left(\lambda_o^2\right)\mathcal{U}_{12}^2\left(\lambda_o^2\right) - \mathcal{U}_{12}^1\left(\lambda_o^2\right)\mathcal{U}_{11}^2\left(\lambda_o^2\right)\right] \tag{4.31}$$

$$Z_{even}\left(\lambda_o^2\right) = \left[\mathcal{U}_{21}^1\left(\lambda_o^2\right)\mathcal{U}_{22}^2\left(\lambda_o^2\right) - \mathcal{U}_{22}^1\left(\lambda_o^2\right)\mathcal{U}_{21}^2\left(\lambda_o^2\right)\right]. \tag{4.32}$$

Note that strictly speaking, the integrals in (2.26)-(2.31) are not convergent because of the polynomial order of the integrands. This difficulty is common in analytical GIBC solutions and may be remedied by working with integrated field quantities as discussed in [39] and [44]. It has been shown, though, that the final solution is the same regardless of this remedy and for the sake of simplicity we will proceed with the solution of the dual integral equations as if all Fourier inverse and forward transforms existed in the classical sense.

Equations (4.23) with (4.25) and (4.24) with (4.26) form two uncoupled sets of integral equations which are sufficient to yield a solution for the unknown spectra

$P_{odd}(\lambda)$ and $P_{even}(\lambda)$. Clearly, because of the similarity between the two sets of equations, once a solution for $P_{odd}(\lambda)$ is found, the corresponding one for $P_{even}(\lambda)$ follows by inspection.

4.2 Solution of the Dual Integral Equations

In proceeding with the solution of $P_{odd}(\lambda)$ we first rewrite (4.25) in a more suitable manner, viz.

$$\int_{-\infty}^{\infty} \left\{ \frac{\mathcal{G}_2^{odd}(\lambda^2)\, P_{odd}(\lambda)}{\sqrt{1-\lambda^2}} + \frac{\sin\phi_o e^{jk\tau/2\sin\phi_o} Z_{odd}(\lambda_o^2)}{2\pi j \mathcal{G}_1^{odd}(\lambda_o)(\lambda+\lambda_o)} \right\} e^{-jkx\lambda} d\lambda = 0 \qquad (4.33)$$

for $x > 0$. Closing now the integration paths in (4.23) and (4.33) by semi-infinite contours in the upper- and lower-half λ planes, respectively, leads to the deduction that

$$\frac{\mathcal{G}_1^{odd}(\lambda^2)\, P_{odd}(\lambda)}{\sqrt{1-\lambda^2}} = U_o(\lambda) \qquad (4.34)$$

$$\frac{\mathcal{G}_2^{odd}(\lambda^2)\, P_{odd}(\lambda)}{\sqrt{1-\lambda^2}} + \frac{\sin\phi_o e^{jk\tau/2\sin\phi_o} Z_{odd}(\lambda_o^2)}{2\pi j \mathcal{G}_1^{odd}(\lambda_o^2)(\lambda+\lambda_o)} \frac{E_{odd}(\lambda)}{E_{odd}(-\lambda_o)} = L_o(\lambda) \qquad (4.35)$$

where $U_o(\lambda)$ and $L_o(\lambda)$ are unknown functions regular in the upper- or lower-half of the λ plane. Also, $E_{odd}(\lambda)$ is an unknown entire function to be determined along with $P_{odd}(\lambda)$, $U_o(\lambda)$ and $L_o(\lambda)$. To solve for these, it is necessary to exploit the analyticity properties of (4.34) and (4.35) in the different regions of the complex λ plane. An important part of this process is the factorization of the $\mathcal{G}$ functions in (4.34) and (4.35) into a product of upper and lower functions (that is, functions free of poles, zeros, and branch cuts in the upper- or lower-half λ plane, respectively). This task is described in the appendix. We have

$$\mathcal{G}_1^{odd}\left(\lambda^2\right) = \mathcal{G}_{1+}^{odd}(\lambda)\,\mathcal{G}_{1-}^{odd}(\lambda)$$

$$\mathcal{G}_1^{even}\left(\lambda^2\right) = \mathcal{G}_{1+}^{even}(\lambda)\,\mathcal{G}_{1-}^{even}(\lambda)$$

$$\begin{aligned} \mathcal{G}_2^{odd}\left(\lambda^2\right) &= \mathcal{G}_{2+}^{odd}(\lambda)\,\mathcal{G}_{2-}^{odd}(\lambda) \\ \mathcal{G}_2^{even}\left(\lambda^2\right) &= \mathcal{G}_{2+}^{even}(\lambda)\,\mathcal{G}_{2-}^{even}(\lambda) \end{aligned} \tag{4.36}$$

where the superscipts $\pm$ denote upper or lower functions, respectively. Combining (4.34) with (4.35) in conjunction with (4.36) and rearranging terms we obtain

$$\frac{\mathcal{G}_{2-}^{odd}(\lambda)\,U_o(\lambda)}{\mathcal{G}_{1+}^{odd}(\lambda)} + \frac{S(\lambda)\,\mathcal{G}_{1-}^{odd}(\lambda)}{(\lambda+\lambda_o)\,\mathcal{G}_{2-}^{odd}(\lambda)} = \frac{L_o(\lambda)\,\mathcal{G}_{1-}^{odd}(\lambda)}{\mathcal{G}_{2-}^{odd}(\lambda)} \tag{4.37}$$

where

$$S(\lambda) = \frac{\sin\phi_o e^{jk\tau/2\sin\phi_o}\,Z_{odd}(\lambda_o^2)}{2\pi j\mathcal{G}_1^{odd}(\lambda_o^2)}\,\frac{E_{odd}(\lambda)}{E_{odd}(-\lambda_o)}. \tag{4.38}$$

The second term of (4.37) may be easily split into a sum of upper and lower functions, and when this is done, (4.37) can be rewritten as

$$\begin{aligned} \frac{\mathcal{G}_{2-}^{odd}(\lambda)\,U_o(\lambda)}{\mathcal{G}_{1+}^{odd}(\lambda)} + \frac{S(\lambda)\,\mathcal{G}_{1+}^{odd}(\lambda_o)}{(\lambda+\lambda_o)\,\mathcal{G}_{2+}^{odd}(\lambda_o)} &= \frac{L_o(\lambda)\,\mathcal{G}_{1-}^{odd}(\lambda)}{\mathcal{G}_{2-}^{odd}(\lambda)} \\ &\quad - \frac{S(\lambda)}{(\lambda+\lambda_o)}\left[\frac{\mathcal{G}_{1-}^{odd}(\lambda)}{\mathcal{G}_{2-}^{odd}(\lambda)} - \frac{\mathcal{G}_{1+}^{odd}(\lambda_o)}{\mathcal{G}_{2+}^{odd}(\lambda_o)}\right] \end{aligned} \tag{4.39}$$

The left hand side of (4.39) is now regular in the upper half of the λ plane while its right hand side is regular in the lower half of the λ plane. By Liouville's theorem, both sides must then be equal to a polynomial, and to determine the order of this polynomial it is necessary to examine the asymptotic behavior of the individual terms in (4.39). From (4.4) and (4.13) $\mathcal{G}_{2\pm}^{odd}(\lambda) \sim \lambda^{N_2^{odd}/2}$, $\mathcal{G}_{1\pm}^{odd}(\lambda) \sim \lambda^{N_1^{odd}/2}$, implying that the left hand side of (4.39) behaves as $|\lambda|^{(N_1^{odd}+N_2^{odd})/2-1-s_{odd}}$ when $|\lambda| \to \infty$, provided that $E_{odd}(\lambda)$ behaves no worse than $|\lambda|^{(N_{odd}^1+N_{odd}^2)/2-s_{odd}}$ as $|\lambda| \to \infty$. The right hand side of (4.39) will then behave as the greater of $|\lambda|^{N_1^{odd}-1-s_{odd}}$ and $|\lambda|^{(N_1^{odd}+N_2^{odd})/2-1-s_{odd}}$ when $|\lambda| \to \infty$. In accordance with Liouville's theorem, both sides of (4.39) will then be equal to a polynomial of order $int\left\{\frac{N_1^{odd}+N_2^{odd}}{2} - 1 - s_{odd}\right\}$. In terms of this unknown polynomial, we may solve first for $U_o(\lambda)$ and subsequently for $P_{odd}(\lambda)$ to

find that

$$P_{odd}(\lambda) = \frac{j}{2\pi}\frac{\sin\phi_o\sqrt{1-\lambda^2}}{\lambda+\lambda_o}\frac{e^{jk\tau/2\sin\phi_o}}{\mathcal{G}_{1-}^{odd}(\lambda)\,\mathcal{G}_{1-}^{odd}(\lambda_o)\,\mathcal{G}_{2+}^{odd}(\lambda)\,\mathcal{G}_{2+}^{odd}(\lambda_o)} \cdot\left[Z_{odd}\left(\lambda_o^2\right)\frac{E_{odd}(\lambda)}{E_{odd}(-\lambda_o)}+\sum_{m=1}^{\widetilde{N}_{odd}-1}\sum_{n=0}^{\widetilde{N}_{odd}-1-m}a_{mn}(\lambda+\lambda_o)^m(\lambda\lambda_o)^n\right] \tag{4.40}$$

In this, $\widetilde{N}_{odd} = int\{1/2(N_{odd}^1 + N_{odd}^2 + 1)\}$, and a_{mn} are arbitrary constants as yet undetermined, and correspond to the coefficients of the polynomial resulting from the application of Liouville's theorem. The chosen symmetric form of this polynomial is not unique but will be found most useful later in constructing a reciprocal form for $P_{odd}(\lambda)$.

Following a similar procedure we also obtain $P_{even}(\lambda)$ as

$$P_{even}(\lambda) = \frac{j}{2\pi}\frac{\sin\phi_o\sqrt{1-\lambda^2}}{\lambda+\lambda_o}\frac{e^{jk\tau/2\sin\phi_o}}{\mathcal{G}_{1-}^{even}(\lambda)\,\mathcal{G}_{1-}^{even}(\lambda_o)\,\mathcal{G}_{2+}^{even}(\lambda)\,\mathcal{G}_{2+}^{even}(\lambda_o)} \cdot\left[Z_{even}\left(\lambda_o^2\right)\frac{E_{even}(\lambda)}{E_{even}(-\lambda_o)}+\sum_{m=1}^{\widetilde{N}_{even}-1}\sum_{n=0}^{\widetilde{N}_{even}-1-m}b_{mn}(\lambda+\lambda_o)^m(\lambda\lambda_o)^n\right] \tag{4.41}$$

with $E_{even}(\lambda)$, $\widetilde{N}_{even}$ and b_{mn} being the counterparts of $E_{odd}(\lambda)$, $\widetilde{N}_{odd}$ and a_{mn}, respectively. We note that (4.40) and (4.41) imply that the powers s_{odd} and s_{even} governing the behavior of the equivalent currents $J_{odd}(x)$ and $J_{even}(x)$, respectively, are given as

$$s_{odd} = \begin{cases} 1 & N_{odd}^1 + N_{odd}^2 \text{ is even} \\ 1/2 & N_{odd}^1 + N_{odd}^2 \text{ is odd} \end{cases} \tag{4.42}$$

$$s_{even} = \begin{cases} 1 & N_{even}^1 + N_{even}^2 \text{ is even} \\ 1/2 & N_{even}^1 + N_{even}^2 \text{ is odd} \end{cases} \tag{4.43}$$

To determine the unknown entire functions $E_{odd}(\lambda)$ and $E_{even}(\lambda)$, we observe that the spectra $P_{odd}(\lambda)$ and $P_{even}(\lambda)$ must exhibit a reciprocal form, which may be

achieved by setting $E_{odd}(\lambda)$ and $E_{even}(\lambda)$ equal to any of the following functions:

$$E_{odd}(\lambda) = \begin{cases} Z_{odd}(-\lambda\lambda_o) & \text{or} \\ Z^{-}_{odd}(\lambda) & \text{or} \\ Z^{+}_{odd}(\lambda) \end{cases} \tag{4.44}$$

$$E_{even}(\lambda) = \begin{cases} Z_{even}(-\lambda\lambda_o) & \text{or} \\ Z^{-}_{even}(\lambda) & \text{or} \\ Z^{+}_{even}(\lambda) \end{cases} \tag{4.45}$$

where $Z^{+}_{odd,even}(\lambda)$ and $Z^{-}_{odd,even}(\lambda)$ are upper and lower functions satisfying the relation

$$Z_{odd,even}\left(\lambda^2\right) = Z^{+}_{odd,even}(\lambda)\, Z^{-}_{odd,even}(\lambda) \tag{4.46}$$

Taking into account the choices (4.44) and (4.45), we may substitute (4.40) and (4.41) into (4.15) and subsequently perform a steepest descent path evaluation to obtain for $\rho \to \infty$ (all surface wave contributions are neglected in this evaluation)

$$F(\rho,\phi) \sim [D_{odd}(\phi,\phi_o) + D_{even}(\phi,\phi_o)] \frac{e^{-jk\rho}}{\sqrt{k\rho/2\pi}} \tag{4.47}$$

where (ρ,ϕ) are the usual cylindrical coordinates and $D_{odd}(\phi,\phi_o) + D_{even}(\phi,\phi_o)$ is the far zone diffraction coefficient symmetric with respect to ϕ and ϕ_o. We have

$$D_{odd}(\phi,\phi_o) = -\frac{e^{-j\pi/4}}{2\pi}\frac{\sin\phi_o \sin\phi}{\cos\phi + \cos\phi_o} \cdot \frac{e^{jk\tau/2(\sin\phi_o + |\sin\phi|)}}{\mathcal{G}^{odd}_{1-}(\cos\phi)\,\mathcal{G}^{odd}_{1-}(\cos\phi_o)\,\mathcal{G}^{odd}_{2+}(\cos\phi)\,\mathcal{G}^{odd}_{2+}(\cos\phi_o)} \left[\tilde{Z}_{odd}(\cos\phi,\cos\phi_o) + \sum_{m=1}^{\tilde{N}_{odd}-1}\sum_{n=0}^{\tilde{N}_{odd}-1-m} a_{mn}(\cos\phi+\cos\phi_o)^m(\cos\phi\cos\phi_o)^n\right] \tag{4.48}$$

$$D_{even}(\phi,\phi_o) = -\frac{e^{-j\pi/4}}{2\pi}\frac{\sin\phi_o|\sin\phi|}{\cos\phi + \cos\phi_o} \cdot \frac{e^{jk\tau/2(\sin\phi_o + |\sin\phi|)}}{\mathcal{G}^{even}_{1-}(\cos\phi)\,\mathcal{G}^{even}_{1-}(\cos\phi_o)\,\mathcal{G}^{even}_{2+}(\cos\phi)\,\mathcal{G}^{even}_{2+}(\cos\phi_o)} \left[\tilde{Z}_{even}(\cos\phi,\cos\phi_o) + \sum_{m=1}^{\tilde{N}_{even}-1}\sum_{n=0}^{\tilde{N}_{even}-1-m} b_{mn}(\cos\phi+\cos\phi_o)^m(\cos\phi\cos\phi_o)^n\right] \tag{4.49}$$

in which the functions $\tilde{Z}_{odd,even}(\cos\phi, \cos\phi_o)$ are given by (see (4.44) and (4.45))

$$\tilde{Z}_{odd}(\cos\phi, \cos\phi_o) = \begin{cases} Z_{odd}(-\cos\phi\cos\phi_o) & \text{or} \\ Z^{-}_{odd}(\cos\phi)\, Z^{-}_{odd}(\cos\phi_o) & \text{or} \\ Z^{+}_{odd}(\cos\phi)\, Z^{+}_{odd}(\cos\phi_o) & \end{cases} \tag{4.50}$$

$$\tilde{Z}_{even}(\cos\phi, \cos\phi_o) = \begin{cases} Z_{even}(-\cos\phi\cos\phi_o) & \text{or} \\ Z^{-}_{even}(\cos\phi)\, Z^{-}_{even}(\cos\phi_o) & \text{or} \\ Z^{+}_{even}(\cos\phi)\, Z^{+}_{even}(\cos\phi_o) & \end{cases} \tag{4.51}$$

Because the above three choices for $\tilde{Z}_{odd}$ and $\tilde{Z}_{even}$ differ only by terms of the form $(\cos\phi + \cos\phi_o)^m (\cos\phi\cos\phi_o)^n$, it is immaterial which of them we choose, although one of the choices may likely lead to a more compact representation. Nevertheless, regardless of the choice of $\tilde{Z}_{odd}$ and $\tilde{Z}_{even}$, one is still faced with the determination of the unknown constants a_{mn} and b_{mn} in (4.48) and (4.49), respectively. These are a manifestation of the non-uniqueness of the finite-order GSTC sheet model employed herein, and their explicit determination requires the introduction of additional constraints pertaining to the physics of the problem as discussed in chapter five. In some cases, however, these constants can be determined by comparison with alternative diffraction solutions, and this is considered next.

4.3 Discussion of the Solution and Some Applications

4.3.1 Diffraction by thin single layer discontinuous slabs

The diffraction coefficient given by (4.48) and (4.49) is very general and can model a wide variety of geometries. To check its validity, display its versatility, and assess the relative importance of the unknown constants, we consider several simple configurations which can be modelled with the proposed GSTCs. Their geometries are shown in Figures 4.4(a)-4.4(c) and include the single layer join, the material-metal join, and the material half plane, all of thickness $2w$. Herewith, these are modeled

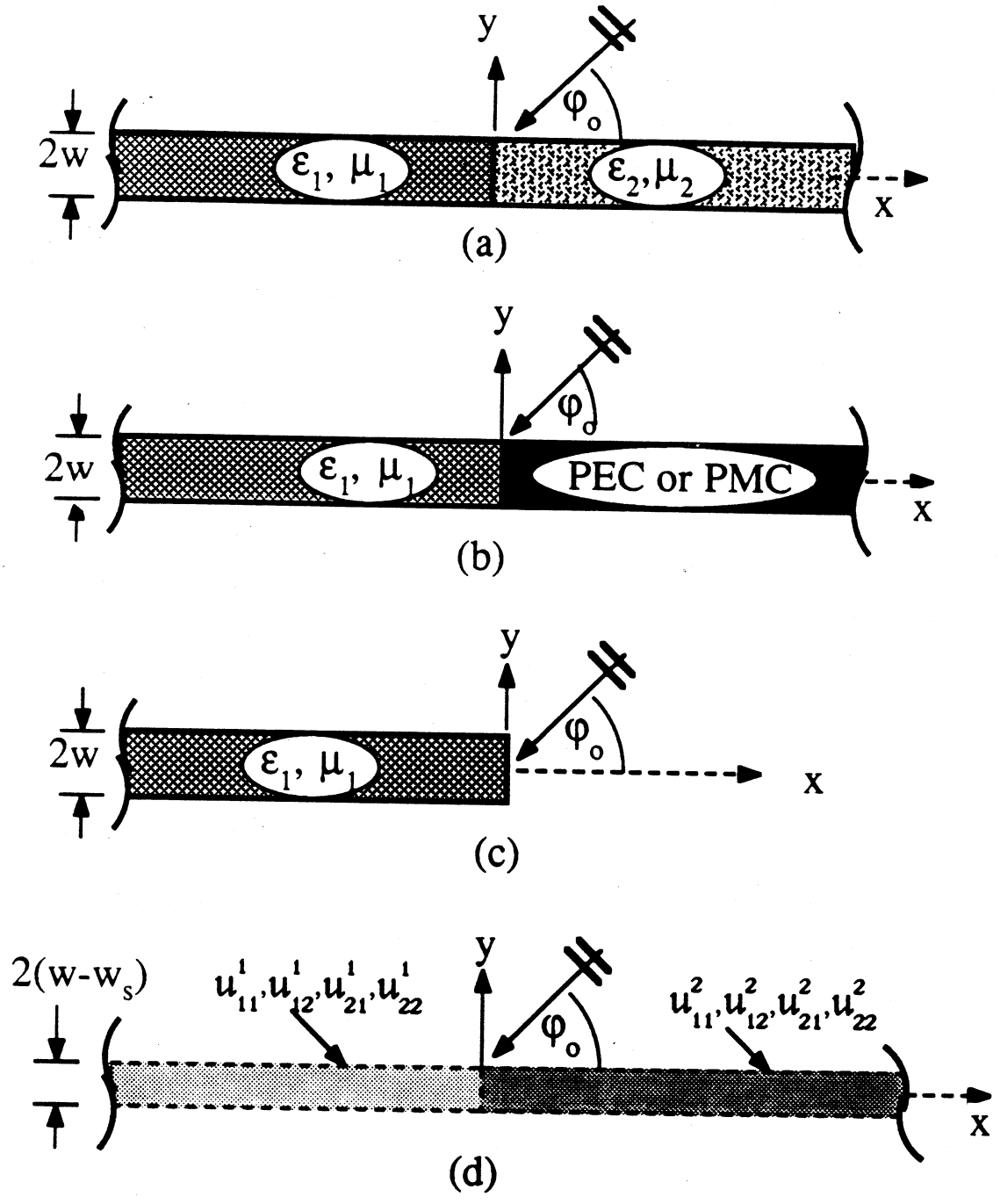

Figure 4.4: Thin slab structures and their distributed sheet representation (a) Material-material junction. (b) Material-metallic join. (c) Material half-plane. (d) Equivalent distributed sheet.

by a distributed sheet discontinuity of thickness $2(w - w_s)$ (see Figure 4.4(d)) and although, in general, it is not necessary to employ a sheet thickness different from that of the slab, this is useful here for comparison with previous results.

If the left hand side of the slab is assumed to be thin and having a low index of refraction, it may be modeled by a low contrast GSTC sheet. Thus, an $O(w^1, w_s^1)$ approximation with terms of $O(w_s w)$ neglected is sufficient for the representation of the operators or polynomials $\mathcal{U}_{ij}^1$. In particular, we have

$$\begin{aligned}
\mathcal{U}_{11}^1\left(-\partial x^2/k^2\right) &= 1 \\
\mathcal{U}_{12}^1\left(-\partial x^2/k^2\right) &= jk\left(u_1 w - w_s\right) \\
\mathcal{U}_{21}^1\left(-\partial x^2/k^2\right) &= jk\left(\frac{w\epsilon_1\mu_1}{u_1} - w_s\right) + \frac{j}{k}\left(\frac{w}{u_1} - w_s\right)\partial x^2 \\
\mathcal{U}_{22}^1\left(-\partial x^2/k^2\right) &= 1
\end{aligned} \tag{4.52}$$

where ϵ_1 and μ_1 are the relative permittivity and permeability of the left hand slab, respectively, and

$$u_1 = \begin{cases} \mu_1, & E_z \text{ polarization} \\ \epsilon_1 & H_z \text{ polarization} \end{cases} \tag{4.53}$$

Also, when $w_s = w$, these are simply the transition conditions derived first by Weinstein [59] and later by Senior and Volakis [39]. The corresponding polynomials to be employed in (4.27) - (4.32) are given by

$$\begin{aligned}
\mathcal{U}_{11}^1\left(-\cos\phi\cos\phi_o\right) &= 1 \\
\mathcal{U}_{12}^1\left(-\cos\phi\cos\phi_o\right) &= jk\left(u_1 w - w_s\right) \\
\mathcal{U}_{21}^1\left(-\cos\phi\cos\phi_o\right) &= jk\left(\frac{w\epsilon_1\mu_1}{u_1} - w_s\right) + jk\left(\frac{w}{u_1} - w_s\right)\cos\phi\cos\phi_o \\
\mathcal{U}_{22}^1\left(-\cos\phi\cos\phi_o\right) &= 1
\end{aligned} \tag{4.54}$$

Incorporating these into (4.48) and (4.49) and setting

$$\tilde{Z}_{odd}\left(\cos\phi, \cos\phi_o\right) = Z_{odd}\left(-\cos\phi\cos\phi_o\right) \tag{4.55}$$

$$\tilde{Z}_{even}(\cos\phi,\cos\phi_o) = Z_{even}(-\cos\phi\cos\phi_o) \tag{4.56}$$

yields

$$D_{odd}(\phi,\phi_o) = -\frac{e^{-j\pi/4}}{2\pi}\frac{\sin\phi_o\sin\phi}{\cos\phi+\cos\phi_o}e^{jk\tau/2(\sin\phi_o+|\sin\phi|)} \cdot\frac{\mathcal{U}_{12}^2(-\cos\phi\cos\phi_o)-jk(u_1w-w_s)\mathcal{U}_{11}^2(-\cos\phi\cos\phi_o)}{M_-(\cos\phi;\gamma^{odd,1})M_-(\cos\phi_o;\gamma^{odd,1})\mathcal{G}_{2+}^{odd}(\cos\phi)\mathcal{G}_{2+}^{odd}(\cos\phi_o)} \tag{4.57}$$

$$D_{even}(\phi,\phi_o) = -\frac{e^{-j\pi/4}}{2\pi}\frac{\sin\phi_o|\sin\phi|}{\cos\phi+\cos\phi_o}e^{jk\tau/2(\sin\phi_o+|\sin\phi|)} \cdot\left\{\frac{[\alpha_1+\alpha_2\cos\phi\cos\phi_o]\mathcal{U}_{22}^2(-\cos\phi\cos\phi_o)-\mathcal{U}_{21}^2(-\cos\phi\cos\phi_o)}{\alpha_3\left[\prod_{m=1}^{2}M_-\left(\cos\phi;\gamma_m^{even,1}\right)M_-\left(\cos\phi_o;\gamma_m^{even,1}\right)\right]\mathcal{G}_{2+}^{even}(\cos\phi)\mathcal{G}_{2+}^{even}(\cos\phi_o)}\right. + \left.\frac{b_{10}(\cos\phi+\cos\phi_o)}{\alpha_3\left[\prod_{m=1}^{2}M_-\left(\cos\phi;\gamma_m^{even,1}\right)M_-\left(\cos\phi_o;\gamma_m^{even,1}\right)\right]\mathcal{G}_{2+}^{even}(\cos\phi)\mathcal{G}_{2+}^{even}(\cos\phi_o)}\right\} \tag{4.58}$$

where the split function $M_-(\cos\phi;\gamma)$ is given in the appendix.

$$\begin{aligned}\alpha_1 &= jk\left(\frac{w\epsilon_1\mu_1}{u_1}-w_s\right)\\ \alpha_2 &= jk\left(\frac{w}{u_1}-w_s\right)\\ \alpha_3 &= \frac{jkw}{u_1}(\epsilon_1\mu_1-1)\end{aligned} \tag{4.59}$$

and

$$\begin{aligned}\gamma^{odd,1} &= \frac{-j}{k(u_1w-w_s)}\\ \gamma_{1,2}^{even,1} &= \frac{u_1\pm\sqrt{u_1^2+4k^2w(\epsilon_1\mu_1-1)(w-u_1w_s)}}{2jk(w-w_su_1)}\end{aligned} \tag{4.60}$$

with $\gamma^{odd\ or\ even}$ representing possible surface wave poles. To complete the definition of (4.57) and (4.58), the functions associated with the right hand side properties of the slab (i.e. those functions with the superscript 2) must be specified. Referring to the configurations in Figure 4.4(a)-4.4(c), Table 4.1 and Table 4.2 provide explicit expressions for the functions $\mathcal{U}_{ij}^2(-\cos\phi\cos\phi_o)$, $\mathcal{G}_{2+}^{odd}(\cos\phi)\mathcal{G}_{2+}^{odd}(\cos\phi_o)$ and

Geometry, $x > 0$	$\mathcal{U}_{11}^2(-\cos\phi\cos\phi_o)$	$\mathcal{U}_{12}^2(-\cos\phi\cos\phi_o)$	$\mathcal{G}_{2+}^{odd}(\cos\phi)\,\mathcal{G}_{2+}^{odd}(\cos\phi_o)$	$\gamma^{odd,2}$
Low Contrast O(w, w_s)	1	$jk(u_2 w - w_s)$	$M_+\left(\cos\phi;\gamma_1^{odd,2}\right) M_+\left(\cos\phi_o;\gamma_1^{odd,2}\right)$	$\frac{-j}{k(u_2 w - w_s)}$
Free Space Limit	1	$jk(w - w_s)$	$M_+\left(\cos\phi;\gamma_1^{odd,2}\right) M_+\left(\cos\phi_o;\gamma_1^{odd,2}\right)$	$\frac{-j}{k(w - w_s)}$
PEC(Ez-pol) or PMC(Hz-pol)	1	0	1	———
PMC(Ez-pol) or PEC(Hz-pol)	0	1	$\sqrt{1-\cos\phi}\sqrt{1-\cos\phi_o}$	———

Table 4.1: Odd symmetry parameters for distributed sheet similation of right hand side material $x > 0$. See Appendix 1 for definition of M_+ split functions.

Geometry, $x > 0$	$\mathcal{U}_{21}^2(-\cos\phi\cos\phi_o)$, $\mathcal{U}_{22}^2(-\cos\phi\cos\phi_o)$	$\mathcal{G}_{2+}^{even}(\cos\phi)\,\mathcal{G}_{2+}^{even}(\cos\phi_o)$
Low Contrast, $O(w, w_s)$	$\mathcal{U}_{21}^2 = jk\left(\frac{w\epsilon_2\mu_2}{u_2} - w_s\right) + jk\cos\phi\cos\phi_o\left(\frac{w}{u_2} - w_s\right)$ $\mathcal{U}_{22}^2 = 1$	$\frac{jkw}{u_2}(\epsilon_2\mu_2 - 1)\prod_{m=1}^{2} M_+(\cos\phi;\gamma_m^{even,2})\,M_+(\cos\phi_o;\gamma_m^{even,2})$ with $\gamma_{1,2}^{even,2} = \frac{u_2 \pm \sqrt{u_2^2 + 4k^2\omega(\epsilon_2\mu_2-1)(w-u_2w_s)}}{2jk(w-w_su_2)}$
Free Space Limit	$\mathcal{U}_{21}^2 = jk(w - w_s)(1 + \cos\phi\cos\phi_o)$ $\mathcal{U}_{22}^2 = 1$	$\sqrt{1-\cos\phi}\sqrt{1-\cos\phi_o}M_+\left(\cos\phi;\gamma_1^{even,2}\right)M_+\left(\cos\phi_o;\gamma_1^{even,2}\right)$ with $\gamma_1^{even,2} = \frac{-1}{k(w-w_s)}$
PEC(Ez-pol) ($b_{10} = 0$) or PMC(Hz-pol) ($b_{10} = 0$)	$\mathcal{U}_{21}^2 = 1$ $\mathcal{U}_{22}^2 = 0$	1
PMC(Ez-pol) or PEC(Hz-pol)	$\mathcal{U}_{21}^2 = 0$ $\mathcal{U}_{22}^2 = 1$	$\sqrt{1-\cos\phi}\sqrt{1-\cos\phi_o}$

Table 4.2: Even symmetry parameters for distributed sheet similation of right hand side material $x > 0$. See Appendix 1 for definition of M_+ split functions.

$\mathcal{G}_{2+}^{even}(\cos\phi)\,\mathcal{G}_{2+}^{even}(\cos\phi_o)$ terms. By edge condition considerations, all of the constants a_{mn} and b_{mn} have been set to zero except b_{10} appearing in the definition of D_{even}, which is non-zero unless the right hand side slab is a PEC/PMC under an E_z/H_z excitation (see Table 4.2).

4.3.2 Diffraction by a resistive-resistive junction

When $w = w_s$, and the material parameters of the slab geometries in Figures 4.4(a) and 4.4(c) take the limits

$$\begin{aligned} \epsilon_{1,2} &\rightarrow \infty \\ \mu_{1,2} &\rightarrow \infty \\ \tau &\rightarrow 0 \\ jkw(\epsilon_{1,2}-1) &\rightarrow \frac{1}{\eta^e_{1,2}} \\ jkw(\mu_{1,2}-1) &\rightarrow \frac{1}{\eta^m_{1,2}} \end{aligned} \tag{4.61}$$

the resulting configuration corresponds to coincident resistive and conductive sheet junctions [37], where $\eta^e_{1,2}$ and $\eta^m_{1,2}$ denote the resistivities and conductivities of the respective sheets. In this case, the constant b_{10} is forced to zero by the edge condition, and (4.57) and (4.58) simplify to

$$D_{odd}(\cos\phi,\cos\phi_o) = \frac{\sin\phi\; d(\cos\phi,\cos\phi_o)\,(1/\eta^m_2 - 1/\eta^m_1)}{M_-(\cos\phi;1/\eta^m_1)\,M_-(\cos\phi_o;1/\eta^m_1)\,M_+(\cos\phi;1/\eta^m_2)\,M_+(\cos\phi_o;1/\eta^m_2)} \tag{4.62}$$

$$D_{even}(\cos\phi,\cos\phi_o) = \frac{|\sin\phi|\; d(\cos\phi,\cos\phi_o)\,(\eta^e_2 - \eta^e_1)}{M_-(\cos\phi;1/\eta^e_1)\,M_-(\cos\phi_o;1/\eta^e_1)\,M_+(\cos\phi;1/\eta^e_2)\,M_+(\cos\phi_o;1/\eta^e_2)} \tag{4.63}$$

for E_z polarization and

$$D_{odd}(\cos\phi,\cos\phi_o) =$$

$$\frac{\sin\phi\, d(\cos\phi,\cos\phi_o)\,(1/\eta_2^e - 1/\eta_1^e)}{M_-(\cos\varphi;1/\eta_1^e)\,M_-(\cos\varphi_o;1/\eta_1^e)\,M_+(\cos\varphi;1/\eta_2^e)\,M_+(\cos\varphi_o;1/\eta_2^e)} \tag{4.64}$$

$$D_{even}(\cos\phi,\cos\phi_o) =$$

$$\frac{|\sin\phi|\, d(\cos\phi,\cos\phi_o)\,(\eta_2^m - \eta_1^m)}{M_-(\cos\varphi;1/\eta_1^m)\,M_-(\cos\varphi_o;1/\eta_1^m)\,M_+(\cos\varphi;1/\eta_2^m)\,M_+(\cos\varphi_o;1/\eta_2^m)} \tag{4.65}$$

for H_z polarization, where

$$d(\cos\varphi,\cos\phi_o) = -\frac{e^{-j\pi/4}}{2\pi}\frac{\sin\phi_o}{\cos\phi+\cos\varphi_o} \tag{4.66}$$

Note that if both η_1^e, $\eta_1^e \to \infty$ (i.e., the resistive sheets disappear), then $D_{odd}(\cos\phi,\cos\phi_o)$ and $D_{even}(\cos\phi,\cos\phi_o)$ tend to zero for H_z and E_z polarizations, respectively. On the other hand, if both η_1^m, $\eta_1^m \to \infty$ (i.e., the conductive sheets disappear),then $D_{odd}(\cos\phi,\cos\phi_o)$ and $D_{even}(\cos\phi,\cos\phi_o)$ tend to zero for E_z and H_z polarizations, respectively. This is, of course, because resistive and conductive sheets scatter independently of each other. Consequently, the field diffracted by a resistive to conductive sheet junction is the superposition of the individual sheet contributions [39].

4.3.3 Diffraction by grounded metal-dielectric junctions

Of the geometries shown in Figure 4.4, the diffracted field associated with the metal-dielectric junction (Figure 4.4(b)) is given in chapter three and can therefore be used to partially validate the derived solution. However, in order to study only the effect of the constant b_{10}, we need to exclude the odd-symmetry portion of the metal-dielectric join diffraction coefficient. To this end, we focus on the recessed slab geometry of Figure 4.5(a), whose H_z polarization diffraction coefficient is related (through image theory) to that of the metal-dielectric join by

$$D_{rs}(\cos\phi,\cos\phi_o) = 2D_{even}(\cos\phi,\cos\phi_o) \tag{4.67}$$

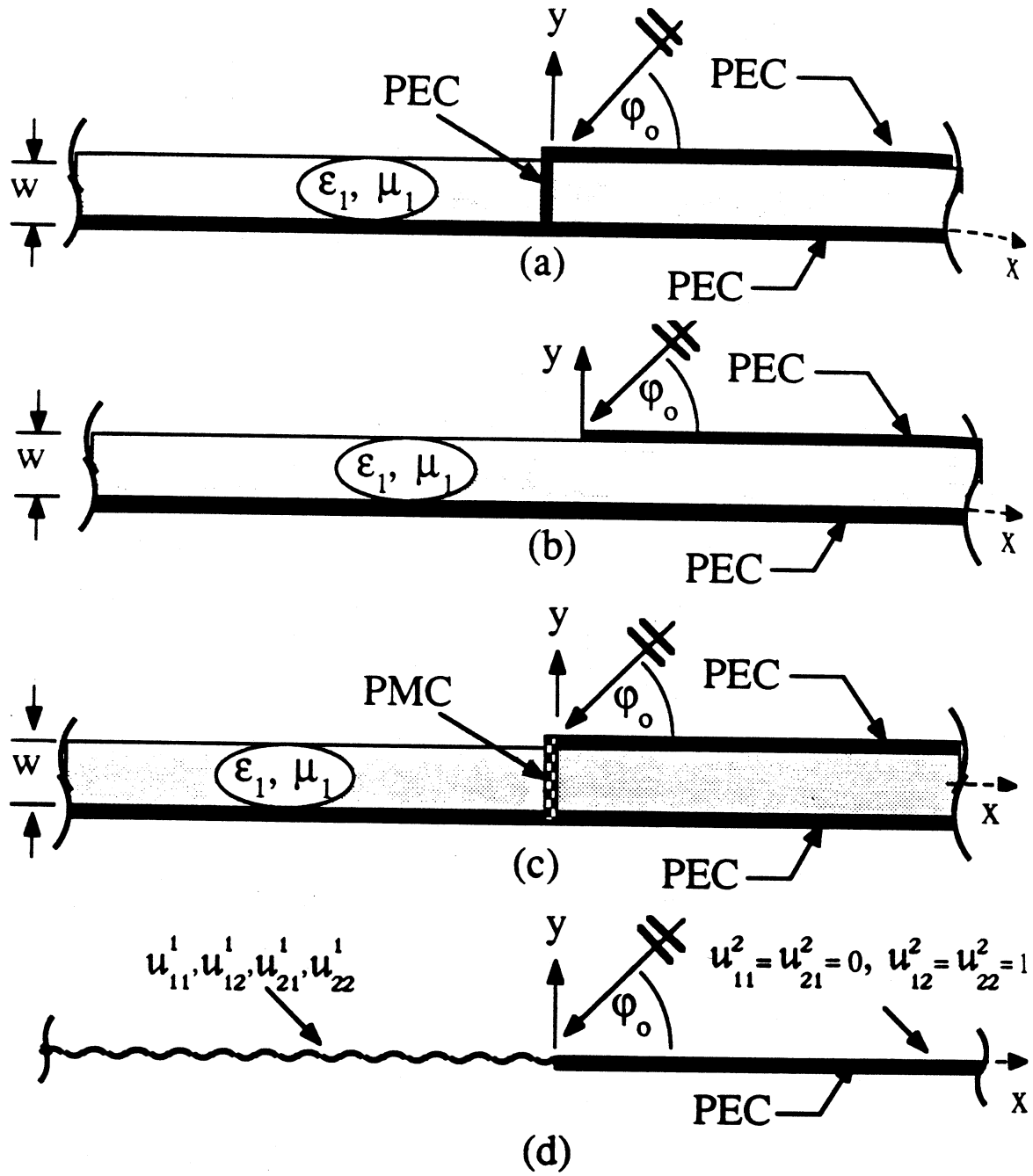

Figure 4.5: (a) Recessed slab (PEC stub) (b) Grounded slab with truncated upper plate (c) Recessed slab (PMC stub) (d) GIBC sheet

with D_{even} given by (4.58) along with the PEC(H_z-pol.) entries of Table 4.2. As noted above, for a right hand side PEC slab with E_z polarization, the edge condition demands $b_{10} = 0$ in this case.

For the recessed slab geometry illuminated with an H_z polarized plane wave, the GSTC (4.11) and (4.12) become the GIBC

$$\mathcal{U}_{21}^{1}\left(-\frac{\partial x^2}{k^2}\right)\left\{F^{+}\right\} + \frac{j}{k}\mathcal{U}_{22}^{1}\left(-\frac{\partial x^2}{k^2}\right)\left\{\partial y F^{+}\right\} = 0, \tag{4.68}$$

for $-\infty < x < 0$ and

$$\mathcal{U}_{21}^{2}\left(-\frac{\partial x^2}{k^2}\right)\left\{F^{+}\right\} + \frac{j}{k}\mathcal{U}_{22}^{2}\left(-\frac{\partial x^2}{k^2}\right)\left\{\partial y F^{+}\right\} = 0 \tag{4.69}$$

for $0 < x < \infty$, with the $\mathcal{U}_{ij}^{1}$ operators given in (4.52). Clearly, these GIBC can represent any of the configurations displayed in Figure 4.5(a)-(c) without regard to whether a stub (PEC or PMC) or not is placed at the junction. This information can only be carried by the constant b_{10} as the term distinguishing the diffraction coefficients among the geometries of Figure 4.5(a)-(c). Thus, the determination of b_{10} must somehow involve the properties of the junction across its thickness and this is discussed in chapter five. However, since the solution of the configuration in Figure 4.5(a)-(c) are already available in chapter three, b_{10} can be identified for each geometry by comparing (4.58) with the appropriate solutions given in chapter three. Upon setting $w_s = 0$, we find

$$\begin{aligned}
b_{10}^{\text{no stub}} &= jkw\sqrt{\frac{\mu_1}{\epsilon_1}} \\
b_{10}^{\text{pec stub}} &= \frac{jkw\sqrt{\frac{\mu_1}{\epsilon_1}}}{\frac{jkw}{4\epsilon_1}\left(\sqrt{\epsilon_1\mu_1}-1\right)\left[M_{-}\left(\sqrt{\epsilon\mu},\gamma_1^{even,1}\right)M_{-}\left(\sqrt{\epsilon_1\mu_1},\gamma_2^{even,1}\right)\right]^2 + 1/2} \\
b_{10}^{\text{pmc stub}} &= \frac{jkw\sqrt{\frac{\mu_1}{\epsilon_1}}}{\frac{jkw}{4\epsilon_1}\left(\sqrt{\epsilon_1\mu_1}-1\right)\left[M_{-}\left(\sqrt{\epsilon_1\mu_1},\gamma_1^{even,1}\right)M_{-}\left(\sqrt{\epsilon_1\mu_1},\gamma_2^{even,1}\right)\right]^2 - 1/2}
\end{aligned} \tag{4.70}$$

corresponding to the constants associated with the diffraction coefficients for the geometries in Figure 4.5(b), Figure 4.5(a), and Figure 4.5(c), respectively. We note that these constants are based on the choice of $\tilde{Z}_{even}(\cos\varphi, \cos\phi_o)$ as given in (4.56). Had this function been chosen as

$$\tilde{Z}_{even}(\cos\phi, \cos\phi_o) = Z^{-}_{even}(\cos\phi)\, Z^{-}_{even}(\cos\phi_o) \tag{4.71}$$

the resulting constants would have been

$$\begin{aligned}
b_{10}^{\text{no stub}} &= 0 \\
b_{10}^{\text{pec stub}} &= -jkw\sqrt{\frac{\mu_1}{\epsilon_1}} \\
&\quad + \frac{jkw\sqrt{\frac{\mu_1}{\epsilon_1}}}{\frac{jkw}{4\epsilon_1}\left(\sqrt{\epsilon_1\mu_1}-1\right)\left(M_-\left(\sqrt{\epsilon_1\mu_1}, \gamma_1^{even,1}\right) M_-\left(\sqrt{\epsilon_1\mu_1}, \gamma_2^{even,1}\right)\right)^2 + 1/2} \\
b_{10}^{\text{pec stub}} &= -jkw\sqrt{\frac{\mu_1}{\epsilon_1}} \\
&\quad + \frac{jkw\sqrt{\frac{\mu_1}{\epsilon_1}}}{\frac{jkw}{4\epsilon_1}\left(\sqrt{\epsilon_1\mu_1}-1\right)\left(M_-\left(\sqrt{\epsilon_1\mu_1}, \gamma_1^{even,1}\right) M_-\left(\sqrt{\epsilon_1\mu_1}, \gamma_2^{even,1}\right)\right)^2 - 1/2}
\end{aligned} \tag{4.72}$$

and the more compact representation of the no-stub diffraction coefficient is at once evident.

To assess the importance of the constant b_{10} with respect to $\tilde{Z}_{even}(\cos\phi, \cos\phi_o)$ as given in (4.56), we plotted in Figure 4.6 the backscatter echo width patterns associated with the three configurations in Figure 4.5(a)-(c) and have compared these patterns with that computed by setting $b_{10} = 0$. The chosen relative constitutive parameters for the left hand side slab are $\epsilon = 2$ and $\mu = 1.2$, and the entire slab is of thickness $w = .04\lambda$ (where here λ denotes the free space wavelength). We observe that the backscatter patterns are, in general, substantially different, underscoring the importance of the constant. Although $b_{10}^{pec\ stub}$ is nearly zero in this case, it will

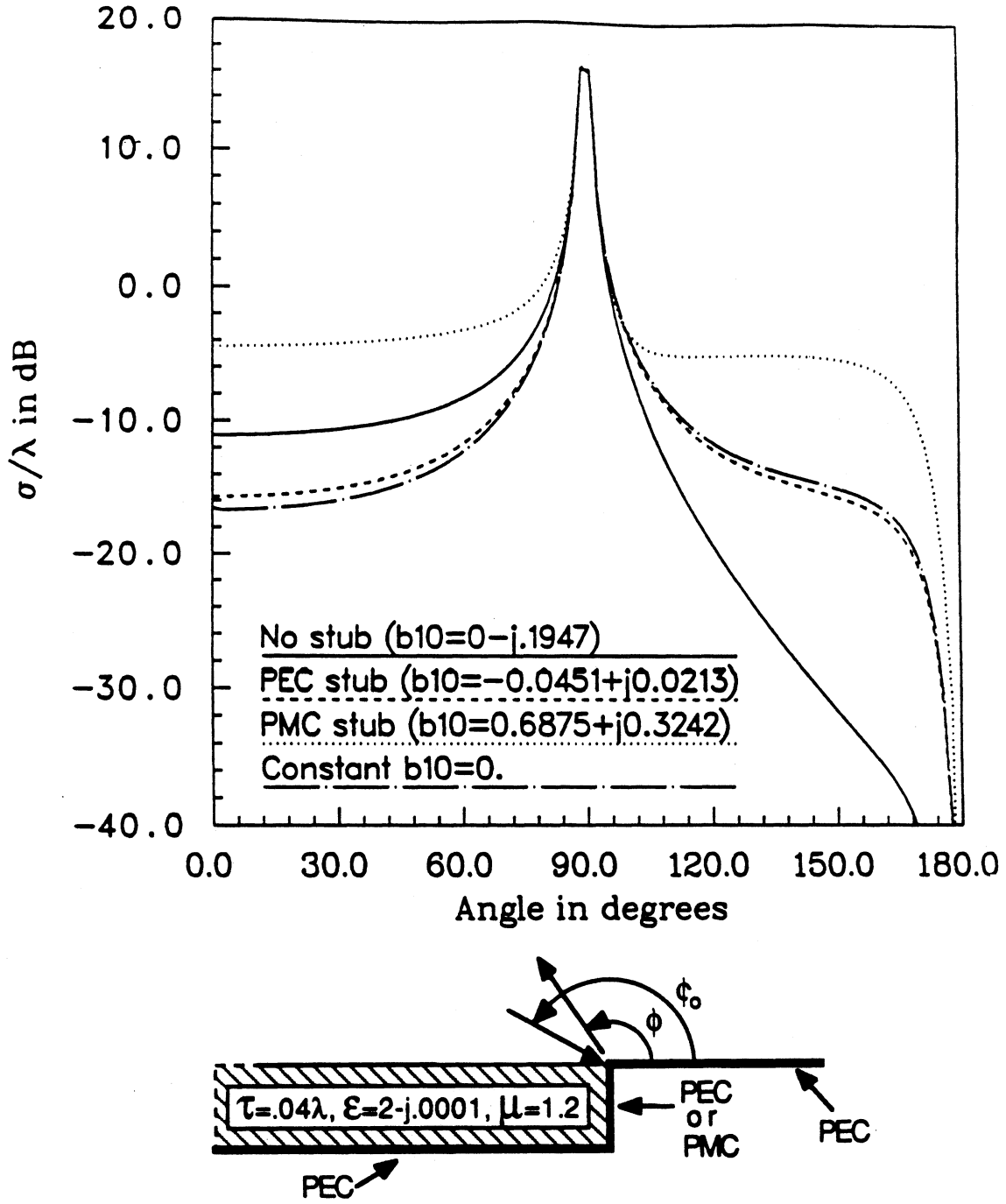

Figure 4.6: H_z polarization backscatter echo width for a material insert having $w = .04\lambda$, $\epsilon = 2 - j.0001$, $\mu = 1.2$ modeled with $O(w)$ low contrast GIBCs

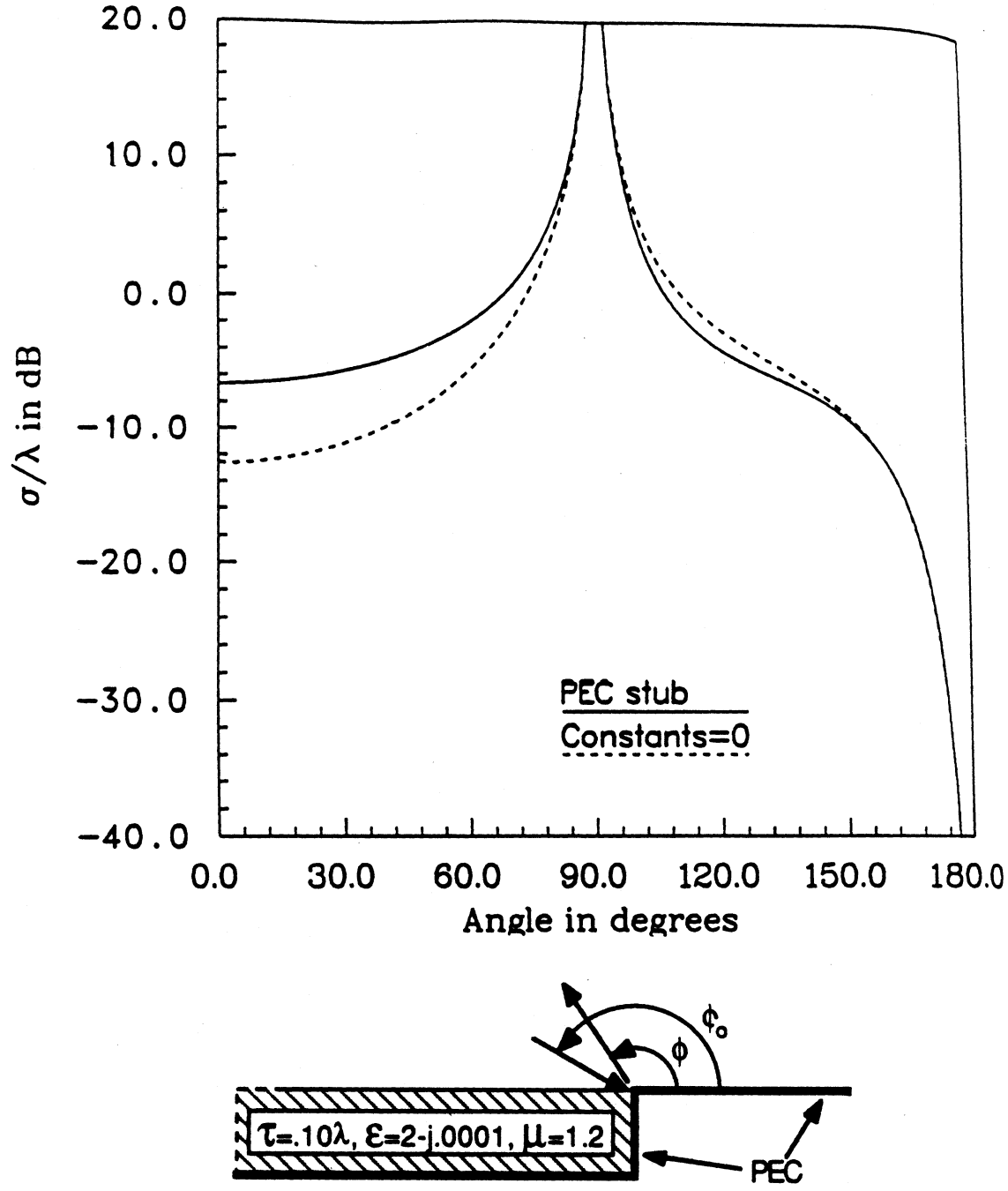

Figure 4.7: H_z polarization backscatter echo width for a material insert having $w = .10\lambda$, $\epsilon = 2 - j.0001$, $\mu = 1.2$ modeled with $O(w^3)$ low contrast GIBCs; $b_{10} = -.4578 + j.2593$, $b_{11} = -.0408 - j.0111$, $b_{20} = -.0401 - j.0388$.

not be so when w becomes larger. For example, if w is increased to 0.1λ, a 3^{rd} order low contrast GIBC with terms up to $O(w^3)$ is required for an accurate simulation of the dielectric. In this case the constants b_{10}, b_{11} and b_{20} are non-zero and as shown in Figure 4.7 they play a major role in providing the correct diffracted field by the recessed slab of Figure 4.5(a).

4.3.4 Diffraction by a thin dielectic/ferrite half plane

Another configuration whose diffraction has been examined in the past is the thin dielectric half plane shown in Figure 4.4(c). If a 2^{nd} order GSTC with terms up to $O(w)$ is employed for the simulation of the layer, the resulting diffracted field is given by (4.57) and (4.58) in conjunction with the "free space limit" entries in Table 4.1 and Table 4.2 for the right hand slab. The constant b_{10} must again be specified for a complete determination of the diffraction coefficient. We remark, however, that if b_{10} is arbitrarily set to zero, then for $w_s = w$ the sum of (4.57) and (4.58) reduces to the diffraction coefficient already derived in [54]. Similar assumptions about the value of the constant have also been made in [32] and although this may be acceptable in some cases (i.e. for extremely thin layers or layers of certain composition), it was already demonstrated above that the constant(s) play an important role and must be accurately determined. This is the subject of chapter five.

4.4 Conclusion

In conclusion, we have derived a general solution for the diffraction by a discontinuous distributed sheet representing a multilayered slab discontinuity. The solution can be specialized to a wide variety of material junctions and discontinuities by an appropriate choice for the polynomial operators $\mathcal{U}_{ij}^1$ and $\mathcal{U}_{ij}^2$. Unfortunately, un-

known constants arise in the final solution due to the non-uniqueness of the finite GSTC/GIBC sheet representations. In comparing the derived diffraction coefficient to a previous result for the material half plane, it was shown that the single unknown constant obtained herein was implicitly assumed zero in [54] and [32]. The importance of the constant was examined for the case of three grounded slab geometries whose GIBC modeling differed only by the value of a single constant b_{10}. This comparison demonstrated that for very thin metal-dielectric junctions, the constant b_{10} was approximately zero, whereas for thicker junctions the constant(s) played a more crucial role.

CHAPTER V

RESOLUTION OF NON-UNIQUENESS ASSOCIATED WITH THE GIBC/GSTC SOLUTION

In chapter four, a dual integral equation solution was presented for the diffraction by a multilayer material-to-material junction using a GSTC simulation of the multilayer slab. As expected, the solution was in terms of unknown constants and it was shown that these are dependent on the physical properties of the junction (see Figure 5.1). Consequently, an approach for determining the solution constants is to enforce tangential field continuity across the junction. This, of course, demands a knowledge of the fields internal to the discontinuous slab, which, however, are not readily available when a GSTC simulation is employed. The Weiner-Hopf solution in conjunction with the GSTC provides only the field external to the slab, and the majority of this chapter deals with the determination of the internal field from the external one given in chapter four.

In the following section, a modal representation of the internal field is proposed comprised of discrete and continuous spectral components. This representation is compatible with that given by Shevchenko [45] whose eigenfunctions are chosen to satisfy the continuity boundary conditions across all layer interfaces including the air-dielectric interface. Consequently the representation is valid inside and outside

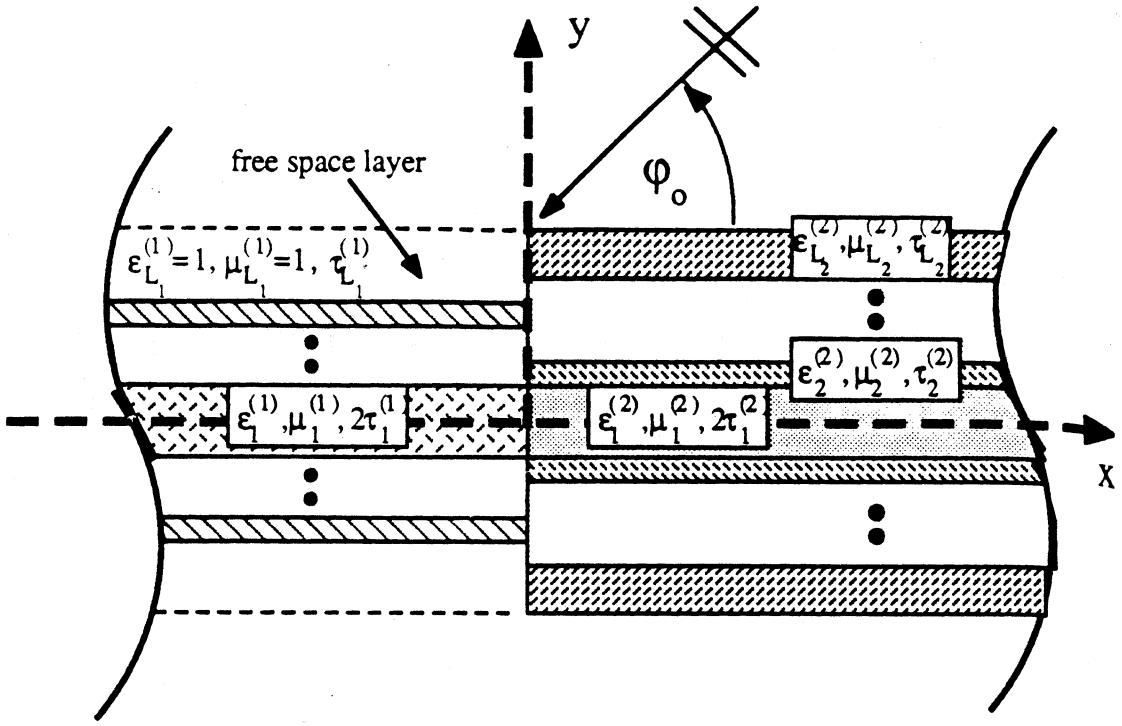

Figure 5.1: Symmetric multilayer slab discontinuity illuminated by a plane wave

the dielectric once the coefficients of the modal representation are determined. This is accomplished by recasting the Weiner-Hopf or dual integral equation solution of the same problem from chapter four in a form compatible with the proposed modal representation, thus permitting the identification of the modal or eigenfunction coefficients. These are, of course, in terms of the unknown constants appearing in the Weiner-Hopf solution and the enforcement of field continuity across the junction leads to a linear system of equations to be solved for the constants. In the final section of the paper, several scattering calculations are presented for a few material-to-material junctions which demonstrate the importance of the constants and the accuracy of the solution.

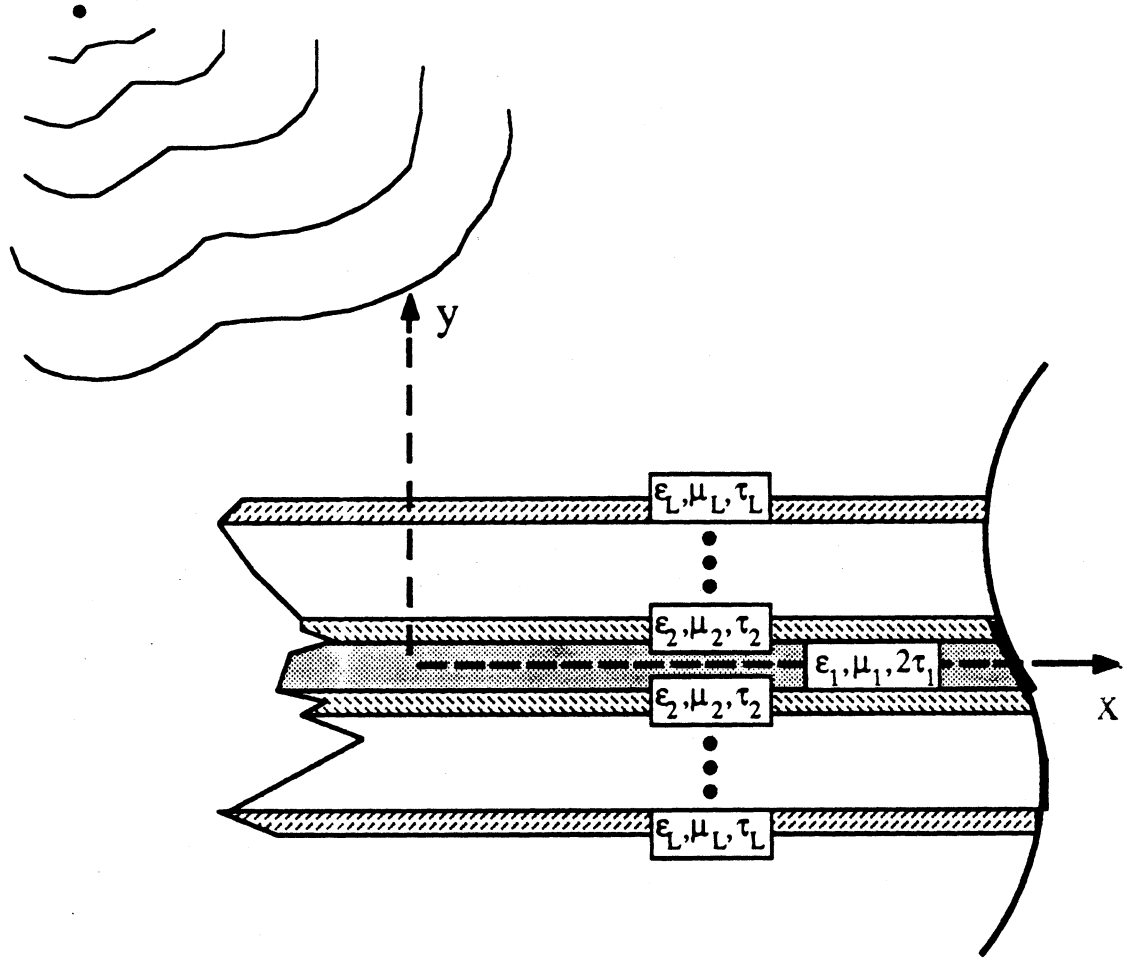

Figure 5.2: Symmetric multilayer slab with irregular termination illuminated by a polarized field excitation

5.1 Modal Decomposition for the Symmetric Slab Problem

Consider a symmetric slab of total thickness τ with an irregular termination to its left, as illustrated in Figure 5.2. The slab is herewith assumed to consist of L homogeneous layers with the m^{th} layer being of thickness τ_m and having relative permittivity and permeability ϵ_m and μ_m, respectively. When this truncated slab is subjected to some polarized field excitation, the field to the right of the junction at

the point x can be written as a sum of odd- and even-symmetry fields. That is

$$F(x,y) = F^{odd}(x,y) + F^{even}(x,y) \tag{5.1}$$

where

$$F = \begin{cases} E_z, & E_z \text{ polarization,} \\ Z_o H_z, & H_z \text{ polarization,} \end{cases} \tag{5.2}$$

$F^{odd}(x,y) = -F^{odd}(x,-y)$ and $F^{even}(x,y) = F^{even}(x,-y)$. Following [45], the odd and even fields everywhere interior and exterior to the slab may be decomposed into discrete and continuous eigenmodes as

$$\begin{aligned} F^{odd}(x,y) &= \sum_{m=1}^{N_{go}} A_m^{odd} \Psi^{odd}\left((\lambda_m^{go})^2, y\right) e^{-jkx\lambda_m^{go}} + \sum_{m=1}^{N_{sw}^{odd}} B_m^{odd} \Phi_m^{odd}(y)\, e^{-jkx\lambda_m^{odd}} \\ &\quad + \int_0^{\infty} C^{odd}(\beta)\, \Psi^{odd}\left(\lambda^2, y\right) e^{-jkx\lambda} d\beta \end{aligned} \tag{5.3}$$

$$\begin{aligned} F^{even}(x,y) &= \sum_{m=1}^{N_{go}} A_m^{even} \Psi^{even}\left((\lambda_m^{go})^2, y\right) e^{-jkx\lambda_m^{go}} + \sum_{m=1}^{N_{sw}^{even}} B_m^{even} \Phi_m^{even}(y)\, e^{-jkx\lambda_m^{even}} \\ &\quad + \int_0^{\infty} C^{even}(\beta)\, \Psi^{even}\left(\lambda^2, y\right) e^{-jkx\lambda} d\beta \end{aligned} \tag{5.4}$$

where $Im\{\lambda_m^{odd,even}\} < 0$ and $\lambda = \sqrt{1-\beta^2}$, with the branch of the square root chosen so that $Im\{\sqrt{1-\beta^2}\} < 0$. In (5.3) and (5.4), $\Psi^{odd,even}$ are referred to as the cross section functions corresponding to the continuous modal fields whereas $\Phi_m^{odd,even}$ are the corresponding cross section functions for the discrete modal fields associated with the surface waves. The cross section function associated with the geometrical optics fields is also $\Psi^{odd,even}$ evaluated at $\lambda = \lambda_m^{go}$, where $\lambda_m^{go}$is a parameter to be determined later. As can be observed from (5.3) and (5.4), the cross section functions specify the field behavior in the plane normal to the slab, and hence all information pertaining to the fields interior to the slab are embedded in these functions. They will be chosen to satisfy the orthogonality relations (where $u(y)$ is $\mu(y)$ or $\epsilon(y)$ for E_z or H_z polarization, respectively)

$$\int_{-\infty}^{\infty} \frac{\Psi(\lambda^2, y)\, \Psi\left(\tilde{\lambda}^2, y\right)}{u(y)} dy = 0 \quad \text{for } \lambda \neq \tilde{\lambda}$$

$$\int_{-\infty}^{\infty} \frac{\Phi_m(y)\,\Psi(\lambda^2,y)}{u(y)}dy = 0 \qquad (5.6)$$

and thus each discrete eigenmode $\Phi_m(y)\,e^{-jkx\lambda}$ and each continuous eigenmode $\Psi(\lambda^2,y)\,e^{-jkx\lambda}$ must satisfy the wave equation. Additional details pertaining to the cross section functions are given in [45].

5.1.1 Exterior Cross Section Functions

To compute the cross section functions in the exterior slab region $|y| > \tau/2$, we recall that in accordance with the slab simulation based on the generalized sheet transition conditions (GSTCs), the external fields satisfy the conditions (see chapter two)

$$\mathcal{U}_{11}\left(-\frac{\partial x^2}{k^2}\right)\left\{F^{odd,+}\right\} + \frac{j}{k}\mathcal{U}_{12}\left(-\frac{\partial x^2}{k^2}\right)\left\{\partial y F^{odd,+}\right\} = 0, \quad x>0 \qquad (5.7)$$

$$\mathcal{U}_{21}\left(-\frac{\partial x^2}{k^2}\right)\left\{F^{even,+}\right\} + \frac{j}{k}\mathcal{U}_{22}\left(-\frac{\partial x^2}{k^2}\right)\left\{\partial y F^{even,+}\right\} = 0, \quad x>0. \qquad (5.8)$$

where $F^{+}= F(x, y=\tau/2)$, $\partial x F^{+}= \frac{\partial}{\partial x}F(x, y=\tau/2)$, and $\partial y F^{+}= \frac{\partial}{\partial y}F(x,y)\,|_{y=\tau/2}$. The operators $\mathcal{U}_{ij}\left(-\frac{\partial x^2}{k^2}\right)$ are polynomials in $-\partial x^2/k^2$ and their explicit forms for the multilayer slab are derived in chapter two as a product of the functions $q_{ij}(u_m, \kappa_m, \tau_m, -\partial x^2/k^2)$ which are completely dependent on the properties of the m^{th} layer. In these, the parameter u_m is μ_m for E_z polarization and ϵ_m for H_z polarization, and $\kappa_m = \sqrt{\mu_m \epsilon_m}$ is the refractive index of the m^{th} layer comprising the slab. Because of the orthogonality conditions (5.5) and (5.6), each of the cross section functions $\Psi(\lambda^2, y)$ and $\Phi_m(y)$ must satisfy the odd or even GSTC (5.7) or (5.8). In view of this

$$\Psi^{odd}\left(\lambda^2, y\right) = \frac{|y|}{y}\left\{\mathcal{U}_{11}\left(\lambda^2\right) j\frac{\sin\left[k\left(|y|-\tau/2\right)\sqrt{1-\lambda^2}\right]}{\sqrt{1-\lambda^2}} + \mathcal{U}_{12}\left(\lambda^2\right)\cos\left[k\left(|y|-\tau/2\right)\sqrt{1-\lambda^2}\right]\right\}$$

$$
\begin{aligned}
&= \frac{|y|}{y}\left\{\mathcal{U}_{11}\left(\lambda^2\right)\tilde{q}_{12}(1,1,|y|-\tau/2,\lambda^2)\right. \\
&\quad \left.+\mathcal{U}_{12}\left(\lambda^2\right)\tilde{q}_{22}(1,1,|y|-\tau/2,\lambda^2)\right\} \\
\Psi^{even}\left(\lambda^2,y\right) &= \left\{\mathcal{U}_{21}\left(\lambda^2\right) j\frac{\sin\left[k\left(|y|-\tau/2\right)\sqrt{1-\lambda^2}\right]}{\sqrt{1-\lambda^2}}\right. \\
&\quad \left.+\mathcal{U}_{22}\left(\lambda^2\right)\cos\left[k\left(|y|-\tau/2\right)\sqrt{1-\lambda^2}\right]\right\} \\
&= \left\{\mathcal{U}_{21}\left(\lambda^2\right)\tilde{q}_{12}(1,1,|y|-\tau/2,\lambda^2)\right. \\
&\quad \left.+\mathcal{U}_{22}\left(\lambda^2\right)\tilde{q}_{22}(1,1,|y|-\tau/2,\lambda^2)\right\}
\end{aligned}
$$

where $\mathcal{U}_{ij}\left(\lambda^2\right)$ are the same polynomials appearing in (5.7) and(5.8), and $\tilde{q}_{ij}$ represent the infinite order form of the q_{ij} layer operators given in chapter two. Once each of the modes comprising (5.3) or (5.4) is substituted into (5.7) or (5.8), respectively, the differentiation implied by $-\partial x^2/k^2$ reduces to a multiplication by λ^2 and the above Ψ^{odd} and Ψ^{even} are then readily shown to satisfy the associated GSTC.

The cross section functions $\Psi^{odd}\left(\lambda^2,y\right)$ and $\Psi^{even}\left(\lambda^2,y\right)$ may also be rewritten in the form

$$
\begin{aligned}
\Psi^{odd}\left(\lambda^2,y\right) &= \frac{|y|}{y}\xi_+^{odd}\left(\lambda^2\right)e^{-jk(|y|-\tau/2)\sqrt{1-\lambda^2}} \\
&\quad +\frac{|y|}{y}\xi_-^{odd}\left(\lambda^2\right)e^{jk(|y|-\tau/2)\sqrt{1-\lambda^2}} \qquad (5.11) \\
\Psi^{even}\left(\lambda^2,y\right) &= \xi_+^{even}\left(\lambda^2\right)e^{-jk(|y|-\tau/2)\sqrt{1-\lambda^2}} \\
&\quad +\xi_-^{even}\left(\lambda^2\right)e^{jk(|y|-\tau/2)\sqrt{1-\lambda^2}} \qquad (5.12)
\end{aligned}
$$

for $|y|>\tau/2$, where it can be easily shown that (5.11) and (5.12) satisfy the orthogonality relations (5.5) and (5.6). This representation is customarily employed for the surface wave cross section functions. In particular we set

$$
\begin{aligned}
\Phi_m^{odd}(y) &= \frac{|y|}{y}e^{-jk(|y|-\tau/2)\sqrt{1-\left(\lambda_m^{odd}\right)^2}} \quad ;|y|>\tau/2 \qquad (5.13) \\
\Phi_m^{even}(y) &= e^{-jk(|y|-\tau/2)\sqrt{1-\left(\lambda_m^{even}\right)^2}} \quad ;|y|>\tau/2 \qquad (5.14)
\end{aligned}
$$

where $\lambda_m^{even,odd}$ must now be chosen so that (5.13) and (5.14) satisfy their associated GSTC. By substituting (5.13) and (5.14) into (5.7) and (5.8), respectively, we find that $\lambda_m^{odd,even}$ must satisfy the polynomial equations

$$\sqrt{1-(\lambda_m^{odd})^2}\mathcal{U}_{12}\left(\left[\lambda_m^{odd}\right]^2\right)+\mathcal{U}_{11}\left(\left[\lambda_m^{odd}\right]^2\right) = 0 \tag{5.15}$$

$$\sqrt{1-(\lambda_m^{even})^2}\mathcal{U}_{22}\left([\lambda_m^{even}]^2\right)+\mathcal{U}_{21}\left([\lambda_m^{even}]^2\right) = 0. \tag{5.16}$$

and can be also identified as the poles of the slab plane wave reflection coefficient. It is also interesting to note that

$$\Phi_m^{odd}(y) = \frac{\Psi^{odd}\left(\left[\lambda_m^{odd}\right]^2, y\right)}{\mathcal{U}_{12}\left([\lambda_m^{odd}]^2\right)}; \quad |y|>\tau/2 \tag{5.17}$$

$$\Phi_m^{even}(y) = \frac{\Psi^{even}\left([\lambda_m^{even}]^2, y\right)}{\mathcal{U}_{22}\left([\lambda_m^{even}]^2\right)}; \quad |y|>\tau/2 \tag{5.18}$$

implying that for the multilayer slab the cross section function associated with the discrete and continuous eigenmodes are of the same generic form given by (5.9) and (5.10).

5.1.2 Interior Cross Section Functions

We consider now the determination of the cross section functions for the region interior to the slab (i.e. in the region $|y|<\tau/2$). For simplicity let us first assume a single layer slab of thickness $\tau = 2\tau_1$, whose upper face is located at $y=\tau_1$. In accordance with the preceeding, the cross section functions associated with the external fields are given by

$$\begin{aligned}\Psi^{odd}\left(\lambda^2,y\right) &= \frac{|y|}{y}\Big\{q_{11}\left(u_1,\kappa_1,\tau_1,\lambda^2\right)\tilde{q}_{12}(1,1,|y|-\tau_1,\lambda^2)\\ &\quad +q_{12}\left(u_1,\kappa_1,\tau_1,\lambda^2\right)\tilde{q}_{22}(1,1,|y|-\tau_1,\lambda^2)\Big\}; \quad |y|>\tau_1 \end{aligned}\tag{5.19}$$

$$\begin{aligned}\Psi^{even}\left(\lambda^2,y\right) &= \Big\{q_{21}\left(u_1,\kappa_1,\tau_1,\lambda^2\right)\tilde{q}_{12}(1,1,|y|-\tau_1,\lambda^2)\\ &\quad +q_{22}\left(u_1,\kappa_1,\tau_1,\lambda^2\right)\tilde{q}_{22}(1,1,|y|-\tau_1,\lambda^2)\Big\}; \quad |y|>\tau_1 \end{aligned}\tag{5.20}$$

obtained by setting $\mathcal{U}_{ij}(\lambda^2) = q_{ij}(u_1, \kappa_1, \tau_1, \lambda^2)$ in (5.7), (5.9) and (5.10). These are orthogonal functions and each must, therefore, satisfy the continuity conditions

$$\Psi^{odd}\left(\lambda^2, \tau_1^-\right) = \Psi^{odd}\left(\lambda^2, \tau_1^+\right) \tag{5.21}$$

$$\frac{1}{u_1}\partial y \Psi^{odd}\left(\lambda^2, \tau_1^-\right) = \partial y \Psi^{odd}\left(\lambda^2, \tau_1^+\right) \tag{5.22}$$

$$\Psi^{even}\left(\lambda^2, \tau_1^-\right) = \Psi^{even}\left(\lambda^2, \tau_1^+\right) \tag{5.23}$$

$$\frac{1}{u_1}\partial y \Psi^{even}\left(\lambda^2, \tau_1^-\right) = \partial y \Psi^{even}\left(\lambda^2, \tau_1^+\right) \tag{5.24}$$

(due to symmetry it is not necessary to enforce similar conditions at $y = -\tau_1$). It is now straightforward to deduce that possible cross section functions satisfying (5.21) - (5.24) are of the form

$$\Psi^{odd}\left(\lambda^2, y\right) = \frac{|y|}{y} q_{12}(u_1, \kappa_1, |y|, \lambda^2) \tag{5.25}$$

$$\Psi^{even}\left(\lambda^2, y\right) = q_{22}(u_1, \kappa_1, |y|, \lambda^2) \tag{5.26}$$

for $|y| < \tau_1$. Also, in view of (5.21) - (5.24), the cross section functions for the surface wave modes remain as given in (5.17) - (5.18), provided (5.25) and (5.26) are used in place of $\Psi^{odd,even}$.

As a specific example, let us consider a low contrast $O(\tau_1)$ representation of a single layer. From chapter four, the truncated GSTC operators $\mathcal{U}_{ij}(-\partial x^2/k^2)$ are given to $O(\tau_1)$ by

$$\mathcal{U}_{11}\left(-\frac{\partial x^2}{k^2}\right) = \mathcal{U}_{11}\left(-\frac{\partial x^2}{k^2}\right) = 1 \tag{5.27}$$

$$\mathcal{U}_{12}\left(-\frac{\partial x^2}{k^2}\right) = jku_1\tau_1 \tag{5.28}$$

$$\mathcal{U}_{21}\left(-\frac{\partial x^2}{k^2}\right) = \frac{jk\tau_1\kappa_1^2}{u_1} + \frac{j\tau_1}{ku_1}\partial x^2 \tag{5.29}$$

and the corresponding $q_{ij}(\lambda^2)$ polynomials become

$$q_{11}\left(u_1, \kappa_1, \tau_1, \lambda^2\right) = q_{22}\left(u_1, \kappa_1, \tau_1, \lambda^2\right) = 1 \tag{5.30}$$

$$q_{12}\left(u_1,\kappa_1,\tau_1,\lambda^2\right) = jku_1\tau_1 \tag{5.31}$$

$$q_{21}\left(u_1,\kappa_1,\tau_1,\lambda^2\right) = \frac{jk\tau_1}{u_1}\left(\kappa_1^2-\lambda^2\right) \tag{5.32}$$

and

$$q_{12}\left(u_1,\kappa_1,|y|,\lambda^2\right) = jku_1|y| \tag{5.33}$$

$$q_{22}\left(u_1,\kappa_1,|y|,\lambda^2\right) = 1. \tag{5.34}$$

When these are substituted into (5.19), (5.20), (5.25) and (5.26) we obtain

$$\Psi^{odd}\left(\lambda^2,y\right) = \frac{|y|}{y}\begin{cases} j\frac{\sin\left[k(|y|-\tau_1)\sqrt{1-\lambda^2}\right]}{\sqrt{1-\lambda^2}} \\ \quad +jku_1\tau_1\cos\left[k\left(|y|-\tau_1\right)\sqrt{1-\lambda^2}\right]; & |y|>\tau_1 \\ jku_1|y|; & |y|<\tau_1 \end{cases} \tag{5.35}$$

$$\Psi^{even}\left(\lambda^2,y\right) = \begin{cases} \frac{-k\tau_1}{u_1}\left(\kappa_1^2-\lambda^2\right)\frac{\sin\left[k(|y|-\tau_1)\sqrt{1-\lambda^2}\right]}{\sqrt{1-\lambda^2}} \\ \quad +\cos\left[k\left(|y|-\tau_1\right)\sqrt{1-\lambda^2}\right]; & |y|>\tau_1 \\ 1; & |y|<\tau_1 \end{cases} \tag{5.36}$$

as the cross section functions for a single layer slab modelled with an $O(\tau_1)$ GSTC.

For the general case of a multilayer slab, it is necessary that each of the internal cross sections functions satisfy the continuity conditions at all layer interfaces comprising the slab. From chapter two, we obtain that the boundary conditions at the interface between the $L-1^{th}$ and L^{th} layer are

$$\mathcal{P}_{11}^{L-1}\left(-\frac{\partial x^2}{k^2}\right)\left\{u_L F^{odd}\left(x,y=y_{L-1}^{+}\right)\right\} + \frac{j}{k}\mathcal{P}_{12}^{L-1}\left(-\frac{\partial x^2}{k^2}\right)\left\{\partial y F^{odd}\left(x,y=y_{L-1}^{+}\right)\right\} = \tag{5.37}$$

$$\mathcal{P}_{21}^{L-1}\left(-\frac{\partial x^2}{k^2}\right)\left\{u_L F^{even}\left(x,y=y_{L-1}^{+}\right)\right\} + \frac{j}{k}\mathcal{P}_{22}^{L-1}\left(-\frac{\partial x^2}{k^2}\right)\left\{\partial y F^{even}\left(x,y=y_{l-1}^{+}\right)\right\} = \tag{5.38}$$

where y_L is the y coordinate associated with the top surface of the L^{th} layer and the

operators $\mathcal{P}_{ij}^{L-1}\left(-\frac{\partial x^2}{k^2}\right)$ are given by

$$\begin{pmatrix} \mathcal{P}_{11}^{L-1}\left(-\frac{\partial x^2}{k^2}\right) & \mathcal{P}_{12}^{L-1}\left(-\frac{\partial x^2}{k^2}\right) \\ \mathcal{P}_{21}^{L-1}\left(-\frac{\partial x^2}{k^2}\right) & \mathcal{P}_{22}^{L-1}\left(-\frac{\partial x^2}{k^2}\right) \end{pmatrix} = \prod_{m=1}^{L-1} \begin{pmatrix} q_{11}(u_m, \kappa_m, \tau_m, -\frac{\partial x^2}{k^2}) & q_{12}(u_m, \kappa_m, \tau_m, -\frac{\partial x^2}{k^2}) \\ q_{21}(u_m, \kappa_m, \tau_m, -\frac{\partial x^2}{k^2}) & q_{22}(u_m, \kappa_m, \tau_m, -\frac{\partial x^2}{k^2}) \end{pmatrix} \tag{5.39}$$

Possible interior cross section functions satisfying these conditions are

$$\begin{aligned} \Psi^{odd}\left(\lambda^2, y\right) &= \frac{|y|}{y}\left\{D_{1,L}^{odd}\left(\lambda^2\right) q_{12}(u_L, \kappa_L, |y| - y_{L-1}, \lambda^2)\right. \\ &\quad \left. + D_{2,L}^{odd}\left(\lambda^2\right) q_{22}(u_L, \kappa_L, |y| - y_{L-1}, \lambda^2)\right\} \quad y_{L-1} < |y| < y_L \end{aligned} \tag{5.40}$$

$$\begin{aligned} \Psi^{even}\left(\lambda^2, y\right) &= \left\{D_{1,L}^{even}\left(\lambda^2\right) q_{12}(u_L, \kappa_L, |y| - y_{L-1}, \lambda^2)\right. \\ &\quad \left. + D_{2,L}^{even}\left(\lambda^2\right) q_{22}(u_L, \kappa_L, |y| - y_{L-1}, \lambda^2)\right\} \quad y_{L-1} < |y| < y_L \end{aligned} \tag{5.41}$$

in which $D^{even,odd}(\lambda^2)$ are to be determined by demanding that the interior and exterior cross section functions are continuous at $y = \tau/2 (= y_L)$. Setting $y = \tau/2$ in the expressions for the external cross section functions (5.9) and (5.10), we obtain

$$\Psi^{odd}\left(\lambda^2, y = \tau/2\right) = \mathcal{U}_{12}\left(\lambda^2\right) \tag{5.42}$$

$$\Psi^{even}\left(\lambda^2, y = \tau/2\right) = \mathcal{U}_{22}\left(\lambda^2\right) \tag{5.43}$$

and when these are equated to (5.40) and (5.41) we find

$$\begin{aligned} \Psi^{odd}\left(\lambda^2, y\right) &= \frac{|y|}{y}\left\{\mathcal{P}_{11}^{L-1}\left(\lambda^2\right) q_{12}(u_L, \kappa_L, |y| - y_{L-1}, \lambda^2)\right. \\ &\quad \left. + \mathcal{P}_{12}^{L-1}\left(\lambda^2\right) q_{22}(u_L, \kappa_L, |y| - y_{L-1}, \lambda^2)\right\} \end{aligned} \tag{5.44}$$

$$\begin{aligned} \Psi^{even}\left(\lambda^2, y\right) &= \mathcal{P}_{21}^{L-1}\left(\lambda^2\right) q_{12}(u_L, \kappa_L, |y| - y_{L-1}, \lambda^2) \\ &\quad + \mathcal{P}_{22}^{L-1}\left(\lambda^2\right) q_{22}(u_L, \kappa_L, |y| - y_{L-1}, \lambda^2) \end{aligned} \tag{5.45}$$

for $y_L > |y| > y_{L-1}$.

To derive the cross section functions for the other layers, the above procedure may be repeated in a recursive manner until all layers are accounted for. Doing so,

we find that a complete representation of the cross section function everywhere is

$$\Psi^{odd}\left(\lambda^2, y\right) = \frac{|y|}{y}\begin{cases} \mathcal{U}_{11}(\lambda^2)\,\tilde{q}_{12}(1,1,|y|-\tau/2,\lambda^2) \\ \quad +\mathcal{U}_{12}(\lambda^2)\,\tilde{q}_{22}(1,1,|y|-\tau/2,\lambda^2); & |y|>\tau/2 \\ \mathcal{P}_{11}^{l-1}(\lambda^2)\,q_{12}(u_l,\kappa_l,|y|-y_{l-1},\lambda^2) & \\ \quad +\mathcal{P}_{12}^{l-1}(\lambda^2)\,\tilde{q}_{22}(u_l,\kappa_l,|y|-y_{l-1},\lambda^2); & y_l>|y|>y_{l-1} \\ q_{12}(u_1,\kappa_1,|y|,\lambda^2); & |y|<y_1 \end{cases} \tag{5.46}$$

$$\Psi^{even}\left(\lambda^2, y\right) = \begin{cases} \mathcal{U}_{21}(\lambda^2)\,\tilde{q}_{12}(1,1,|y|-\tau/2,\lambda^2) \\ \quad +\mathcal{U}_{22}(\lambda^2)\,\tilde{q}_{22}(1,1,|y|-\tau/2,\lambda^2); & |y|>\tau/2 \\ \mathcal{P}_{21}^{l-1}(\lambda^2)\,q_{12}(u_l,\kappa_l,|y|-y_{l-1},\lambda^2) & \\ \quad +\mathcal{P}_{22}^{l-1}(\lambda^2)\,q_{22}(u_l,\kappa_l,|y|-y_{l-1},\lambda^2); & y_l>|y|>y_{l-1} \\ q_{22}(u_1,\kappa_1,|y|,\lambda^2); & |y|<y_1 \end{cases} \tag{5.47}$$

when these are used in (5.3) and (5.4) in conjunction with (5.17) and (5.18) we have a complete field representation for $x > 0$.

5.2 Recasting of the Dual Integral Equation Solution for a Material Discontinuity

The expansions (5.3) and (5.4) can be used to represent the fields interior and exterior to the discontinuous slab shown in Figure 5.1. For $x > 0$, the material parameters used in the definition of the cross section functions (5.46) - (5.47) must then be associated with the right hand portion of the slab. Similarly, for $x < 0$, the material parameters in (5.46) - (5.47) must be those of the left hand portion of the slab.

The diffraction by the slab discontinuity shown in Figure 5.1 was the subject of chapter four where a complete expression for the scattered field was given by employing a GSTC simulation of the slab. However, owing to the non-uniqueness of the GSTC, the resulting diffraction coefficient was in terms of unknown constants whose

determination was shown to require additional constraints. One such constraint is the enforcement of a boundary condition demanding field continuity at the material junction, but this requires a knowledge of the slab interior fields and the solution given in chapter four pertains only to external fields. However, as shown in the preceeding section, the expansion (5.3) and (5.4) is valid everywhere when used in conjunction with the cross section functions given in (5.46)-(5.47). Moreover, since the expansion coefficients remain unchanged for the exterior and interior fields, once determined, the representation (5.3) and (5.4) can be used to find the field everywhere. Since the exterior field associated with the slab discontinuity in Figure 5.1 has already been given in chapter four, it can be used to identify the expansion coefficients. This requires that the solution in chapter four is first recast into a form compatible with that in (5.3) and (5.4), making possible the identification of the unknown constants which can then be determined by enforcing field continuity across the junction. In the following, upon stating the exterior solution we then proceed with the identification of the expansion coefficients.

In chapter four, the discontinuous multilayer symmetric slab shown in Figure 5.1 was simulated by the GSTCs

$$\mathcal{U}^1_{11}\left(-\frac{\partial x^2}{k^2}\right)\left\{F^{odd,+}\right\}+\frac{j}{k}\mathcal{U}^1_{12}\left(-\frac{\partial x^2}{k^2}\right)\left\{\partial y F^{odd,+}\right\} = 0, \quad -\infty < x < 0 \tag{5.48}$$

$$\mathcal{U}^1_{21}\left(-\frac{\partial x^2}{k^2}\right)\left\{F^{even,+}\right\}+\frac{j}{k}\mathcal{U}^1_{22}\left(-\frac{\partial x^2}{k^2}\right)\left\{\partial y F^{even,+}\right\} = 0, \quad -\infty < x < 0 \tag{5.49}$$

$$\mathcal{U}^2_{11}\left(-\frac{\partial x^2}{k^2}\right)\left\{F^{odd,+}\right\}+\frac{j}{k}\mathcal{U}^2_{12}\left(-\frac{\partial x^2}{k^2}\right)\left\{\partial y F^{odd,+}\right\} = 0, \quad 0 < x < \infty \tag{5.50}$$

$$\mathcal{U}^2_{21}\left(-\frac{\partial x^2}{k^2}\right)\left\{F^{even,+}\right\}+\frac{j}{k}\mathcal{U}^2_{22}\left(-\frac{\partial x^2}{k^2}\right)\left\{\partial y F^{even,+}\right\} = 0, \quad 0 < x < \infty. \tag{5.51}$$

with the superscripts 1 and 2 again denoting the material to the left and right of the junction, respectively. The total field is the sum of the even and odd components

and can be represented as

$$\begin{aligned} F(x,y) &= F^{odd}(x,y) + F^{even}(x,y) \\ &= \begin{cases} F_{inc}(x,y) + F_s(x,y) + F_{refl}(x,y) & y > \tau/2 \\ F_{tran}(x,y) + F_s(x,y) & y < -\tau/2 \end{cases} \end{aligned} \tag{5.52}$$

where

$$F_{inc}(x,y) = e^{jk(x\cos\phi_o + y\sin\phi_o)} \tag{5.53}$$

is the incident plane wave field, $F_{refl}(x,y)$ denotes the reflected field, which from (4.5) and (4.7) is given by

$$F_{refl}(x,y) = \frac{e^{jk\tau\sin\phi_o}}{2}\left[R_1^{even} + R_1^{odd}\right] e^{jk(x\cos\phi_o - y\sin\phi_o)} \tag{5.54}$$

with R_1^{odd} and R_1^{even} given by (4.9) and (4.10), respectively. Similarly, $F_{trans}(x,y)$ is the transmitted field, which from (4.6) and (4.8) is given as

$$F_{tran}(x,y) = \frac{e^{jk\tau\sin\phi_o}}{2}\left[R_1^{even} - R_1^{odd}\right] e^{jk(x\cos\phi_o + y\sin\phi_o)}. \tag{5.55}$$

Finally, $F_s(x,y)$ is the field scattered by the discontinuity and upon employing the dual integral equation method in conjunction with the GSTC (5.48) - (5.51), we find (from chapter four)

$$F_s(x,y) = F_s^{odd}(x,y) + F_s^{even}(x,y) \tag{5.56}$$

where

$$\begin{aligned} F_s^{odd}(x,y) &= \frac{y}{|y|}\int_{-\infty}^{\infty}\frac{j}{2\pi}\frac{\sqrt{1-\lambda_o^2}\sqrt{1-\lambda^2}}{\lambda+\lambda_o}\frac{e^{jk\tau/2\left(\sqrt{1-\lambda_o^2}+\sqrt{1-\lambda^2}\right)}}{\mathcal{G}_{1-}^{odd}(\lambda)\,\mathcal{G}_{1-}^{odd}(\lambda_o)\,\mathcal{G}_{2+}^{odd}(\lambda)\,\mathcal{G}_{2+}^{odd}(\lambda_o)} \\ &\left[Z_{odd}(-\lambda\lambda_o) + \sum_{m=1}^{\tilde{N}_{odd}-1}\sum_{n=0}^{\tilde{N}_{odd}-1-m} a_{mn}(\lambda+\lambda_o)^m(\lambda\lambda_o)^n\right]\frac{e^{-jk|y|\sqrt{1-\lambda^2}}e^{-jkx\lambda}d\lambda}{\sqrt{1-\lambda^2}} \end{aligned} \tag{5.57}$$

$$\begin{aligned} F_s^{even}(x,y) &= \int_{-\infty}^{\infty}\frac{j}{2\pi}\frac{\sqrt{1-\lambda_o^2}\sqrt{1-\lambda^2}}{\lambda+\lambda_o}\frac{e^{jk\tau/2\left(\sqrt{1-\lambda_o^2}+\sqrt{1-\lambda^2}\right)}}{\mathcal{G}_{1-}^{even}(\lambda)\,\mathcal{G}_{1-}^{even}(\lambda_o)\,\mathcal{G}_{2+}^{even}(\lambda)\,\mathcal{G}_{2+}^{even}(\lambda_o)} \\ &\left[Z_{even}(-\lambda\lambda_o) + \sum_{m=1}^{\tilde{N}_{even}-1}\sum_{n=0}^{\tilde{N}_{even}-1-m} b_{mn}(\lambda+\lambda_o)^m(\lambda\lambda_o)^n\right]\frac{e^{-jk|y|\sqrt{1-\lambda^2}}e^{-jkx\lambda}d\lambda}{\sqrt{1-\lambda^2}} \end{aligned} \tag{5.58}$$

In these expressions, $\lambda_o = \cos\phi_o$, and

$$\widetilde{N}_{odd} = int\left\{1/2\left(N^1_{odd} + N^2_{odd} + 1\right)\right\} \quad (5.59)$$

$$\widetilde{N}_{even} = int\left\{1/2\left(N^1_{even} + N^2_{even} + 1\right)\right\} \quad (5.60)$$

$$\mathcal{G}^{odd}_{1+}(\lambda)\,\mathcal{G}^{odd}_{1-}(\lambda) = \mathcal{G}^{odd}_{1}\left(\lambda^2\right) = \mathcal{U}^1_{11}\left(\lambda^2\right) + \sqrt{1-\lambda^2}\,\mathcal{U}^1_{12}\left(\lambda^2\right) \quad (5.61)$$

$$\mathcal{G}^{even}_{1+}(\lambda)\,\mathcal{G}^{even}_{1-}(\lambda) = \mathcal{G}^{even}_{1}\left(\lambda^2\right) = \mathcal{U}^1_{21}\left(\lambda^2\right) + \sqrt{1-\lambda^2}\,\mathcal{U}^1_{22}\left(\lambda^2\right) \quad (5.62)$$

$$\mathcal{G}^{odd}_{2+}(\lambda)\,\mathcal{G}^{odd}_{2-}(\lambda) = \mathcal{G}^{odd}_{2}\left(\lambda^2\right) = \mathcal{U}^2_{11}\left(\lambda^2\right) + \sqrt{1-\lambda^2}\,\mathcal{U}^2_{12}\left(\lambda^2\right) \quad (5.63)$$

$$\mathcal{G}^{even}_{2+}(\lambda)\,\mathcal{G}^{even}_{2-}(\lambda) = \mathcal{G}^{even}_{2}\left(\lambda^2\right) = \mathcal{U}^2_{21}\left(\lambda^2\right) + \sqrt{1-\lambda^2}\,\mathcal{U}^2_{22}\left(\lambda^2\right) \quad (5.64)$$

$$Z_{odd}(-\lambda\lambda_o) = \left[\mathcal{U}^1_{11}(-\lambda\lambda_o)\,\mathcal{U}^2_{12}(-\lambda\lambda_o) - \mathcal{U}^1_{12}(-\lambda\lambda_o)\,\mathcal{U}^2_{11}(-\lambda\lambda_o)\right] \quad (5.65)$$

$$Z_{even}(-\lambda\lambda_o) = \left[\mathcal{U}^1_{21}(-\lambda\lambda_o)\,\mathcal{U}^2_{22}(-\lambda\lambda_o) - \mathcal{U}^1_{22}(-\lambda\lambda_o)\,\mathcal{U}^2_{21}(-\lambda\lambda_o)\right] \quad (5.66)$$

$$N^1_{odd} = O(\lambda) \text{ of } \mathcal{G}^{odd}_{1}\left(\lambda^2\right) \quad (5.67)$$

$$N^2_{odd} = O(\lambda) \text{ of } \mathcal{G}^{odd}_{2}\left(\lambda^2\right) \quad (5.68)$$

$$N^1_{even} = O(\lambda) \text{ of } \mathcal{G}^{even}_{1}\left(\lambda^2\right) \quad (5.69)$$

$$N^2_{even} = O(\lambda) \text{ of } \mathcal{G}^{even}_{2}\left(\lambda^2\right) \quad (5.70)$$

As seen, the scattered field expressions are in terms of unknown constants a_{mn} and b_{mn} and to determine these via the procedure outlined above, we must first rewrite $F(x,y)$ in a form compatible with (5.3) and (5.4). To do this we need to identify from (5.52) to (5.58) the discrete and continuous spectral components. The discrete portion of the spectrum is, of course, comprised of the geometrical optics and the surface wave fields. These can be identified by detouring the integration path in (5.57) and (5.58) as shown in Figure 5.3. In particular, for $x < 0$ the integration path may be deformed to one over the branch cut in the upper half of the λ plane, capturing any surface wave poles attributed to the zeros of $\mathcal{G}^{odd}_{1-}(\lambda)$ and $\mathcal{G}^{even}_{1-}$. Similarly, for $x > 0$, the integration path may be deformed to one over the bra

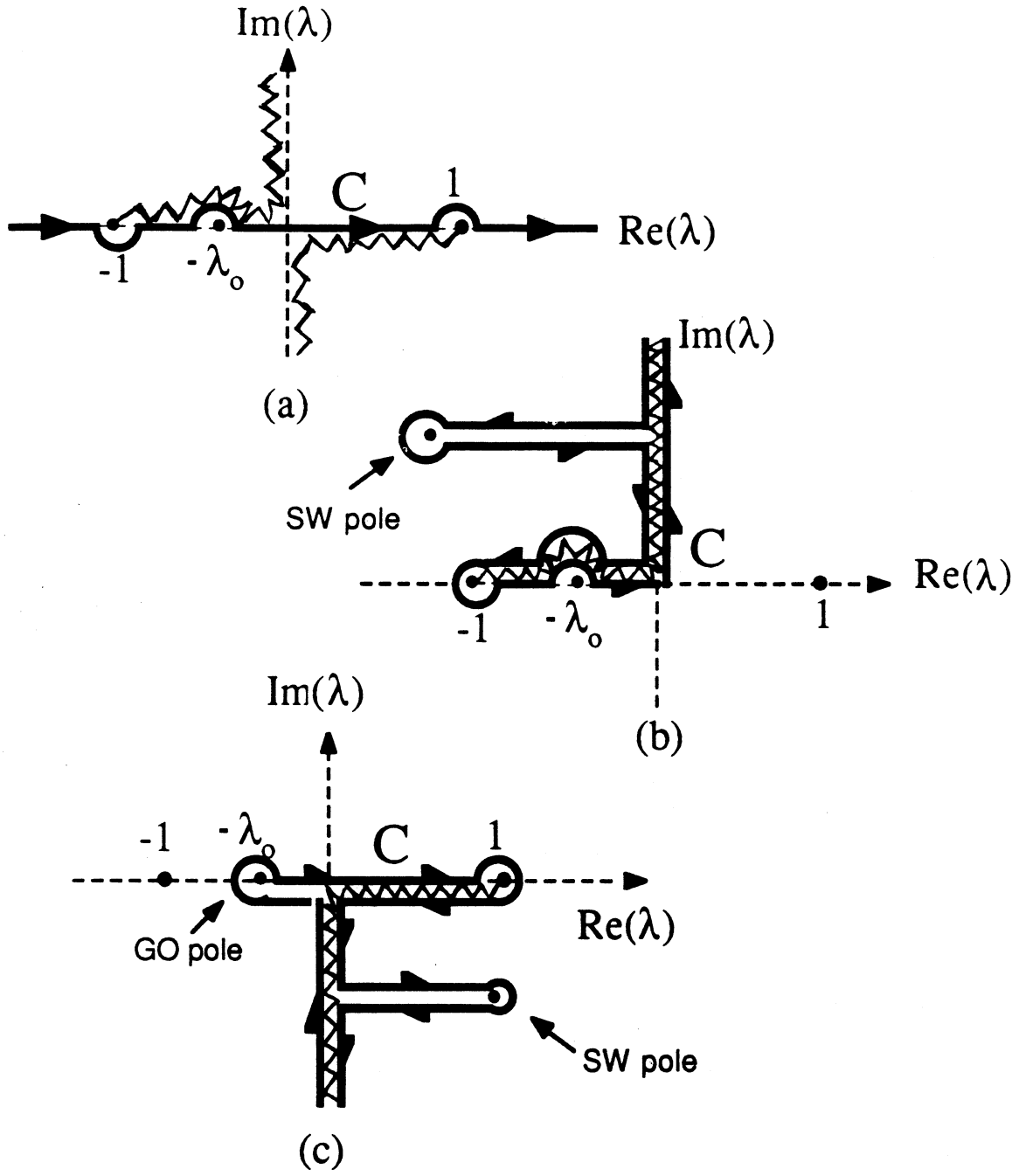

Figure 5.3: (a) C contour in the complex λ plane. (b) Deformation for region 1 integrals. (c) Deformation for region 2 integrals.

cut in the lower half of the λ plane causing the capture of the geometrical optics pole at $\lambda = -\lambda_o$ in addition to any surface wave poles attributed to the zeros of $\mathcal{G}_{2+}^{odd}(\lambda)$ and $\mathcal{G}_{2+}^{even}(\lambda)$.

Through the above deformation of the integration paths in (5.57) and (5.58) we obtain

$$F^{odd}(x,y) = \begin{cases} F_{go}^{1,odd}(x,y) + F_{sw}^{1,odd}(x,y) + F_{diff}^{1,odd}(x,y) & x<0 \\ F_{go}^{2,odd}(x,y) + F_{sw}^{2,odd}(x,y) + F_{diff}^{2,odd}(x,y) & x>0 \end{cases} \tag{5.71}$$

$$F^{even}(x,y) = \begin{cases} F_{go}^{1,even}(x,y) + F_{sw}^{1,even}(x,y) + F_{diff}^{1,even}(x,y) & x<0 \\ F_{go}^{2,even}(x,y) + F_{sw}^{2,even}(x,y) + F_{diff}^{2,even}(x,y) & x>0 \end{cases} \tag{5.72}$$

where for $|y| > \tau/2$

$$F_{go}^{1,odd}(x,y) = \frac{y}{|y|}\frac{e^{jkx\cos\phi_o}}{2}\left\{e^{jk|y|\sin\phi_o} + R_1^{odd}e^{-jk(|y|-\tau)\sin\phi_o}\right\} \tag{5.73}$$

$$F_{go}^{2,odd}(x,y) = \frac{y}{|y|}\frac{e^{jkx\cos\phi_o}}{2}\left\{e^{jk|y|\sin\phi_o} + R_2^{odd}e^{-jk(|y|-\tau)\sin\phi_o}\right\} \tag{5.74}$$

$$F_{go}^{1,even}(x,y) = \frac{e^{jkx\cos\phi_o}}{2}\left\{e^{jk|y|\sin\phi_o} + R_1^{even}e^{-jk(|y|-\tau)\sin\phi_o}\right\} \tag{5.75}$$

$$F_{go}^{2,even}(x,y) = \frac{e^{jkx\cos\phi_o}}{2}\left\{e^{jk|y|\sin\phi_o} + R_2^{even}e^{-jk(|y|-\tau)\sin\phi_o}\right\} \tag{5.76}$$

$$R_2^{odd} = \frac{\sin\phi_o\mathcal{U}_{12}^2(\cos^2\phi_o) - \mathcal{U}_{11}^2(\cos^2\phi_o)}{\sin\phi_o\mathcal{U}_{12}^2(\cos^2\phi_o) + \mathcal{U}_{11}^2(\cos^2\phi_o)} \tag{5.77}$$

$$R_2^{even} = \frac{\sin\phi_o\mathcal{U}_{22}^2(\cos^2\phi_o) - \mathcal{U}_{21}^2(\cos^2\phi_o)}{\sin\phi_o\mathcal{U}_{22}^2(\cos^2\phi_o) + \mathcal{U}_{21}^2(\cos^2\phi_o)}. \tag{5.78}$$

$$F_{sw}^{1,odd}(x,y) = \frac{y}{|y|}\sum_{l=1}^{N_{sw}^{1,odd}}\frac{-\sin\phi_o}{\lambda_l^{1,odd}+\lambda_o}\frac{e^{j\frac{k\tau}{2}\left(\sin\phi_o+\sqrt{1-(\lambda_l^{1,odd})^2}\right)}e^{-jkx\lambda_l^{1,odd}}e^{-jk|y|\sqrt{1-(\lambda_l^{1,odd})^2}}}{\mathcal{G}_{2+}^{odd}\left(\lambda_l^{1,odd}\right)\mathcal{G}_{2+}^{odd}(\lambda_o)\mathcal{G}_{1-}^{odd}(\lambda_o)\left[\frac{\partial\mathcal{G}_{1-}^{odd}(\lambda)}{\partial\lambda}\right]_{\lambda=\lambda_l^{1,odd}}}$$
$$\left[Z_{odd}\left(-\lambda_o\lambda_l^{1,odd}\right) + \sum_{m=1}^{\tilde{N}_{odd}-1}\sum_{n=0}^{\tilde{N}_{odd}-1-m}a_{mn}\left(\lambda_l^{1,odd}+\lambda_o\right)^m\left(\lambda_l^{1,odd}\lambda_o\right)^n\right] \tag{5.79}$$

$$F_{sw}^{2,odd}(x,y) = \frac{y}{|y|}\sum_{l=1}^{N_{sw}^{2,odd}}\frac{-\sin\phi_o}{\lambda_l^{2,odd}+\lambda_o}\frac{e^{j\frac{k\tau}{2}\left(\sin\phi_o+\sqrt{1-(\lambda_l^{2,odd})^2}\right)}e^{-jkx\lambda_l^{2,odd}}e^{-jk|y|\sqrt{1-(\lambda_l^{2,odd})^2}}}{\mathcal{G}_{1-}^{odd}\left(\lambda_l^{2,odd}\right)\mathcal{G}_{1-}^{odd}(\lambda_o)\mathcal{G}_{2+}^{odd}(\lambda_o)\left[\frac{\partial\mathcal{G}_{2+}^{odd}(\lambda)}{\partial\lambda}\right]_{\lambda=\lambda_l^{2,odd}}}$$
$$\left[Z_{odd}\left(-\lambda_o\lambda_l^{2,odd}\right) + \sum_{m=1}^{\tilde{N}_{odd}-1}\sum_{n=0}^{\tilde{N}_{odd}-1-m}a_{mn}\left(\lambda_l^{2,odd}+\lambda_o\right)^m\left(\lambda_l^{2,odd}\lambda_o\right)^n\right] \tag{5.80}$$

$$F_{sw}^{1,even}(x,y)=\sum_{l=1}^{N_{sw}^{1,even}}\frac{-\sin\phi_o}{\lambda_l^{1,even}+\lambda_o}\frac{e^{j\frac{k\tau}{2}\left(\sin\phi_o+\sqrt{1-(\lambda_l^{1,even})^2}\right)}e^{-jkx\lambda_l^{1,even}}e^{-jk|y|\sqrt{1-(\lambda_l^{1,even})^2}}}{\mathcal{G}_{2+}^{even}\left(\lambda_l^{1,even}\right)\mathcal{G}_{2+}^{even}(\lambda_o)\mathcal{G}_{1-}^{even}(\lambda_o)\left[\frac{\partial\mathcal{G}_{1-}^{even}(\lambda)}{\partial\lambda}\right]_{\lambda=\lambda_l^{1,even}}}$$
$$\cdot\left[Z_{even}\left(-\lambda_o\lambda_l^{1,even}\right)+\sum_{m=1}^{\widetilde{N}_{even}-1}\sum_{n=0}^{\widetilde{N}_{even}-1-m}b_{mn}\left(\lambda_l^{1,even}+\lambda_o\right)^m\left(\lambda_l^{1,even}\lambda_o\right)^n\right] \quad (5.81)$$

$$F_{sw}^{2,even}(x,y)=\sum_{l=1}^{N_{sw}^{2,even}}\frac{-\sin\phi_o}{\lambda_l^{2,even}+\lambda_o}\frac{e^{j\frac{k\tau}{2}\left(\sin\phi_o+\sqrt{1-(\lambda_l^{2,even})^2}\right)}e^{-jkx\lambda_l^{2,even}}e^{-jk|y|\sqrt{1-(\lambda_l^{2,even})^2}}}{\mathcal{G}_{1-}^{even}\left(\lambda_l^{2,even}\right)\mathcal{G}_{1-}^{even}(\lambda_o)\mathcal{G}_{2+}^{even}(\lambda_o)\left[\frac{\partial\mathcal{G}_{2+}^{even}(\lambda)}{\partial\lambda}\right]_{\lambda=\lambda_l^{2,even}}}$$
$$\cdot\left[Z_{even}\left(-\lambda_o\lambda_l^{2,even}\right)+\sum_{m=1}^{\widetilde{N}_{even}-1}\sum_{n=0}^{\widetilde{N}_{even}-1-m}b_{mn}\left(\lambda_l^{2,even}+\lambda_o\right)^m\left(\lambda_l^{2,even}\lambda_o\right)^n\right] \quad (5.82)$$

$$F_{diff}^{1,odd}(x,y)=\frac{y}{|y|}\int_{C_{br}^U}\frac{j}{2\pi}\frac{\sqrt{1-\lambda_o^2}\sqrt{1-\lambda^2}}{\lambda+\lambda_o}\frac{e^{jk\tau/2\left(\sqrt{1-\lambda_o^2}+\sqrt{1-\lambda^2}\right)}}{\mathcal{G}_{1-}^{odd}(\lambda)\mathcal{G}_{1-}^{odd}(\lambda_o)\mathcal{G}_{2+}^{odd}(\lambda)\mathcal{G}_{2+}^{odd}(\lambda_o)}$$
$$\cdot\left[Z_{odd}(-\lambda\lambda_o)+\sum_{m=1}^{\widetilde{N}_{odd}-1}\sum_{n=0}^{\widetilde{N}_{odd}-1-m}a_{mn}(\lambda+\lambda_o)^m(\lambda\lambda_o)^n\right]\frac{e^{-jk|y|\sqrt{1-\lambda^2}}e^{-jkx\lambda}d\lambda}{\sqrt{1-\lambda^2}} \quad (5.83)$$

$$F_{diff}^{2,odd}(x,y)=\frac{y}{|y|}\int_{C_{br}^L}\frac{j}{2\pi}\frac{\sqrt{1-\lambda_o^2}\sqrt{1-\lambda^2}}{\lambda+\lambda_o}\frac{e^{jk\tau/2\left(\sqrt{1-\lambda_o^2}+\sqrt{1-\lambda^2}\right)}}{\mathcal{G}_{1-}^{odd}(\lambda)\mathcal{G}_{1-}^{odd}(\lambda_o)\mathcal{G}_{2+}^{odd}(\lambda)\mathcal{G}_{2+}^{odd}(\lambda_o)}$$
$$\cdot\left[Z_{odd}(-\lambda\lambda_o)+\sum_{m=1}^{\widetilde{N}_{odd}-1}\sum_{n=0}^{\widetilde{N}_{odd}-1-m}a_{mn}(\lambda+\lambda_o)^m(\lambda\lambda_o)^n\right]\frac{e^{-jk|y|\sqrt{1-\lambda^2}}e^{-jkx\lambda}d\lambda}{\sqrt{1-\lambda^2}} \quad (5.84)$$

$$F_{diff}^{1,even}(x,y)=\int_{C_{br}^U}\frac{j}{2\pi}\frac{\sqrt{1-\lambda_o^2}\sqrt{1-\lambda^2}}{\lambda+\lambda_o}\frac{e^{jk\tau/2\left(\sqrt{1-\lambda_o^2}+\sqrt{1-\lambda^2}\right)}}{\mathcal{G}_{1-}^{odd}(\lambda)\mathcal{G}_{1-}^{odd}(\lambda_o)\mathcal{G}_{2+}^{odd}(\lambda)\mathcal{G}_{2+}^{odd}(\lambda_o)}$$
$$\cdot\left[Z_{even}(-\lambda\lambda_o)+\sum_{m=1}^{\widetilde{N}_{even}-1}\sum_{n=0}^{\widetilde{N}_{even}-1-m}b_{mn}(\lambda+\lambda_o)^m(\lambda\lambda_o)^n\right]\frac{e^{-jk|y|\sqrt{1-\lambda^2}}e^{-jkx\lambda}d\lambda}{\sqrt{1-\lambda^2}} \quad (5.85)$$

$$F_{diff}^{2,even}(x,y)=\int_{C_{br}^L}\frac{j}{2\pi}\frac{\sqrt{1-\lambda_o^2}\sqrt{1-\lambda^2}}{\lambda+\lambda_o}\frac{e^{jk\tau/2\left(\sqrt{1-\lambda_o^2}+\sqrt{1-\lambda^2}\right)}}{\mathcal{G}_{1-}^{odd}(\lambda)\mathcal{G}_{1-}^{odd}(\lambda_o)\mathcal{G}_{2+}^{odd}(\lambda)\mathcal{G}_{2+}^{odd}(\lambda_o)}$$
$$\cdot\left[Z_{even}(-\lambda\lambda_o)+\sum_{m=1}^{\widetilde{N}_{even}-1}\sum_{n=0}^{\widetilde{N}_{even}-1-m}b_{mn}(\lambda+\lambda_o)^m(\lambda\lambda_o)^n\right]\frac{e^{-jk|y|\sqrt{1-\lambda^2}}e^{-jkx\lambda}d\lambda}{\sqrt{1-\lambda^2}} \quad (5.86)$$

In these, the components F_{go}, F_{sw}, F_{diff} denote the geometrical optics, surface wave, and branch cut (or diffraction) contributions to the total fields. Also $N_{sw}^{1,2}$ is the number of captured surface waves (i.e., those with normalized propagation constants $\lambda_l^{1,2}$ such that $Im\{\lambda_l^1\}>0$ or $Im\{\lambda_l^2\}<0$).

To identify the expansion coefficients A_m, B_m, and $C(\lambda)$ appearing in (5.3) and (5.4), (5.73) - (5.86) must first be rearranged. By making use of (4.9) - (4.10), (5.61) - (5.64), and (5.77) - (5.78), the geometrical optics terms can be rewritten as

$$F_{go}^{1,odd}(x,y) = \frac{y}{|y|}\frac{\sin\phi_o e^{jkx\cos\phi_o}e^{jk\tau/2\sin\phi_o}}{\mathcal{G}_1^{odd}(\lambda_o^2)}\left[\mathcal{U}_{11}^1\left(\lambda^2\right)\frac{j\sin\left(k\sin\phi_o\left[|y|-\tau/2\right]\right)}{\sin\phi_o}\right.$$
$$\left.+\mathcal{U}_{12}^1\left(\lambda^2\right)\cos\left(k\sin\phi_o\left[|y|-\tau/2\right]\right)\right] \quad (5.87)$$

$$F_{go}^{2,odd}(x,y) = \frac{y}{|y|}\frac{\sin\phi_o e^{jkx\cos\phi_o}e^{jk\tau/2\sin\phi_o}}{\mathcal{G}_2^{odd}(\lambda_o^2)}\left[\mathcal{U}_{11}^2\left(\lambda^2\right)\frac{j\sin\left(k\sin\phi_o\left[|y|-\tau/2\right]\right)}{\sin\phi_o}\right.$$
$$\left.+\mathcal{U}_{12}^2\left(\lambda^2\right)\cos\left(k\sin\phi_o\left[|y|-\tau/2\right]\right)\right] \quad (5.88)$$

$$F_{go}^{1,even}(x,y) = \frac{y}{|y|}\frac{\sin\phi_o e^{jkx\cos\phi_o}e^{jk\tau/2\sin\phi_o}}{\mathcal{G}_1^{even}(\lambda_o^2)}\left[\mathcal{U}_{21}^1\left(\lambda^2\right)\frac{j\sin\left(k\sin\phi_o\left[|y|-\tau/2\right]\right)}{\sin\phi_o}\right.$$
$$\left.+\mathcal{U}_{22}^1\left(\lambda^2\right)\cos\left(k\sin\phi_o\left[|y|-\tau/2\right]\right)\right] \quad (5.89)$$

$$F_{go}^{2,even}(x,y) = \frac{y}{|y|}\frac{\sin\phi_o e^{jkx\cos\phi_o}e^{jk\tau/2\sin\phi_o}}{\mathcal{G}_2^{even}(\lambda_o^2)}\left[\mathcal{U}_{21}^2\left(\lambda^2\right)\frac{j\sin\left(k\sin\phi_o\left[|y|-\tau/2\right]\right)}{\sin\phi_o}\right.$$
$$\left.+\mathcal{U}_{22}^2\left(\lambda^2\right)\cos\left(k\sin\phi_o\left[|y|-\tau/2\right]\right)\right] \quad (5.90)$$

The bracketed terms in (5.87) - (5.90) are now readily recognized as the cross section functions given by (5.46) and (5.47) once λ_o is set to $\cos\phi_o$. Thus, from (5.3) and (5.4) the geometrical optics fields may be expressed as

$$F_{go}^{1,odd}(x,y) = A_1^{odd}(\lambda_o)\,\Psi_1^{odd}\left(\lambda_o^2,y\right)e^{jkx\cos\phi_o} \quad (5.91)$$

$$F_{go}^{2,odd}(x,y) = A_2^{odd}(\lambda_o)\,\Psi_2^{odd}\left(\lambda_o^2,y\right)e^{jkx\cos\phi_o} \quad (5.92)$$

$$F_{go}^{1,even}(x,y) = A_1^{even}(\lambda_o)\,\Psi_1^{even}\left(\lambda_o^2,y\right)e^{jkx\cos\phi_o} \quad (5.93)$$

$$F_{go}^{2,even}(x,y) = A_2^{even}(\lambda_o)\,\Psi_2^{even}\left(\lambda_o^2,y\right)e^{jkx\cos\phi_o} \quad (5.94)$$

where the A expansion coefficients are identified as

$$A_1^{odd}(\lambda_o) = \frac{\sin\phi_o e^{jk\tau/2\sin\phi_o}}{\mathcal{G}_1^{odd}(\lambda_o^2)} \quad (5.95)$$

$$A_2^{odd}(\lambda_o) = \frac{\sin\phi_o e^{jk\tau/2\sin\phi_o}}{\mathcal{G}_2^{odd}(\lambda_o^2)} \quad (5.96)$$

$$A_1^{even}(\lambda_o) = \frac{\sin\phi_o e^{jk\tau/2\sin\phi_o}}{\mathcal{G}_1^{even}(\lambda_o^2)} \quad (5.97)$$

$$A_2^{even}(\lambda_o) = \frac{\sin\phi_o e^{jk\tau/2\sin\phi_o}}{\mathcal{G}_2^{even}(\lambda_o^2)} \tag{5.98}$$

Also, $\Psi_1^{odd,even}$ are the same as those given in (5.46)-(5.47) but are associated with material parameters to the left of the slab and likewise $\Psi_2^{odd,even}$ are associated with the material parameters to the right of the slab.

To identify the B expansion coefficients we observe that the surface wave terms are already of the form appearing in (5.3) and (5.4) and can be readily rewritten as

$$F_{sw}^{1,odd}(x,y) = \sum_{l=1}^{N_{sw}^{1,odd}} B_l^{1,odd}(\lambda_o)\left[Z_{odd}\left(-\lambda_o\lambda_l^{1,odd}\right)\right.$$
$$\left.+\sum_{m=1}^{\tilde{N}_{odd}-1}\sum_{n=0}^{\tilde{N}_{odd}-1-m} a_{mn}\left(\lambda_l^{1,odd}+\lambda_o\right)^m\left(\lambda_l^{1,odd}\lambda_o\right)^n\right]\Psi_1^{odd}\left(\left[\lambda_l^{1,odd}\right]^2,y\right)e^{-jkx\lambda_l^{1,odd}} \tag{5.99}$$

$$F_{sw}^{2,odd}(x,y) = \sum_{l=1}^{N_{sw}^{2,odd}} B_l^{2,odd}(\lambda_o)\left[Z_{odd}\left(-\lambda_o\lambda_l^{2,odd}\right)\right.$$
$$\left.+\sum_{m=1}^{\tilde{N}_{odd}-1}\sum_{n=0}^{\tilde{N}_{odd}-1-m} a_{mn}\left(\lambda_l^{2,odd}+\lambda_o\right)^m\left(\lambda_l^{2,odd}\lambda_o\right)^n\right]\Psi_2^{odd}\left(\left[\lambda_l^{2,odd}\right]^2,y\right)e^{-jkx\lambda_l^{2,odd}} \tag{5.100}$$

$$F_{sw}^{1,even}(x,y) = \sum_{l=1}^{N_{sw}^{1,even}} B_l^{1,even}(\lambda_o)\left[Z_{odd}\left(-\lambda_o\lambda_l^{1,even}\right)\right.$$
$$\left.+\sum_{m=1}^{\tilde{N}_{even}-1}\sum_{n=0}^{\tilde{N}_{even}-1-m} b_{mn}\left(\lambda_l^{1,even}+\lambda_o\right)^m\left(\lambda_l^{1,even}\lambda_o\right)^n\right]\Psi_1^{even}\left(\left[\lambda_l^{1,even}\right]^2,y\right)e^{-jkx\lambda_l^{1,even}} \tag{5.101}$$

$$F_{sw}^{2,even}(x,y) = \sum_{l=1}^{N_{sw}^{2,even}} B_l^{2,even}(\lambda_o)\left[Z_{odd}\left(-\lambda_o\lambda_l^{2,even}\right)\right.$$
$$\left.+\sum_{m=1}^{\tilde{N}_{even}-1}\sum_{n=0}^{\tilde{N}_{even}-1-m} b_{mn}\left(\lambda_l^{2,even}+\lambda_o\right)^m\left(\lambda_l^{2,even}\lambda_o\right)^n\right]\Psi_2^{even}\left(\left[\lambda_l^{2,even}\right]^2,y\right)e^{-jkx\lambda_l^{2,even}} \tag{5.102}$$

with

$$B_l^{1,odd}(\lambda_o) = \frac{-\sin\phi_o}{\lambda_l^{1,odd}+\lambda_o}\frac{e^{jk\tau/2\sin\phi_o}}{\left[\frac{\partial\mathcal{G}_{1-}^{odd}(\lambda)}{\partial\lambda}\right]_{\lambda=\lambda_l^{1,odd}}\mathcal{G}_{1-}^{odd}(\lambda_o)\,\mathcal{G}_{2+}^{odd}\left(\lambda_l^{1,odd}\right)\mathcal{G}_{2+}^{odd}(\lambda_o)} \tag{5.103}$$

$$B_l^{2,odd}(\lambda_o) = \frac{-\sin\phi_o}{\lambda_l^{2,odd}+\lambda_o}\frac{e^{jk\tau/2\sin\phi_o}}{\mathcal{G}_{1-}^{odd}\left(\lambda_l^{2,odd}\right)\mathcal{G}_{1-}^{odd}(\lambda_o)\left[\frac{\partial\mathcal{G}_{2+}^{odd}(\lambda)}{\partial\lambda}\right]_{\lambda=\lambda_l^{2,odd}}\mathcal{G}_{2+}^{odd}(\lambda_o)} \tag{5.104}$$

$$B_l^{1,even}(\lambda_o) = \frac{-\sin\phi_o}{\lambda_l^{1,even}+\lambda_o} \frac{e^{jk\tau/2\sin\phi_o}}{\left[\frac{\partial \mathcal{G}_{1-}^{even}(\lambda)}{\partial\lambda}\right]_{\lambda=\lambda_l^{1,even}} \mathcal{G}_{1-}^{even}(\lambda_o)\,\mathcal{G}_{2+}^{even}\left(\lambda_l^{1,even}\right)\mathcal{G}_{2+}^{even}(\lambda_o)} \tag{5.105}$$

$$B_l^{2,even}(\lambda_o) = \frac{-\sin\phi_o}{\lambda_l^{2,even}+\lambda_o} \frac{e^{jk\tau/2\sin\phi_o}}{\mathcal{G}_{1-}^{even}\left(\lambda_l^{2,even}\right)\mathcal{G}_{1-}^{even}(\lambda_o)\left[\frac{\partial \mathcal{G}_{2+}^{even}(\lambda)}{\partial\lambda}\right]_{\lambda=\lambda_l^{2,even}} \mathcal{G}_{2+}^{even}(\lambda_o)} \tag{5.106}$$

It remains to identify the C expansion coefficients and to do this, it is necessary to employ the transformation $\beta = \sqrt{1-\lambda^2}$. Doing so in (5.83) permits us to rewrite $F_{diff}^{1,odd}$ as

$$\begin{aligned} F_{diff}^{1,odd}(x,y) &= \frac{y}{|y|}\int_{-\infty}^{\infty}\frac{j}{2\pi}\frac{-\beta\sqrt{1-\lambda_o^2}}{\sqrt{1-\beta^2}\left(\sqrt{1-\beta^2}+\lambda_o\right)} \\ &\cdot\frac{e^{jk\tau/2\left(\sqrt{1-\lambda_o^2}+\beta\right)}e^{-jk|y|\beta}e^{-jkx\sqrt{1-\beta^2}}}{\mathcal{G}_{1-}^{odd}\left(\sqrt{1-\beta^2}+\delta\frac{\beta}{|\beta|}\right)\mathcal{G}_{1-}^{odd}(\lambda_o)\,\mathcal{G}_{2+}^{odd}\left(\sqrt{1-\beta^2}\right)\mathcal{G}_{2+}^{odd}(\lambda_o)} \\ &\cdot\left[Z_{odd}\left(-\lambda_o\sqrt{1-\beta^2}\right)+\sum_{m=1}^{\tilde{N}_{odd}-1}\sum_{n=0}^{\tilde{N}_{odd}-1-m}a_{mn}\left(\lambda_o+\sqrt{1-\beta^2}\right)^m\left(\lambda_o\sqrt{1-\beta^2}\right)^n\right]d\beta \end{aligned} \tag{5.107}$$

where the branch of the square root is chosen so that $Im(\sqrt{1-\beta^2}) > 0$ and δ is a vanishingly small positive number. The integral may now be split into its positive and negative portions and then recombined to obtain

$$\begin{aligned} F_{diff}^{1,odd}(x,y) = \frac{y}{|y|}\int_0^{\infty}\frac{j}{2\pi}\frac{-\beta\sqrt{1-\lambda_o^2}}{\sqrt{1-\beta^2}\left(\sqrt{1-\beta^2}+\lambda_o\right)}\frac{e^{jk\tau/2\sqrt{1-\lambda_o^2}}\mathcal{Z}_{odd}\left(\sqrt{1-\beta^2},\lambda_o\right)}{\mathcal{G}_{1-}^{odd}(\lambda_o)\,\mathcal{G}_{2+}^{odd}\left(\sqrt{1-\beta^2}\right)\mathcal{G}_{2+}^{odd}(\lambda_o)} \\ \cdot\left\{\frac{e^{-jk(|y|-\tau/2)\beta}}{\mathcal{G}_{1-}^{odd}\left(\sqrt{1-\beta^2}+\delta\right)}-\frac{e^{jk(|y|-\tau/2)\beta}}{\mathcal{G}_{1-}^{odd}\left(\sqrt{1-\beta^2}-\delta\right)}\right\}e^{-jkx\sqrt{1-\beta^2}}d\beta \end{aligned} \tag{5.108}$$

where

$$\begin{aligned} \mathcal{Z}_{odd}\left(\sqrt{1-\beta^2},\lambda_o\right) &= Z_{odd}\left(-\lambda_o\sqrt{1-\beta^2}\right) \\ &+\sum_{m=1}^{\tilde{N}_{odd}-1}\sum_{n=0}^{\tilde{N}_{odd}-1-m}a_{mn}\left(\lambda_o+\sqrt{1-\beta^2}\right)^m\left(\lambda_o\sqrt{1-\beta^2}\right)^n \end{aligned} \tag{5.109}$$

By invoking (5.61), we can show that

$$\frac{e^{-jk(|y|-\tau/2)\beta}}{\mathcal{G}_{1-}^{odd}\left(\sqrt{1-\beta^2}+\delta\right)}-\frac{e^{jk(|y|-\tau/2)\beta}}{\mathcal{G}_{1-}^{odd}\left(\sqrt{1-\beta^2}-\delta\right)}=\frac{-2\beta\mathcal{G}_{1+}^{odd}\left(\sqrt{1-\beta^2}\right)}{\left[\mathcal{U}_{11}^{1}\left(1-\beta^2\right)\right]^2-\beta^2\left[\mathcal{U}_{11}^{1}\left(1-\beta^2\right)\right]^2}$$
$$\cdot\left[j\frac{\sin\left(k\beta\left[|y|-\tau/2\right]\right)}{\beta}\mathcal{U}_{11}^{1}\left(1-\beta^2\right)+\cos\left(k\beta\left[|y|-\tau/2\right]\right)\mathcal{U}_{12}^{1}\left(1-\beta^2\right)\right] \quad (5.110)$$

where the term in square brackets is identified as $\Psi_1^{odd}\left(1-\beta^2,y\right)$ as given in (5.46) for $|y|>\tau/2$. Substituting (5.110) into (5.108) finally yields

$$F_{diff}^{1,odd}(x,y)=\int_0^{\infty}C_1^{odd}(\beta)\,\mathcal{Z}_{odd}\left(\sqrt{1-\beta^2},\lambda_o\right)\Psi_1^{odd}\left(1-\beta^2,y\right)e^{-jkx\sqrt{1-\beta^2}}d\beta \quad (5.111)$$

with the expansion coefficient $C_1^{odd}(\beta)$ given by

$$C_1^{odd}(\beta)=\frac{j}{\pi}\frac{\beta^2\sqrt{1-\lambda_o^2}}{\sqrt{1-\beta^2}\left(\sqrt{1-\beta^2}+\lambda_o\right)}$$
$$\cdot\frac{e^{jk\tau/2\sqrt{1-\lambda_o^2}}\mathcal{G}_{1+}^{odd}\left(\sqrt{1-\beta^2}\right)}{\mathcal{G}_{2+}^{odd}\left(\sqrt{1-\beta^2}\right)\mathcal{G}_{2+}^{odd}\left(\lambda_o\right)\mathcal{G}_{1-}^{odd}\left(\lambda_o\right)\left\{\left[\mathcal{U}_{11}^{1}\left(1-\beta^2\right)\right]^2-\beta^2\left[\mathcal{U}_{12}^{1}\left(1-\beta^2\right)\right]^2\right\}} \quad (5.112)$$

In a parallel manner we obtain

$$F_{diff}^{2,odd}(x,y)=\int_0^{\infty}C_2^{odd}(\beta)\,\mathcal{Z}_{odd}\left(\sqrt{1-\beta^2},\lambda_o\right)\Psi_2^{odd}\left(1-\beta^2,y\right)e^{-jkx\sqrt{1-\beta^2}}d\beta \quad (5.113)$$

$$F_{diff}^{1,even}(x,y)=\int_0^{\infty}C_1^{even}(\beta)\,\mathcal{Z}_{even}\left(\sqrt{1-\beta^2},\lambda_o\right)\Psi_1^{even}\left(1-\beta^2,y\right)e^{-jkx\sqrt{1-\beta^2}}d\beta \quad (5.114)$$

$$F_{diff}^{2,even}(x,y)=\int_0^{\infty}C_2^{even}(\beta)\,\mathcal{Z}_{even}\left(\sqrt{1-\beta^2},\lambda_o\right)\Psi_2^{even}\left(1-\beta^2,y\right)e^{-jkx\sqrt{1-\beta^2}}d\beta \quad (5.115)$$

where

$$\mathcal{Z}_{even}\left(\sqrt{1-\beta^2},\lambda_o\right)=Z_{even}\left(-\lambda_o\sqrt{1-\beta^2}\right)$$
$$+\sum_{m=1}^{\tilde{N}_{even}-1}\sum_{n=0}^{\tilde{N}_{even}-1-m}b_{mn}\left(\lambda_o+\sqrt{1-\beta^2}\right)^m\left(\lambda_o\sqrt{1-\beta^2}\right)^n \quad (5.116)$$

and the spectral expansion coefficients are given by

$$C_2^{odd}(\beta) = \frac{-j}{\pi}\frac{\beta^2\sqrt{1-\lambda_o^2}}{\sqrt{1-\beta^2}\left(\sqrt{1-\beta^2}+\lambda_o\right)} \cdot \frac{e^{jk\tau/2\sqrt{1-\lambda_o^2}}\mathcal{G}_{2-}^{odd}\left(\sqrt{1-\beta^2}\right)}{\mathcal{G}_{1-}^{odd}\left(\sqrt{1-\beta^2}\right)\mathcal{G}_{1-}^{odd}(\lambda_o)\,\mathcal{G}_{2+}^{odd}(\lambda_o)\left\{\left[\mathcal{U}_{11}^2(1-\beta^2)\right]^2-\beta^2\left[\mathcal{U}_{12}^2(1-\beta^2)\right]^2\right\}} \quad (5.117)$$

$$C_1^{even}(\beta) = \frac{j}{\pi}\frac{\beta^2\sqrt{1-\lambda_o^2}}{\sqrt{1-\beta^2}\left(\sqrt{1-\beta^2}+\lambda_o\right)} \cdot \frac{e^{jk\tau/2\sqrt{1-\lambda_o^2}}\mathcal{G}_{1+}^{odd}\left(\sqrt{1-\beta^2}\right)}{\mathcal{G}_{2+}^{odd}\left(\sqrt{1-\beta^2}\right)\mathcal{G}_{2+}^{odd}(\lambda_o)\,\mathcal{G}_{1-}^{odd}(\lambda_o)\left\{\left[\mathcal{U}_{21}^1(1-\beta^2)\right]^2-\beta^2\left[\mathcal{U}_{22}^1(1-\beta^2)\right]^2\right\}} \quad (5.118)$$

$$C_2^{even}(\beta) = \frac{-j}{\pi}\frac{\beta^2\sqrt{1-\lambda_o^2}}{\sqrt{1-\beta^2}\left(\sqrt{1-\beta^2}+\lambda_o\right)} \cdot \frac{e^{jk\tau/2\sqrt{1-\lambda_o^2}}\mathcal{G}_{2-}^{odd}\left(\sqrt{1-\beta^2}\right)}{\mathcal{G}_{1-}^{odd}\left(\sqrt{1-\beta^2}\right)\mathcal{G}_{1-}^{odd}(\lambda_o)\,\mathcal{G}_{2+}^{odd}(\lambda_o)\left\{\left[\mathcal{U}_{21}^2(1-\beta^2)\right]^2-\beta^2\left[\mathcal{U}_{22}^2(1-\beta^2)\right]^2\right\}} \quad (5.119)$$

From (5.3) and (5.4), the modal terms (5.91) - (5.94), (5.99)-(5.102), (5.111), and (5.113) - (5.115) provide a field representation which is valid everywhere. Since the odd and even fields are decoupled, two independent representations are obtained for each of these fields.

5.3 Determination of the Constants

To determine the constants a_{mn} and b_{mn}, we may now enforce the tangential field continuity conditions

$$F\left(x=0^-,y\right) = F\left(x=0^+,y\right); \quad |y|<\tau/2 \quad (5.120)$$

$$\frac{1}{u_1(y)}\partial xF(x,y)_{x=0^-} = \frac{1}{u_2(y)}\partial xF(x,y)_{x=0^+}; \quad |y|<\tau/2 \quad (5.121)$$

with

$$u_{1,2}(y) = \begin{cases} \mu_{1,2}(y) & E_z\text{-pol} \\ \epsilon_{1,2}(y) & H_z\text{-pol} \end{cases} \quad (5.122)$$

and the subscripts 1 and 2 denoting quantities attributed to the left and right side of the slab. Substituting (5.71) - (5.72) into (5.120) and (5.121) , we obtain

$$F_{go}^{1,odd}(x=0^-,y)+F_{sw}^{1,odd}(x=0^-,y)+F_{diff}^{1,odd}(x=0^-,y)$$

$$= F_{go}^{2,odd}(x=0^+,y)+F_{sw}^{2,odd}(x=0^+,y)+F_{diff}^{2,odd}(x=0^+,y) \qquad (5.123)$$

$$\frac{1}{u_1(y)}\partial x\left[F_{go}^{1,odd}(x,y)+F_{sw}^{1,odd}(x,y)+F_{diff}^{1,odd}(x,y)\right]_{x=0^-}$$

$$= \frac{1}{u_2(y)}\partial x\left[F_{go}^{2,odd}(x,y)+F_{sw}^{2,odd}(x,y)+F_{diff}^{2,odd}(x,y)\right]_{x=0^+} \qquad (5.124)$$

$$F_{go}^{1,even}(x=0^-,y)+F_{sw}^{1,even}(x=0^-,y)+F_{diff}^{1,even}(x=0^-,y)$$

$$= F_{go}^{2,even}(x=0^+,y)+F_{sw}^{2,even}(x=0^+,y)+F_{diff}^{2,even}(x=0^+,y) \qquad (5.125)$$

$$\frac{1}{u_1(y)}\partial x\left[F_{go}^{1,even}(x,y)+F_{sw}^{1,even}(x,y)+F_{diff}^{1,even}(x,y)\right]_{x=0^-}$$

$$= \frac{1}{u_2(y)}\partial x\left[F_{go}^{2,even}(x,y)+F_{sw}^{2,even}(x,y)+F_{diff}^{2,even}(x,y)\right]_{x=0^+} \qquad (5.126)$$

to be solved for all a_{mn} and b_{mn}. In particular, for an odd GSTC of $O(N_1^{odd})$ to the left and of $O(N_2^{odd})$ to the right of the discontinuity, the number of a_{mn} to be determined is equal to

$$N_a = \frac{\widetilde{N}_{odd}\left(\widetilde{N}_{odd}-1\right)}{2} = \begin{cases} \frac{\left(N_{odd}^1+N_{odd}^2\right)\left(N_{odd}^1+N_{odd}^2-2\right)}{8}; & N_{odd}^1+N_{odd}^2 \text{ is even} \\ \frac{\left(N_{odd}^1+N_{odd}^2\right)^2-1}{8}; & N_{odd}^1+N_{odd}^2 \text{ is odd} \end{cases} \qquad (5.127)$$

To determine all a constants, (5.123) and/or (5.124) must then be enforced or sampled at a minimum of N_a points across $|y| < \tau/2$ and $0 < \phi_o < \pi$. Similarly for an even GSTC of $O(N_1^{even})$ to the left and of $O(N_2^{even})$ to the right of the discontinuity,

$$N_b = \frac{\widetilde{N}_{even}\left(\widetilde{N}_{even}-1\right)}{2} = \begin{cases} \frac{\left(N_{even}^1+N_{even}^2\right)\left(N_{even}^1+N_{even}^2-2\right)}{8}; & N_{even}^1+N_{even}^2 \text{ is even} \\ \frac{\left(N_{even}^1+N_{even}^2\right)^2-1}{8}; & N_{even}^1+N_{even}^2 \text{ is odd} \end{cases} \qquad (5.128)$$

and thus, the b constants can be determined by enforcing (5.125) and/or (5.126) at a minimum of N_b points.

Substituting for the fields in (5.123) and (5.124) as given in the previous section.

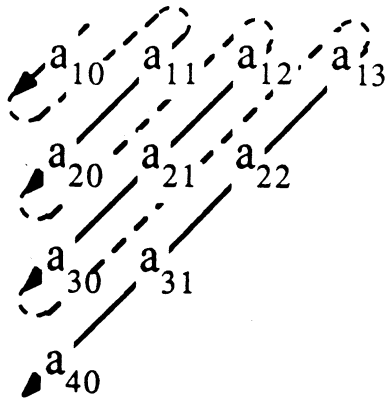

Figure 5.4: Indexing scheme for constants.

we obtain the equations

$$V_F^{odd}(\lambda_o, y) = \sum_{p=1}^{N_a} a_p Q_F^{odd}(m(p), n(p), \lambda_o, y) \tag{5.129}$$

$$V_{\partial xF}^{odd}(\lambda_o, y) = \sum_{p=1}^{N_a} a_p Q_{\partial xF}^{odd}(m(p), n(p), \lambda_o, y) \tag{5.130}$$

where $a_p = a_{m(p)n(p)}$ with

$$p = \frac{(n+m-1)(m+n)}{2} + m \tag{5.131}$$

$$m(p) = p - \frac{1}{2} Int\left\{\frac{\sqrt{1+8(p-1)}-1}{2}\right\} Int\left\{\frac{\sqrt{1+8(p-1)}+1}{2}\right\} \tag{5.132}$$

$$n(p) = Int\left\{\frac{\sqrt{1+8(p-1)}+1}{2}\right\} - m(p) \tag{5.133}$$

which are in accordance with the ordering of the a_{mn} constants as the order of the GSTC is increased (see Figure 5.4). Also,

$$\begin{aligned} V_F^{odd}(\lambda_o, y) = {} & A_1^{odd}(\lambda_o)\,\Psi_1^{odd}\left(\lambda_o^2, y\right) - A_2^{odd}(\lambda_o)\,\Psi_2^{odd}\left(\lambda_o^2, y\right) \\ & + \sum_{l=1}^{N_{sw}^{1,odd}} B_l^{1,odd}(\lambda_o)\, Z_{odd}\left(-\lambda\lambda_l^{1,odd}\right) \Psi_1^{odd}\left(\left[\lambda_l^{1,odd}\right]^2, y\right) \\ & - \sum_{l=1}^{N_{sw}^{2,odd}} B_l^{2,odd}(\lambda_o)\, Z_{odd}\left(-\lambda\lambda_l^{2,odd}\right) \Psi_2^{odd}\left(\left[\lambda_l^{2,odd}\right]^2, y\right) \end{aligned}$$

$$
\begin{aligned}
&+\int_0^\infty C_1^{odd}(\beta)\, Z_{odd}\left(-\sqrt{1-\beta^2}\lambda_o\right)\Psi_1^{odd}\left(1-\beta^2,y\right)d\beta \\
&-\int_0^\infty C_2^{odd}(\beta)\, Z_{odd}\left(-\sqrt{1-\beta^2}\lambda_o\right)\Psi_2^{odd}\left(1-\beta^2,y\right)d\beta \qquad (5.134)
\end{aligned}
$$

$$
\begin{aligned}
V_{\partial xF}^{odd}(\lambda_o,y) \;=\;& \frac{\lambda_o A_1^{odd}(\lambda_o)}{u_1(y)}\Psi_1^{odd}\left(\lambda_o^2,y\right)-\frac{\lambda_o A_2^{odd}(\lambda_o)}{u_2(y)}\Psi_2^{odd}\left(\lambda_o^2,y\right) \\
&-\sum_{l=1}^{N_{sw}^{1,odd}}\frac{\lambda_l^{1,odd}B_l^{1,odd}(\lambda_o)}{u_1(y)}Z_{odd}\left(-\lambda\lambda_l^{1,odd}\right)\Psi_1^{odd}\left(\left[\lambda_l^{1,odd}\right]^2,y\right) \\
&+\sum_{l=1}^{N_{sw}^{2,odd}}\frac{\lambda_l^{2,odd}B_l^{2,odd}(\lambda_o)}{u_2(y)}Z_{odd}\left(-\lambda\lambda_l^{2,odd}\right)\Psi_2^{odd}\left(\left[\lambda_l^{2,odd}\right]^2,y\right) \\
&-\int_0^\infty\frac{\sqrt{1-\beta^2}C_1^{odd}(\beta)}{u_1(y)}Z_{odd}\left(-\sqrt{1-\beta^2}\lambda_o\right)\Psi_1^{odd}\left(1-\beta^2,y\right)d\beta \\
&+\int_0^\infty\frac{\sqrt{1-\beta^2}C_2^{odd}(\beta)}{u_2(y)}Z_{odd}\left(-\sqrt{1-\beta^2}\lambda_o\right)\Psi_2^{odd}\left(1-\beta^2,y\right)d\beta
\end{aligned}
\qquad (5.135)
$$

and

$$
\begin{aligned}
&Q_F^{odd}(m,n,\lambda_o,y) \\
&-\sum_{l=1}^{N_{sw}^{1,odd}}B_l^{1,odd}(\lambda_o)\left(\lambda_o+\lambda_l^{1,odd}\right)^m\left(\lambda_o\lambda_l^{1,odd}\right)^n\Psi_1^{odd}\left(\left[\lambda_l^{1,odd}\right]^2,y\right) \\
&+\sum_{l=1}^{N_{sw}^{2,odd}}B_l^{2,odd}(\lambda_o)\left(\lambda_o+\lambda_l^{2,odd}\right)^m\left(\lambda_o\lambda_l^{2,odd}\right)^n\Psi_2^{odd}\left(\left[\lambda_l^{2,odd}\right]^2,y\right) \\
&-\int_0^\infty C_1^{odd}(\beta)\left(\sqrt{1-\beta^2}+\lambda_o\right)^m\left(\sqrt{1-\beta^2}\lambda_o\right)^n\Psi_1^{odd}\left(1-\beta^2,y\right)d\beta \\
&+\int_0^\infty C_2^{odd}(\beta)\left(\sqrt{1-\beta^2}+\lambda_o\right)^m\left(\sqrt{1-\beta^2}\lambda_o\right)^n\Psi_2^{odd}\left(1-\beta^2,y\right)d\beta \qquad (5.136)
\end{aligned}
$$

$$
\begin{aligned}
&Q_{\partial xF}^{odd}(\lambda_o,y) \;= \\
&\sum_{l=1}^{N_{sw}^{1,odd}}\frac{\lambda_l^{1,odd}B_l^{1,odd}(\lambda_o)}{u_1(y)}\left(\lambda_o+\lambda_l^{1,odd}\right)^m\left(\lambda_o\lambda_l^{1,odd}\right)^n\Psi_1^{odd}\left(\left[\lambda_l^{1,odd}\right]^2,y\right) \\
&-\sum_{l=1}^{N_{sw}^{2,odd}}\frac{\lambda_l^{2,odd}B_l^{2,odd}(\lambda_o)}{u_2(y)}\left(\lambda_o+\lambda_l^{2,odd}\right)^m\left(\lambda_o\lambda_l^{2,odd}\right)^n\Psi_2^{odd}\left(\left[\lambda_l^{2,odd}\right]^2,y\right) \\
&+\int_0^\infty\frac{\sqrt{1-\beta^2}C_1^{odd}(\beta)}{u_1(y)}\left(\sqrt{1-\beta^2}+\lambda_o\right)^m\left(\sqrt{1-\beta^2}\lambda_o\right)^n\Psi_1^{odd}\left(1-\beta^2,y\right)d\beta \\
&-\int_0^\infty\frac{\sqrt{1-\beta^2}C_2^{odd}(\beta)}{u_2(y)}\left(\sqrt{1-\beta^2}+\lambda_o\right)^m\left(\sqrt{1-\beta^2}\lambda_o\right)^n\Psi_2^{odd}\left(1-\beta^2,y\right)d\beta
\end{aligned}
\qquad (5.137)
$$

Provided $N_{1,2}^{odd}$ are even, the integrals in (5.135) and (5.137) converge (see Table 5.1) and (5.129) - (5.130) can be solved for the constants a_p by matching (5.129) at N_{a1} points and (5.130) at N_{a2} points such that $N_{a1} + N_{a2} \geq N_a$.

To solve for the b_p constants we substitute for the fields in (5.125) and/or (5.126), giving

$$V_F^{even}(\lambda_o, y) = \sum_{\tilde{p}=1}^{N_b} b_p Q_F^{even}(m(p), n(p), \lambda_o, y) \tag{5.138}$$

$$V_{\partial xF}^{even}(\lambda_o, y) = \sum_{\tilde{p}=1}^{N_b} b_p Q_{\partial xF}^{even}(m(p), n(p), \lambda_o, y) \tag{5.139}$$

with

$$\begin{aligned} V_F^{even}(\lambda_o, y) &= A_1^{even}(\lambda_o)\,\Psi_1^{even}\left(\lambda_o^2, y\right) - A_2^{even}(\lambda_o)\,\Psi_2^{even}\left(\lambda_o^2, y\right) \\ &+ \sum_{l=1}^{N_{sw}^{1,even}} B_l^{1,even}(\lambda_o)\, Z_{even}\left(-\lambda\lambda_l^{1,even}\right) \Psi_1^{even}\left(\left[\lambda_l^{1,even}\right]^2, y\right) \\ &- \sum_{l=1}^{N_{sw}^{2,even}} B_l^{2,even}(\lambda_o)\, Z_{even}\left(-\lambda\lambda_l^{2,even}\right) \Psi_2^{even}\left(\left[\lambda_l^{2,even}\right]^2, y\right) \\ &+ \int_0^\infty C_1^{even}(\beta)\, Z_{even}\left(-\sqrt{1-\beta^2}\lambda_o\right) \Psi_1^{even}\left(1-\beta^2, y\right) d\beta \\ &- \int_0^\infty C_2^{even}(\beta)\, Z_{even}\left(-\sqrt{1-\beta^2}\lambda_o\right) \Psi_2^{even}\left(1-\beta^2, y\right) d\beta \end{aligned} \tag{5.140}$$

$$\begin{aligned} V_{\partial xF}^{even}(\lambda_o, y) &= \frac{\lambda_o A_1^{even}(\lambda_o)}{u_1(y)} \Psi_1^{even}\left(\lambda_o^2, y\right) - \frac{\lambda_o A_2^{even}(\lambda_o)}{u_2(y)} \Psi_2^{even}\left(\lambda_o^2, y\right) \\ &- \sum_{l=1}^{N_{sw}^{1,even}} \frac{\lambda_l^{1,even} B_l^{1,even}(\lambda_o)}{u_1(y)} Z_{even}\left(-\lambda\lambda_l^{1,even}\right) \Psi_1^{even}\left(\left[\lambda_l^{1,even}\right]^2, y\right) \\ &+ \sum_{l=1}^{N_{sw}^{2,even}} \frac{\lambda_l^{2,even} B_l^{2,even}(\lambda_o)}{u_2(y)} Z_{even}\left(-\lambda\lambda_l^{2,even}\right) \Psi_2^{even}\left(\left[\lambda_l^{2,even}\right]^2, y\right) \\ &- \int_0^\infty \frac{\sqrt{1-\beta^2} C_1^{even}(\beta)}{u_1(y)} Z_{even}\left(-\sqrt{1-\beta^2}\lambda_o\right) \Psi_1^{even}\left(1-\beta^2, y\right) d\beta \\ &+ \int_0^\infty \frac{\sqrt{1-\beta^2} C_2^{even}(\beta)}{u_2(y)} Z_{even}\left(-\sqrt{1-\beta^2}\lambda_o\right) \Psi_2^{even}\left(1-\beta^2, y\right) d\beta \end{aligned} \tag{5.141}$$

and

$$Q_F^{even}(\lambda_o, y) =$$

N_1^{odd} or N_1^{even}	N_2^{odd} or N_2^{even}	Junction Field	Branch cut integral (odd or even)	Order of branch cut integrand
even	even	E_z or H_z	$F^1_{diff}(x=0^-,y)$	$\|\beta\|^{-3}$
			$F^2_{diff}(x=0^+,y)$	$\|\beta\|^{-3}$
odd	odd	E_z or H_z	$F^1_{diff}(x=0^-,y)$	$\|\beta\|^{-2}$
			$F^2_{diff}(x=0^+,y)$	$\|\beta\|^{-2}$
even	odd	E_z or H_z	$F^1_{diff}(x=0^-,y)$	$\|\beta\|^{-5/2}$
			$F^2_{diff}(x=0^+,y)$	$\|\beta\|^{-3/2}$
odd	even	E_z or H_z	$F^1_{diff}(x=0^-,y)$	$\|\beta\|^{-3/2}$
			$F^2_{diff}(x=0^+,y)$	$\|\beta\|^{-5/2}$
even	even	H_y or E_y	$F^1_{diff}(x=0^-,y)$	$\|\beta\|^{-2}$
			$F^2_{diff}(x=0^+,y)$	$\|\beta\|^{-2}$
odd	odd	H_y or E_y	$F^1_{diff}(x=0^-,y)$	$\|\beta\|^{-1}$
			$F^2_{diff}(x=0^+,y)$	$\|\beta\|^{-1}$
even	odd	H_y or E_y	$F^1_{diff}(x=0^-,y)$	$\|\beta\|^{-3/2}$
			$F^2_{diff}(x=0^+,y)$	$\|\beta\|^{-1/2}$
odd	even	H_y or E_y	$F^1_{diff}(x=0^-,y)$	$\|\beta\|^{-1/2}$
			$F^2_{diff}(x=0^+,y)$	$\|\beta\|^{-3/2}$

Table 5.1: Asymptotic behavior of integrand for the functions $F_{diff}(x=0^{\pm},y)$.

$$
\begin{aligned}
&- \sum_{l=1}^{N_{sw}^{1,even}} B_l^{1,even}(\lambda_o)\left(\lambda_o+\lambda_l^{1,even}\right)^m\left(\lambda_o\lambda_l^{1,even}\right)^n \Psi_1^{even}\left(\left[\lambda_l^{1,even}\right]^2, y\right) \\
&+ \sum_{l=1}^{N_{sw}^{2,even}} B_l^{2,even}(\lambda_o)\left(\lambda_o+\lambda_l^{2,even}\right)^m\left(\lambda_o\lambda_l^{2,even}\right)^n \Psi_2^{even}\left(\left[\lambda_l^{2,even}\right]^2, y\right) \\
&- \int_0^{\infty} C_1^{even}(\beta)\left(\sqrt{1-\beta^2}+\lambda_o\right)^m\left(\sqrt{1-\beta^2}\lambda_o\right)^n \Psi_1^{even}\left(1-\beta^2, y\right) d\beta \\
&+ \int_0^{\infty} C_2^{even}(\beta)\left(\sqrt{1-\beta^2}+\lambda_o\right)^m\left(\sqrt{1-\beta^2}\lambda_o\right)^n \Psi_2^{even}\left(1-\beta^2, y\right) d\beta
\end{aligned} \tag{5.142}
$$

$$
\begin{aligned}
&Q_{\partial xF}^{even}(\lambda_o, y) \;=\; \\
&\sum_{l=1}^{N_{sw}^{1,even}} \frac{\lambda_l^{1,even} B_l^{1,even}(\lambda_o)}{u_1(y)}\left(\lambda_o+\lambda_l^{1,even}\right)^m\left(\lambda_o\lambda_l^{1,even}\right)^n \Psi_1^{even}\left(\left[\lambda_l^{1,even}\right]^2, y\right) \\
&- \sum_{l=1}^{N_{sw}^{2,even}} \frac{\lambda_l^{2,even} B_l^{2,even}(\lambda_o)}{u_2(y)}\left(\lambda_o+\lambda_l^{2,even}\right)^m\left(\lambda_o\lambda_l^{2,even}\right)^n \Psi_2^{even}\left(\left[\lambda_l^{2,even}\right]^2, y\right) \\
&+ \int_0^{\infty} \frac{\sqrt{1-\beta^2} C_1^{even}(\beta)}{u_1(y)}\left(\sqrt{1-\beta^2}+\lambda_o\right)^m\left(\sqrt{1-\beta^2}\lambda_o\right)^n \Psi_1^{even}\left(1-\beta^2, y\right) d\beta \\
&- \int_0^{\infty} \frac{\sqrt{1-\beta^2} C_2^{even}(\beta)}{u_2(y)}\left(\sqrt{1-\beta^2}+\lambda_o\right)^m\left(\sqrt{1-\beta^2}\lambda_o\right)^n \Psi_2^{even}\left(1-\beta^2, y\right) d\beta
\end{aligned} \tag{5.143}
$$

As before $b_p = b_{m(p)n(p)}$ with p, $m(p)$, and $n(p)$ given in (5.131)-(5.133). Again, provided $N_{1,2}^{even}$ are even, the integrals in (5.141) and (5.143) converge and (5.138) - (5.139) can be solved for the constants b_p by matching (5.138) at N_{b1} points and (5.139) at N_{b2} points such that $N_{b1} + N_{b2} \geq N_b$. Results based on the solution of (5.129) - (5.130) and (5.138) - (5.139) are considered next.

5.4 Validation of the Solution

In this section we address the validation of the GSTC solution. In particular, several diffraction patterns are presented for selected material junctions and these are compared with data obtained by other means. Issues related to the numerical implementation are also discussed, including those pertaining to the convergence of the solution and sampling criteria. Finally, some family curves are given for selected

junction geometries in which the slab thickness is varied.

Figures 5.5, 5.6, and 5.7 present the echowidth of several recessed slab geometries. These results were computed with the GSMF-GIBC solution of chapter three and the more general GIBC solution of chapters four and five. The slab having $\tau = .04$, $\epsilon = 2$, $\mu = 1.2$ (see Figure 5.5) may be adequately simulated by a low contrast second order GIBC, whose solution is distinguished by the presence of a single unknown constant b_{10}. The computed value of this constant is given in Tables 5.2 and 5.3, which also contain the values of the constants pertaining the simulations given in Figures 5.5 to 5.14. It is observed that the constants predicted by the GIBC and GIBC-GSMF solutions are practically identical, and the corresponding diffraction curves overlay one another for the PEC stub case as well as the PMC stub case.

The solution constants for the GIBC solution corresponding to the PEC stub were determined by applying the boundary condition $E_y = 0$ at the junction. In particular it was found that a satisfactory solution for b_{10} could be obtained by enforcing this condition at a single point along the junction and for a single angle of incidence. The nearly-exact values in Table 5.2 result from enforcing the vanishing electric field at a single junction point for four distinct angles of incidence. We remark that there is no need for additional sampling points along the junction, since the interior Ψ function is constant with respect to y for a second order low contrast GIBC. A question may arrise, however, as to why it is desirable to sample at a greater number of sampling points than the number of unknowns. This is because the GIBC solution should ideally satisfy the boundary condition over all angles of incidence and at all points on the junction. Hence by using a sampling grid which spans the junction, it is possible to obtain a solution which satisfies the boundary conditions across the junction in an average sense. Once the overdetermined system is generated, a

solution for the constant(s) may be obtained by standard least-squares techniques.

With regard to the computation of the field quantities at the edge, care must be exercised in evaluating the branch cut integrals. As seen from Table 5.1, the convergence of these integrals is not always guaranteed, since the integrand must have an asymptotic behavior of $|\lambda|^{-1-\delta}$ with $\delta > 0$. It may then be deduced from Table 5.1 that one cannot match E_y or H_y at the junction unless the order of all GIBC/GSTC for finitely-conducting bodies is even. We remark, however, that although the branch cut integrals for the PEC and PMC cases above always converge (they behave asymptotically as $|\lambda|^{-3/2}$ and $|\lambda|^{-5/2}$ respectively), their evaluation is not trivial by virtue of the infinite limits of integration. Herewith the infinite interval is transformed to a finite one. In addition, in case of a pole near the integration path, the addition and subtraction process described in [51] is employed to regularize the integrand.

In Figure 5.6, the slab thickness is increased to $.1\lambda$ and it is now seen that fourth order conditions are required, resulting in three constants to be determined. It is found that nearly 12 junction constraints are needed to adequately specify the constants by enforcing field continuity at three points across the junction for four angles of incidence. The agreement between the GIBC, GIBC-GSMF, and GSMF-exact are excellent, and the same is, of course, true for the GIBC and GIBC-GSMF constants (see Table 5.2). Note that the error in setting the constants to zero in this case is significant. The final recessed slab geometry has $\tau = .4$, $\epsilon = 5$, $\mu = 3$ modeled by second order high contrast GIBCs. Again all solutions agree quite well as do the values of the constant b_{10} as given in Table 5.2.

Figures 5.8 to 5.14 present diffraction patterns for material half-planes of increasing thickness and are compared to data from a numerical model. The numerical

model was constructed by first generating the transient response of a finite length slab using bandlimited frequency domain data. The contribution from the half-plane edge was then extracted by time gating the transient response. This numerical model is valid except near grazing, where the surface wave and ray field excited by the back edge arrives at the front edge in concert with the incident plane wave. Figures 5.8 to 5.11 present the echowidth for low contrast simulations of a half-plane having $\epsilon = 2$, $\mu = 1.2$. Clearly, the agreement between the numerical data and GSTC solution is excellent. The reader should also note the small values obtained for the constants as the thickness tends to zero, and this is in agreement with the second order GSTC solutions proposed in [53] and [54]. However, for thicker half-planes the constant plays a more significant role as evidenced by the erroneous result predicted in Figure 5.11 when the constants are set to zero.

Data based on two high contrast simulations are presented in Figures 5.12 and 5.13 for a material half plane having $\epsilon = 5$ and $\mu = 3$. Because of the higher sampling required, numerical results could only be furnished for a thickness of up to $.05\lambda$ (see Figure 5.13). We observe that the results for the $.01\lambda$ thick half-plane given in Figure 5.12 are in agreement and the same is generally true for the curves in Figure 5.13 despite the obvious instabilities of the numerical data. In Figure 5.14 a GSTC simulation is constructed for a two layer half-plane having $\tau_1 = .005$, $\epsilon_1 = 5$, $\mu_1 = 3$ and $\tau_2 = .03$, $\epsilon_2 = 2$, $\mu_2 = 1.2$. The agreement of the GSTC solution with the numerical data is quite good except at edge on incidence, and judging by the abnormal behavior of the numerical data in this region it is conjectured that these data are in error.

Finally, in Figures 5.16 to 5.21, family curves are given for various half-planes and grounded junctions. These are limited in thickness by computational restric-

tions stemming from the rapid increase in the number of constants as the order is increased, and additionally from the numerical intensiveness of the routine which determines the unknown constants. It is, therefore, necessary that the proper order (the one providing adequate simulation and converged results) of the GSTC be determined beforehand. This can be generally found by leaving out the constants and computing the diffraction coefficient for increasing order of GSTC until convergence is reached. The constants can then be determined for the order of the GSTC rendering convergence. This procedure was found quite adequate and was employed to generate the data in Figures 5.15 to 5.21.

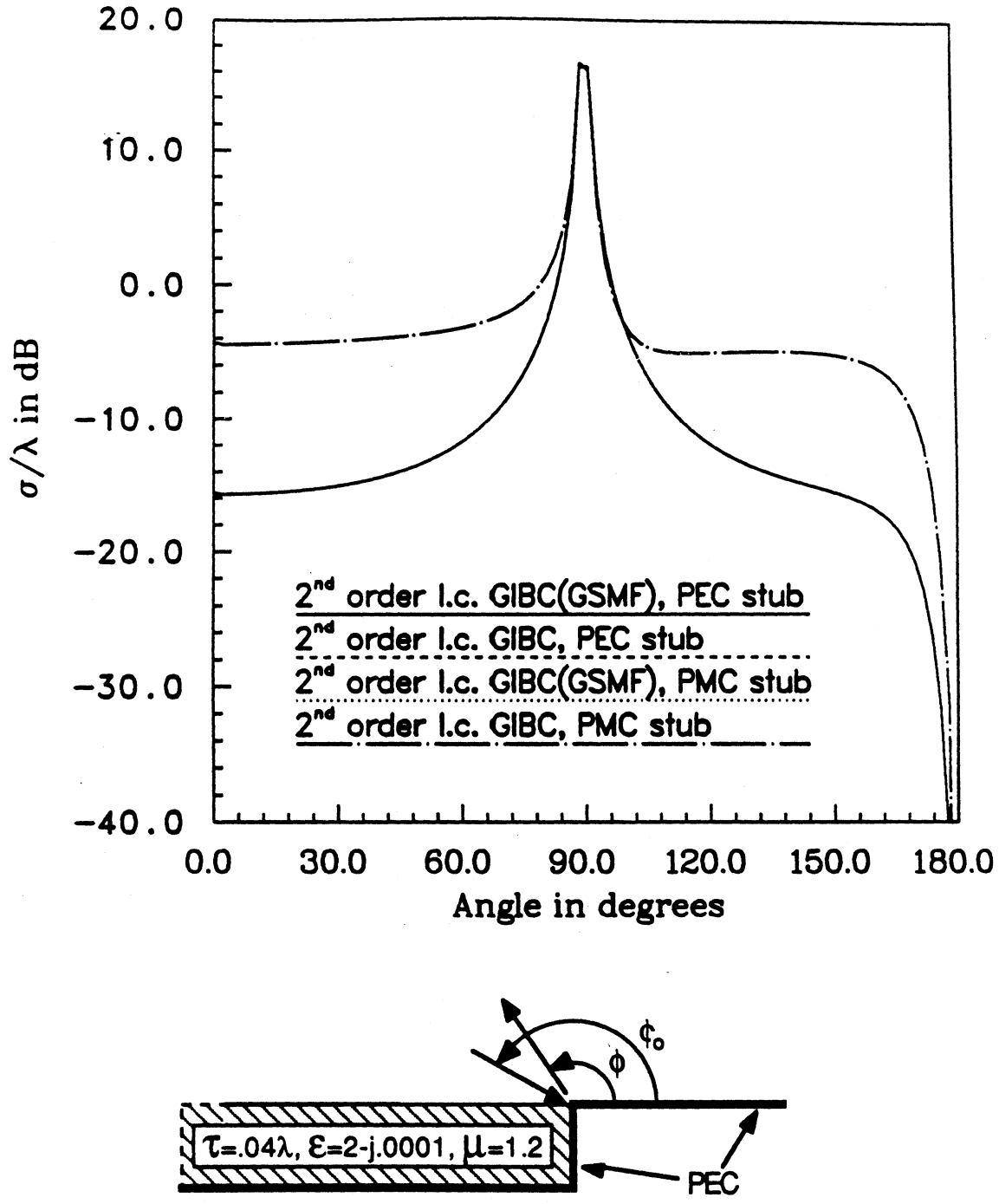

Figure 5.5: H_z polarization backscatter echo width for a recessed slab with $\tau = .4$, $\epsilon = 2$, $\mu = 1.2$ modeled by $O(\tau)$ second order low contrast GIBC (see Table 5.2 for constants).

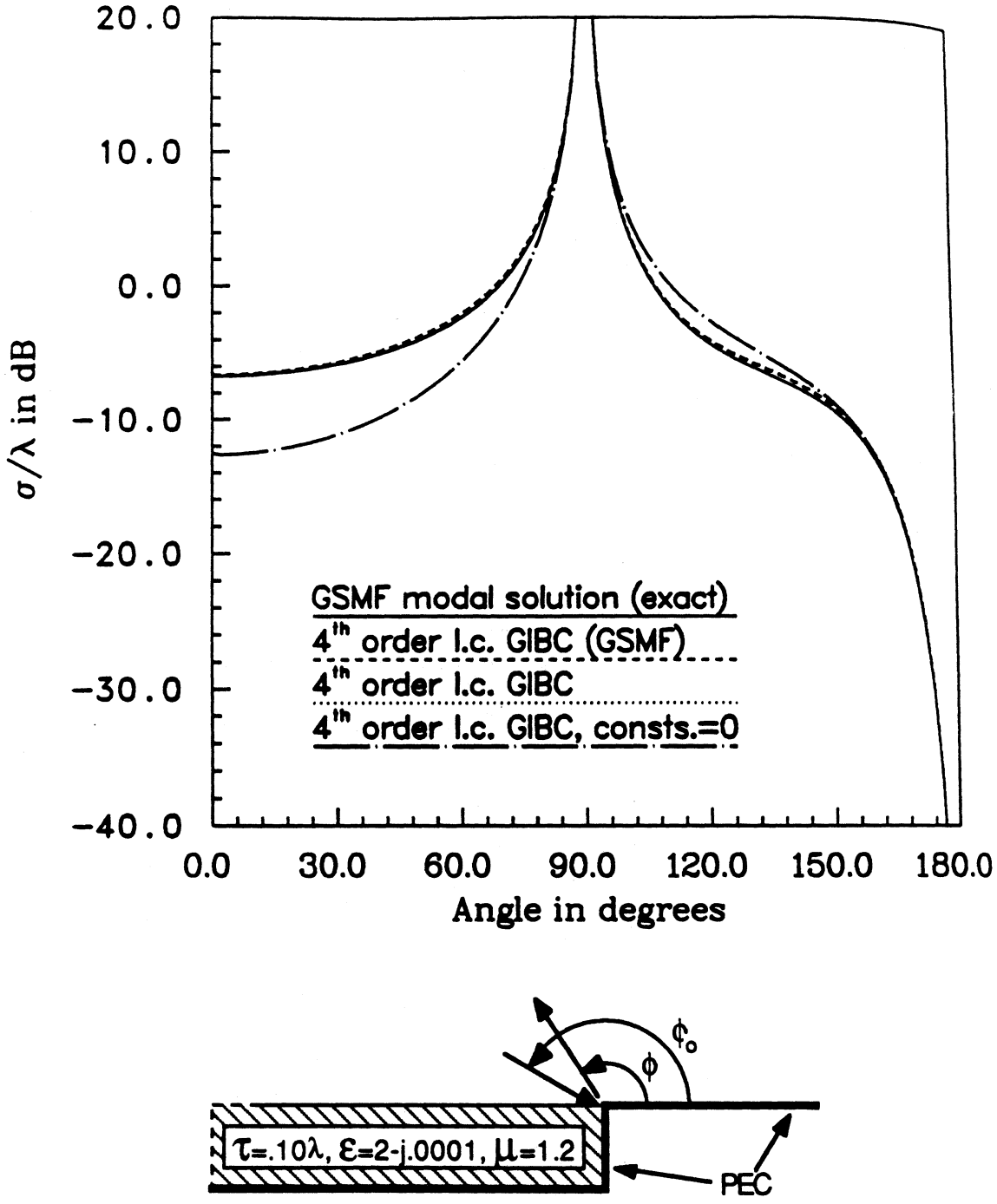

Figure 5.6: H_z polarization backscatter echo width for a recessed slab with $\tau = .1$, $\epsilon = 2$, $\mu = 1.2$ modeled by $O(\tau^3)$ fourth order low contrast GIBC (see Table 5.2 for constants).

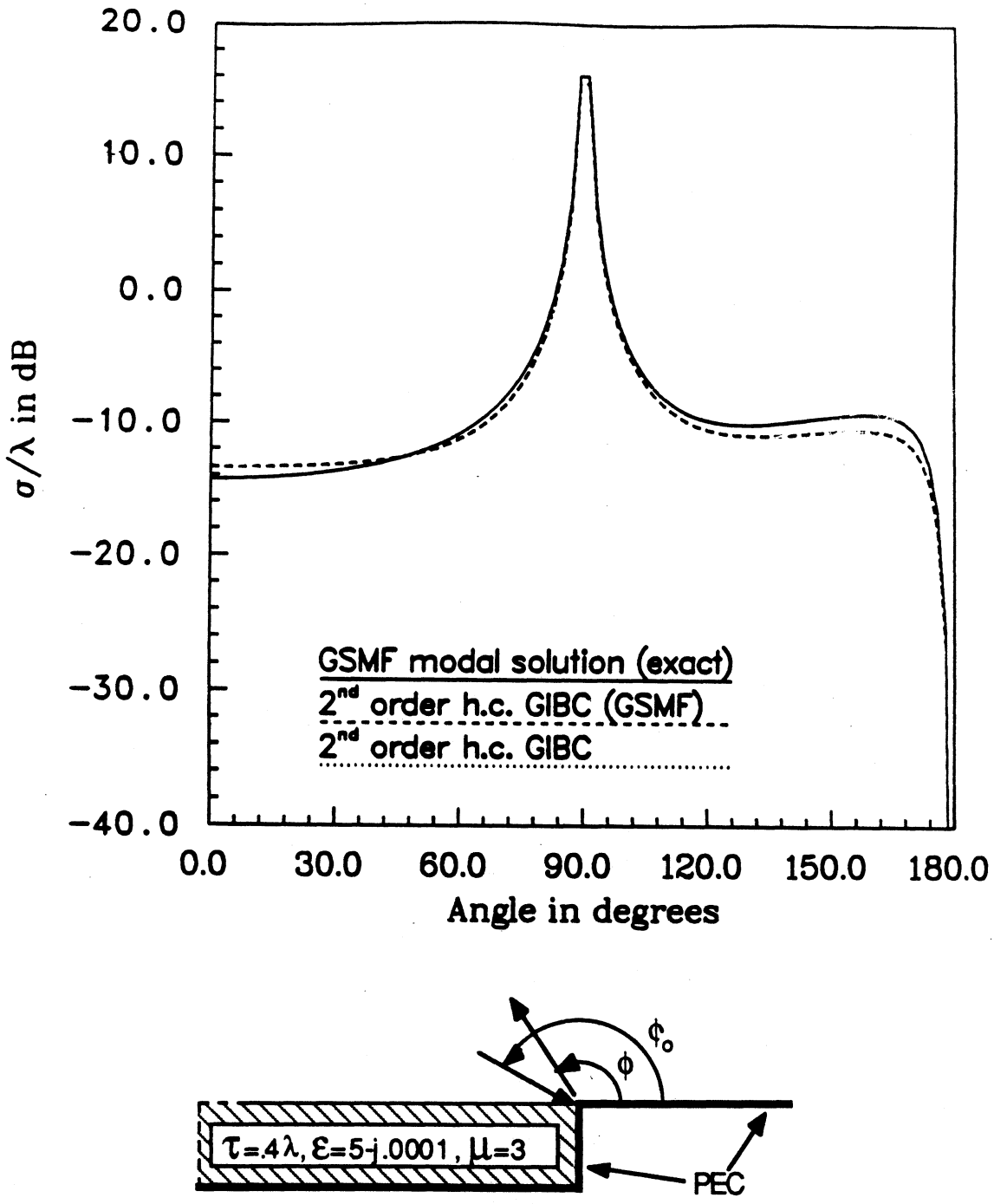

Figure 5.7: H_z polarization backscatter echo width for a recessed slab with $\tau = .4$, $\epsilon = 5$, $\mu = 3$ modeled by $O(\kappa^{-1})$ second order high contrast GIBC (see Table 5.2 for constants).

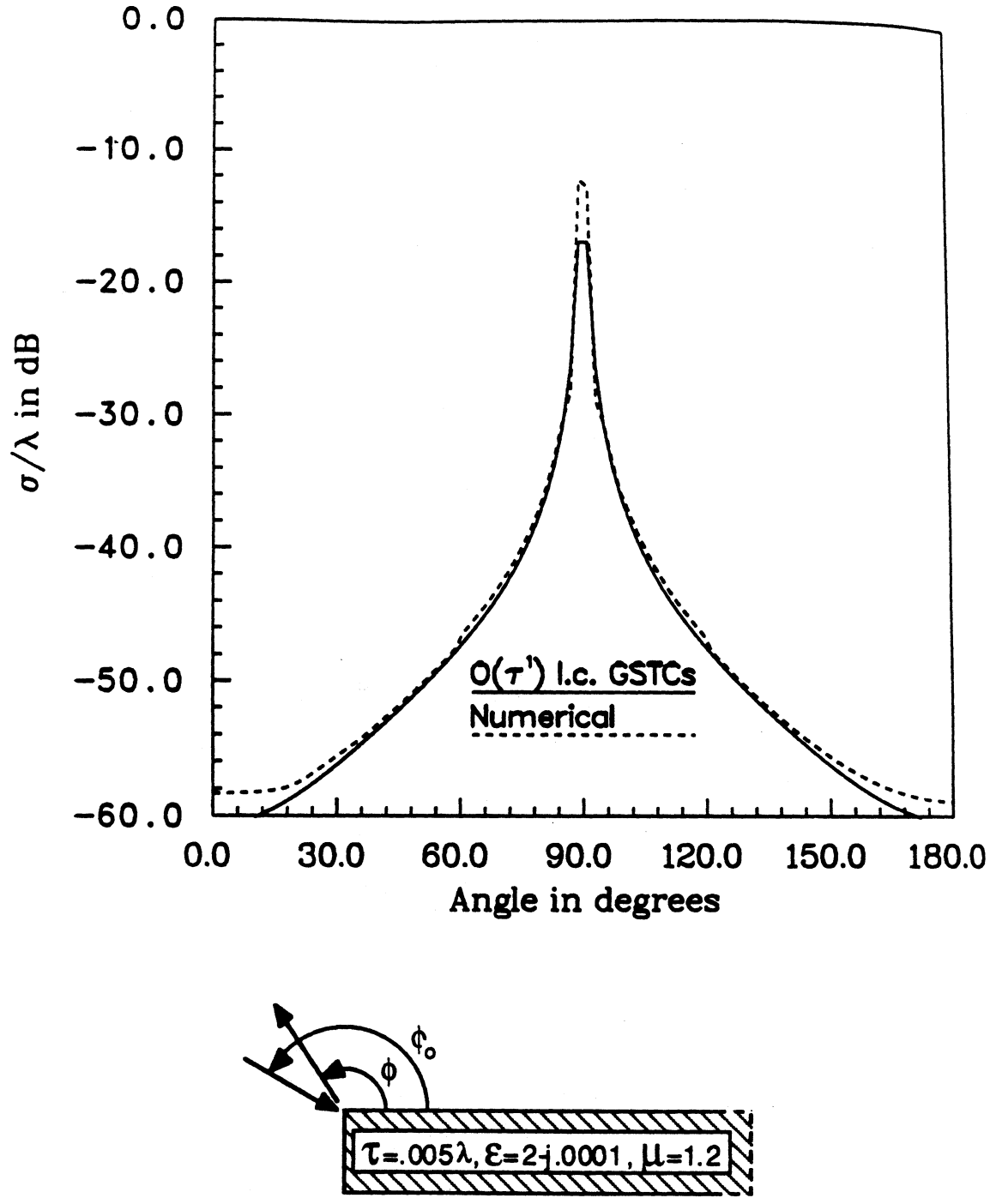

Figure 5.8: H_z polarization backscatter echo width for a material half-plane with $\tau = .005$, $\epsilon = 2$, $\mu = 1.2$ modeled by $O(\tau)$ low contrast GSTC (see Table 5.2 for constants).

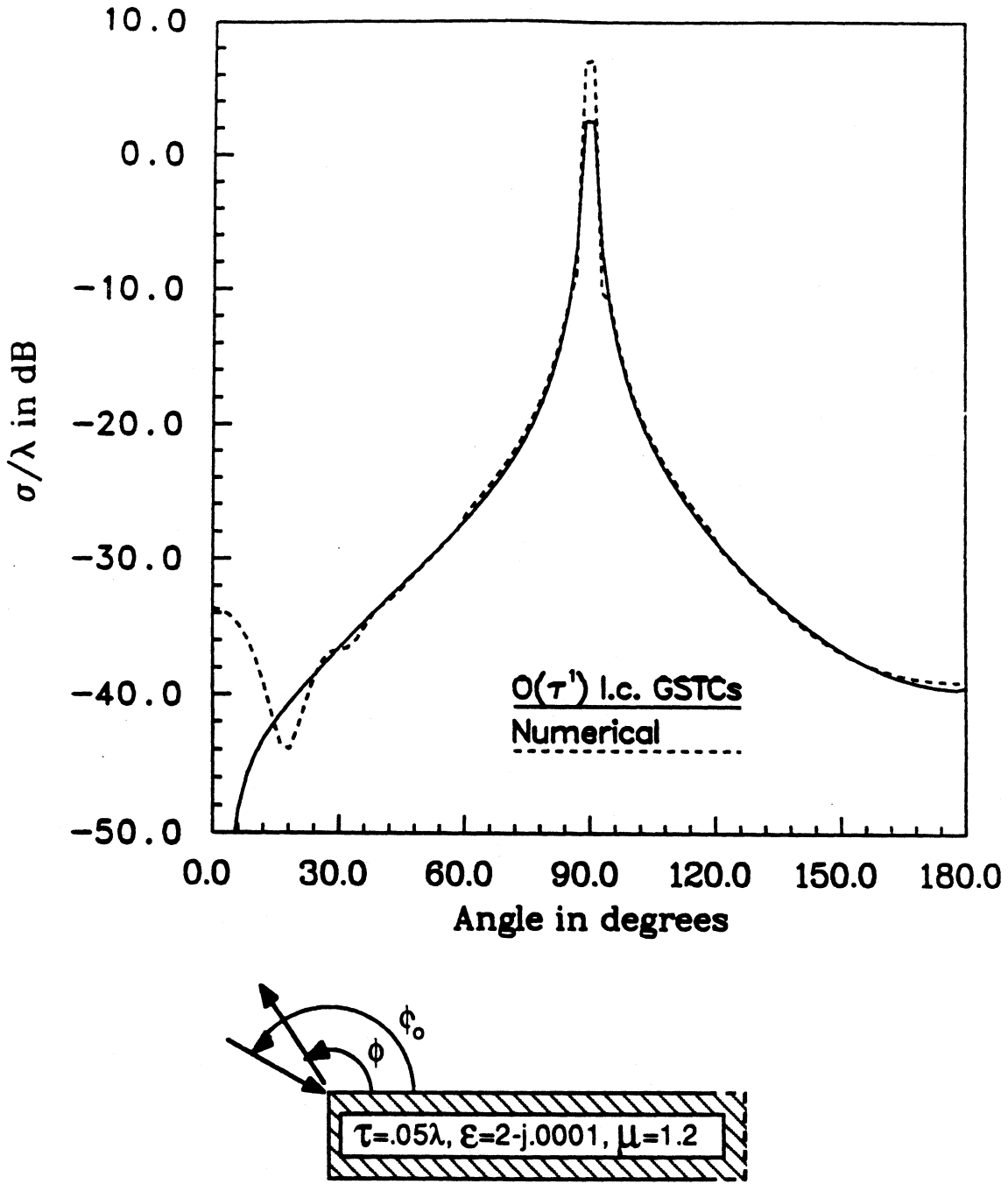

Figure 5.9: H_z polarization backscatter echo width for a material half-plane with $\tau = .05$, $\epsilon = 2$, $\mu = 1.2$ modeled by $O(\tau)$ low contrast GSTC (see Table 5.2 for constants).

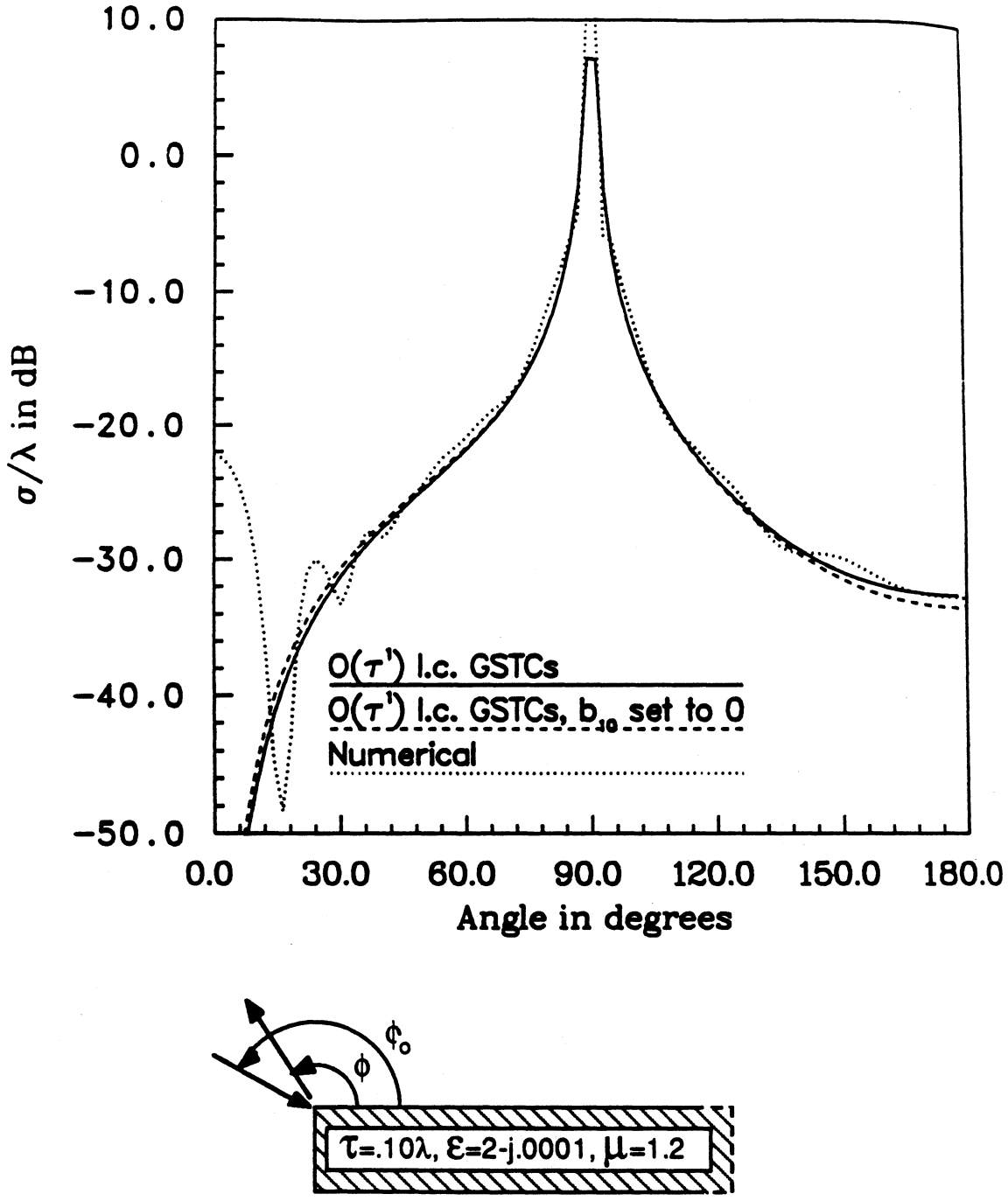

Figure 5.10: H_z polarization backscatter echo width for a material half-plane with $\tau = .10$, $\epsilon = 2$, $\mu = 1.2$ modeled by $O(\tau)$ low contrast GSTC (see Table 5.2 for constants).

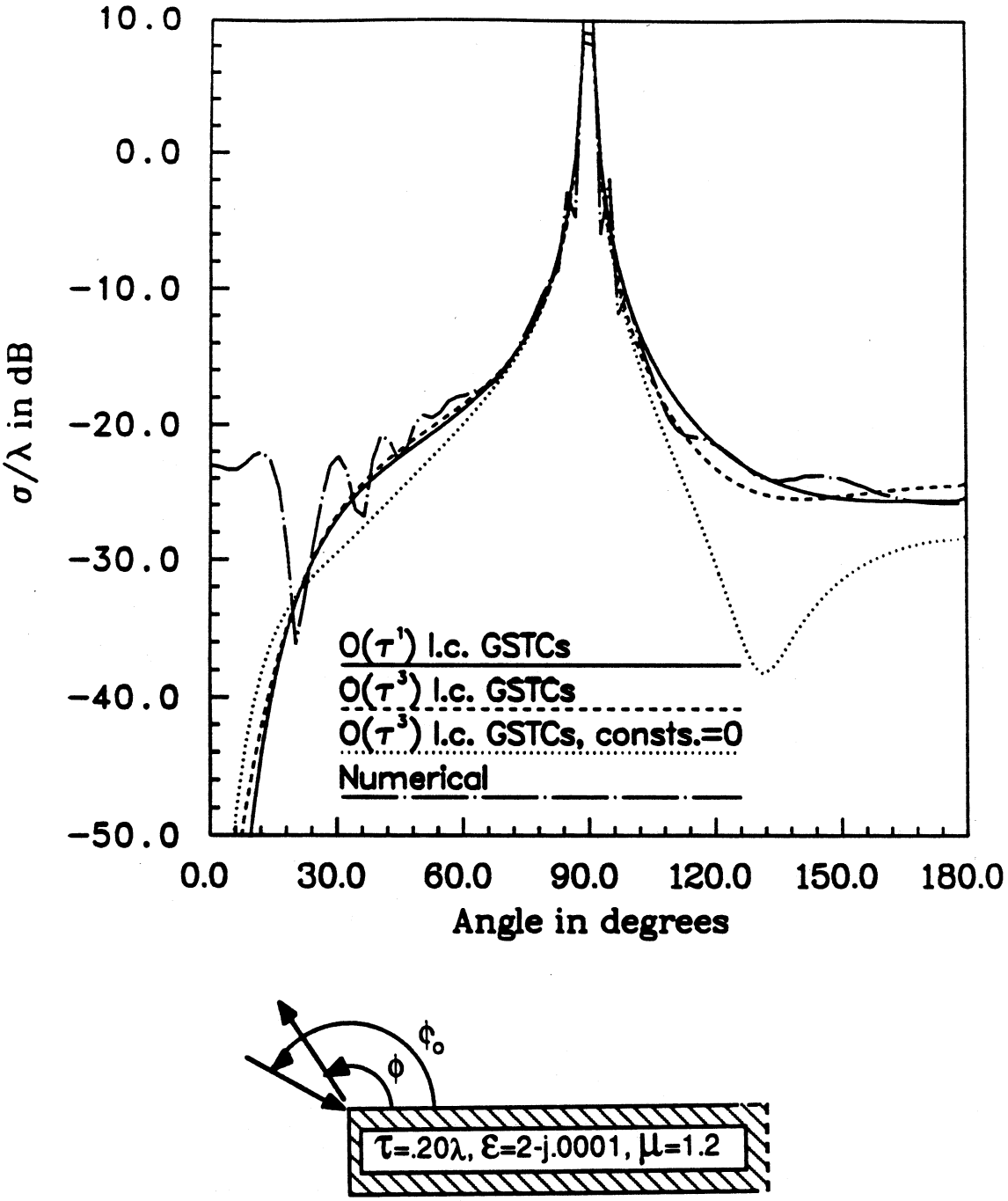

Figure 5.11: H_z polarization backscatter echo width for a material half-plane with $\tau = .20$, $\epsilon = 2$, $\mu = 1.2$ modeled by $O(\tau)$ and $O(\tau^3)$ low contrast GSTC (see Table 5.2 for constants).

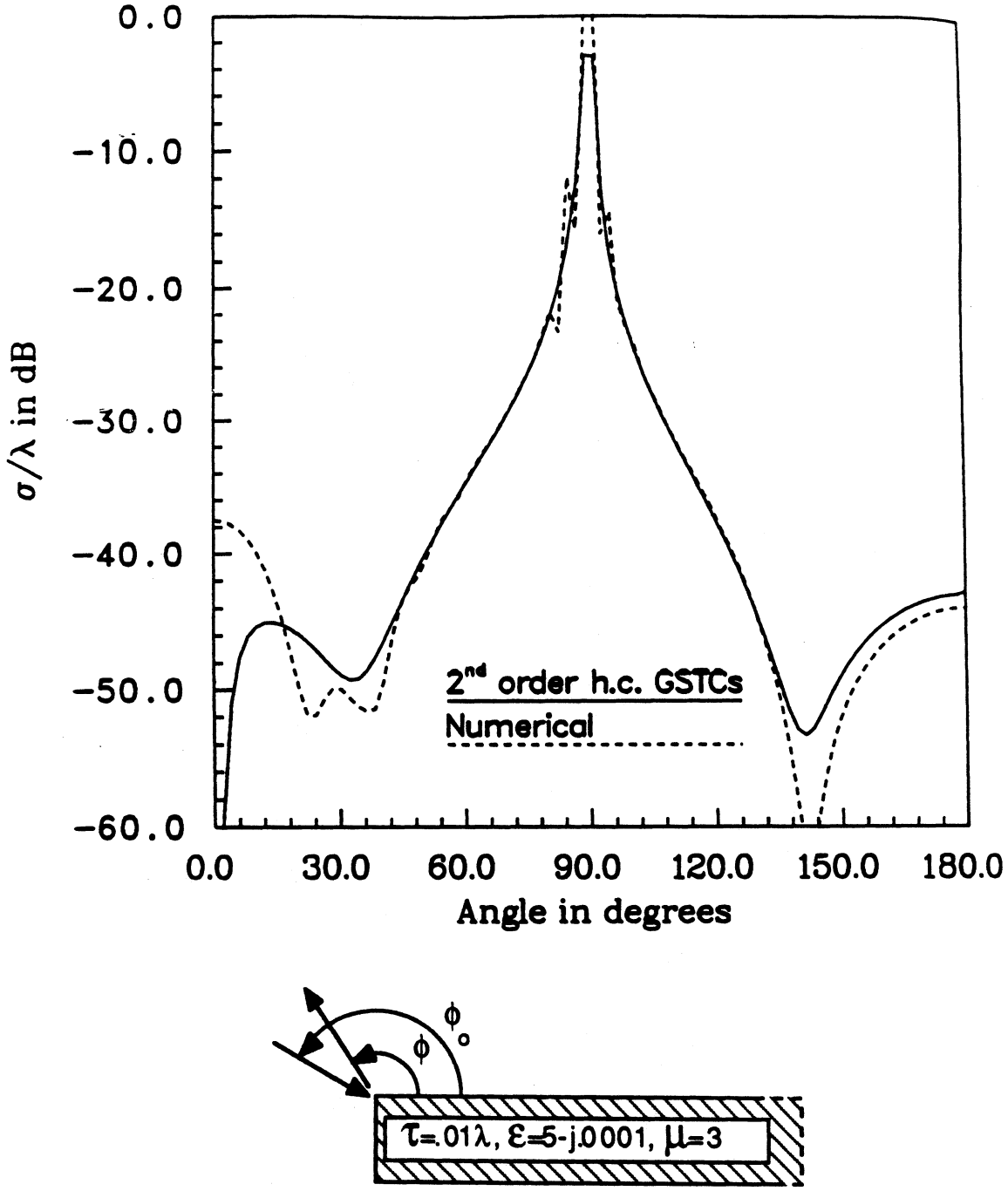

Figure 5.12: H_z polarization backscatter echo width for a material half-plane with $\tau = .01$, $\epsilon = 5$, $\mu = 3$ modeled by $O(\kappa^0)$ (even symmetry) and $O(\kappa^{-1})$ (odd symmetry) high contrast GSTC. The free space side is modeled by $O(\tau)$ (even symmetry) $O(\tau^2)$ (odd symmetry) low contrast GSTC. (see Table 5.3 for constants).

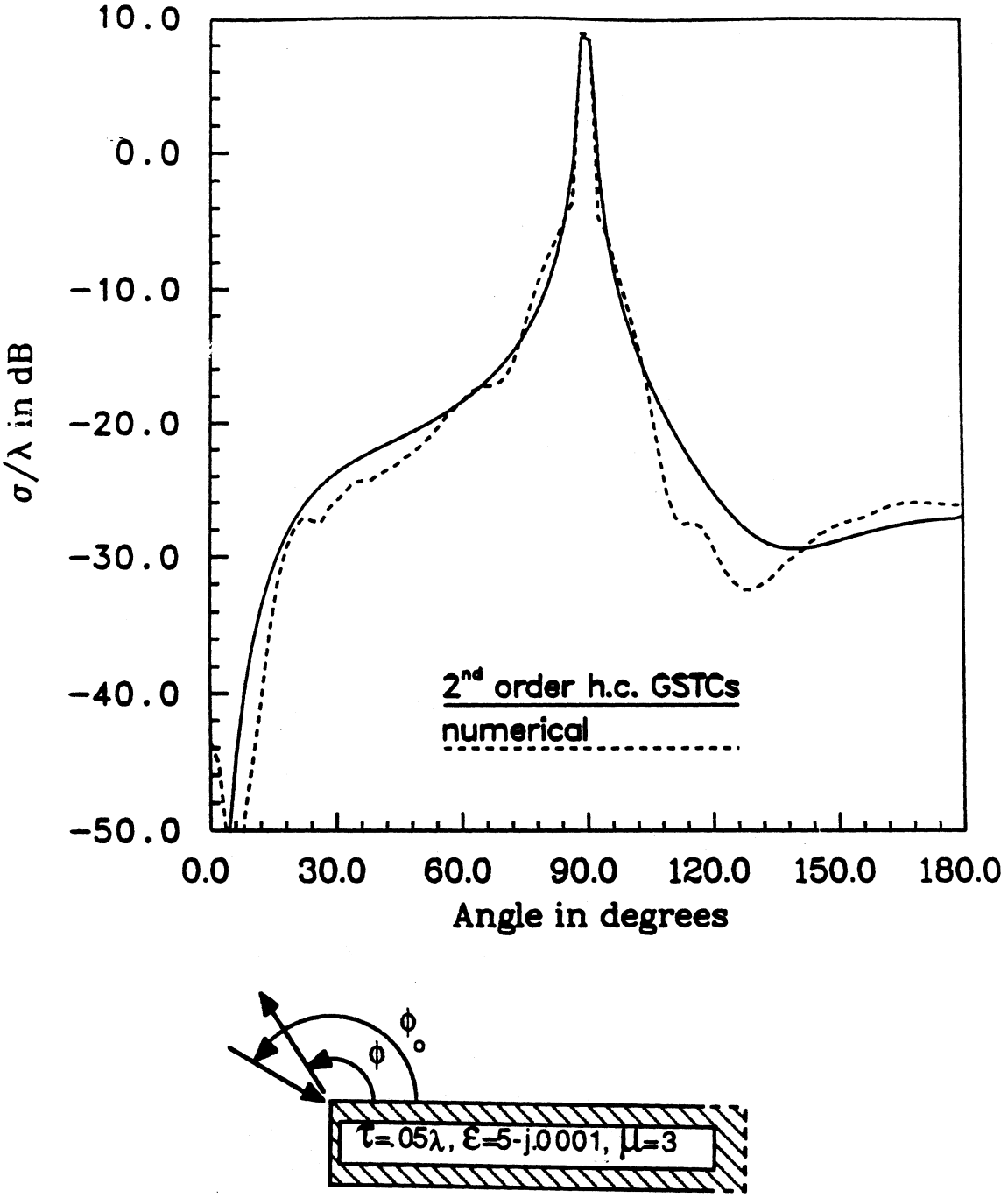

Figure 5.13: H_z polarization backscatter echo width for a material half-plane with $\tau = .05$, $\epsilon = 5$, $\mu = 3$ modeled by $O(\kappa^0)$ (even symmetry) and $O(\kappa^{-1})$ (odd symmetry) high contrast GSTC. The free space side is modeled by $O(\tau)$ (even symmetry) $O(\tau^2)$ (odd symmetry) low contrast GSTC. (see Table 5.3 for constants).

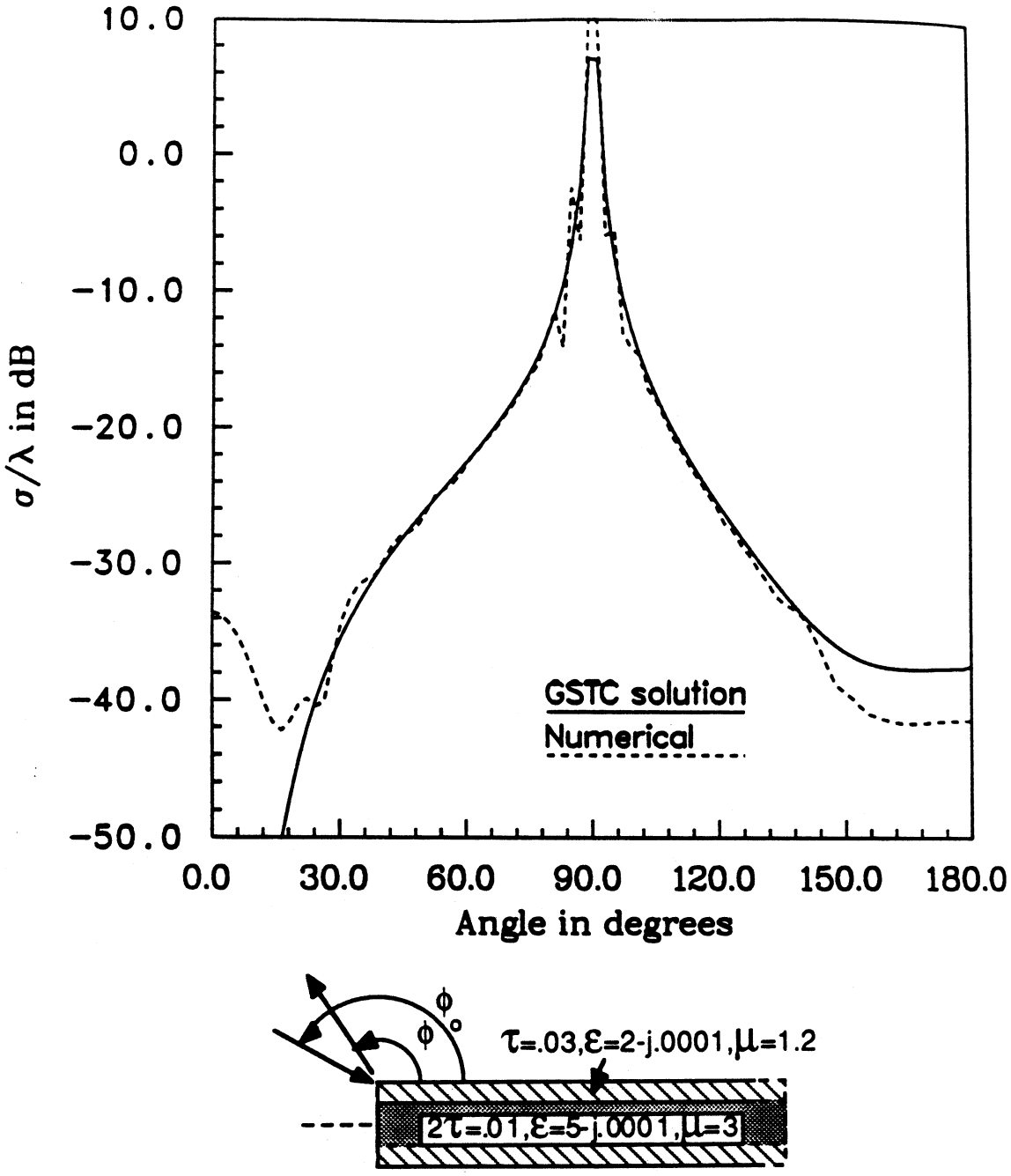

Figure 5.14: H_z polarization backscatter echo width for a two layer $.07\lambda$ symmetric material half-plane with $\tau_1 = .005$, $\epsilon_1 = 5$, $\mu_1 = 3$ and $\tau_2 = .03$, $\epsilon = 2$, $\mu = 1.2$. Layer 1 is modeled by $O(\kappa^0)$ GSTC, layer 2 and the free space layer are modeled by $O(\tau)$ (even symmetry) $O(\tau^2)$ (odd symmetry) low contrast GSTC (see Table 5.3 for constants).

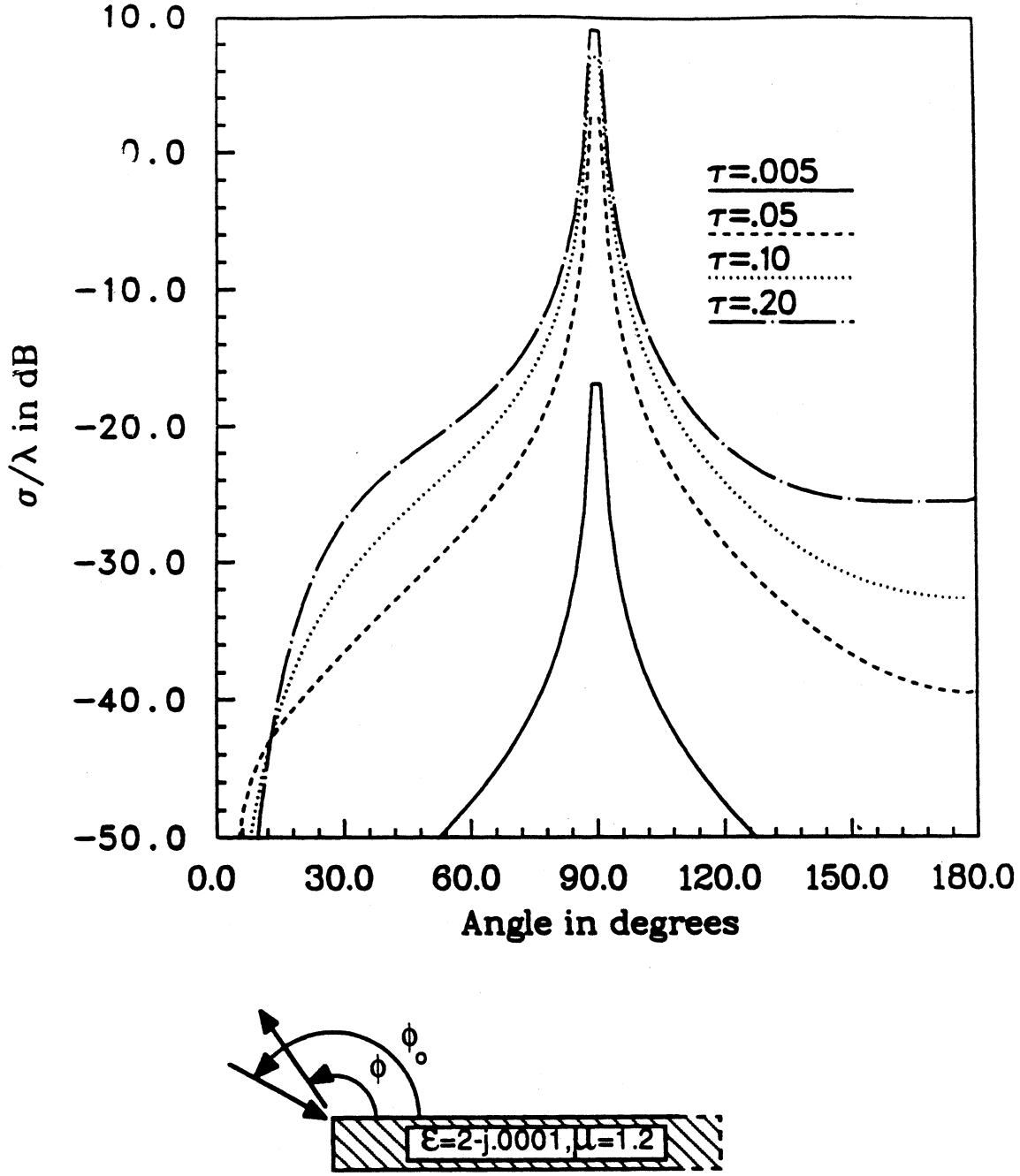

Figure 5.15: H_z polarization backscatter echo width curves for different thickness material half-planes with $\epsilon = 2$, $\mu = 1.2$. All cases are modeled by $O(\tau)$ low contrast GSTC (see Table 5.3 for constants).

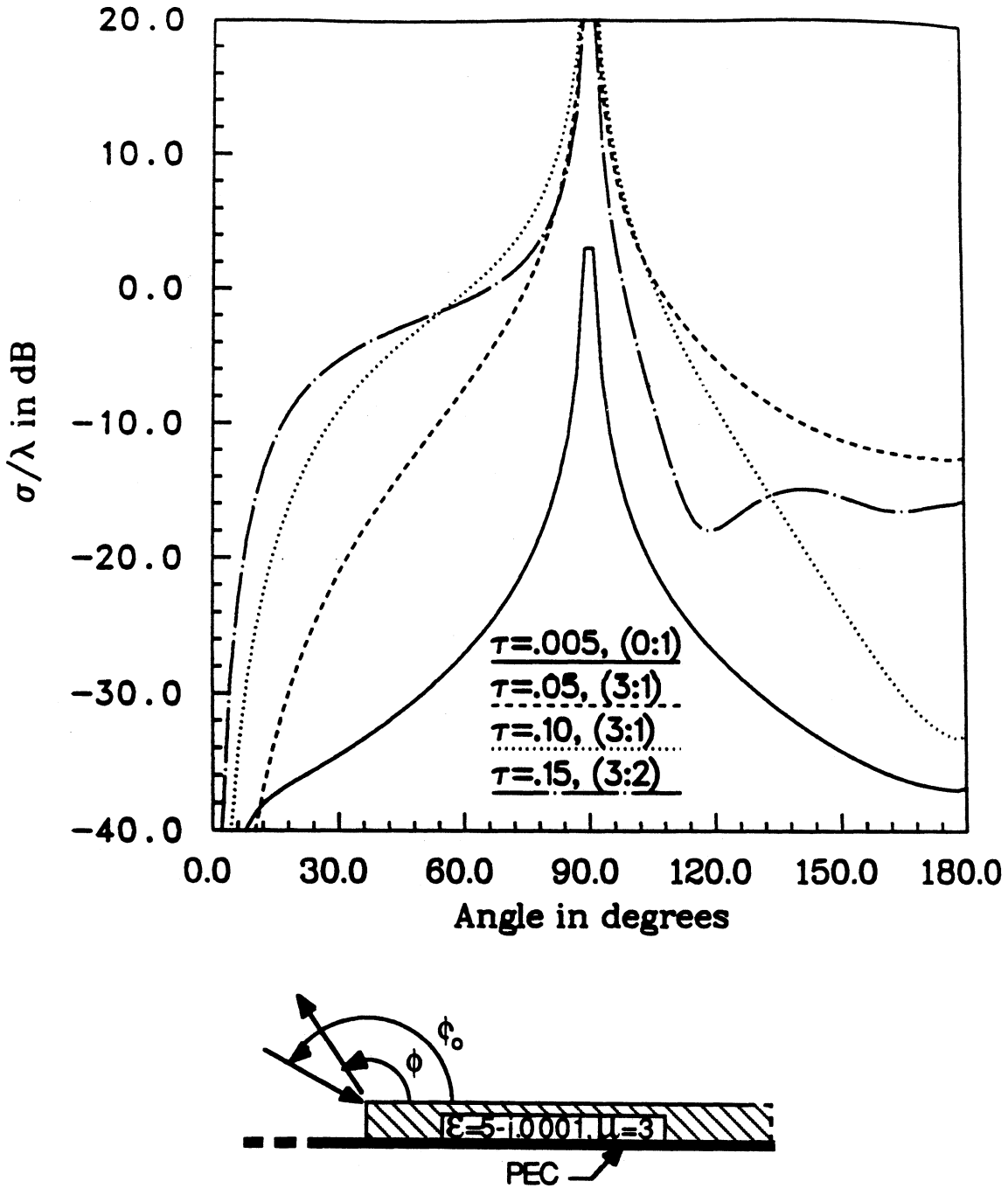

Figure 5.16: H_z polarization backscatter echo width curves for different thickness grounded slabs with $\epsilon = 5$, $\mu = 3$. The number to the left of the colon denotes the $O(\tau)$ of the l.c. GIBC for the free space side, and the number to the right of the colon denotes the $O(\kappa^{-1})$ of the h.c. slab GIBC.

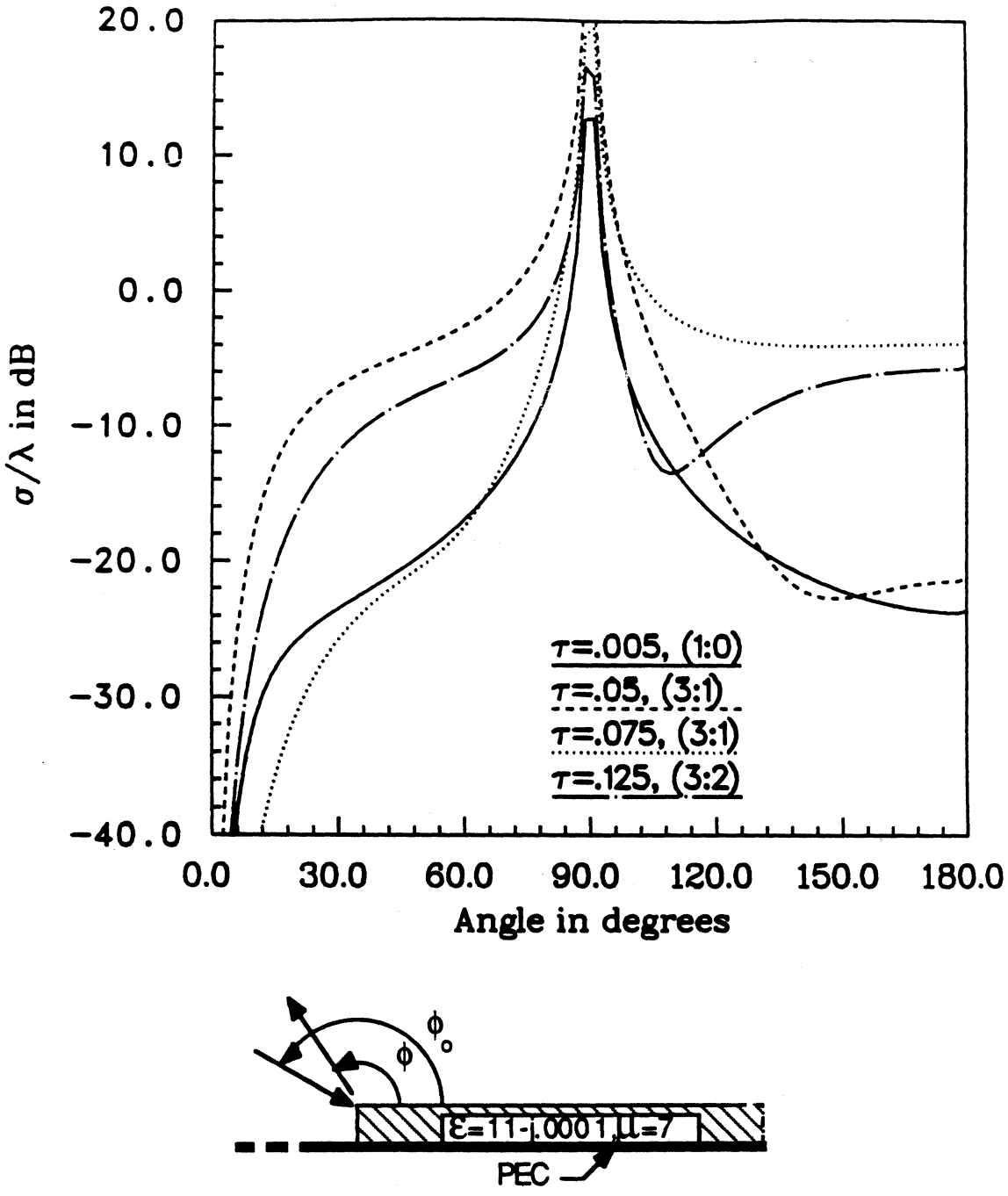

Figure 5.17: H_z polarization backscatter echo width curves for different thickness grounded slabs with $\epsilon = 11$, $\mu = 7$. The number to the left of the colon denotes the $O(\tau)$ of the l.c. GIBC for the free space side, and the number to the right of the colon denotes the $O(\kappa^{-1})$ of the h.c. GIBC for the right hand slab.

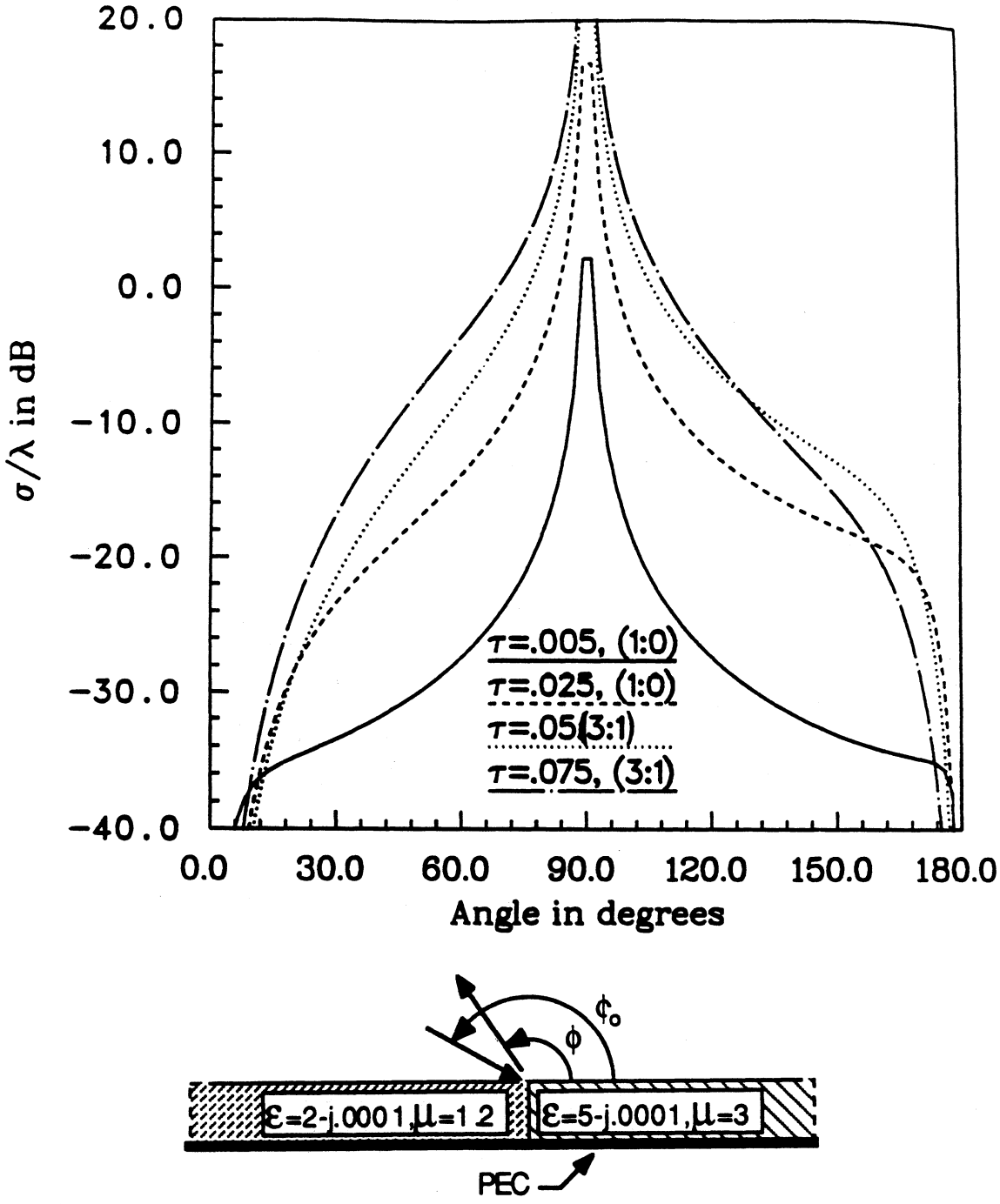

Figure 5.18: H_z polarization backscatter echo width curves for different thickness grounded junctions, with $\epsilon_1 = 2$, $\mu_1 = 1.2$ and $\epsilon_2 = 5$, $\mu_2 = 3$. The number to the left of the colon denotes the $O(\tau)$ of the l.c. GIBC for the left hand slab and the number to the right of the colon denotes the $O(\kappa^{-1})$ of the h.c. GIBC for the right hand slab.

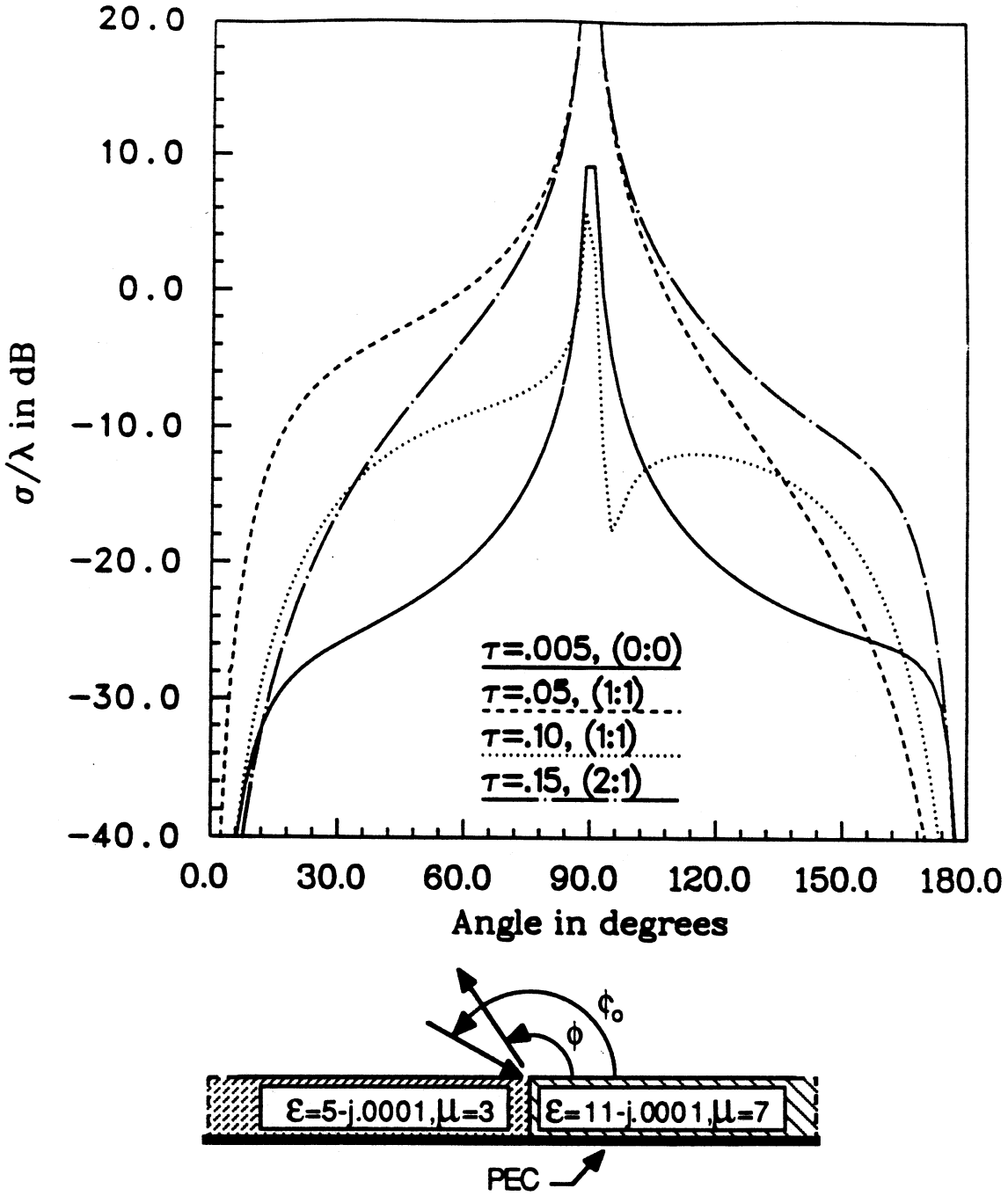

Figure 5.19: H_z polarization backscatter echo width curves for different thickness grounded junctions, with $\epsilon_1 = 5$, $\mu_1 = 3$ and $\epsilon_2 = 11$, $\mu_2 = 7$. The number to the left of the colon denotes the $O(\kappa^{-1})$ of the h.c. GIBC for the left hand slab and the number to the right of the colon denotes the $O(\kappa^{-1})$ of the h.c. GIBC for the right hand slab.

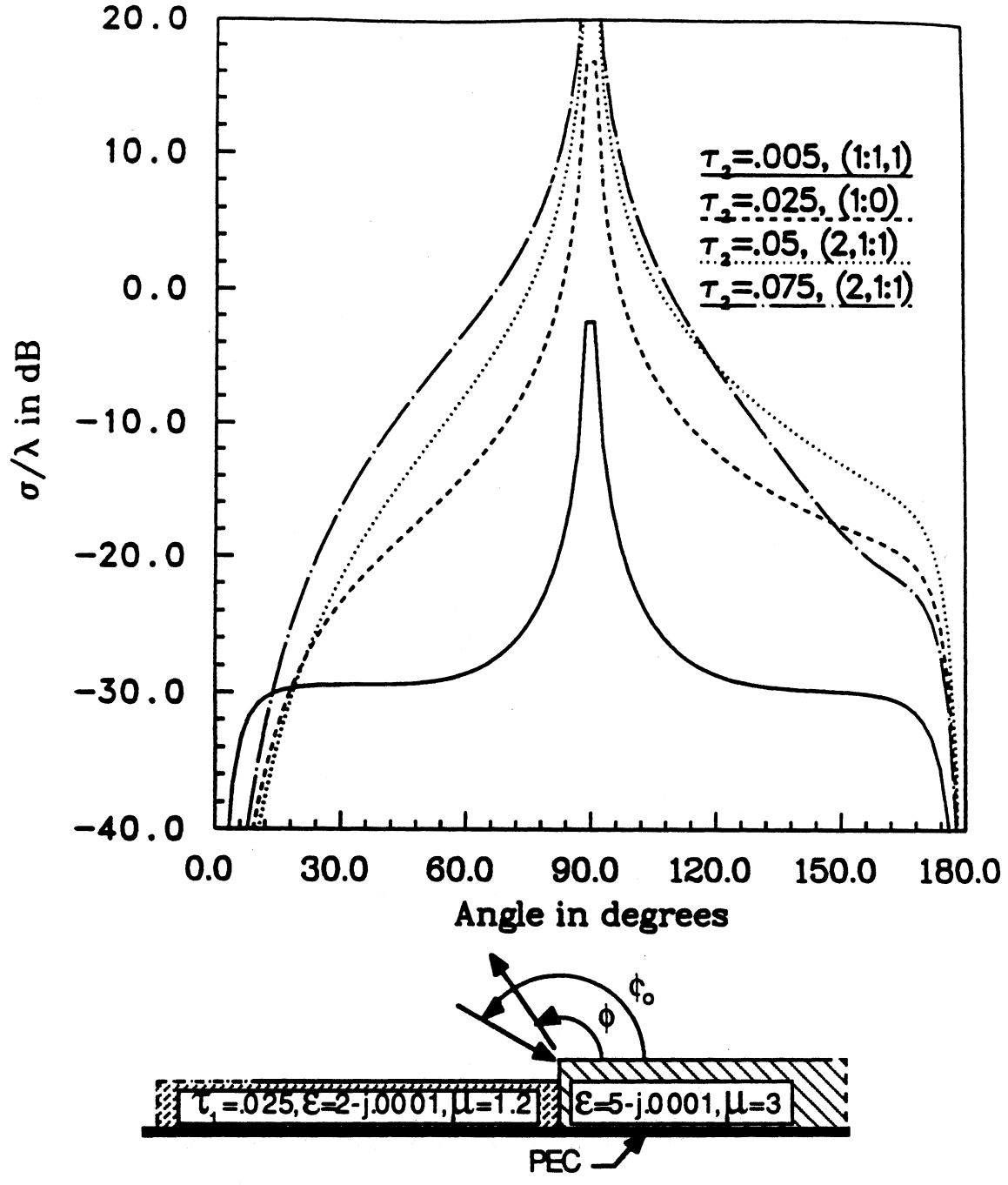

Figure 5.20: H_z polarization backscatter echo width curves a grounded junctions, with $\epsilon_1 = 2$, $\mu_1 = 1.2$, $\tau_1 = .025$ and $\epsilon_2 = 5$, $\mu_2 = 3$. The first number to the left of the colon denotes the $O(\tau)$ of the l.c. GIBC for the left hand slab and the first number to the right of the colon denotes the $O(\kappa^{-1})$ of the h.c. GIBC for the right hand slab. The second number on either side of the colon denotes the $O(\tau)$ of the l.c. GIBC for the free space slab needed to give the two sides the same thickness.

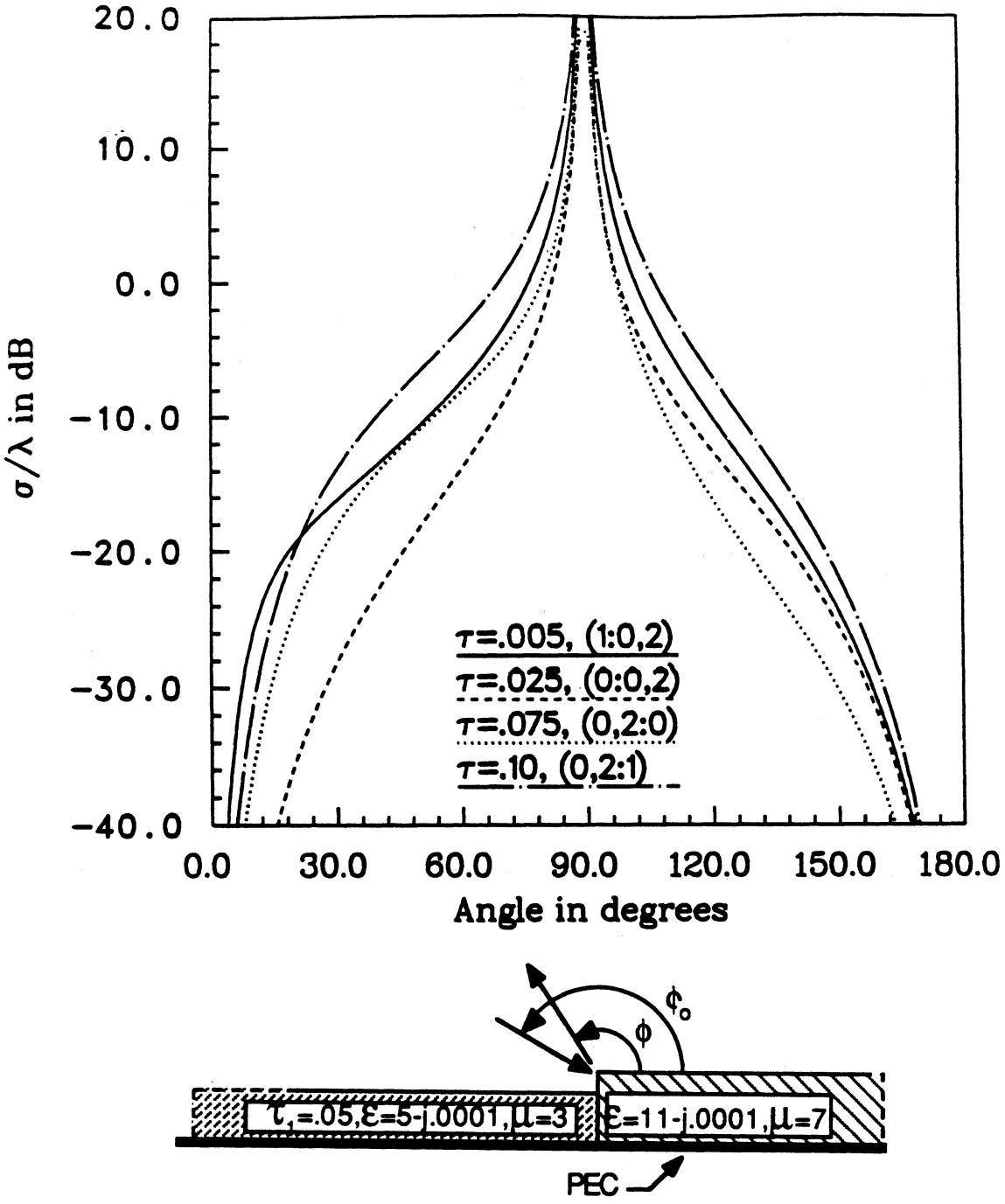

Figure 5.21: H_z polarization backscatter echo width curves a grounded junctions, with $\epsilon_1 = 5$, $\mu_1 = 3$, $\tau_1 = .05$ and $\epsilon_2 = 11$, $\mu_2 = 7$. The first number to the left of the colon denotes the $O(\kappa^{-1})$ of the h.c. GIBC for the left hand slab and the first number to the right of the colon denotes the $O(\kappa^{-1})$ of the h.c. GIBC for the right hand slab. The second number on either side of the colon denotes the $O(\tau)$ of the l.c. GIBC for the free space slab needed to give the two sides the same thickness.

```
       FIGURE 5.5
GIBC(GSMF)-PEC STUB          GIBC-PEC STUB
  b10 = -0.0451+j0.0212        b10 = -0.0451+j0.0213
GIBC(GSMF)-PMC STUB          GIBC-PMC STUB
  b10 = 0.6875+j0.3242         b10 = 0.6875+j0.3242

      FIGURE 5.6
GIBC(GSMF)
  b10 = -0.4578+j0.2593  b11 = -0.0408-j0.0111
  b20 = -0.0401-j0.0388
GIBC
  b10 = -0.4596+j0.2599  b11 = -0.0410-j0.0110
  b20 = -0.0400-j0.0388

      FIGURE 5.7
GIBC(GSMF)                   GIBC
  b10 = -0.0831+j0.0489        b10 = -0.0837+j0.0489
      FIGURE 5.8
GIBC
  b10 = -.0000+j.0000

      FIGURE 5.9
GIBC
  b10 = .0022-j.0009

      FIGURE 5.10
GIBC
  b10 = .0008-j.2323

      FIGURE 5.11
GIBC 2nd order
  b10 = 0.0152-j0.0166
GIBC 4th order
  a10 = -0.0734+j0.0138  a11= 0.0145-j0.0010
  a20 = -0.0022+j0.0103

  b10 =  0.0350-j0.0368  b11 =  0.0146+j0.0097  b12 = 0.0035-j0021
  b20 = -0.0013+j0.0565  b21 = -0.0004+j0.0125
  b30 = -0.0022-j0.0015
```

Table 5.2: Values of solution constants for curves presented in Figures 5 to 12

```
      FIGURE 5.12
  a10 =  -0.0012-j0.0000

  b10 =   0.0019-j0.0005

      FIGURE 5.13
  a10 = -0.0798-j0.0054

  b10 =  0.0171-j0.0239  b11 =  0.0090+j0.0002
  b20 = -0.0019+j0.0011

      FIGURE5.14
  a10 = 0.0003-j0.0000

  b10 =  0.0180-j0.0102  b11 = -0.0060+j0.0002
  b20 =  0.0002-j0.0001

      FIGURE5.15
t=.005
  b10 = -.0000+j.0000
t=.05
  b10 =  .0022-j.0009
t=.10
  b10 =  .0008-j.2323
t=.20
  b10 =  0.0152-j0.0166
```

Table 5.3: Values of solution constants for curves presented in Figures 12 to 15

5.5 Summary

In this chapter a method was proposed and demonstrated for determining the unknown constants. Specifically, an eigenfunction expansion was presented as a representation for both the interior and exterior fields. The solution of chapter four was then recast into this form, allowing the unknown constants to be determined by imposing additional continuity conditions across the junction. Various scattering patterns were given validating the derived diffraction solution for several material half-planes and junctions.

CHAPTER VI

SUMMARY

The goal of this dissertation was to develop a plane wave diffraction coefficient for thick multilayered symmetric slab junctions using simulations based on the generalized impedance boundary conditions and generalized sheet transition conditions. This task was accomplished in four chapters dealing with the derivation of the GIBC/GSTC, the formulation and formal solution of the plane wave diffraction by a class of slab junctions, and the subsequent resolution of the unknown constants which arise in these solutions.

To model multilayered slab junctions, it was first necessary to develop GIBC and GSTC for multilayered planar slabs, and this was the subject of chapter two. Recurrence relations were initially developed to relate fields in the adjacent layers of a multilayered structure, and these were subsequently used to derive infinite order boundary/transition conditions, conveniently expressed in a matrix product with each matrix corresponding to a layer. Low and high contrast approximations were then introduced to approximate the individual elements of each layer-matrix leading to a finite order GIBC/GSTC for the multilayered slab. Since each individual layer in the slab was characterized by a separate matrix, a low or a high contrast approximation could be employed for each individual matrix as dictated by the refractive

index of the layer. The accuracy of the derived conditions was evaluated by comparing the GIBC/GSTC reflection coefficients to their exact counterparts and design curves were given for various single layer geometries based on the maximum phasor error of the approximation.

In chapter three, the plane wave diffraction by a recessed slab in a ground plane was formulated and solved via the GSMF in conjunction with the dual integral equation method. The motivation for studying this geometry stemmed from the availability of exact data for uniform slabs. It thus served as a reference for evaluating the accuracy of GIBC in junction simulations. Furthermore, the employed GIBC simulation resulted in a unique solution, thus bypassing the non-uniqueness issue associated with GIBC/GSTC simulations of more arbitrary material junctions.

The diffraction by a material discontinuity in a thick dielectric/ferrite slab was considered in chapter four. The slab was modeled by a distributed current sheet obeying generalized sheet transition conditions (GSTCs). This representation was then used to develop dual integral equations in terms of even and odd unknown spectral functions, which were proportional to the sheet currents. The solution for the spectra paralleled standard procedure but resulted in expressions involving unknown constants, revealing the non-uniqueness of the GSTC. It was demonstrated that the unknown constant(s) could be determined explicitly for the recessed slab discussed in chapter three by comparison with the results therein and it was also shown that the obtained solution reduces to simpler known solutions, including that for combinations of resistive and conductive sheets junctions.

One way of determining the unknown solution constants discussed in chapter four is to employ field continuity across the junction. This however requires knowledge of the interior fields and in an effort to determine them, an eigenfunction decompo-

sition was developed for arbitrary symmetric multilayered slabs valid in the exterior and interior regions. The solution given in chapter four was then recast in this form permitting the determination of the interior slab field via analytic continuation. The unknown constants were then resolved by applying field continuity accross the junction. Specifically, a point matching scheme was proposed in which the junction was sampled across its width for different angles of incidence. The resulting unique solution was then verified for a number of recessed slab geometries by comparison with the GSMF solution in chapter three, and also for thin material half-planes whose scattering patterns were computed numerically. It was observed that the constants are very small for thin slab structures, but become significant with increasing slab thickness. Finally, family curves were generated for a number of half-plane and junction geometries, and it was found that the convergence of the GIBC/GSTC solutions can be estimated by leaving out the solution constants.

Clearly, the most challenging part of this work was the determination of the unknown solution constants. The mere fact that this was possible proved that the GSTC/GIBC are useful for practical simulations. Certainly, the method used in chapter five for determining the constants could be employed or paralleled in other applications. However, as noted therein, the evaluation of the constants for higher order GSTC simulations becomes numerically intensive and it would, therefore, be desirable to find alternative means for accomplishing this. For example, instead of point matching one could explore the orthogonality of the expansion modes or perhaps use a more efficient evaluation of the integrals.

In this work we explored one application of the GSTC/GIBC simulation, that of diffraction by multilayered material slab junctions. As can be expected there are numerous other applications where the GSTC/GIBC can permit analytical solu-

tions. Examples include the extension of this work to skew incidence; possible characterization of junctions other than vertical where this solution may be employed in conjunction with a numerical one; and the diffraction by material junctions on curved surfaces at normal and skew incidences. Also, the characterization of multiple diffraction effects among material junctions is a straightforward process following the method already employed in [13].

APPENDICES

APPENDIX A

MULTIPLICATIVE SPLIT FUNCTIONS

In this appendix we consider the splitting of

$$\mathcal{G}\left(\lambda^2\right) = \mathcal{U}_A\left(\lambda^2\right) + \sqrt{1-\lambda^2}\mathcal{U}_B\left(\lambda^2\right) \tag{A.1}$$

as a product of two functions, one of which is free of poles, zeros and branch cuts in the upper half of the λ plane and the other having the same properties in the lower half of the λ plane. That is, we seek to write $\mathcal{G}\left(\lambda^2\right)$ in the form

$$\mathcal{G}\left(\lambda^2\right) = \mathcal{G}_+\left(\lambda\right)\mathcal{G}_-\left(\lambda\right) \tag{A.2}$$

where the superscript + and - indicate an upper or lower function, respectively. Noting that

$$\mathcal{U}_A\left(\lambda^2\right) = \sum_{n=0}^{N_A} A_n\left[1-\lambda^2\right]^n \tag{A.3}$$

$$\mathcal{U}_B\left(\lambda^2\right) = \sum_{n=0}^{N_B} B_n\left[1-\lambda^2\right]^n \tag{A.4}$$

with $N_A = N_B$ or $N_A = N_B + 1$, we may rewrite $\mathcal{G}\left(\lambda^2\right)$ as

$$\mathcal{G}\left(\lambda^2\right) = \sum_{n=0}^{N_S} S_n\left[\sqrt{1-\lambda^2}\right]^n \tag{A.5}$$

where $N_s = Max(2N_A, 2N_B + 1)$ and $S_n = A_{n/2}$ if n is even and $S_n = B_{(n-1)/2}$ if n is odd. However, since we seek a multiplicative splitting of (A.5), a more convenient

form to represent $\mathcal{G}(\lambda^2)$ is

$$\mathcal{G}\left(\lambda^2\right) = S_0 \prod_{n=1}^{N_S} \left(1 + \frac{\sqrt{1-\lambda^2}}{\gamma_n}\right) \tag{A.6}$$

in which γ_n denote the zeros of the polynomial $\sum_{l=0}^{N_S} S_l (-\lambda)^l$. We immediately now identify that each of the product terms in (A.6) can be factored as

$$1 + \frac{\sqrt{1-\lambda^2}}{\gamma} \stackrel{def}{=} M_+(\lambda;\gamma)\, M_-(\lambda;\gamma) \tag{A.7}$$

where

$$K_+(\lambda; 1/\gamma) = \frac{\sqrt{1-\lambda}}{M_+(\lambda;\gamma)} \tag{A.8}$$

is the split function characteristic to the impedance half plane having a constant surface impedance $1/\gamma$ [34]. With the branch choosen so that $Im(\sqrt{1-\lambda^2}) < 0$, $M_+(\lambda;\gamma)$ is explicitly given by

$$M_+(\lambda;\gamma) = M_-(-\lambda;\gamma) = \begin{cases} \widetilde{M}_+(\lambda;\gamma) & Im(\gamma) \le 0 \\ \frac{j\eta\left(\lambda - \sqrt{1-\gamma^2}\right)}{\widetilde{M}_+(\lambda;-\gamma)} & Im(\gamma) > 0, \end{cases} \tag{A.9}$$

$$\widetilde{M}_+(\cos\alpha; 1/\eta) = \frac{\Psi_\pi^4(\pi/2)\left[1 + \sqrt{2}\cos\left(\frac{\pi/2-\alpha+\theta}{2}\right)\right]\left[1 + \sqrt{2}\cos\left(\frac{3\pi/2-\alpha-\theta}{2}\right)\right]}{\sqrt{\frac{8}{\eta}}\left[\Psi_\pi(3\pi/2-\alpha-\theta)\,\Psi_\pi(\pi/2-\alpha+\theta)\right]^2} \tag{A.10}$$

In this,

$$Im(\eta) \ge 0$$

$$\lambda = \cos\alpha$$

$$Im\left(\sqrt{1-1/\eta^2}\right) \le 0$$

$$\theta = \sin^{-1}(\eta) \text{ with } 0 \le Re(\theta),$$

and $\Psi_\pi(\alpha)$ is the Maliuzhinets function [22] whose evaluation in algebraic form has been given in [50]. We remark that in the limit as $\gamma \to 0$,

$$M_+(\lambda;\gamma \to 0) = \frac{\sqrt{1-\lambda^2}}{\sqrt{\gamma}} \tag{A.12}$$

and as $\gamma \to \infty$

$$M_+(\lambda; \gamma \to \infty) = 1 \tag{A.13}$$

The determination of $\mathcal{G}^{\pm}(\lambda)$ is now rather trivial. By substituting (A.7) into (A.6) we easily obtain

$$\mathcal{G}_+(\lambda) = \mathcal{G}_-(-\lambda) = \sqrt{S_0} \prod_{n=1}^{N_S} M_+(\lambda; \gamma_n) \tag{A.14}$$

BIBLIOGRAPHY

BIBLIOGRAPHY

[1] Anderson, I., "Plane wave diffraction by a thin dielectric half-plane," *IEEE Trans. on Antennas and Propagat.*, Vol. AP-27, No. 5, pp. 584-589, September 1979.

[2] Angulo, C. M., "Diffraction of surface waves by a semi-infinite dielectric slab," *IRE Trans. on Antennas and Propagat.*, Vol. AP-5, pp. 100-109, January 1957.

[3] Aoki, K. and K. Uchida, "Scattering of a plane electromagnetic wave by two semi-infinite dielectric slabs," *The Trans. of the IECE of Japan*, Vol. 62-B, No. 12, pp. 1132-1139, 1979.

[4] Bernard, J. M. L., "Diffraction by Metallic Wedge Covered with a Dielectric Material," *Wave Motion*, Vol. 9, No. 6, pp. 543-561, November 1987.

[5] Büyükaksoy, Alinur, Gökhan Uzgören, and A. Hamit Serbest, "Diffraction of an obliquely incident plane wave by the discontinuity of a two part thin dielectric plane," *International Journal of Engineering Science*, Vol. 27, No. 6, pp. 701-710, 1989.

[6] Bates, C. P., and R. Mittra, "Waveguide excitation of dielectric and plasma slabs," *Radio Science*, Vol. 3, No. 3, pp. 251-266, March 1968.

[7] Chakrabarti, A., "Diffraction by a dielectric half-plane," *IEEE Trans. on Antennas and Propagat.*, Vol. AP-34, No. 6, pp. 830-833, June 1986.

[8] Chang, D.C., and E. F. Kuester, "Total and partial reflection from the end of a parallel-plate waveguide with an extended dielectric slab," *Radio Science*, Vol. 16, No. 1, pp. 1-13, January-February 1981.

[9] Chuang, C. W., "Surface wave diffraction by a truncated inhomogeneous dielectric slab recessed in a conducting surface," *IEEE Trans. on Antennas and Propagat.*, Vol. AP-34, pp. 496-502, April 1986.

[10] Clemmow, P. C., "A method for the exact solution of a class of two-dimensional diffraction problems," *Proc. Roy. Soc. A*, Vol. 205, pp. 286-308, 1951.

[11] Fong, T. T., "Radiation from an open-ended waveguide with extended dielectric loading," *Radio Science*, Vol. 7, No. 10, pp. 965-972, October 1972.

[12] Harrington, R. F. and J. R. Mautz, "An impedance sheet approximation for thin dielectric shells," *IEEE Trans. Antennas Propagat.*, Vol. AP-23, pp. 531-534, July 1975.

[13] Herman, M. I., and J. L. Volakis, "High frequency scattering from polygonal impedance cylinders and strips," *IEEE Trans. on Antennas and Propagat.*, Vol. AP-36, pp. 679-689, May 1988.

[14] Jones, W. R., "A new approach to the diffraction of a surface wave by a semi-infinite grounded dielectric slab," *IEEE Trans. on Antennas and Propagat.*, Vol. AP-12, pp. 767-777, November 1964.

[15] Kane, J. and S. N. Karp, "An Accurate Boundary Condition to Replace Transition Condition at Dielectric-Dielectric Interfaces," Institute of Mathematical Sciences Division of E.M. Research, New York University, New York, N. Y., Research Report EM-153, May 1960a.

[16] Kane, J. and S. N. Karp, "Radio Propagat. past a Pair of Dielectric Interfaces," Institute of Mathematical Sciences Division of E.M. Research, New York University, New York, N. Y., Research Report EM-154, May 1960b.

[17] Karp, S. N. and F. C. Karal Jr., "Generalized Impedance Boundary Conditions with Applications to Surface Wave Structures," in Electromagnetic Wave Theory, Part 1, ed. J. Brown, pp. 479-483, Pergamon: New York, 1965.

[18] Kay, A. F., "Scattering of a surface wave by a discontinuity in reactance," *IRE Trans. on Antennas and Propagat.*, Vol. AP-7, pp. 22-31, January 1959.

[19] Kouyoumjian, R. G., "The general theory of diffraction and its applica tions," in Numerical and Asymptotic Techniques in Electromagnetics, R. Mittra, Ed., New York, Springer-Verlag, 1975.

[20] Lee, S. W., and R. Mittra, "Diffraction by thick conducting half-plane and a dielectric-loaded waveguide," *IEEE Trans. Antennas and Propagat.*, Vol. AP-16, No. 4, pp. 454-461, July 1968.

[21] Leppington, F. G., "Traveling waves in a dielectric slab with an abrupt change in thickness," *Proc. Roy. Soc.* (London), Vol. A386, pp. 443-460, 1983.

[22] Maliuzhinets, G.D., " Excitation, Reflection and Emission Of Surface Waves From a Wedge With Given Face Impedances," *Sov. Phys. Dokl.*, Engl. Transl., Vol. 3, 752-755, 1958.

[23] Mitzner, K. M., "Effective boundary conditions for reflection and transmission by an absorbing shell of arbitrary shape," *Trans. on Antennas and Propagat.*, Vol. AP-16, pp. 706-712, November 1968.

[24] Noble, B., Methods based on the Weiner Hopf Technique, Pergamon Press, 1958.

[25] Pace, J. R. and R. Mittra, "Generalized scattering matrix analysis of waveguide discontinuity problems," Proc. Symp. Quasi-Optics, Vol. 14, Brooklyn, N.Y., Polytechnic Inst. of Brooklyn Press, pp. 177-197, 1964.

[26] Pathak, P. H., and R. G. Kouyoumjian, "Surface wave diffraction by a truncated dielectric slab recessed in a perfectly conducting surface," *Radio Science*, Vol. 14, No. 3, pp. 405-417, May-June 1979.

[27] Pathak, P. H., and R. G. Rojas, "A UTD analysis of the em diffraction by an impedance discontinuity in a planar surface," *Journal of Wave-Material Interaction*, Vol. 1, pp. 16-37, January 1986.

[28] Ricoy, M. A., and J. L. Volakis, "*E*-Polarization diffraction by a thick metal-dielectric join," *Journal of Electromagnetic Waves and Applications*, Vol. 3, No. 5, pp. 383-407, 1989.

[29] Rojas, R. G., "A uniform GTD analysis of the em diffraction by a thin dielectric/ferrite half-plane and related configurations," Ph.D. Dissertation, The Ohio State University, Department of Electrical Engineering, Columbus, Ohio, 1985.

[30] Rojas, R. G., "Weiner-Hopf Analysis of the em diffraction by an impedance discontinuity in a planar surface and by an impedance half-plane," *IEEE Trans. on Antennas and Propagat.*, Vol. AP-36, No. 1, pp. 71-83, January 1988.

[31] Rojas, R. G., and Z. Al-hekail, "Generalized Impedance/Resistive Boundary Conditions for Electromagnetic Scattering Problems," *Radio Science*, Vol. 24, No. 1, pp. 1-12, Jan-Feb 1989.

[32] Rojas, R. G., "Diffraction of EM Waves by a Dielectric/Ferrite Half Plane and Related Configurations," *IEEE Trans. on Antennas and Propagat.*, Vol. AP-37, pp. 751-763, June 1989.

[33] Rojas, R. G., "EM plane wave diffraction by two- and three-part thin, planar dielectric/ferrite slab," presented at the 1990 AP-S/URSI Symposium, Dallas, Texas, May 9, 1990.

[34] Senior, T. B. A., "Diffraction by a semi-infinite metallic sheet, *Proc. Roy. Soc.* (London), Vol. A213, pp. 436-458, 1952.

[35] Senior, T. B. A., "Impedance Boundary Conditions for Imperfectly Conducting Surfaces," *Appl. Sci. Res.*, Vol. 8(B), pp. 418-436, 1960.

[36] Senior, T. B. A., "Approximate Boundary Conditions," *IEEE Trans. on Antennas and Propagat.*, Vol. AP-29, pp. 826-829, 1981.

[37] Senior, T. B. A., "Combined Resistive and Conductive Sheets," *IEEE Trans. on Antennas and Propagat.*, Vol. AP-33, No. 5, pp. 577-579, May 1985.

[38] Senior, T. B. A., "A Critique of Certain Half Plane Diffraction Analyses," *Electromagnetics*, Vol. 7, pp. 81-90, 1987.

[39] Senior, T. B. A., and J. L. Volakis, "Sheet Simulation of a Thin Dielectric Layer," *Radio Science*, Vol. 22, No. 7, pp. 1261-1271, December 1987.

[40] Senior, T. B. A., "Skew Incidence on a Dielectric Half-Plane," *Electromagnetics*, Vol. 9, No. 2, pp. 187-200, 1989.

[41] Senior, T. B. A., "Diffraction by a Generalized Impedance Half Plane," presented at URSI International Electromagnetic Wave Theory Symposium, Stockholm, Sweden, 14-17 August 1989.

[42] Senior, T. B. A., and M. A. Ricoy, "On the Use of Generalized Impedance Boundary Conditions," presented at the 1990 AP-S/URSI Symposium, Dallas, Texas, May 8, 1990.

[43] Senior, T. B. A. and J. L. Volakis, "Derivation and Application of a Class of Generalized Boundary Conditions," *IEEE Trans. on Antennas and Propagat.*, Vol. AP-37, No. 12, December 1989.

[44] Senior, T. B. A., "Diffraction by a Material Junction," submitted to *IEEE Trans. Antennas and Propagat.*

[45] Shevchenko, V. V., Continuous Transitions in Open Waveguides, Golem Press: Boulder, CO., 1971.

[46] Sunahara, Y., and T. Sekiguchi, "Ray theory of diffraction by a half-sheet parallel to a flat earth," *Radio Science*, Vol. 16, No. 1, pp. 141-155, January-February 1981.

[47] Tiberio, R., and G. Pelosi, "High frequency scattering from the edges of impedance discontinuities on a flat plane," *IEEE Trans. on Antennas and Propagat.*, Vol. AP-31, No. 4, pp. 590-596, July 1983.

[48] Uchida, K., and K. Aoki, "Radiation from and surface whave excitation by an open-ended dielectric-loaded parallel-plate waveguide," *Trans. IECE Japan*, Vol. E-67, No. 4, pp. 218-224, April 1984.

[49] Van Bladel, J., "Field singularities at metal-dielectric wedges," *IEEE Trans. on Antennas and Propagat.*, Vol. AP-33, No. 4, pp. 450-455, April 1985.

[50] Volakis, J. L., and T. B. A. Senior, "Simple expressions for a function occurring in diffraction theory," *IEEE Trans. Antennas Propag.*, Vol. AP-33, pp. 678-680, June 1985.

[51] Volakis, J. L., and M. I. Herman, "A uniform asymptotic evaluation of integrals," *Proceedings of the IEEE*, Vol. 74, No. 7, pp. 1043-1044, July 1986.

[52] Volakis, J. L., and M. A. Ricoy, "Diffraction by a thick perfectly conducting half-plane," *IEEE Trans. on Antennas and Propagat.*, Vol. AP-35, No. 1, pp. 62-72, January 1987.

[53] Volakis, J. L., and T. B. A. Senior, "Diffraction by a Thin Dielectric Half Plane," *IEEE Trans. on Antennas and Propagat.*, Vol. AP-35, No. 12, pp. 1483-1487, December 1987.

[54] Volakis, J. L., "High Frequency Scattering by a Material Half-Plane and Strip," *Radio Science*, Vol. 23, No. 3, pp. 450-462, May-June 1988.

[55] Volakis, J. L., and T. B. A. Senior, "Diffraction by a coated wedge using second and third order generalized boundary conditions," Radiation Laboratory Report 388967-8-T, The University of Michigan, Ann Arbor, Michigan, September 1988.

[56] Volakis, J. L., and T. B. A. Senior, "Application of a Class of Generalized Boundary Conditions to Scattering by a Metal-Backed Dielectric Half Plane," *Proceedings of the IEEE*, pp 796-805, May 1989.

[57] Volakis, J. L., and H. H. Syed, "Application of Higher Order Boundary Conditions to Scattering by Multilayered Coated Cylinders," University of Michigan Radiation Laboratory Report 389757-2-T, 1989.

[58] Volakis, J. L., and M. A. Ricoy, "*H*-Polarization diffraction by a thick metal-dielectric join," *IEEE Trans. on Antennas and Propagat.*, AP-37, No. 11, pp. 1453-1462, November 1989.

[59] Weinstein, L. A., The Theory of Diffraction and the Factorization Method, Golem Press: Boulder, CO., 1969.